The Search for CP Violation in Neutrino Oscillations at T2K

Raj K. Shah

Worcester College

University of Oxford

A thesis submitted in fulfilment of the requirements for the degree of

Doctor of Philosophy

Trinity Term, 2017

The Search for CP Violation in Neutrino Oscillations at T2K

Raj K. Shah

Worcester College, University of Oxford

A thesis submitted in fulfilment of the requirements for the degree of Doctor of Philosophy

Trinity Term, 2017

Abstract

T2K is a long-baseline neutrino oscillation experiment, designed to study the oscillation of a high-intensity muon neutrino beam produced by the J-PARC accelerator facility. Neutrinos are detected 295 km downstream of the production point at Super-Kamiokande, a 50 kt water Cherenkov detector capable of differentiating between muon neutrino and electron neutrino events. Two beam configurations are possible at T2K, each used to create neutrino beams composed of predominantly neutrinos or anti-neutrinos. Comparisons of the disappearance of muon neutrinos and the appearance of electron neutrinos in the neutrino and anti-neutrino beams are used to measure the neutrino oscillation parameters $\sin^2\theta_{23}$, Δm^2_{32}, $\sin^2\theta_{13}$ and δ_{CP}.

Presented in this thesis are the results of many analyses designed to study various combinations of the Super-Kamiokande oscillation data sets. Analyses considering the antineutrino beam data sets found no substantial evidence for $\bar{\nu}_e$ appearance in a $\bar{\nu}_\mu$ beam or $\bar{\nu}_\mu$ oscillation inconsistent with observed ν_μ oscillation. A combined study of all available Super-K oscillation samples measured $\delta_{CP} = -1.791^{+1.027}_{-0.998}$ rad and $\sin^2\theta_{13} = 0.0271^{+0.0071}_{-0.0062}$ under the normal mass ordering hypothesis with T2K data alone. With the addition of a constraint on $\sin^2\theta_{13}$ from external reactor experiments the study found $\sin^2\theta_{23} = 0.550^{+0.051}_{-0.085}$ and $\Delta m^2_{32} = 2.54^{+0.081}_{-0.080} \times 10^{-3} eV^2 c^{-4}$ under the normal mass ordering hypothesis. Due to the importance of the measurement, a different method was chosen to construct limits on the value of δ_{CP} with correct frequentist coverage.

This analysis excluded $\delta_{CP} = 0$ at the 2σ confidence level under both normal and inverted ordering hypotheses and produced a constraint of -2.978 rad $< \delta_{CP}$ $<$ -0.467 rad in the normal ordering hypothesis.

Statement of Originality

The work presented in this thesis is my own and was produced by me for the fulfilment of the degree of doctor of philosophy, at the University of Oxford. The work presented is based on my own original research, undertaken during the time I was a degree candidate, and has not been submitted for any other qualification. Figures and results from published works have all been attributed, and I have endeavoured to indicate, where necessary, work which was not carried out by myself throughout this thesis.

Chap. 2 includes a historical background of the field constructed from a review of work performed by others over the previous century. Chap. 3 is a description of the T2K experiment, which produced the data analysed in this thesis. Details of the construction, calibration and reconstruction software given in Chap. 3 are presented in this thesis for context and were performed by T2K collaborators. Chap. 4 details important components, which were built by collaborators, used for the work presented in this thesis. These have been clearly referenced where applicable. The development of the event selections at both near and far detectors, presented in Chap. 5, and all T2K near detector constraints, used for the work presented in this thesis, were also produced by collaborators.

The oscillation analyses presented in all subsequent chapters were performed by myself using the VALOR analysis framework, developed by myself, Costas Andreopoulos, Chris Barry, Francis Bench, Andrew Chappell, Thomas Dealtry, Steve Dennis, Lorena Escudero, Rhiannon Jones, Nick Grant, Marco Roda and Davide Sgalaberna. My main contributions to the work presented here include the results of all analyses presented in this thesis, the partial development and validation of the 5 sample Super-K fitting framework, the development and validation of tools for the production of response functions to include interaction uncertainties oscillation analyses, and the development of studies presented in Chaps. 9 to 12.

Acknowledgements

I'd like to thank the Oxford and RAL academics, Costas Andreopoulos, Giles Barr, Alfons Weber and Dave Wark, for their guidance and support throughout my DPhil. A special thanks to Helen, Trevor and Debra for their eternal support during my time as a DAQ expert.

The entire VALOR group, the work of which most of this thesis was built upon, for their support and indispensable advice. My fellow analyser in particular, Davide, who didn't seem to sleep and was always available for support.

I'd like to thank the TITUS and Hyper-K oscillation analysis groups with whom I produced countless sensitivity studies, all of which could sadly not make it into this document.

The T2K oscillation analysis group, in particular conveners, Claudio Giganti, Mark Hartz, and Atsuko Ichikawa for their leadership, and Mark Scott, the driving force behind the studies of interaction model bias. Also Ko, Leila, and Kirsty, without whom I would still be struggling with the oscillation analysis.

My family for their immeasurable support throughout my time at Oxford.

Finally, I must thank my fellow students for their friendship and for making my DPhil more fun and exciting than I could have ever hoped.

To Nivika,
thank you for your patience

Contents

List of Figures

List of Tables

Chapter 1

Introduction

From its origin in the 1930s neutrino physics has grown into one of the most vibrant and exciting fields of research, which has claimed a total of four Nobel prizes over the last thirty years. Neutrinos are notoriously difficult to detect, even though they remain one of the most abundant particles in the universe, and they require detectors of unprecedented size for their study due to their low interaction cross-section. The breadth of physics available when studying the neutrino includes but is not limited to solar physics, supernovas, geophysics, astrophysical sources of neutrinos and the large scale structure of the universe from the cosmic neutrino background. This is in addition to measurements of neutrino properties, some of which are beyond the standard model, such as possible mechanisms responsible for generating neutrino masses and neutrino oscillations.

The field of neutrino oscillations was given a decisive boost when measurements of neutrino mixing parameters $\sin^2\theta_{13}$, $\sin^2\theta_{23}$ and $\sin^2\theta_{12}$ allowed for the possibility of CP violation in neutrino oscillations. The last of the parameters to be measured, $\sin^2\theta_{13}$, which was found to be surprisingly larger than expected, implies that it is possible to make preliminary statements about the nature of CP violation in neutrino oscillations with the current generation of experiments.

Consequently, all of the studies presented in this thesis are connected by a common theme, which is CP asymmetry between neutrinos and anti-neutrinos.

The matter–antimatter asymmetry in the observable universe is apparent for all to see and the origin of which remains unexplained by particle physics or any other known mechanism. Although CP violation has been observed in the quark sector, first seen in kaon decay, the amount measured is insufficient to produce the asymmetry which is observed in the universe. In fact, the lack of CP violation observed in QCD has been labelled in the community as the "strong CP problem". Although the amount of possible CP violation in neutrino oscillations is unable to explain the matter–antimatter asymmetry, models have been put forward which relate the CP violation observed in neutrino oscillations to that which is responsible for the final baryon asymmetry in leptogenesis.

This thesis begins with Chap. 2, which contains a brief history of neutrino physics and a description of the current theory of neutrino oscillations. An overview of the current constraints on neutrino oscillation parameters is also given at the end of Chap. 2. Chap. 3 introduces the T2K experiment including a description of the neutrino beam, the near detector suite, the far detector and physics objectives. Essential components required for the oscillation analysis presented in this thesis are described in Chap. 4. Chap. 5 is a description of the structure of the oscillation analysis, with details of the near detector fit, the far detector selections and the effect of systematic uncertainties. Sec. 6.1 is a discussion of important statistical methods used in the analysis and how results may be interpreted. The expected sensitivity of the oscillation analysis is presented in Chap. 7 and results of the data fit in Chap. 8. Chaps. 9 and 10 describe further studies of the observed T2K data set which aid the interpretation of results. Additional studies, which consider the effect of interaction model choices, are presented in Chap. 11. Chap. 12 is a discussion of future long-baseline neutrino experiments, including optimisation studies performed for the Hyper-

Kamiokande experiment. Finally, a brief conclusion can be found in Chap. 13.

Chapter 2

Neutrino Theory

2.1 Postulation

The neutrino was first postulated to solve the problems surrounding beta radioactivity early in the 20th century which implied the non-conservation of energy and angular momentum. As the electron was the only particle observed to be emitted in beta decay, conservation of energy implied that the emitted electron should have a fixed energy. The problem arose when the energy spectrum of beta electrons was measured, by James Chadwick, to be continuous [1]. The observation was finally reconciled with the conservation of energy and angular momentum when Wolfgang Pauli proposed the existence of a light neutral particle, with a spin of 1/2, which he called the "neutron". When a heavier neutral particle was discovered by Chadwick two years after Pauli's original proposal [2], Pauli's "neutron" went on to become the neutrino, while Chadwick's neutral particle became the neutron we have today. A year after the discovery of the neutron Enrico Fermi introduced a weak coupling to describe the observations of beta decay which underpins the theory, still used today, as an effective theory for the weak interaction at low energies. A translation of Fermi's original paper can be found in [3].

2.2 Discovery

Using Fermi's effective theory, it was known that an intense source of neutrinos would be required to make a direct observation remotely possible on account of their low cross-section. Reines and Cowan proposed the use of a nuclear reactor at the Savannah River Plant in South Carolina as a high intensity source of anti-neutrinos and modern organic liquid scintillator as the detection material [4]. The interaction of anti-neutrinos with free protons in the liquid scintillator via inverse beta decay lead to a prompt positron signal and a delayed signal when the neutron captured on an atomic nucleus. The combination of the prompt and delayed signals, separated by a characteristic delay timescale, is what made it possible to separate the neutrino interaction signal from other backgrounds. Without the use of this "delayed coincidence", a much more intense source would have been required to observe neutrino interactions above background and leading physicists to suggest even nuclear weapons as a possible source. The experiment thus confirmed the existence of a very light neutral particle.

With the discovery the muon in 1937, and the observation of its decay into an electron and two light neutral particles in 1948, questions were raised as to whether the two neutral particles in the decay were in fact the same neutrino. This question was resolved in 1962 at the Brookhaven National Laboratory (BNL), New York State [5]. The experiment consisted of a proton beam incident on a fixed target producing pions which subsequently decayed into muons and their associated neutral partners, as shown in Eq. (2.1).

$$\pi^{\pm} \rightarrow \mu^{\pm} + \overset{(-)}{\nu}_{\mu} \tag{2.1}$$

The resulting beam of neutrinos and muons were directed to an aluminium spark chamber via a steel shield to remove the muons. 34 muon events were identified in comparison to 6 electron, when an equal number would have been expected if only one neutrino existed. The results therefore confirmed the existence of muon flavour neutrinos which are distinct from electron flavour neutrinos produced in beta decay. This was confirmed later, at a much higher significance, with measurements made at CERN in 1963 using spark and bubble chambers [6] [7].

Although by the late 1970s three charged leptons had been discovered along with two neutrinos to pair with the electron and the muon, it took until the year 2000 for the tau neutrino to be observed directly. The "Direct Observation of ν Tau" (DONUT) experiment at Fermilab, using photographic emulsion technology and an 800 GeV proton beam from the Tevatron particle accelerator, was the first to directly observe the tau neutrino [8]. Tau neutrino events were identified via their signature kinked tracks produced as taus decay shortly after being produced in a neutrino interaction.

Before the direct observation at DONUT, there was however very strong evidence of a third neutrino flavour to match the tau from the experiments studying heavy particle decays with missing momentum. The most compelling evidence, that was also able to put a constraint on the total number of light neutrino flavours, came from experiments in the LEP beam line at CERN in the 1990s [9].

The third neutrino flavour was inferred from the properties of the neutral weak gauge boson, the mediator of weak elastic lepton scattering. The lifetime, and therefore the width of the Z-pole, can be directly predicted in the standard model from the total number of particles the Z can decay into, and the corresponding coupling factors. The width of the Z-pole can be found from two complementary methods; first by direct measurement of the line-shape of the Z-pole in e^+e^- collisions, and also from the sum of the partial widths of all other observable decays. The difference between the total line-shape width Γ_{Tot} and the sum of the partial widths Γ_{Obs} is then defined to be the invisible width Γ_{Inv}

related by Eq. (2.2).

$$\Gamma_{Tot} = \Gamma_{Obs} + \Gamma_{Inv} \tag{2.2}$$

The invisible width is therefore expected to be the result of decays to neutrinos which are effectively undetectable by modern collider experiments. With the invisible width of the Z boson and the Standard Model prediction of the neutrino partial width, a combined measurement from the ALEPH, DELPHI, L3, OPAL and SLD collaborations found the number of light neutrinos to be N_ν = 2.984 ± 0.008. The precision of the result is highlighted in Fig. 2.1.

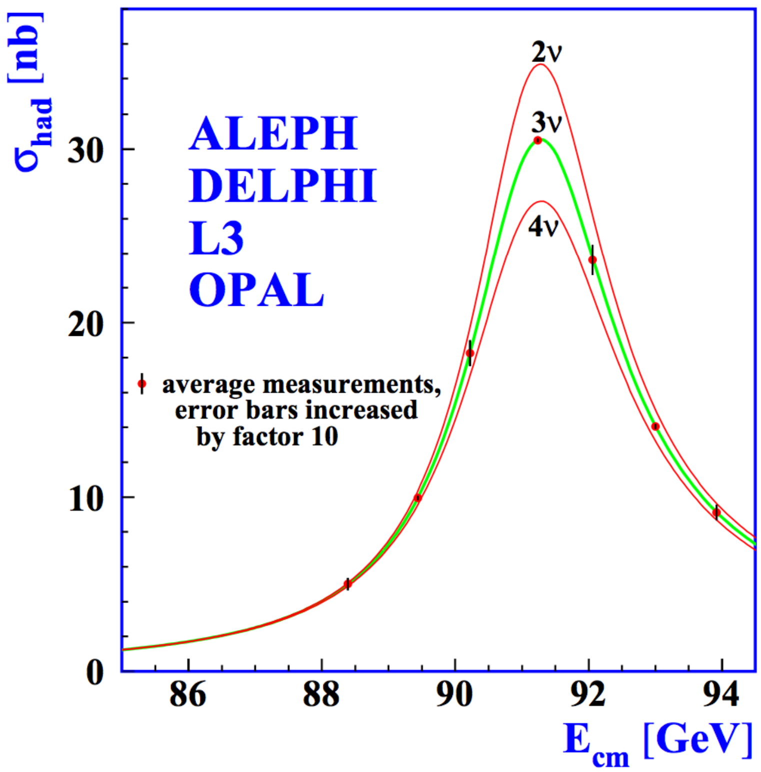

Figure 2.1: A comparison of the predicted hadron production cross-section at the Z boson resonance for various numbers of neutrino flavours and the data from the ALEPH, DELPHI, L3, OPAL and SLD collaborations. Neutrinos were assumed to have negligible mass and standard model couplings. Figure taken from [9].

2.3 Neutrino Properties

2.3.1 Neutrino Helicity

The helicity of the neutrino was first measured in 1957 in the Goldharber, Grodzins and Sunyar experiment at BNL [10]. ^{152m}Eu atoms, known to decay via orbital electron capture as shown in Eq. (2.3), were used to infer the neutrino helicity.

$$^{152m}Eu + e^- \rightarrow \nu + {}^{152}Sm^* \tag{2.3}$$

Around 20% of the decays of ^{152m}Eu were known to be from the capture of K shell electrons which carry no orbital angular momentum and the initial state was known to have a total spin of $1/2$ due to the electron. The helicity of the final ^{152}Sm, a spin 1 state, was determined to be the same as that of the neutrino as a consequence of the conservation of both momentum and angular momentum. The helicity of the ^{152}Sm state was then determined from the polarisation of the gamma ray emitted as it decayed into the ground state. Preferential selection of gamma rays which were emitted in the direction of the recoiling nucleus allowed the helicity of the nucleus, and therefore the neutrino, to be measured directly.

2.3.2 Charge

The neutrino is believed not to carry any electrostatic charge. The tightest constraint on the charge of the neutrino comes from observations of neutrinos from supernova 1987a which put an upper limit of $2 \times 10^{-15}e$ [11].

2.3.3 Magnetic Moment

The tightest constraint of the neutrino magnetic moment comes from the GEMMA experiment, at the Kalinin Nuclear Power Plant, from measurements of anti-neutrinos originating from a nuclear reactor [12]. GEMMA places an upper limit on the neutrino magnetic moment of $2.9 \times 10^{-11} \mu_b$.

2.3.4 Mass

The strongest constraints on the neutrino masses from direct measurements are produced from experiments studying electrons from the beta decay of tritium nuclei. The lowest current upper limit is produced using data from the Troitsk experiment using molecular tritium and an electrostatic spectrometer, with a resolution of 4 eV [13]. A best-fit value of -0.67 was found with an upper limit of 2.05 eV at 95% confidence. A similar constraint is also found by the Mainz experiment [14]. As described in more detail in Sec. 2.5 the neutrino flavour states are not eigenstates of the Hamiltonian of free space. Consequently, the constraint produced is on the effective electron neutrino mass which is an admixture of the three neutrino mass states.

Complementary limits have been placed on the sum of the masses of the three neutrinos using cosmological data, with the strongest current constraint of $m_{tot} \leq 0.18\ eV$ coming from a combination of the Planck CMB and BOSS Lyman α data [15].

2.3.5 Lifetime

Krakauer et. al. placed a limit on the lifetime of the muon neutrino in 1991, through observation of muon neutrinos and anti-neutrinos, searching for decays with a photon in the final state [16]. The experiment found an upper limit of 68 gamma ray events, which placed a lower bound on the lifetime of the muon antineutrino of $\tau/\mu_{\nu_\mu} \geq 15.4\ seceV^{-1}$ at the 90% confidence level.

2.3.6 Majorana Neutrinos

The small but non-zero neutrino mass may be included in the standard model, in a similar way to all other fermions, by a Dirac mass term, which is a coupling of the left-handed and unobservable right-handed neutrino fields. Without a right-handed neutrino state, the mass term must vanish. Therefore, the existence of the right-handed neutrino field is required if the observed neutrino mass is in fact a Dirac mass, even though it does not appear anywhere else in the standard model Lagrangian. This "sterile" right-handed neutrino is unappealing to some physicists as it does not couple to the weak interaction, and therefore can never be directly observed, and only exists in the theory to account for the Dirac neutrino mass.

Majorana proposed an alternative model in which the right-handed field is manufactured from a charge conjugation of the left-handed field [17], making the neutrino and the anti-neutrino the same particle. The neutrino is unique in this respect as it is the only known standard model particle for which this mechanism is possible, by merit of the fact that it is electromagnetically neutral.

The most common method used to determine if neutrinos are Majorana particles is the search for neutrinoless double beta decay. Double beta decay is a nuclear process in which two protons (or neutrons) convert into neutrons (or protons) via emission of two positrons (or electrons) and two neutrinos (or anti-neutrinos). If neutrinos were Majorana particles, an alternative process may occur where by the two neutrinos effectively annihilate each other within the interaction, leading to only two nucleons and two electrons in the final state. The Schechter-Valle theorem implies that an observation of neutrinoless double beta decay demonstrates that at least one neutrino is a Majorana fermion [18].

The experimental signatures of neutrinoless double beta decay arise from the kinematics of the decay process, which allow it to be distinguished from the standard double beta decay background. These include a peak in the tail of the two electron invariant mass distribution, or in the sum of the energies as the recoiling nucleus often carries little of the kinetic energy. Neutrinoless double beta decay has yet to be observed but the field is very active and many experiments are planned to take data in the coming years [19].

2.4 The History of Neutrino Oscillation

2.4.1 The Solar Neutrino Problem

The first hints of flavour change and neutrino oscillation came in the late 1960s from the Homestake (Chlorine) Experiment [20]. The experiment consisted of a 350 m^3 tank of perchloroethylene (C_2Cl_4), placed at 4,850 ft underground. Detection occurred as neutrinos from the sun interacted with chlorine atoms in the perchloroethylene via inverse beta decay.

$$^{37}Cl + \nu_e \rightarrow {}^{37}Ar + e^- \tag{2.4}$$

The sensitivity of the experiment was dependent on the ability to recover and count the Argon atoms resulting from the neutrino interactions. Helium gas was bubbled through the perchloroethylene liquid to collect the Argon atoms every few weeks.

The experiment was the first to detect neutrinos originating from the sun and measured a flux of 2.56±0.16 (stat) ± 0.16 (syst) SNU[1] for neutrinos above the 0.814 *MeV* energy threshold from 108 runs between 1970 and 1995 [21]. This was significantly lower than the prediction of 7.5 SNU.

Other regions of the solar neutrino flux were probed by subsequent experiments, such as the germanium experiments, SAGE [22] and GALLEX [23], and a water Cherenkov experiment Kamiokande [24], all of which found a deficit of solar electron neutrinos. The germanium experiments had a much lower energy

[1]Solar Neutrino Unit (flux to produce 10^{-36} captures per target atom per second)

threshold and were therefore able to detect neutrinos from the solar pp-cycle, a process which was assumed to be well understood and predicted at the time. This deficit came to be known as the "solar neutrino problem".

The solar neutrino predictions were finally reconciled with measurements with the results of the Solar Neutrino Observatory (SNO) experiment in 2002 [25]. The breakthrough made by the SNO experiment was the ability to measure both charged current and neutral current neutrino interactions, which allowed for a measurement of the total, flavour independent, neutrino flux. The SNO target mass consisted of 1,000 tonnes of heavy water, contained in a 6 m radius acrylic vessel, inside a detector cavity filled with water for shielding. 9,600 photomultiplier tubes surrounded the acrylic vessel to identify neutrino events within through Cherenkov radiation via three channels shown in Eq. (2.5).

$$CC: \ \nu_e + d \rightarrow p + p + e^- \qquad (E_\nu \geq MeV) \tag{2.5}$$

$$NC: \ \nu_x + d \rightarrow p + n + \nu_x \qquad (E_\nu \geq MeV) \tag{2.6}$$

$$Elastic: \ \nu_x + e^- \rightarrow \nu_x + e^- \qquad (E_\nu \geq 5.7 MeV) \tag{2.7}$$

As with previous experiments, the charged current interaction was only sensitive to the ν_e component of the solar flux as it required a charged lepton to be produced. The elastic interaction was sensitive to all neutrino flavours, however the cross-section is much larger for electron neutrinos than muon or tau neutrinos at the solar neutrino energies. The neutral current channel was however independent of neutrino flavour and therefore each neutrino flavour contributed equally to the signal. The signature for a NC event was the detection of a free neutron produced from the dissociation of the heavy water molecule as the neutrino interacted.

The SNO experiment ran in three phases, each with a different method of neutron detection. Phases one and two relied on the detection of a gamma ray produced when the neutron was captured. Pure heavy water was used in phase one and 6.3 MeV signals were a result of capture on deuterium nuclei. In phase two the heavy water was doped with two tonnes of $NaCl$, with the Cl atoms significantly increasing the neutron capture rate. Finally, in phase three proportional counters were deployed in the heavy water which detected neutrons via capture on ^3He.

The total neutrino flux, measured via the NC channel, was found to be consistent with the standard solar model, while a deficit was found in the CC channel. The combination of these measurements was considered to be definitive evidence of neutrino flavour change.

2.4.2 The Atmospheric Neutrino Anomaly

Atmospheric neutrinos were first detected in the 1960s, at the Kolar Gold Fields experiment consisting of several detector modules 2.3 km underground in Karnataka, India [26]. Muons, resulting from neutrino interactions in the surrounding rock, excited scintillator planes in each module and were read out by photo-multiplier tubes. Neutrino events were distinguished from cosmic muons using the angle they traversed the detection planes. At 2.3 km underground, only neutrino interactions could be responsible for muons passing the detector horizontally.

Atmospheric neutrinos are produced in the collisions of cosmic rays with light nuclei in the upper atmosphere. The majority of neutrinos are produced in the decay of pions and muons as shown in Eq. (2.8).

$$\pi^{\pm} \rightarrow \mu^{\pm} + \overset{(-)}{\nu}_{\mu} \tag{2.8}$$

$$\mu^{\pm} \rightarrow e^{\pm} + \overset{(-)}{\nu}_{\mu} + \overset{(-)}{\nu}_{e} \tag{2.9}$$

This leads to a simple relationship between the expected number of muon and electron type neutrinos expected from the atmosphere. In 1988, when studying neutrino events as a background to a nucleon decay search, the Kamiokande experiment found a significant deficit of muon neutrinos compared to the Monte Carlo prediction, and an electron neutrino flux which was consistent. Similar experiments such as Soudan-2 [27] and IMB [28] also saw similar deficit of muon neutrinos from the atmosphere around the same time.

The cause of the deficit was deemed almost certainly to be due to neutrino oscillation with the results from the Super-Kamiokande experiment. Super-K, described in more detail in Sec. 3.4, is a 50 kton water Cherenkov detector operational and taking atmospheric neutrino data at this time. Super-Kamiokande is an order of magnitude larger than its predecessors and the resulting statistics allowed for a much more sophisticated analysis [29].

The Super-Kamiokande experiment found a zenith angle dependence in the deficit of muon neutrinos, inconsistent with the prediction of the atmospheric neutrino flux. With data binned in zenith angle, Super-Kamiokande has access to multiple neutrino baselines and found that the data were consistent with two flavour ($\nu_\mu \leftrightarrow \nu_\tau$) neutrino oscillations. The atmospheric neutrino data set at Super-Kamiokande continues to grow and competitive limits on the neutrino oscillation parameters continue to be produced by the collaboration almost 20 years after the original confirmation.

2.4.3 Reactor Neutrino Experiments

Nuclear reactors, used in the original discovery of the neutrino in the 1950s, offer large neutrino fluxes predicted with enough precision to study neutrino oscillations.

KamLAND was the first experiment to confirm the results published by the SNO collaboration with an independent source of neutrinos. The KamLAND detector consisted of an 18 m diameter containment vessel lined with 1,879 photo-multiplier tubes, which pointed toward a 13 m diameter nylon balloon filled with 1,000 tonnes of liquid scintillator. The detector site was surrounded by over 50 nuclear reactors at an average distance of 180 km. Electron anti-neutrinos were detected via inverse beta decay and events selected using a coincidence of the signals from the emitted positron and delayed gamma, produced when the free neutron was captured by a nucleus. The experiment found a deficit of the electron anti-neutrino flux originating from nuclear reactors which was consistent with the neutrino oscillation parameters measured at SNO, assuming CPT symmetry [30].

2.5 Oscillation Theory

Neutrino flavour oscillation, predicted by Maki, Nakagawa and Sakata in 1962 [31], and also developed by Pontecorvo [32], is a theory used to explain the neutrino flavour change measured as a function of distance. In the standard model of particle physics, all processes are predicted to conserve individual lepton number. This is ensured by the absence of any lepton flavour changing neutral currents and charged currents which only couple charged leptons to their neutrino partners. Neutrino flavours are therefore defined by the flavour of the changed lepton which participates at the interaction vertex of their creation or destruction. For example, in the decay of a pion to a muon and an anti-neutrino, the neutrino is defined to be a muon neutrino, and in inverse beta decay, it is defined to be an electron neutrino.

All neutrino oscillation phenomena observed thus far are consistent with the mechanism developed by Pontecorvo, Maki, Nakagawa and Sakata.

In the Pontecorvo-Maki-Nakagawa-Sakata (PMNS) oscillation mechanism, neutrino oscillations which are observed today are a consequence of the fact that the neutrino flavour eigenstates differ from the eigenstates of the free space Hamiltonian. The relation between the mass and flavour states is given by a unitary transformation U_{PMNS}, denoted as the PMNS matrix after those that participated in its development.

$$|\nu_\alpha\rangle = \sum_i^n U_{i\alpha}|\nu_i\rangle \tag{2.10}$$

$$|\nu_i\rangle = \sum_\alpha^n U^*_{i\alpha}|\nu_\alpha\rangle \tag{2.11}$$

The action of the matrix is shown in Eq. (2.10) with $|\nu_\alpha\rangle$ denoting states of definite mass, and $|\nu_i\rangle$ those of definite flavour. Any general n dimensional complex matrix can be parameterised by $2n^2$ parameters, the unitarity condition provides n^2 independent constraints and therefore removes n^2 degrees of freedom. The n^2 parameters can be divided into $n(n-1)/2$ rotation angles and $n(n+1)/2$ phases. For Dirac neutrinos, $2n-1$ phases can be removed by a rephasing the neutrino fields leaving only $(n-2)(n-1)/2$ physically observable phases.

For the case of three flavours of neutrinos, the matrix is parameterised by three angles and one[2] phase and is commonly broken down into the product of

[2] Three phases for the case of Majorana neutrinos however the additional two have no impact on neutrino oscillation

three rotation matrices:

$$U = \begin{bmatrix} 1 & 0 & 0 \\ 0 & c_{23} & s_{23} \\ 0 & -s_{23} & c_{23} \end{bmatrix} \begin{bmatrix} c_{13} & 0 & s_{13}e^{-i\delta_{CP}} \\ 0 & 1 & 0 \\ -s_{13}e^{i\delta_{CP}} & 0 & c_{13} \end{bmatrix} \begin{bmatrix} c_{12} & s_{12} & 0 \\ -s_{12} & c_{12} & 0 \\ 0 & 0 & 1 \end{bmatrix} \tag{2.12}$$

(2.13)

$$= \begin{bmatrix} c_{12}c_{13} & s_{12}c_{13} & s_{13}e^{-i\delta_{CP}} \\ -s_{12}c_{23} - c_{12}s_{23}s_{13}e^{i\delta_{CP}} & c_{12}c_{23} - s_{12}s_{23}s_{13}e^{i\delta_{CP}} & s_{23}c_{13} \\ -s_{12}s_{23} - c_{12}c_{23}s_{13}e^{i\delta_{CP}} & -c_{12}s_{23} - s_{12}c_{23}s_{13}e^{i\delta_{CP}} & c_{23}c_{13} \end{bmatrix} \tag{2.14}$$

where $s_{ij} = sin\theta_{ij}$ and $c_{ij} = cos\theta_{ij}$.

Current neutrino oscillation theory provides almost no indication of what any of the free parameters in the PMNS matrix may be, other than mathematical constraints, and therefore they must be measured experimentally.

To predict the evolution of a neutrino as it propagates through space, we can express it as a linear combination of the neutrino mass eigenstates. As the neutrino mass states are eigenstates of the Hamiltonian, the time evolution is predicted by the Schrodinger equation:

$$|\nu_i(t)\rangle = \sum_{\alpha}^{n} U^*_{i\alpha}|\nu_\alpha(t)\rangle = \sum_{\alpha}^{n} U^*_{i\alpha}|\nu_\alpha\rangle e^{-iE_\alpha t} \tag{2.15}$$

Neutrino oscillation occurs because the mass eigenstates evolve at different rates which cause phase differences. The phase differences alter the interference between the mass states, and as a result change the propagating neutrino state from one of definite flavour into a superposition of flavour states. If the neutrino mass states had the same mass, or some other mechanism caused them to evolve at the same frequency, neutrino oscillations would not occur. As a consequence, neutrino oscillations give a unique insight into the scale of neutrino masses, with observation of neutrino oscillation seen as conclusive evidence that neutrinos in fact had mass.

Expressing the mass state as a linear combination of flavour states:

$$|\nu_i(t)\rangle = \sum_{\alpha}^{n} U_{i\alpha}^{*} e^{-iE_\alpha t} \sum_{k}^{n} U_{k\alpha} |\nu_k\rangle \tag{2.16}$$

$$\tag{2.17}$$

the amplitude for the oscillation of a neutrino of flavour i into flavour j is thus given by:

$$A_{i\to j} = \langle \nu_j | \nu_i(t) \rangle = \sum_{\alpha k}^{n} U_{i\alpha}^{*} e^{-iE_\alpha t} U_{k\alpha} |\nu_k\rangle \tag{2.18}$$

$$= \sum_{\alpha}^{n} U_{i\alpha}^{*} e^{-iE_\alpha t} U_{j\alpha} \tag{2.19}$$

and the oscillation probability by:

$$P_{\nu_i \to \nu_j}(t) \equiv |A_{\nu_i \to \nu_j}|^2 = (\sum_{\alpha}^{n} U_{i\alpha}^{*} e^{-iE_\alpha t} U_{j\alpha})(\sum_{\beta}^{n} U_{i\beta}^{*} e^{-iE_\beta t} U_{j\beta})^{*} \tag{2.20}$$

$$= \sum_{\alpha\beta}^{n} U_{i\alpha}^{*} e^{-iE_\alpha t} U_{j\alpha} U_{i\beta} e^{+iE_\beta t} U_{j\beta}^{*} \tag{2.21}$$

$$= \sum_{\alpha\beta}^{n} U_{i\alpha}^{*} U_{j\alpha} U_{i\beta} U_{j\beta}^{*} e^{-i(E_\alpha - E_\beta)t}. \tag{2.22}$$

Taking advantage of the small neutrino mass, the energy can be approximated by:

$$E_\alpha = (p^2 + m_\alpha^2)^{\frac{1}{2}} \tag{2.23}$$
$$= p(1 + (\frac{m_\alpha}{p})^2)^{\frac{1}{2}} \tag{2.24}$$
$$\approx p + \frac{m_\alpha^2}{2p} \tag{2.25}$$

and the energy difference by:

$$E_\alpha - E_\beta \approx \frac{m_\alpha^2 - m_\beta^2}{2p} \equiv \frac{\Delta m_{\alpha\beta}^2}{2p} \tag{2.26}$$

which, in the ultra-relativistic limit, becomes:

$$E_\alpha - E_\beta \approx \frac{\Delta m_{\alpha\beta}^2}{2E}. \tag{2.27}$$

The oscillation probability, as a function of time and distance, in the ultra-relativistic limit is thus given by:

$$P_{\nu_i \to \nu_j} = \sum_{\alpha\beta}^{n} U_{i\alpha}^* U_{j\alpha} U_{i\beta} U_{j\beta}^* e^{-i\frac{\Delta m_{\alpha\beta}^2 L}{2E}}. \tag{2.28}$$

By making use of the unitarity of the PMNS matrix, and assuming CPT invariance in neutrino oscillations, the oscillation probability can be expressed as:

$$P_{\overset{(-)}{\nu}_i \rightarrow \overset{(-)}{\nu}_j} = \delta_{ij} - 4\sum_{\alpha>\beta} \mathbb{R}(U^*_{i\alpha}U_{i\beta}U_{j\alpha}U^*_{j\beta}) \sin^2(\frac{\Delta m^2_{\alpha\beta}L}{4E}) \tag{2.29}$$

$$\overset{(-)}{+} 2\sum_{\alpha>\beta} \mathbb{I}(U^*_{i\alpha}U_{i\beta}U_{j\alpha}U^*_{j\beta}) \sin(\frac{\Delta m^2_{\alpha\beta}L}{2E}). \tag{2.30}$$

The expression for neutrino oscillation in Eq. (2.29) can provide great insight into the nature of neutrino oscillation. Firstly it clearly shows why neutrino oscillation is named as such. The probability oscillates in a way determined by the combined effect of sinusoidal oscillations with frequencies defined by the neutrino mass squared differences. As alluded to earlier, the mass differences are necessary for this oscillation to occur. If all mass differences were set to zero, the right hand side of Eq. (2.29) would reduce to the Kronecker delta. Another consequence of this fact is that neutrino oscillations are unable to be used for measurements of the absolute neutrino mass scale. Lastly, if the PMNS matrix is entirely real, there can be no difference between neutrino and anti-neutrino oscillations, and thus no CP violation.

The only parameters which it is possible for an experiment to influence are the neutrino energy and oscillation length. The T2K experiment has a highly tuned relationship between the baseline and beam energy to maximise the amount of observable neutrino oscillation. Oscillation parameters are inferred from the disappearance of muon neutrinos and appearance of electron neutrinos from a predominantly muon neutrino beam at T2K, the leading terms of which are given in terms of the PMNS mixing angles and mass splittings by [3]:

$$P_{\overset{(-)}{\nu}_\mu \rightarrow \overset{(-)}{\nu}_\mu} \approx 1 - 4\cos^2\theta_{13}\sin^2\theta_{23}(1-\cos^2\theta_{13}\sin^2\theta_{23})\sin^2\frac{\Delta m^2_{32}L}{4E} \tag{2.31}$$

$$+ \text{(CP even term, solar term, matter effect term)} \tag{2.32}$$

[3] Assuming $\Delta m^2_{32} \approx \Delta m^2_{31}$. Terms which T2K has little sensitivity to have been omitted

$$P_{\overset{(-)}{\nu}_\mu \rightarrow \overset{(-)}{\nu}_e} \approx \sin^2\theta_{23}\sin^2 2\theta_{13}\sin^2\frac{\Delta m^2_{31}L}{4E} \tag{2.33}$$

$$\overset{(+)}{-}\frac{\sin 2\theta_{12}\sin 2\theta_{23}\sin^2 2\theta_{13}}{2\sin\theta_{13}}\sin\frac{\Delta m^2_{31}L}{4E}\sin\frac{\Delta m^2_{32}L}{4E}\sin\frac{\Delta m^2_{21}L}{4E}\sin\delta_{CP} \tag{2.34}$$

$$+\,(\text{CP even term, solar term, matter effect term}). \tag{2.35}$$

CP even terms in the oscillation formula are proportional to $\cos\delta_{CP}$ and therefore do not change sign under a CP transform. The terms are explored further in Chap. 7. Solar terms depend on the square of the sine of the solar mass splitting. As the mass splitting is small in comparison to the ratio of beam energy to baseline, the solar terms can be neglected at T2K. Finally, as matter effects are a result of coherent scattering in the earth, terms in the oscillation formula are small due to the relatively short baseline at T2K.

At T2K, the disappearance measurement provides information about the mass splitting, Δm^2_{32}, and the mixing angle, θ_{23}, whereas the appearance constrains Δm^2_{32}, θ_{13}, δ_{CP} and θ_{23}.

2.5.1 Matter Effects

The predictions presented thus far are however only valid for oscillations in a vacuum and must be modified to include the effects of matter on neutrinos as they traverse the earth. These are so called "matter effects". The matter effect is the consequence of a flavour dependent perturbation to the neutrino Hamiltonian due to coherent forward scattering of neutrinos as they propagate through the earth.

Neutrinos predominantly coherently forward scatter through two mechanisms; through neutral current interactions on protons, neutrons and electrons or charged current interactions on electrons shown in Sec. 2.5.1. Electron neutrinos

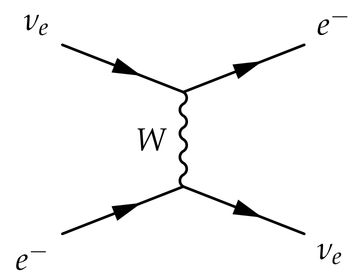

Figure 2.2: Charged current scattering.

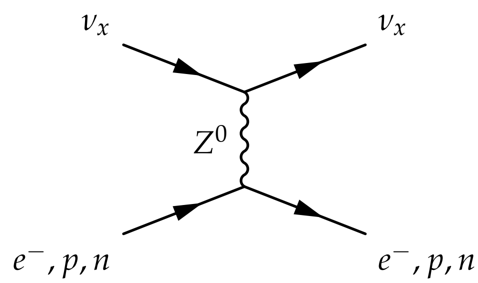

Figure 2.3: Neutral current scattering.

are unique in this respect as only they are able to undergo the latter process. Subsequently, when in the presence of matter, each neutrino flavour passes through a potential different to that of the vacuum and therefore gains an additional effective mass. As the neutrino mass states each have a specific contribution of each neutrino flavour, defined by the PMNS matrix, each is affected in a different way by the matter effect. The effect is analogous to coherent forward scattering of light in an insulator, leading to a refractive index. As the potential of each neutrino flavour is affected equally by the neutral current component, the effect of matter on neutrino oscillation is driven only by the electron number density.

These matter effects give modern neutrino experiments the sensitivity to provide constraints on the neutrino mass ordering which is one of the remaining open questions in neutrino oscillation physics. The neutrino mass ordering is a binary choice of the order of neutrino mass states, as shown in Fig. 2.4. Both mass ordering hypotheses are currently consistent with all observations thus far. The reason why the mass ordering is difficult to measure is because the leading terms in the neutrino oscillation formula depend on the square of the sine of the mass splittings, and therefore have no sensitivity to their signs. Matter effects are however sensitive to the neutrino mass ordering such that precise measurements of the matter effects also constrain the mass ordering.

Lastly there is the issue of a slight degeneracy between the matter effects and CP violation in neutrino oscillations. The fact that the earth is made out of matter and not antimatter introduces an explicit asymmetry between neutrino and anti-

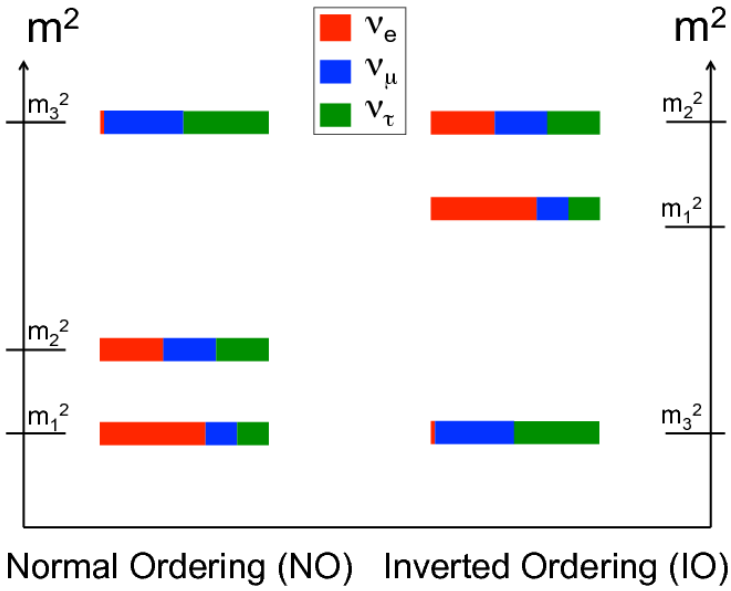

Figure 2.4: The two alternative hypotheses for the order of the neutrino mass states. Figure taken from [33]
.

neutrino propagation. It is therefore important to untangle any CP asymmetry observed in neutrino oscillation, caused by δ_{CP}, from that resulting from matter effects in the earth. Due to the relatively short baseline, this is not of significant concern at T2K, however the effect is not negligible and thus a full treatment of neutrino oscillation is required for the analysis presented in this thesis.

2.6 Oscillation Parameter Constraints

As we enter the era of precision measurements of neutrino oscillation parameters, it is important to include as much information in an analysis as feasible in order to provide the best constraints. By design, the T2K experiment is less sensitive to some oscillation parameters than others, therefore constraints on these parameters are often included from external experiments, so to improve the sensitivity to the parameters of interest.

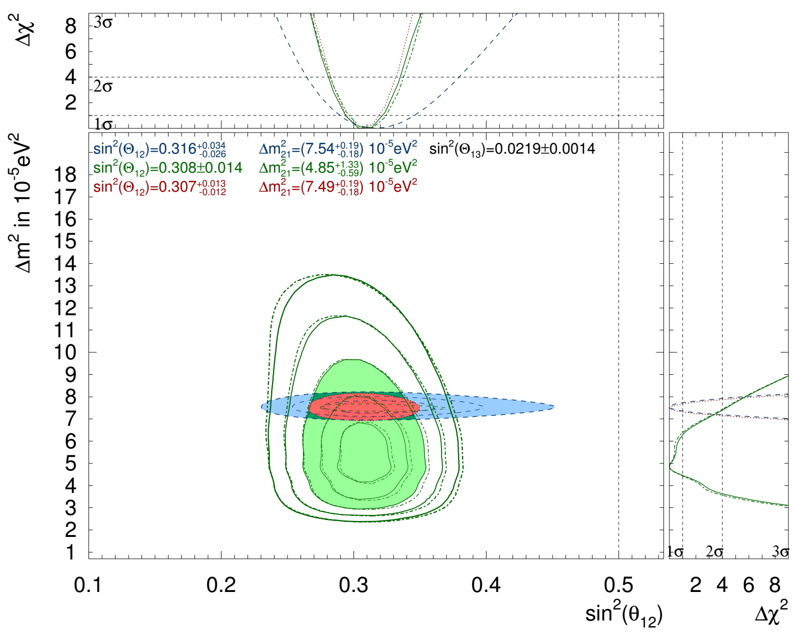

Figure 2.5: Combined constraint on the solar mixing and mass splitting parameters from the SNO, Super-K and KamLAND experiments, shown in red. The combined SNO and Super-K constraint is shown in green and the KamLAND constraint shown in blue. Coloured regions indicate the 3σ confidence level. Figure taken from [34].

2.6.1 Solar and Reactor Constraints (1-2 Sector)

The expected T2K oscillation spectra are mostly unaffected by variations of the parameters θ_{12} and Δm^2_{21}, however their effects are not negligible so constraints are included from measurements made by SNO, Super-K and KamLAND [34]. Due to resonance effects which occur in the sun, a consequence of similar matter effects described in Sec. 2.5.1, the measurement of the flavour content of neutrinos in a particular energy range[4] is a direct measurement of the ν_e flavour content of the ν_2 mass state. The result is a precise measurement of $\sin^2\theta_{12}$ but loose bound on Δm^2_{21} as highlighted by the green bound in Fig. 2.5. Importantly, this is complemented by the measurement made by KamLAND using reactor neutrinos for which the oscillation baseline was well known in comparison to the solar experiments.

[4] Neutrinos from fusion of $^8B \sim$ 6-7 MeV

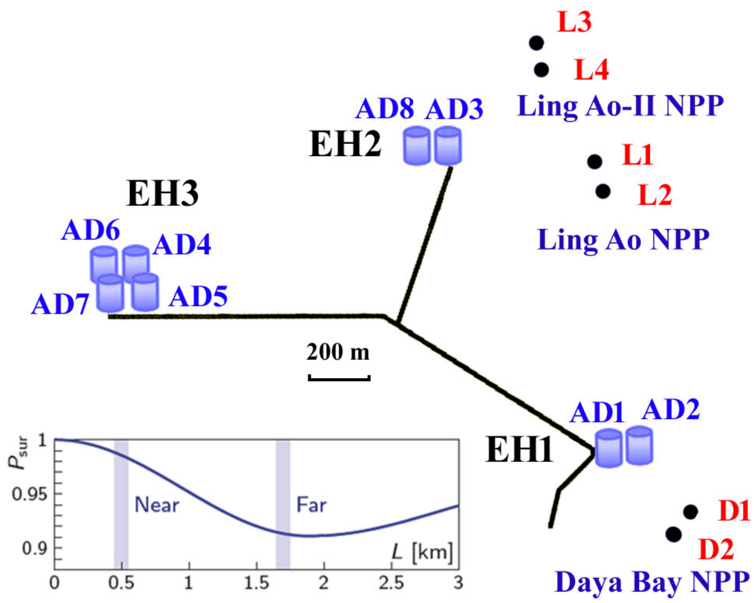

Figure 2.6: The Daya Bay experiment, dots represent reactors and detectors are labelled "AD". Also shown is the expected ν_e survival probability as a function of the effective baseline. Figure taken from [36].

2.6.2 Reactor Experiments (θ_{13})

The measurement of θ_{13} was one of the primary goals of the T2K experiment, which was in fact designed to search for a much smaller value than that measured by Daya Bay in 2012 [35]. Daya Bay consists of eight detector modules, each with 20 tonnes of target mass, using gadolinium-doped liquid scintillator to observe electron anti-neutrinos from six reactors arranged as shown in Fig. 2.6. Those at EH2 and EH1 are near detectors, to provide a measurement of the mostly un-oscillated neutrino flux, and those at EH3 the far detectors.

In general experiments which study the disappearance of $\bar{\nu}$ over short baselines (O(1 km)) from nuclear reactors lead the field in providing precision measurements of θ_{13}. They follow a very similar set-up to that of Daya Bay and are labelled in this thesis as the "reactor experiments" which produce the "reactor constraint". The reactor constraint on $\sin^2\theta_{13}$, used for the analysis presented in this thesis, is made from a combination of the measurements made at Daya Bay, CHOOZ [37] and RENO [38], produced by the particle data group [39]. Provided

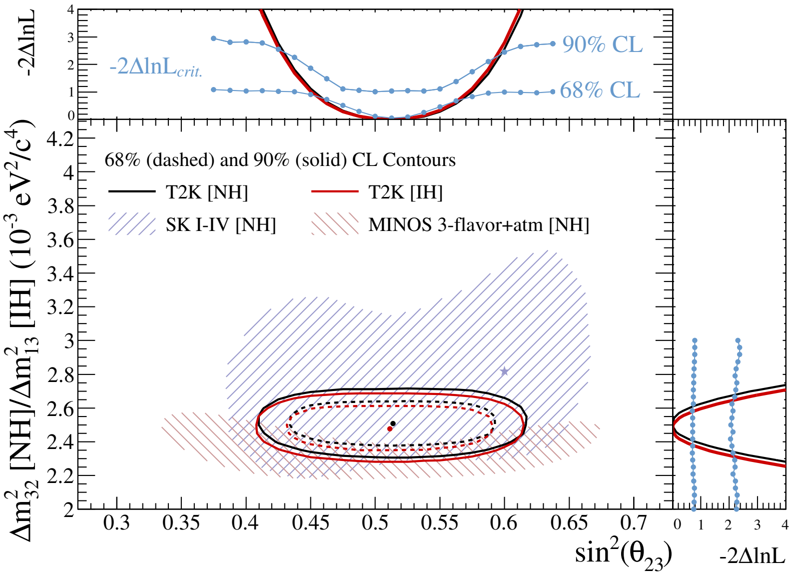

Figure 2.7: A comparison of the θ_{23} and Δm^2_{32} constraints from ν_μ disappearance measurements at T2K and MINOS. 68% and 90% confidence level contours are shown with dashed and solid lines respectively for T2K and only the 90% contour is shown for MINOS. The T2K 1D likelihood surfaces are also shown for both $\sin^2\theta_{23}$ and Δm^2_{32}. Figure taken from [41].

is a constraint on θ_{13}, independent of the value of δ_{CP}, which can be used in T2K oscillation analyses.

2.6.3 Previous measurements of the 2-3 Sector

The most significant results of θ_{23} and Δm^2_{32}, prior to the most recent results, come from MINOS [40] and previous T2K results [41]. MINOS was a long baseline neutrino oscillation experiment similar to T2K based in the USA using an on-axis neutrino beam peaked near 3 GeV and a 735 km baseline. A comparison of the final MINOS result and that produced from the T2K neutrino data taken up to May 2013 is shown in Fig. 2.7. Consistency between the measurements is highlighted from the overlap of the 90% confidence contours near $\Delta m^2_{32} = 2.4 \times 10^{-3}$ and over a wide range of values of $\sin^2\theta_{23}$.

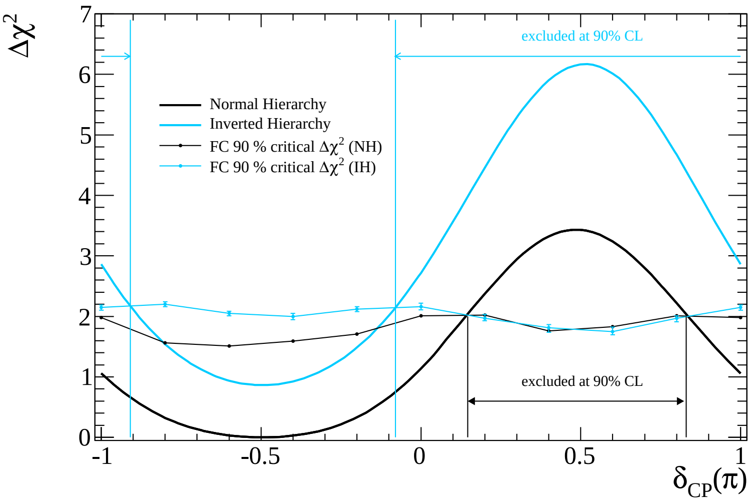

Figure 2.8: Measurement of δ_{CP} from a joint fit to the ν_e appearance and ν_μ disappearance channels at T2K. Figure taken from [42].

2.6.4 δ_{CP}

The strongest indication of δ_{CP}, before the combination of the neutrino and antineutrino oscillation data sets at T2K, come from a combined fit of appearance and disappearance data sets at T2K up to May 2013 [42]. Although the measurement considered only neutrino data, and was therefore unable to probe CP violation directly, a constraint was produced on δ_{CP} from the effect it had on the ν_e appearance rate. The data were found to prefer maximally CP violating value of δ_{CP}, -$\pi/2$, as shown in Fig. 2.8, and exclude $\pi/2$ at the 90% confidence level.

Chapter 3

The T2K Experiment

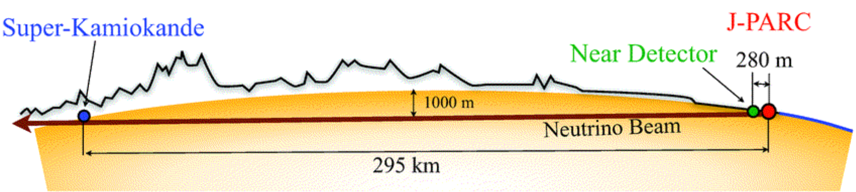

Figure 3.1: A brief schematic of the T2K experiment. Figure from [43].

Tokai to Kamioka (T2K), shown in Fig. 3.1, is a neutrino oscillation experiment designed to measure the oscillation of muon neutrinos produced with a particle accelerator. The experiment consists of J-PARC, a facility which provides the neutrino beam, a suite of near detectors to determine the composition of the un-oscillated neutrino beam, and a far detector, Super-K, to measure the oscillated neutrino flux.

The neutrino beam is produced by directing an intense beam of 30 GeV protons into a graphite target at J-PARC, located in Tokai, Japan. As the protons undergo interactions in the target, secondary hadrons are produced. The secondary hadron beam, composed of mainly protons and pions but with a small contamination of kaons, is then focused using a system of magnetic focusing horns. The magnetic horns also facilitate mass and charge selection in order to produce a neutrino beam composed primarily of π^+ or π^- when required. The majority of neutrinos in the beam are then produced in the leptonic decay of hadrons, as they pass through a 96 m decay tunnel, filled with *He* gas. The decay volume is followed by a graphite beam dump, the purpose of which is to stop all particles in the secondary beam other than neutrinos and high energy muons.

The beam composition, before oscillations are expected to occur, is measured by a series of detectors within the J-PARC facility. Muon monitors are placed 110 m downstream from the target, which are used for a measurement of the beam direction using high energy muons which pass through the beam dump. INGRID [44], a multi-module iron (passive) and plastic scintillator (active) detector, is an on-axis neutrino detector situated 280 m from the target. The primary function of INGRID in the oscillation analysis is to provide current measurements of the neutrino beam direction and intensity. ND280, a composite detector situated at 280 m away from the target and 2.5° from the proton beam direction, is also a neutrino detector, and is used to constrain the un-oscillated beam spectrum composition and neutrino cross-sections.

The T2K far detector, located in Kamioka, Japan, is 295 km from the target and at the same 2.5° off-axis angle as ND280. It is a large, 50 kt, tank of water, instrumented with photo multiplier tubes used to detect the Cherenkov light from neutrino interactions which occur within.

These three components play a vital role in neutrino oscillation measurements at T2K, which stem from a comparison of the predicted event rate at Super-K, given the measurements at the near detectors, and a particular oscillation model, with that which is measured. During construction, the primary goals of T2K were to measure the mixing angle θ_{13} via an observation of ν_e appearance in a ν_μ beam, and perform a precision measurement of parameters $\sin^2\theta_{23}$ and

Δm^2_{32} from an observation of ν_μ disappearance in a ν_μ beam.

3.1 The Neutrino Beam

The T2K beam is composed of the proton beam, and primary, and secondary beamlines. The proton beamline consists of 3 accelerators which ramp up the beam energy to 30 GeV in succession. The primary beamline transports the beam up to the target station and the secondary beamline is composed of the target station and the decay volume.

3.1.1 The Proton and Primary Beamlines

The 30 GeV proton beam is produced by a series of accelerators in the J-PARC accelerator complex. JPARC consists of a linear accelerator (LINAC), a rapid-cycling synchrotron (RCS), and a main ring (MR) synchrotron shown in Fig. 3.2. H^- ions are accelerated to a kinetic energy of 400 MeV and H^- pulses from the LINAC of 500 μs are injected into the RCS at a rate of 50 Hz.

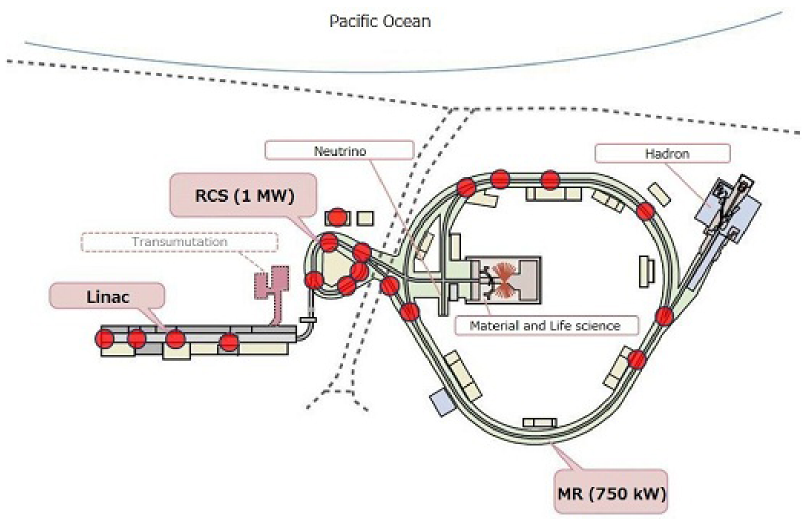

Figure 3.2: The layout of the J-PARC accelerator complex showing the LINAC, RCS and MR. Figure from [45].

As they are injected, the H^- pass through carbon charge stripping foils, which remove the electrons and leave H^+ ions in the beam. Upon entering the RCS, each beam pulse is chopped into two distinct "bunches" which the RCS maintains.

The H^+ bunches are accelerated to 3 GeV inside the RCS, with a repetition rate of 25 Hz. Every 3 seconds, bunches from the RCS are extracted to the MR synchrotron with a repetition rate of $\frac{1}{3}$ Hz. The MR can hold up to 8 bunches, filled from the RCS two at a time, which make up the beam pulse.

Once the 8 bunches have been filled, the MR begins ramping up the beam energy to 30 GeV (designed for up to 50 GeV). Upon reaching 30 GeV, the proton beam is fast extracted to the neutrino production target. After extraction, the MR returns to its previous state ready for injection. At extraction, the length of a spill is $\sim$5 μs and the bunches within are approximately 100 ns in length and separated by 560 ns. In addition to providing a high-power pulsed beam for T2K, the J-PARC accelerator facility is also a vital component of many other experiments [46]. Approximately 95% of protons accelerated in the RCS are delivered to the Material and Life Science Facility at J-PARC. The MR, when not used for T2K, can provide a slow extracted beam to the Hadron Experimental Hall where it is used to create secondary proton and Kaon beams.

Precise timing of the spill is essential in a long baseline neutrino oscillation experiment, such as T2K, as a narrow beam window at both the near and far detectors greatly reduces the coincident cosmic background rate. Along with the timing, accurate measurements of the intensity, position and profile of the proton beam are vital for producing a consistent beam, and simulations of the secondary beamline. Fig. 3.3 shows a schematic of the primary beamline after extraction from the MR. Current transformer intensity monitors provide a measurement of the content in each bunch in the spill, and secondary emission monitors provide an accurate measurement of the position of each bunch.

By the end of the primary beamline, the beam is directed into the ground at 3.637° with respect to the horizontal to achieve the necessary 2.5° off-axis position of ND280 and Super-K.

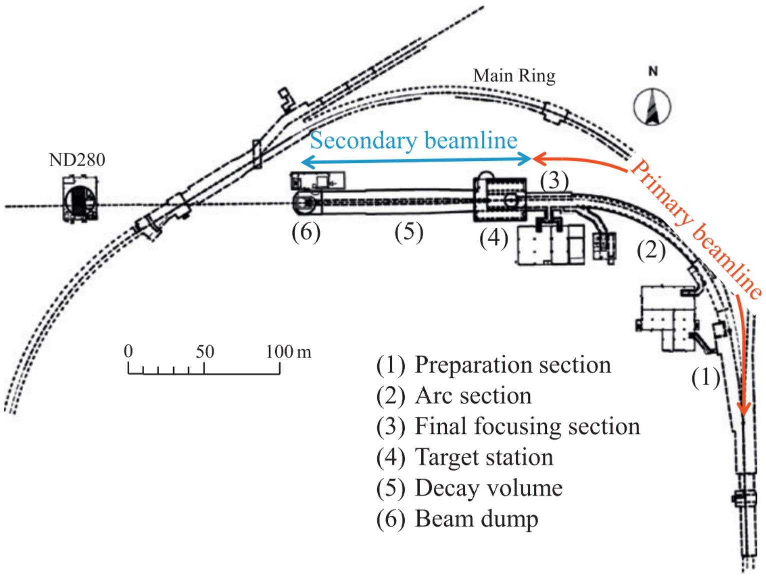

Figure 3.3: Schematic of the primary and secondary T2K beamlines including positions of the target station, decay volume, beam dump and ND280 detector suite. Figure taken from [43]

3.1.2 The Secondary Beamline

The secondary beamline begins with the beam window, which separates the one atmosphere of pressure from the vacuum of the beam, the proton target station, which includes a baffle with a 30 mm beam hole to collimate the proton beam and protect downstream components, an optical transition radiation monitor (OTR), the graphite target, and three magnetic focusing horns.

The OTR is used to provide a precise measurement of the beam profile directly before it impinges on the graphite target. The measurement is made using the transition radiation produced as the beam passes through a thin film, made from titanium alloy [47]. The target is a 91.4 cm long and 2.6 cm diameter graphite rod, chosen to be 1.9x the 30 *GeV* proton interaction length. The core of the target is encased in a 2 mm thick graphite tube, inside a 0.3 mm titanium case, in which helium gas is pumped in for cooling. A series of 3 magnetic horns, shown in Fig. 3.4, are used to focus the secondary hadrons, produced in the target, in the forward direction. The magnetic horns, made up of two coaxial conductors, which create a toroidal magnetic field, are pulsed with a 320 kA current as the beam arrives and produce a 2.1 T field [48]. The graphite target sits in the middle of the first horn with the second and third horns placed downstream.

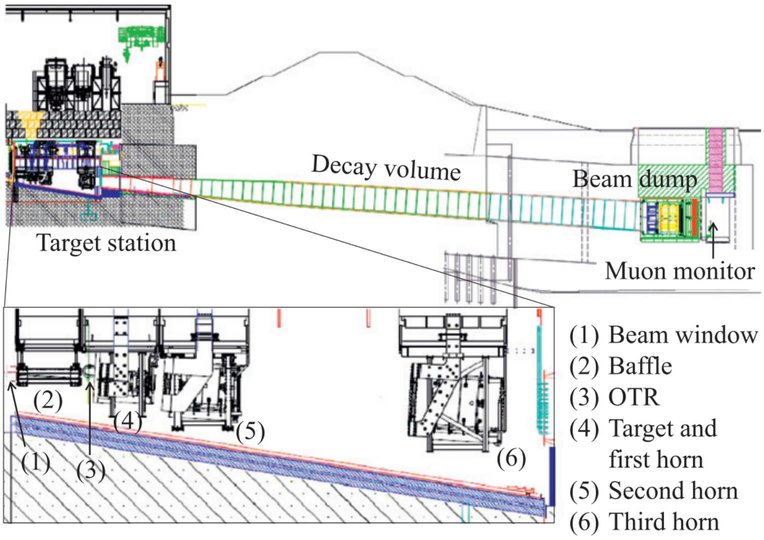

Figure 3.4: Detailed diagram of the secondary beamline showing the position of the target, magnetic focusing horns, decay volume and beam dump. Figure from [49].

The horn has two operational modes; positive focusing (PF) and negative focusing (NF), which are determined by the direction of the current in the magnetic horns. When in PF, positively charged particles are focused toward the beam direction and the negatively charged are defocused. In this configuration the subsequent neutrino beam is primarily composed of ν. The opposite occurs when in NF and a predominantly $\bar{\nu}$ beam is produced. As the analysis presented here is dependant on the beam configuration, ν-mode and $\bar{\nu}$-mode are used to refer to the PF and NF horn configuration respectively.

After the focusing horns, the hadrons enter the 96 m decay volume where neutrinos are produced from the decay of charged mesons. The most relevant for the T2K neutrino beam are detailed in Tab. 3.1. Daughter charged leptons which are produced in the mesonic decays can also decay leading to more neutrinos. These are also listed in Tab. 3.1. The majority of the mesons which are produced in the target are pions, which almost exclusively produce muon decay products. This results in a predominantly muon neutrino beam. The small fraction of Kaons and the secondary muons in the beam are the cause of the non-negligible ν_e contamination in the subsequent neutrino beam.

Decay	Branching fraction
$\pi^+ \rightarrow \mu^+ + \nu_\mu$	99.99%
$\pi^- \rightarrow \mu^- + \bar{\nu}_\mu$	99.99%
$k^- \rightarrow \pi^0 + \mu^- + \bar{\nu}_\mu$	3.35%
$k^+ \rightarrow \pi^0 + \mu^+ + \nu_\mu$	3.35%
$k^- \rightarrow \mu^- + \bar{\nu}_\mu$	63.56%
$k^+ \rightarrow \mu^+ + \nu_\mu$	63.56%
$k^+ \rightarrow \pi^0 + e^+ + \nu_e$	5.07%
$k^0_L \rightarrow \pi^- + \mu^+ + \nu_\mu$	27.04%
$k^0_L \rightarrow \pi^- + e^+ + \nu_e$	40.55%
$k^- \rightarrow \pi^0 + e^- + \bar{\nu}_e$	5.07%
$\mu^+ \rightarrow \bar{\nu}_\mu + e^+ + \nu_e$	100%
$\mu^- \rightarrow \nu_\mu + e^- + \bar{\nu}_e$	100%

Table 3.1: Branching fractions of various particles which may decay in the secondary beamline taken from [39].

The small ν_e contribution is particularly important for the measurement of $\nu_\mu \rightarrow \nu_e$ oscillation as it becomes an irreducible background at Super-K, almost indistinguishable from the signal. A precise measurement of the contamination from the near detectors is therefore vital.

At the end of the decay volume is a beam dump made of a 75 ton graphite core, 3.174 m long, 1.94 m wide and 4.69 m tall, with aluminium cooling plates either side. The beam dump stops all particles except neutrinos and high energy muons. The neutrinos contribute to the beam whereas the muons are measured by muon monitors to study the stability of the beam on a bunch-by-bunch basis. The muon monitor system is made up of silicon PIN photo-diodes 1.2 m downstream of ionisation chambers placed 117.5 m from the target and emulsion trackers further downstream to measure the muon flux. Due to the correlation between the high energy muon and ν_μ flux beyond the beam dump, the muon monitors are able to determine the neutrino beam direction with a precision of 0.25 mrad and intensity with an uncertainty below 3%.

The resulting neutrino flux at Super-K, without considering oscillations, is shown for both ν-mode and $\bar{\nu}$-mode in Fig. 3.5. In both cases, the neutrino beams peak close to 0.6 GeV and are dominated by muon neutrinos, with a less than 1% contamination of electron neutrinos. Two clear differences can be seen between the ν-mode and the $\bar{\nu}$-mode fluxes.

Firstly the size of the "wrong-sign", ν_μ, contamination in the $\bar{\nu}$-mode beam is much more significant than the $\bar{\nu}$ flux in ν-mode. As a positively charged H^+ beam and a matter target, as opposed to one made up of anti-matter, are used; the production of positively charged mesons is much more common than negatively charged. Although the magnetic horns work to deflect these particles away, they are not perfect.

The horns work by amplifying or reducing the component of each particles momentum which is transverse to the beam. In this way, positively charged particles are deflected away and negatively charged are focused into a beam. Positively charged mesons with little or no transverse momentum are however able to pass through the horn system almost unaffected. Secondly, at energies beyond 2 GeV, the ν and $\bar{\nu}$ fluxes are of the same size in $\bar{\nu}$-mode but not in ν-mode. The high energy component of the neutrino beam is a result of high energy mesons which have a large longitudinal momentum and low transverse momentum. As a result of their low transverse, their trajectories are less affected by the horn focusing system which leads to a dominant ν component at high energies.

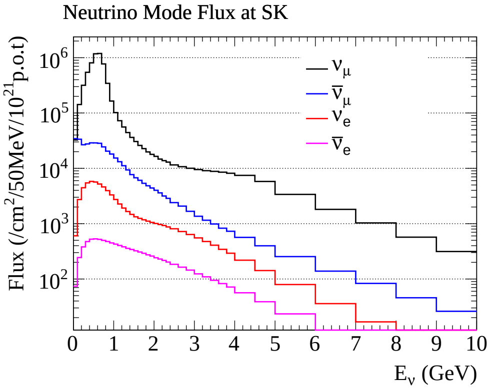

(a) ν-mode

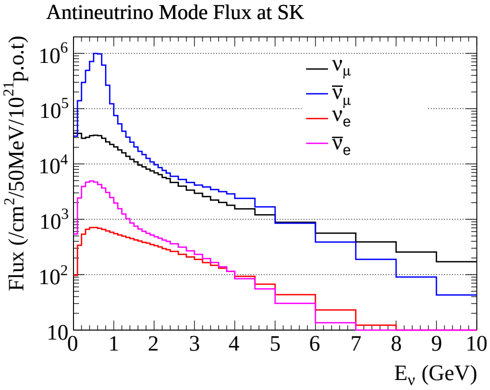

(b) $\bar{\nu}$-mode

Figure 3.5: The predicted un-oscillated neutrino flux at Super-K for each neutrino flavour in ν-mode and $\bar{\nu}$-mode. Figure from [50].

3.1.3 The "Off-Axis" Beam

The T2K experiment was designed so that Super-K would be able to make a precise measurement of the disappearance of muon neutrinos in a muon neutrino beam. With a predetermined baseline of 295 km between J-PARC and Super-K, there only remained freedom in the choice of the neutrino energy spectrum to maximise the oscillation seen at the far detector, whilst also reducing the effect of backgrounds. The beamline was therefore directed 2.5° away from the direction of Super-K resulting in an "off-axis" neutrino beam to fulfil these requirements.

Moving away from the axis of proton (and subsequently meson) beam has two effects on the neutrino spectrum; the peak energy of the spectrum moves to a lower energy and the width of the energy spectrum narrows when moving further off-axis. This feature is due to the fact that most of the neutrinos in the beam are a result of pion decays, $\pi \rightarrow \mu + \nu_\mu$. As this is a simple two body decay, there is a simple relation between the energy of the neutrino, E_ν, the pion kinematics, E_π and p_π, and the angle the neutrino momentum makes with respect to the pion direction, θ_ν:

$$E_\nu = \frac{m_\pi^2 - m_\mu^2}{2(E_\pi - p_\pi cos(\theta_\nu))} \quad (3.1)$$

where m_π and m_μ are the pion and muon mass.

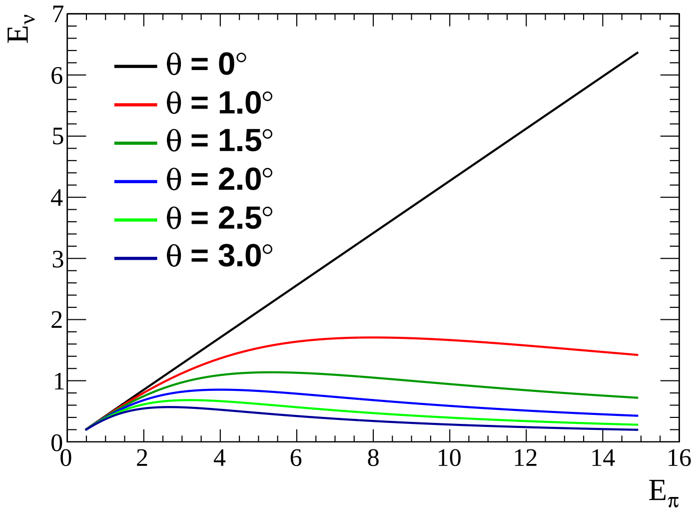

Figure 3.6: The energy of a neutrino from a pion decay as a function of the parent pion energy for fixed angles with respect to the pion momentum.

Fig. 3.6 highlights the power of the off-axis method given the relation between the parent pion energy and the daughter neutrino energy for fixed angles of θ_ν. It clearly shows that, when considering larger angles, the neutrino energy has a weak dependence on the parent pion energy. This leads to a much narrower neutrino energy distribution. When considering a full simulation of the T2K neutrino beam the effect of the off-axis angle on the neutrino spectrum is shown in Fig. 3.7. It shows how an angle of 2.5° off-axis is preferred as it results in a narrow neutrino energy spectrum, peaked in the region of maximum ν_μ disappearance given reasonable oscillation parameters and also suppresses background events at higher energy which are often poorly reconstructed.

3.1.4 Global Alignment and Time Synchronisation

As stated in Sec. 3.1.1 a precise measurement of the time structure of the beam is essential to analyses at T2K as it greatly reduces the coincident cosmic back-

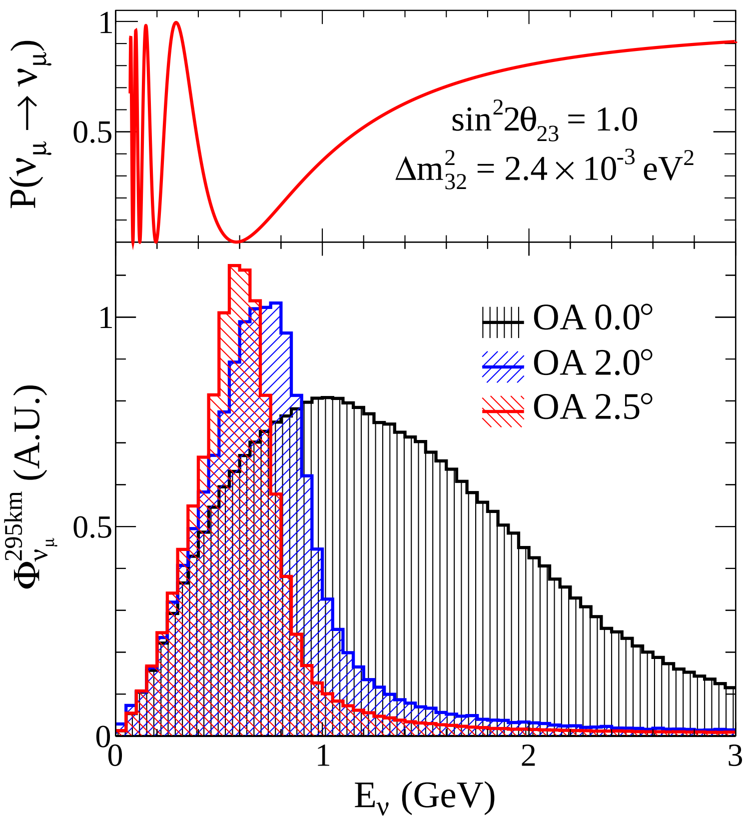

Figure 3.7: The muon neutrino survival probability at 295 km as a function of the energy and the T2K flux simulation for various off-axis angles. Each flux spectrum has been independently normalised and therefore only their shapes can be compared. Figure from [49]

ground. Accurate alignment, positioning, and synchronisation is required over all detectors in the experiment in order to achieve this. Global Positioning System (GPS) surveys were performed to measure the off-axis angle, and the distance between the target and the centre of Super-K which were found to be 295335.2 $\pm$ 0.7 m and 2.504 $\pm$ 0.0004 $^\circ$ respectively [43]. The timing system provides a synchronisation between the beam spill time-stamps at J-PARC and neutrino event triggers at Super-K on the scale of 50 ns. This is done by custom electronics boards which use a local time clock from a rubidium atomic clock and is referenced by a GPS time signal. The time signal, synchronised with the MR, is transmitted to Super-K through a private network and relayed back to monitor consistency [43]. The T2K near detectors receive beam trigger information using an independent optical fibre link.

3.2 ND280

ND280 is the off-axis near detector located 280 m from the target, with an off-axis position which matches that of Super-K.

The primary purpose of ND280 is to assist in providing an accurate prediction of the event rate at Super-K. This is realised when a fit to the ND280 data reduces the uncertainties in the flux and cross-sections which affect the prediction at Super-K. In the analysis presented here, measurements made at ND280 were used as prior constraints to the oscillation analysis.

As neutrino oscillations result in a modified flux spectrum at Super-K with respect to that at ND280, accurate constraints on the neutrino interaction rate as a function of neutrino energy are vital for any prediction at Super-K.

ND280 reduces the uncertainty in the oscillation analysis with a measurement of the ν_μ and $\bar{\nu}_\mu$ interaction event rates, across many interaction channels, in both ν-mode and $\bar{\nu}$-mode. With this ND280 is able to constrain neutrino cross-sections along with the beam energy and flavour composition.

Shown in Fig. 3.8, ND280 is a multi-component detector made from several sub-detectors within the recycled UA1 magnet. The sub-detectors include the PØD, a detector which is optimised to identify π^0, time projection chambers (TPCs), fine grained detectors (FGD), the electromagnetic calorimeter (ECAL) and the side muon range detector (SMRD). The PØD, TPCs and FGDs are inside the "basket", which is a 6.5 m by 2.6 m by 2.5 m metal frame which makes up the central region of the detector. The ECAL surrounds the basket and is encased in the magnet. The magnet provides a 0.2 T dipole magnetic field and also serves as the bulk of the SMRD.

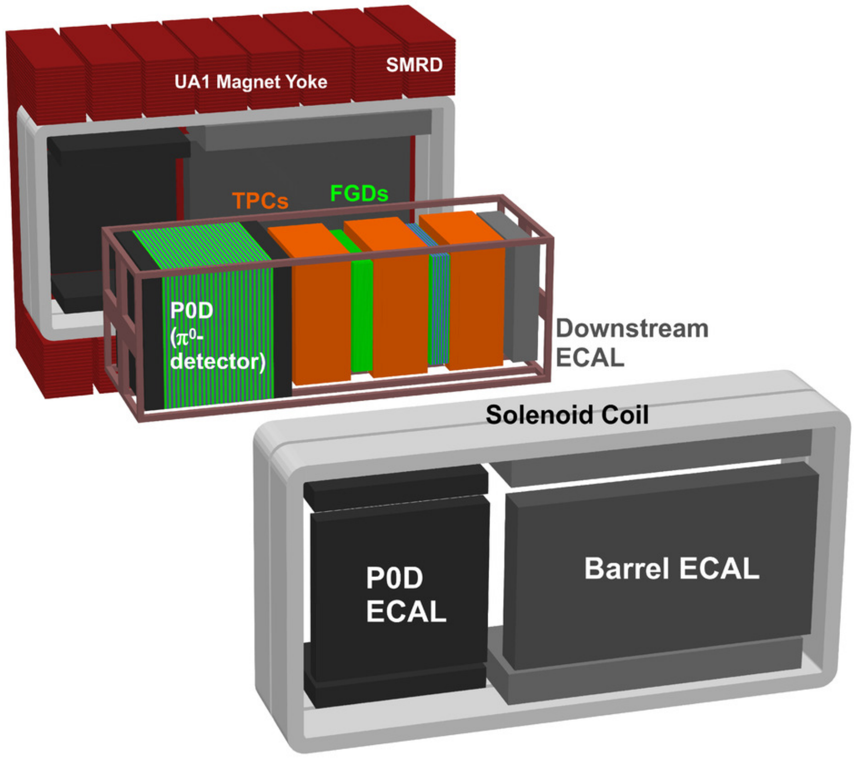

Figure 3.8: A schematic of the sub-detector arrangement which comprises ND280. Figure taken from [51]

3.2.1 The FGDs

There are two FDGs, which provide the majority of the neutrino interaction target material at the near detector for the oscillation analysis. Along with providing target mass, the FGDs also have an excellent tracking and PID capability for short tracks contained in the FGD. The active components of the FGDs are layers of thin rectangular scintillator bars, 9.61 mm by 9.61 mm by 1864.3 mm, made out of polystyrene. Each layer consists of 192 scintillator bars arranged in the plane perpendicular to the beam direction. Two layers with the bars in the horizontal and vertical direction are combined to create an 'XY module'. The signal from the scintillator bars is read out as described in Sec. 3.2.6.

The most upstream FDG, FDG1, is made entirely of scintillator with a target mass of 1.1 ton from 15 XY modules. The second, FGD2, is made from seven layers of XY modules with six 2.5 cm layers of thin walled poly-carbonate filled with water. The water target in FGD2 is particularly important as it facilitates a direct measurement of the neutrino interaction rate on water. Without this, the only option is to use theoretical models to predict the interaction rate at Super-K by extrapolating from the measurement on carbon scintillator.

As neutrinos can interact via a number of different channels, described in Sec. 4.2, an important feature of the FGD is its ability to distinguish between some of these channels so they may be separated statistically. Events in the oscillation analysis are categorised in terms of final state topology from the particles that can be observed in the detector.

Particles which are ejected from the nucleus are often of low energy and are contained within the FGD. When this is the case, it is necessary for the FGD to be able to distinguish between protons and pions. This is done by taking the measured energy deposited and length of each track and comparing it to predictions from simulation. The separation of protons and pions in the FGD from MC simulation is shown in Fig. 3.9.

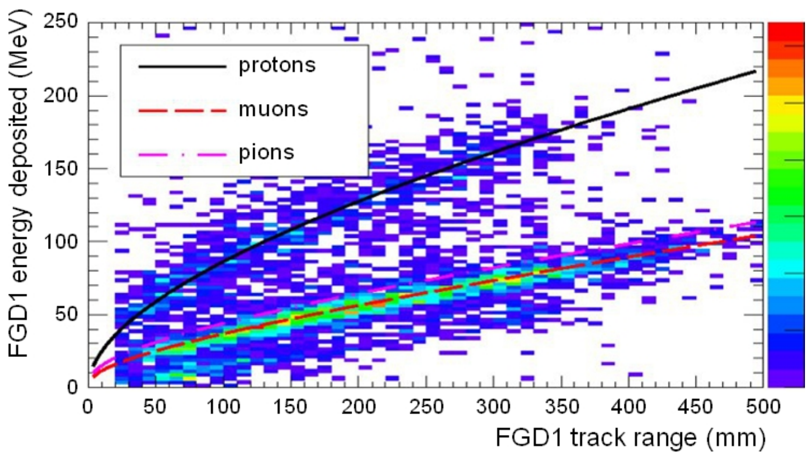

Figure 3.9: Deposited energy vs track range for particles stopping in FGD1. The scatter-plot shows stopping particles in neutrino beam data, while the curves show the expectations for protons, muons, and pions from the MC. Figure taken from [52].

3.2.2 The TPCs

Three TPCs surround the FGDs, as shown in Fig. 3.8, and provide the most reliable tracking information in ND280. The TPCs have excellent 3 dimensional imaging of multiple particle tracks and particle identification. They therefore provide vital information when constructing high purity samples of various neutrino interactions. With the 0.2 T magnetic field, the TPCs are able to measure the momentum of muons transverse to the field with an uncertainty of less than 10% from the track curvature. Accurate measurements of the momentum of outgoing particles is not only useful for event classification, but essential for measuring the event rate as a function of incoming neutrino energy.

Each TPC is made out of an inner box, which acts as a field cage and is filled with argon-based[1] drift gas, inside of an outer box, filled with insulating CO_2 as shown in Fig. 3.10. A central cathode panel, in the plane perpendicular to the magnetic field, is placed at the centre of the TPC. A copper strip pattern is machined onto each of the inner walls facing the cathode to produce a electric drift field aligned with the magnetic field in the detector. Readout modules, Micromegas [53], are also placed on these walls. Micromegas are a type of gaseous detector with a large drift region followed by a region of amplification near the walls and can have spacial resolutions of below 100 μm with fast signals on the order of 100 ns.

Ionisation electrons are produced as charged particles traverse the TPC and drift towards the readout planes. The electrons avalanche as they reach the readout and are measured by 12 Micromegas on each wall. The charge pattern and the arrival time, recorded by the Micromegas, combine to create 3D tracks. This is done by first grouping neighbouring clusters of charge, which could have originated from the same particle track, and then inferring the track momentum and direction using a likelihood fit.

[1] 95% Argon, 3% tetrafluoromethane (CF_4) and 2% isobutane (iC_4H_{10})

Like in the FGD, particle identification in the TPC is done using measurements of energy loss. However, particle tracks in the TPC are much longer which opens up the possibility of a more sophisticated treatment. In the TPC, the ionisation energy loss per unit distance is compared to that of simulation to define the "pull", a statistic for the $i'th$ particle hypothesis, $\delta_E(i)$. Instead of taking the total charge collected along the path length directly, the truncated mean is used. The truncated mean only considers 70% of hit clusters corresponding to the low energy region and was chosen through MC simulation and test beam studies which found it to give better particle separation. Fig. 3.11 shows how the pull statistic, $\delta_E(e)$ for a sample of through going muons with the pull statistic determined under the electron hypothesis, can be used to distinguish muons from electrons.

The separation power of the TPC for other particles is highlighted in Fig. 3.12, which shows a comparison of the measured distribution from beam events and theoretical curves of energy loss as a function of momenta.

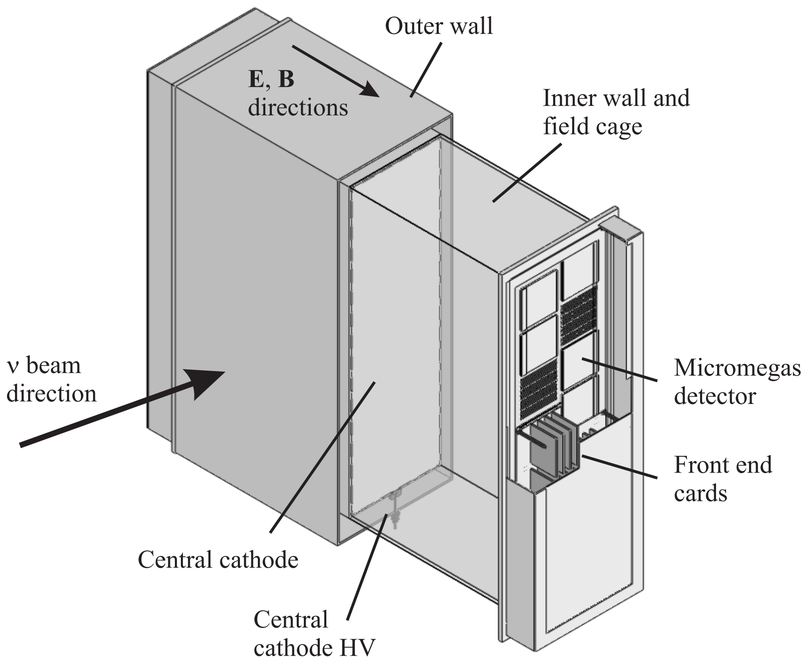

Figure 3.10: Cut-away diagram showing the main components of the TPC design. Figure taken from [54].

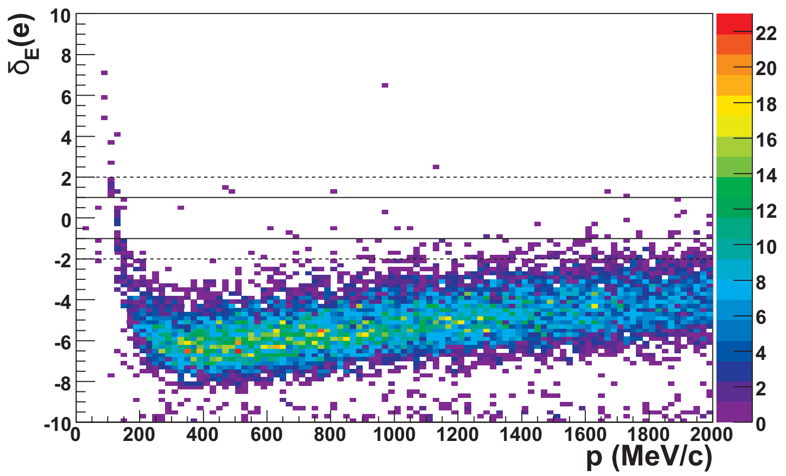

Figure 3.11: Distribution of the energy loss pull statistic, $\delta_E(e)$, for a sample of through going muons in the electron hypothesis. The solid and dashed horizontal lines indicate cuts of $|\delta_E(e)| < 1$ and $|\delta_E(e)| < 2$ respectively. Figure taken from [54].

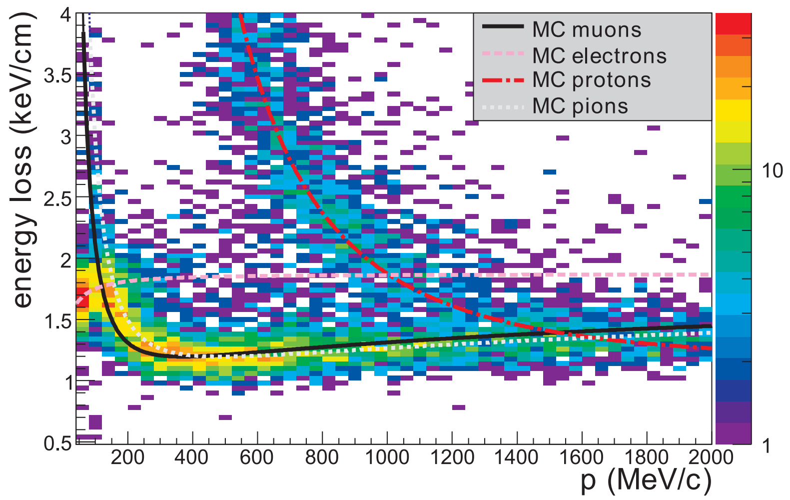

Figure 3.12: Distribution of the energy loss per cm for positively charged particles produced in neutrino interactions. Expected curves from MC simulations are shown for muons, electrons, protons and pions. Figure taken from [54].

3.2.3 The PØD

The neutral current ν_μ interaction with a π^0 in the final state is a process which can mimic the ν_e appearance signal at Super-K. The PØD detector is optimised to make a measurement of the interaction cross-section on water. The active components of the detector are pairs of planes made from horizontally and vertically arranged triangular scintillator bars each with an optical readout as shown in Fig. 3.13.

In between the active layers are sheets of brass, and water bags which can be filled or empty. In the outer region of the detector, which is used as a calorimeter, lead is used instead of brass to improve the containment of showers.

The detector can be operated with the water bags either full or empty, which allows for the possibility of a cross-section measurement on water using the subtraction method. Neutrino interactions which occur in the PØD have not been used as a direct constraint in the analysis presented here.

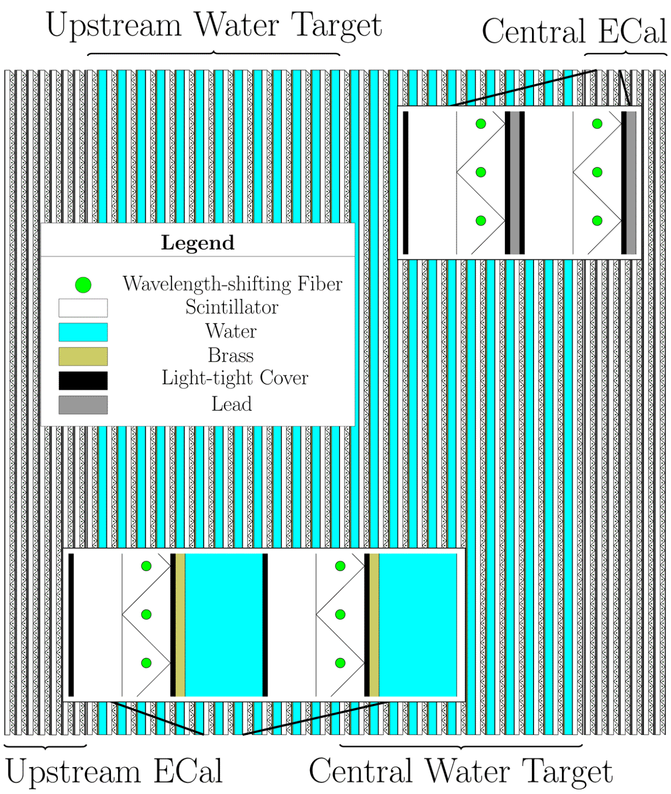

Figure 3.13: A schematic diagram of the PØD highlighting the scintillator bar arrangement in the central region and the ECAL region. Figure taken from [43].

3.2.4 The ECAL

The ECAL surrounds the inner detectors and is used primarily as a calorimeter but can also be used for tracking. It is composed of layers of active plastic scintillator bars and lead to act as an absorber. With a total of 13 modules, it provides almost 4π coverage for particles exiting the basket. The modules include 6 Barrel-ECAL modules which surround the tracker region, six PØD-ECAL modules which surround the PØD detector and 1 module downstream of the tracker region, the Ds-ECAL, which is contained in the basket.

The scintillator bars used in the ECAL have a cross-section of 4.0 cm by 1.0 cm and come in different lengths depending on the module they make up. They are, as in the FGD and PØD, read out as described in Sec. 3.2.6.

The ECAL is an important component when identifying π^0 in the tracker region of ND280. Due to its low density, gammas from a π^0 decay are less likely to convert in the TPC, and therefore leave no signal. Electromagnetic showers in the ECAL can however be used to reconstruct π^0 decays in the tracker, and thus provide a measurement on the NCπ^0 cross-section.

3.2.5 The SMRD

The SMRD is composed of 440 scintillator modules, which are placed in and around the ND280 magnet. It can provide a momentum measurement of high energy and high angle muons which escape the central region. However, its primary function in the oscillation analysis is to provide a cosmic veto.

3.2.6 Optical readout

Scintillator is used to make up the bulk of the active regions in each of the PØD, ECAL, FGD, SMRD and INGRID. Although the shape of the scintillator bars change across the detectors, there are many similarities in their instrumentation.

A TiO_2 reflective coating is used to optically separate all neighbouring scintillator bars and reduce light loss. Each scintillator bar scintillator bar is read out using a wavelength-shifting (WLS) fibre and multi-pixel photon counter (MPPC). For the FGD, ECAL, PØD and INGRID the WLS fibre is threaded through a straight hole drilled through the centre of each scintillator bar. However, as the SMRD scintillator bars are much larger, the WLS fibre follows a curved path to increase absorption as shown in Fig. 3.14. Some scintillator bars are read out with an MPPC attached to one end, with the other mirrored via vacuum deposition of aluminium to reduce light loss, and others are instead read out with an MPPC at both ends.

The absorption spectrum of the material used for the WLS is centred close to the emission spectrum of the scintillator bars to maximise light collection [43]. The emission spectrum of the WLS however has little overlap with the absorption which results in low self-absorption within each fibre.

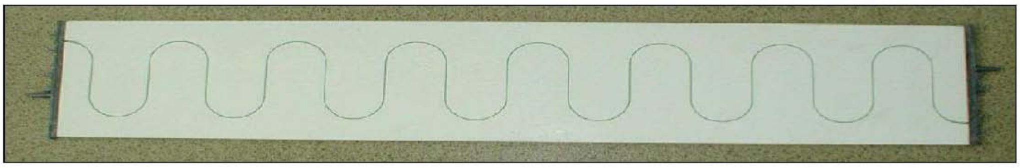

Figure 3.14: An SMRD scintillator bar and embedded WLS fibre. Figure taken from [55].

3.3 INGRID

The on-axis neutrino detector, INGRID [44], is used to make a precise measurement of the neutrino beam direction and profile to ensure the stability of the beam. This is important as the predicted flux at Super-K is very sensitive to deviations in the direction of the neutrino beam, as detailed in Sec. 3.1.3. The measurements at INGRID are used as a prior constraint on the neutrino flux at both ND280 and Super-K in the oscillation analysis. INGRID also used to make cross-section measurements independent from the oscillation analysis [56].

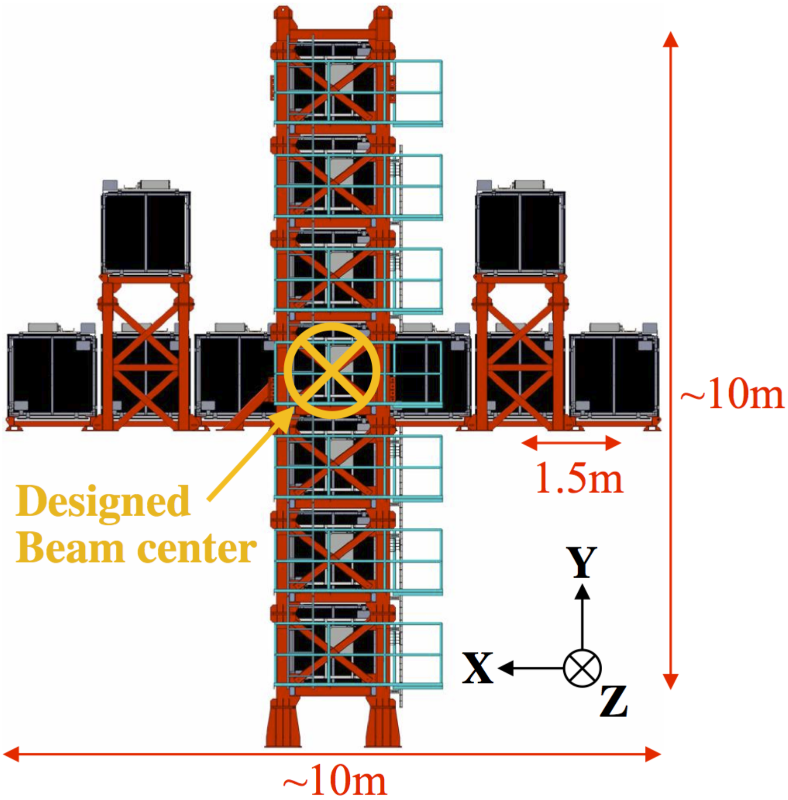

Figure 3.15: The INGRID on-axis near detector. Figure taken from [44]

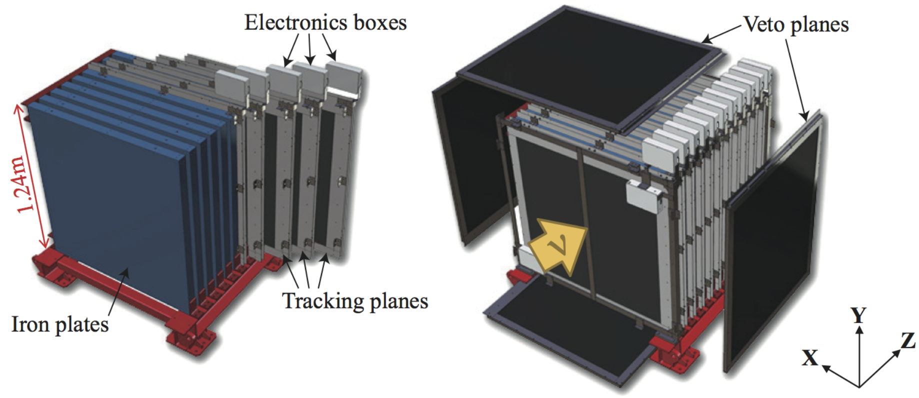

Figure 3.16: Expanded INGRID module showing the arrangement of iron, scintillator and veto planes. Figure taken from [44]

INGRID is made up of fourteen identical modules arranged in a cross formation, as shown in Fig. 3.15, which spans a 10 m by 10 m transverse section of the neutrino beam. The centre of the cross, which is made up of two overlapping modules, is centred on the direction of the primary proton beamline. Two additional identical modules are placed above the arms of the cross to provide a measurement of the axial symmetry of the beam profile. With this setup, INGRID can measure the beam centre to better than 10 cm which corresponds to a 0.4 mrad accuracy at 280 m.

Each module is made from 11 active scintillator planes interleaved with 9 passive iron plates, which provide target material as shown in Fig. 3.16. The iron plates have an area of 124 cm by 124 cm and are 6.5 cm thick providing a neutrino target mass of 7.1 tons for each module. Each tracking plane is constructed from 24 scintillator bars placed horizontally and 24 placed vertically. There is no iron plate between the 10th and 11th scintillator planes due to weight restrictions. Each module is surrounded by 6 veto planes, each made out of one layer of scintillator bars, to reject interactions which occur outside of the module. Each INGRID scintillator bar is read out using wavelength-shifting (WLS) fibres and multi-pixel photon counter (MPPC) as described in Sec. 3.2.6.

Finally, an additional module, the Proton Module, which is fully active and has a finer granularity, is placed upstream at the centre of the beam. The purpose of the Proton Module is to provide a high statistics measurement of protons from quasi-elastic scattering for comparison with the MC. Proton tracking is possible due to the fine granularity [56].

3.4 Super-K

The T2K far detector, Super-K [57], is a 50 kt water Cherenkov detector located under Mt. Ikenoyama in Kamioka, Gifu, Japan. Super-K is positioned 295 km west of J-PARC, inside the Kamioka Observatory. Mt. Ikenoyama provides a mean rock overburden of 1 km (2.7 km water equivalent) to shield Super-K from cosmic backgrounds. The overburden leads to a muon rate in Super-K of 2 Hz, 5 orders of magnitude smaller than the prediction at sea level [58].

Super-K consists of a cylindrical tank filled with ultra-pure water, with a radius of 19.5 m and a height of 42 m, separated into inner (ID) and outer (OD) detector volumes. Between the two volumes is a stainless steel cylindrical metal structure, ∼2 m from the wall, which supports 11,129 inward-facing and 1,885 outward-facing photo-multiplier tubes (PMTs). Those which are inward-facing are 50 cm diameter Hamamatsu R3600 hemispherical PMTs, which have a combined peak quantum and collection efficiency of ∼20% [57], and provide a 40% ID photo-coverage. The outward-facing are 20 cm diameter PMTs, 611 Hamamatsu R1408 PMTs and 1274 Hamamatsu R5912 PMTs, used to veto against entering cosmic or beam related backgrounds.

The walls of the stainless steal structure are used to optically separate the ID and OD. The wall facing the ID is covered with a black plastic sheet to minimise reflections which can affect the reconstruction. The outer facing wall is instead covered in a highly reflective material to maximise light collection in the OD PMT array.

The ID is filled with 32 kt of water, 22.5 kt of which makes up the fiducial volume. Only neutrino interactions which were reconstructed in the fiducial volume were used for the oscillation analysis presented in this thesis.

3.4.1 Super-K Reconstruction

Neutrino interactions are inferred at Super-K from the charged particles they produce. If the charged products travel through the detector faster than the phase velocity of light in water, they produce Cherenkov radiation.

As charged particles propagate through an insulating medium they interact and excite the molecules within. Once in an excited state, the molecules can return to a ground state via the emission of light. If the charged particle is moving faster than the speed of the emitted light, it can cause de-excitation of molecules which are in phase with one another. The resulting light can interfere constructively to form a cone of Cherenkov radiation around the direction of the

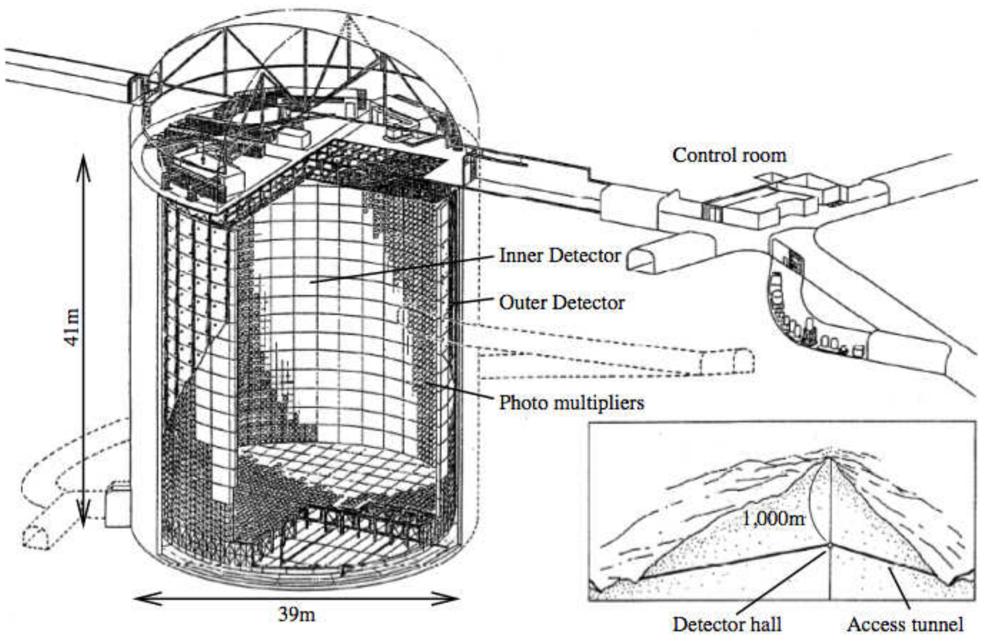

Figure 3.17: The Super-K detector. Figure taken from [57].

particle. Light is emitted in a direction specified by:

$$\cos(\theta_c) = \frac{1}{\beta n} \tag{3.2}$$

where β is the velocity of the particle, n the refractive index of the medium ($\sim \frac{4}{3}$ for water) and θ the opening angle of the cone.

The energy emitted at a given wavelength, per unit length per wavelength interval, taken from [59], is given by:

$$\frac{d^2E}{d\lambda dx} = \frac{4\pi^2 e^2}{\lambda^3}(1 - \frac{1}{\beta^2 n^2}) \tag{3.3}$$

As particles must be travelling faster than the local speed of light to emit Cherenkov radiation, each particle has a unique energy threshold. Momentum thresholds for various particles emitted in neutrino interactions are given in Tab. 3.2. At the T2K beam energy, typically only the lepton (e or μ) from the primary interaction vertex and in some cases a pion are above the Cherenkov threshold. However, pions from neutrino interactions can also be distinguished by their decay products as described in Sec. 5.3.3.

Particle	Momentum threshold (MeV)
e	0.579
μ	119.8
p	1063.9
$\pi^{\pm}$	158.3

Table 3.2: The Cherenkov radiation momentum thresholds (in MeV) for charged particles typically produced in neutrino interactions at Super-K.

Neutrino interaction events used in this analysis are those defined to be "fully-contained", meaning that particles in the event do not exit the ID. Therefore, particles must fall below the Cherenkov threshold while in the ID. The resulting observable at the surface of the ID is a circular band of light with inner and outer radii defined by the path and energy of the charged particle. Ring shaped hit patterns, measured on the ID PMTs, are therefore used to infer the interaction vertex position, and lepton momentum and flavour.

The neutrino interaction vertex is measured in Super-K to a resolution of 34 cm for muons and 25 cm for electrons by considering the PMT timing residuals and the momentum, from total light collected, is measured with an uncertainty of $\pm$(0.6 + 2.6/$\sqrt{(}p(GeV/c)))$% and $\pm$(1.7 + 0.7/$\sqrt{(}p(GeV/c))$ + 0.5)% for electrons and muons respectively [60]. The angular resolution is estimated to be 3.0° for electron events and 1.8° for muon events [61].

Distinguishing between ν_e and ν_μ events at Super-K is vital to the oscillation analysis presented here. This is done by using the PMT hit timing and event topology. Examples of muon and electron hit patterns are shown in Fig. 3.18. The difference in the hit distributions is due to the mass of each lepton. As electrons are much lighter than muons, they are more likely to cause electromagnetic showers, which result in a wider or "fuzzy" ring. Correspondingly, muons create rings with sharp well-defined edges, as they rarely cause showers.

A likelihood is constructed based on the predicted hit distribution from a muon and electron and a cut placed at 0 as shown in Fig. 3.19. Studies performed on a sample of simulated events at Super-K found an expected misidentification rate of 0.7% for muons and 0.8% for electrons [60].

An algorithm that searches for clusters of time-delayed hits after each event is used to identify Michel electrons from the decay of pions and muons. This is even possible when the parent particles are not reconstructed and therefore useful for eliminating multi-particle events at Super-K. A tagging efficiency of above 99% has been found considering a control sample of atmospheric stopping muons [62].

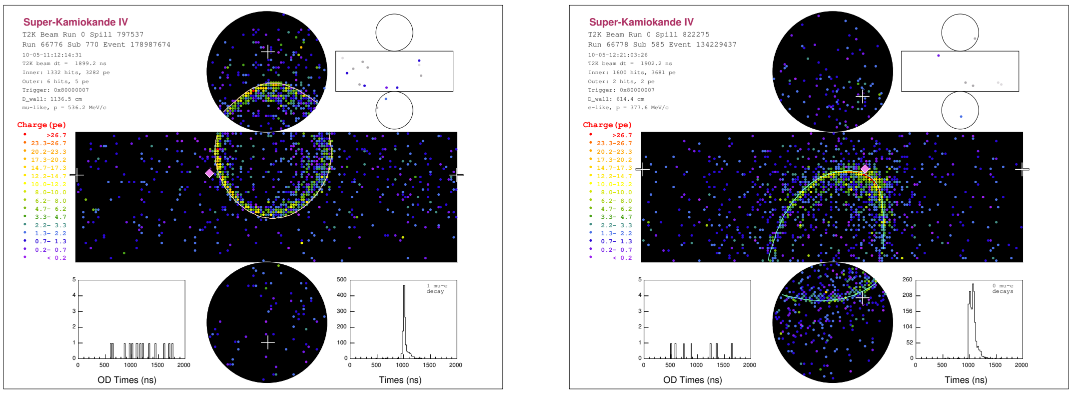

(a) Muon-like. (b) Electron-like.

Figure 3.18: Examples of one ring T2K beam events measured at Super-K. Each pixel is a PMT and with the colour corresponding to the amount of charge collected in the event. The result of the reconstruction is represented by the white line. The white crosses indicate the location of the reconstructed vertex and the diamond marks the point where the neutrino would have exited the detector had it not interacted. In the upper right of each figure there is a hit pattern in the OD. Figure taken from [43]

3.4.2 Calibration

Accurate measurements of the water transparency, PMT gains and timing are vital to the Super-K simulation and reconstruction used in the oscillation analysis. Numerous systems are in place in order to periodically calibrate and verify the stability of Super-K. A detailed overview of the calibration effort at Super-K can

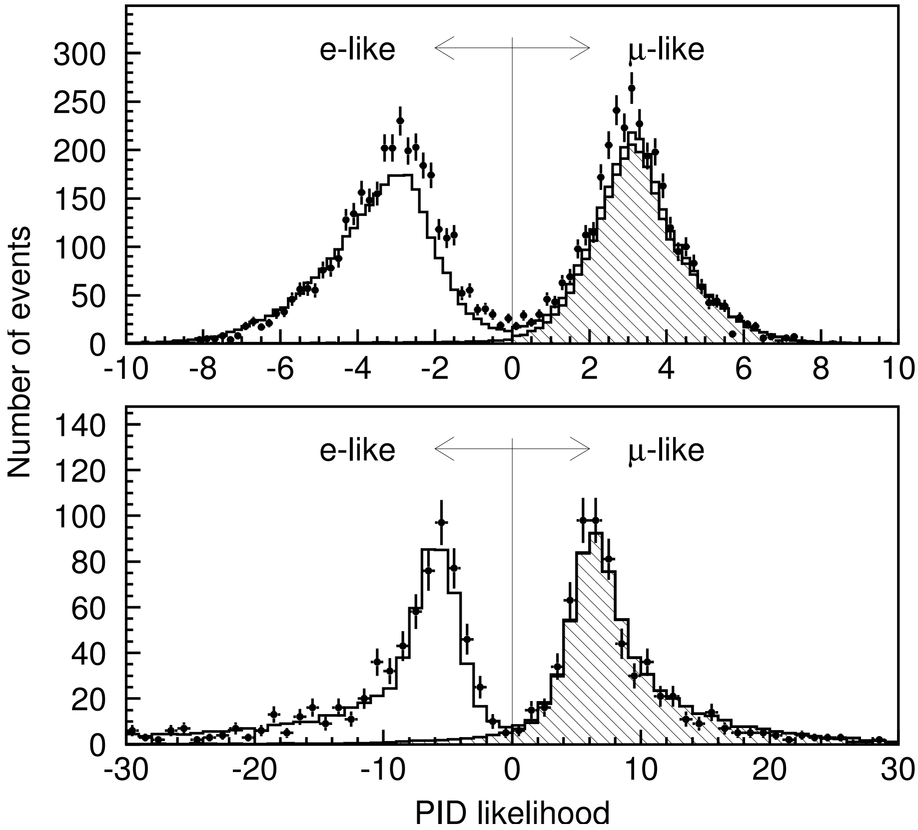

Figure 3.19: The MC (histogram) and data (data points) distribution of the particle identification likelihood for sub-GeV (top) and multi-GeV single-ring events. The MC was generated for neutrino oscillation parameters $\sin^2 2\theta_{23}$=0.5 and $\Delta m^2_{32} = 2.1 \times 10^{-3} eV^2$. The solid (hashed) histograms include charged current ν_e (ν_μ) interactions. Figure taken from [60].

be found in [63].

3.4.2.1 PMT Timing and Gain

Each PMT in the ID has an independent high voltage setting used to tune the amount of charge amplification with incoming light. The aim of gain tuning is to determine the high voltage of each PMT such that the same output charge is measured for a given light intensity. Light is provided by a scintillator ball which can be lowered into various positions inside the water tank and acts as an isotropic light source. Multiple measurements are taken for a range of PMT high voltages and PMT gains are tuned taking into account the uniformity of the source, detector geometry and light attenuation.

Accurate relative timing between ID PMTs is important as it is used to calculate the interaction vertex, used for the first iteration of the event reconstruction [57]. The response time of each readout channel can be affected by the transit time of each PMT, the length of the PMT signal cable, and the processing time of the electronic readout as well the size and shape of the pulse ("time-walk"). The calibration source is a laser light diffusion ball which is inserted into the centre of the Super-K tank and provides fast (0.2 ns) light pulses. The diffusion ball is powered by 337 nm nitrogen laser light which is shifted to 398 nm using wavelength shifting dye and passed through an optical filter. 398 nm light was chosen as it is close to the wavelength where the response of the PMTs is known to be maximal and as the optical filter facilitates calibration with varying pulse heights. The calibration consists of a polynomial fit to the two dimensional distribution of the time-of-flight corrected hit time versus pulse height for each PMT.

3.4.2.2 Water Transparency

The amount of light incident on each PMT in an event is determined by the nature of the event, distance to each PMT and the transparency of the water. Therefore, detailed measurements of the water transparency are required to ensure accurate event reconstruction. The combined effect of absorption and scattering of light is measured using a laser diffuser ball and CCD camera. A pulsed, high energy (2-3 mJ), laser is used to power the diffuser ball which is then imaged by the CCD camera. The procedure is repeated for light between 350 and 500 nm to provide a measurement of the attenuation length as a function of wavelength. Measurements are also taken with the diffuser ball at various depths in Super-K to ensure constant attenuation across the entire tank.

As water transparency is a function of the water quality, and therefore may change with time, the total attenuation is also measured during operation using cosmic ray muons and an additional laser system. The advantage of these methods is that they allow for in-situ measurements during the operation of Super-K and make use of events which otherwise are seen as a background. In both cases the ID PMTs are used for light detection.

High energy cosmic ray muons behave as minimum ionising particles depositing an almost constant ionisation energy of $\sim$2 MeV per cm. Therefore, they can be used as a constant energy calibration source for wavelengths across the entire Cherenkov spectrum. The calibration compares the expected charge on each PMT, a function of the light path length, the incident angle of light and the effective attenuation length, with that measured. The attenuation length found with this method is found to be 105.4 $\pm$ 0.5 m.

The second in-situ transparency measurement system consists of laser light carried to the Super-K ID surface via optical fibres. The optical fibres enter the top of the ID, face the bottom, and are able to provide light of 337, 371, 400 and 420 nm. With this setup, the observed charge on PMTs at the bottom of the tank provide a measurement of the attenuation of light and on the sides and top a measurement of the scattering. The time and spacial distributions of the laser light are compared with that from the MC to infer absorption and scattering coefficients as a function of wavelength. The laser light is however much weaker than that provided by the diffuser ball and therefore measurements are taken every 6 seconds and analysed together every 5 days to ensure reasonable statistics.

3.4.2.3 GeV Scale Energy

Calibration of the absolute energy scale of Super-K in the GeV region is essential for accurate lepton energy reconstruction. Artificial sources at these energies are difficult to produce and therefore Super-K makes use of atmospheric sources which are abundant. These are split into four samples which cover the momentum range from 30 MeV/c to 6 GeV/c.

The first sample makes use of Michel electrons from the decay of cosmic muons which stop in the detector. The sample covers low momentum reconstruction and found a difference of -0.7 $\pm$ 0.3% between the peak positions of the data and MC Michel spectrum. The second sample consists of reconstructed π^0 events from neutral current atmospheric neutrino interactions. From the $\pi^0 \rightarrow \gamma\gamma$ decay an invariant mass peak can be constructed from two electron like rings which appear in Super-K. A selection is applied for invariant masses between 85 and 185 MeV/c^2. As for the Michel sample, Gaussians were fitted to the distributions of data and MC events which found a discrepancy of 0.5 $\pm$ 0.7% between the fitted means.

The final two samples consist of cosmic muons which enter through the top wall and stop in the ID and are split into a low momentum sample containing those between 200 and 440 MeV/c, and a high energy with those above 1 GeV. For the low energy sample the opening angle of the Cherenkov cone produced is used to determine the muon momentum whereas the track length was used for the high energy case. In both cases, the expected MC momentum distributions were compared with that from data in momentum bins to determine any deviation. A maximum difference of 2.4 $\pm$ 0.3% was found in the low energy sample and 1.3 $\pm$ 0.3% in the high energy.

The combined results of the energy scale calibration study can be found in Fig. 3.20. As the uncertainty is largest at the peak of the T2K energy range, an energy scale uncertainty of 2.4% was used in the oscillation analysis for a conservative approach. Further details about the Super-K energy scale calibration can be found in [64].

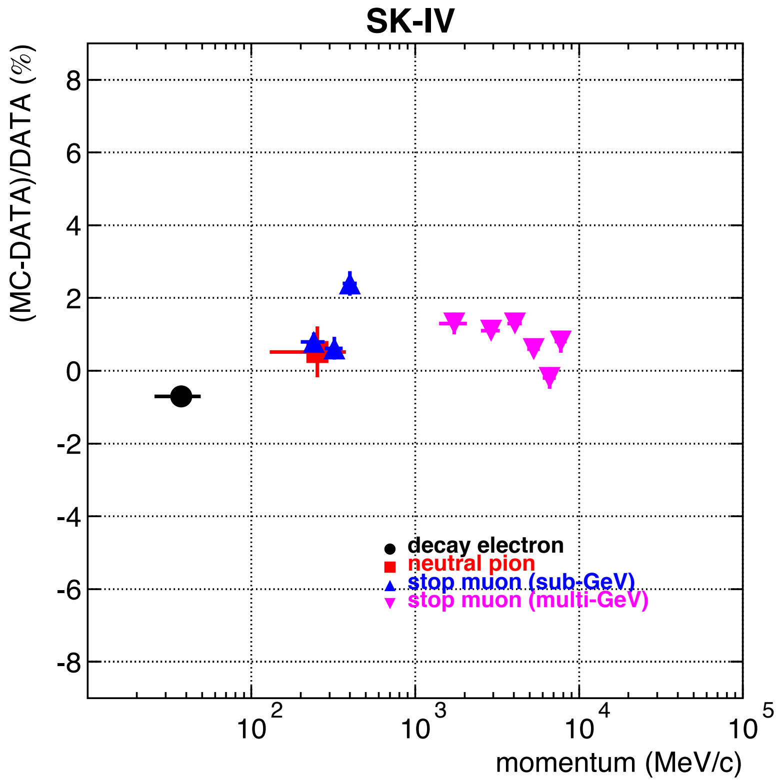

Figure 3.20: The measured data-MC difference from four Super-K momentum scale control samples. The black point is from the decay electron sample, the red from the neutral current π^0 sample, the blue points from the low energy stopping muon sample and pink from the high energy stopping muon sample. The horizontal bars represent the size of the momentum range of each sample bin and the vertical the statistical error. Figure taken from [64].

3.5 Physics Goals

In its conception, the aim of the T2K experiment was to be able to provide a precision measurement of muon neutrino disappearance, providing constraints on $\sin^2 2\theta_{23}$ and Δm^2_{32}, and the first observation of electron neutrino appearance in a muon neutrino beam for a measurement of θ_{13}. The observation of electron neutrino appearance would firstly be a direct observation of the non-zero mixing angle θ_{13} and also allow for the possibility of observing CP violation in neutrino oscillations. These goals were achieved, culminating in the 7.3σ discovery of electron neutrino appearance in 2013 [65]. Furthermore, combining the measurements of muon neutrino disappearance and electron neutrino appearance within T2K with external measurements of θ_{13} from reactor neutrino experiments lead to a hint of CP violation in the neutrino sector [42]. These measurements all came while T2K was running in ν-mode, since then T2K has run in a combination of neutrino and anti-neutrino mode for additional sensitivity to CP violation. The measurement presented in this document is a result of a combined analysis of all available Super-K oscillation data sets at T2K from ν-mode and $\bar{\nu}$-mode, T2K runs 1-7.

In addition to PMNS neutrino oscillation, T2K has a wide physics program including non-standard oscillation studies and neutrino interaction measurements. The non-standard oscillation program includes searches for short baseline sterile neutrino oscillations using the electron neutrino ND280 data set [66] and the search for Lorentz violation via the sidereal effect in INGRID [67].

The ability of ND280 to constrain neutrino interaction parameters for the oscillation analysis is detailed in Sec. 5.2. However, there also exists a strong independent program of neutrino cross-section measurements using the entire near detector suite. These include measurements of coherent pion production on carbon [68], single pion production on water using the PØD [69], a double differential muon neutrino charged current with no pion in the final state cross-section on scintillator [70], and inclusive muon and electron neutrino cross-sections [71] [72] with the off-axis near detector ND280. A number of cross-section results have also been published on iron and scintillator using INGRID. The most recent of which are a measurement of the charged current inclusive muon neutrino cross-section [56] and a muon neutrino charged current quasi-elastic cross-section measurement [73]. T2K beam data has also been used at Super-K for a neutral current elastic measurement via observation of nuclear de-excitation [74].

Additionally, Super-K exists as a stand alone experiment providing measurements of solar and atmospheric neutrino oscillations as well as providing world leading lower limits on the proton lifetime through various decay channels [75] [57].

3.6 Physics Data Set

The analysis presented in this document makes use of T2K data from 2010 to the summer of 2016 which includes Super-K data up to and including "T2K run 7". The T2K data set is broken down into runs based on the period in which the data were collected. Due to accelerator upgrades and some unforeseen setbacks the length and amount of data collected in each run can vary significantly. A summary of the total number of accumulated protons on target (POT) and T2K beam power throughout the experiment is shown in Fig. 3.21. Between runs 1 and 5 the T2K beam operated exclusively in ν-mode. Subsequent runs included both ν-mode and $\bar{\nu}$-mode, however $\bar{\nu}$-mode was preferred with the aim of approximately equal exposure between the two. A total of 1.51×10^{21} POT was collected up to run 7 (7.482×10^{20} and 7.471×10^{20} in ν-mode and $\bar{\nu}$-mode respectively), making up approximately 20% of the expected total for T2K (7.8×10^{21}). All ND280 data processed until early 2017 was used for the near detector analysis. This included 5.82×10^{20} and 2.84×10^{20} in ν-mode and $\bar{\nu}$-mode respectively taken from runs 1 to 6.

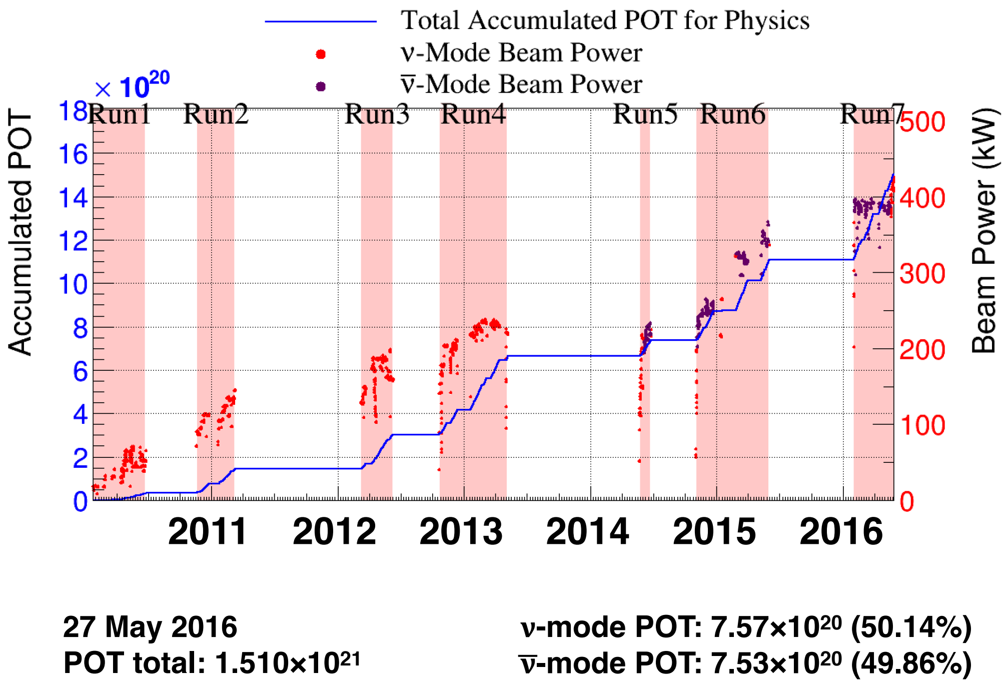

Figure 3.21: The total accumulated T2K POT and as well as the accelerator beam power between 2010 and 2016. Figure taken from [76]

.

Chapter 4

Inputs to the Oscillation Analysis

The neutrino oscillation analysis presented in this thesis is heavily reliant on the predicted T2K detector spectra, under a given neutrino oscillation hypothesis, and the variation of which is a product of interaction, simulation and detection uncertainties. In short, the predicted T2K detector spectra are a result of the prediction of the neutrino flux, neutrino interactions, and the detector response. These respectively determine the beam composition within each detector, the probability for an interaction to occur for a given flux, and the probability for an event to make it into a selection. This section provides a detailed description of the simulations and relevant uncertainties implemented in the analysis presented in this thesis.

The nominal event rates predicted for the T2K detectors are produced via a combination of the following:

- Neutrino Flux
  - A combination of FLUKA [77] and GEANT [78] are used to simulate the neutrino beam flux from the propagation of the proton beam, sec-

ondary particles and particle decays in the target station and decay volume.

  - Neutrino oscillations are modelled in a 3-flavour oscillation framework in constant density matter using a custom package. A matter density of 2.6 g cm^{-3}, chosen from a geological survey of the T2K baseline, is used. The package is validated against Prob3++, a publicly available neutrino oscillation software package [79], and other oscillation analysis groups within T2K [80,81].

- NEUT, a neutrino event generator described in [82], is used to simulate neutrino interactions in the near and far detectors. The generator has many tuneable parameters, which are carefully selected under guidance from the T2K neutrino interaction working group (NIWG), and also provide a mechanism to incorporate uncertainties within each interaction model.

- Custom GEANT4 and GEANT3 simulation packages are used to simulate the ND280 and Super-K detector responses respectively for each event.

4.1 Neutrino Beam Flux

The oscillation analysis framework employed for this analysis requires a nominal neutrino flux prediction and uncertainties. These are provided by a data-driven Monte Carlo simulation, tuned to data both internal and external to T2K. The data-driven constraint is used to mitigate the uncertainty in the neutrino beam flux as a result of uncertainties in the hadronic interaction modes, the proton beam alignment with respect to the target and the detectors, and the magnetic field provided by the focusing horns.

The beam simulation can be thought of as independent simulations of incident 30 GeV protons within the target, secondary particles within the target, and the decay of particles. The FLUKA simulation is employed to model all interactions and the propagation of particles within the target. Once the particles reach the end of the target, their information is exported to JNUBEAM [83], a simulation package built in GEANT3. The JNUBEAM package simulates the decay, and propagation of particles towards the T2K near and far detectors and any interactions the secondary particles may undergo in the surrounding target area using the GCALOR [84] package, which is also tuned to data.

NA61/SHINE is an experiment, based at CERN, which is currently making measurements of secondary particles as a 30 GeV proton beam is incident on replica T2K targets [85]. Measurements of the double-differential ($d^2\sigma/dpd\theta$) hadron production distribution are used to tune and reduce uncertainties on pion and kaon multiplicities, which are integral to the neutrino flux prediction.

NA61/SHINE has taken data with both a thin target (2 cm in length), and a full length T2K target, however the current beam simulation includes only constraints from thin target data taken up until 2009. The thin target data is currently the most significant data set when considering the final flux uncertainty and future improvement is expected with the inclusion of the full length replica target data.

INGRID and proton beam OTR measurements are used to constrain the neutrino beam direction and off-axis angle uncertainty in the vertical direction, as described in Sec. 3.1.

The full extent of work that goes into the flux prediction is detailed in [50]. The uncertainties on the dominant neutrino flux in both ν-mode and $\bar{\nu}$-mode are summarised in Fig. 4.1 which shows an uncertainty between 10% and 20% and highlights the dominant contribution from the hadron interaction uncertainties.

The result is a beam flux prediction and constraint which is tuned using multiple independent data sets. The uncertainty on the flux is modelled in terms of a finite but large dimensional covariance matrix in the Gaussian approximation. The value of each parameter determines the fractional shift from the nominal prediction for a given neutrino type and range in energy. Highly correlated neighbouring energy range bins are then combined to form a set of 100 systematic parameters to be used in the oscillation analysis. 50 for the ND280 flux and 50 for the Super-K flux, split into 11 ν-mode ν_μ parameters, 5 ν-mode $\bar{\nu}_\mu$ parameters, 7 ν-mode ν_e parameters, 2 ν-mode $\bar{\nu}_e$ parameters, 11 $\bar{\nu}$-mode $\bar{\nu}_\mu$ parameters, 5 $\bar{\nu}$-mode ν_μ parameters, 7 $\bar{\nu}$-mode $\bar{\nu}_e$ parameters and 2 $\bar{\nu}$-mode ν_e parameters.

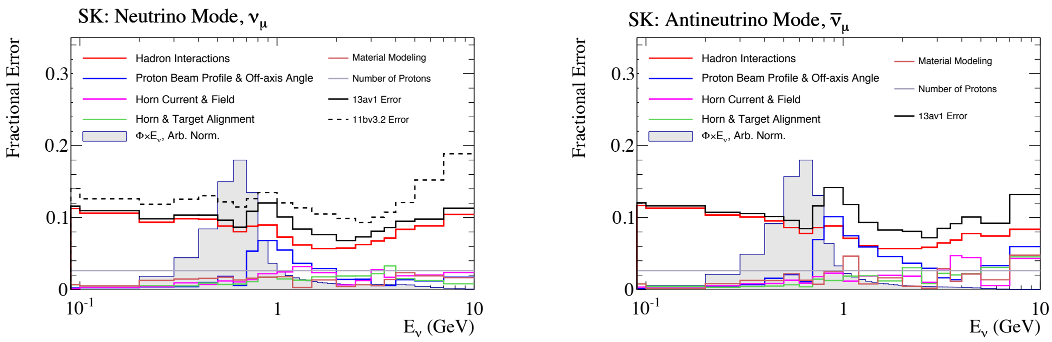

(a) ν-mode ν_μ flux.

(b) $\bar{\nu}$-mode $\bar{\nu}_\mu$ flux.

Figure 4.1: The predicted fraction error on the un-oscillated ν_μ ($\bar{\nu}_\mu$) flux in ν-mode ($\bar{\nu}$-mode). Contributions of sources which lead to the final error are shown for reference along with the T2K flux (grey histogram). Figure from [50].

4.2 NEUT Neutrino Event Generator

NEUT is the Monte Carlo neutrino event generator used to simulate interactions within ND280 and Super-K according to the flux prediction described in Sec. 4.1. Although detailed in [82] and [43], sub-GeV neutrino interaction physics is a rapidly developing field, in part due to the precision required by T2K, and so significant updates were implemented for this analysis from what is described [82]. Listed in this section is a summary of the dominant interaction classes considered in this analysis. Additions to NEUT are mostly developed by members of the T2K collaboration. Confidence in the T2K event rate prediction is a result of the vast effort from the NIWG to include precise predictions of neutrino interaction cross-sections and uncertainties driven by both theory and fits to numerous external data sets [86].

4.2.1 Charged-Current-Quasi-Elastic (CCQE)

The most significant changes to the NEUT software package which affect the T2K predicted event rates are updates to the modelling of CCQE interactions.

CCQE neutrino free-nucleon cross-sections, predicted by NEUT, are based on the Llewellyn-Smith model [87]. The Smith-Moniz [88] relativistic Fermi gas (RFG) model is used to model the perturbation of cross-sections to include effects due to a nucleon which is bound within a nucleus. The parameters which define the RFG model in this analysis are the effective nucleon Fermi Momentum (p_F) and effective binding energy per nucleon (E_B), measured from electron scattering data [89].

Nucleons in the Smith-Moniz model are treated as free for all other purposes. The prediction of the differential cross-section from this model is given by Eq. (4.1)

$$\frac{d\sigma}{d|Q^2|} = \frac{M^2 G_F^2 \cos^2\theta_c}{8\pi E_\nu^2}[A(Q^2) \pm B(Q^2)\frac{(s-u)}{M^2} + C(Q^2)\frac{(s-u)^2}{M^4}] \tag{4.1}$$

θ_c denotes the Cabbibo angle, M the nucleon mass, G_F the Fermi coupling constant and E_ν the neutrino energy. s and u are the Mandelstam variables. A, B and C are functions defined by Q^2 and form factors F_1, F_2, F_A, F_P, F_{3V} and F_{3A} which are also Q^2 dependant.

More recently, the Spectral Function (SF) model from Omar Benhar et. al. described in [90], an alternative to the RFG model, has been made available in NEUT. The SF model is an attempt to provide a more realistic description of the momentum distribution of the initial state nucleons than a simple relativistic Fermi gas. This is done by including the effects of short range nuclear correlations between nucleons inside a nucleus. The result is a momentum and energy distribution for each nucleon, which can be used to calculate a neutrino cross-section under the impulse approximation where the neutrino scatters off of only a single nucleon. More information about the implementation of the SF model in NEUT can be found in [91].

The random phase approximation model (RPA) [92] is another model which accounts for correlations between nucleons inside a nucleus. The RPA model is an attempt to account for a nuclear screening effect, which results from long range nucleon correlations. It is implemented in NEUT as a modification to the CCQE cross-section as a function of Q^2. It is important to note that the NEUT RPA correction is from a calculation based on the Local Fermi Gas (LFG) model of the nucleus, where the calculation of the Fermi sea is localised to a smaller region of the nucleus, and not the SF or RFG models. However, the authors of the calculation state that it can be applied to a traditional Fermi gas prediction considering the whole nucleus, with reasonable precision. The authors provide two RPA corrections labelled 'relativistic' and 'non-relativistic' which differ due to a quenching of the RPA correction at high Q^2.

4.2.2 2p-2h

A key addition to NEUT is the multi-nucleon neutrino neutrino interaction model of Nieves et. al. described in [93]. The calculation is an extension of the impulse approximation of the CCQE models, described in [82] and [94], and includes only interactions where the neutrino scatters off of a bound state composed of multiple nucleons. Events of this type are particularly important at T2K as they are almost indistinguishable from the CCQE signal events at Super-K. This is because the 2p-2h events, unlikely to produce an outgoing particle from the nucleus above the Cherenkov threshold, pass all cuts for the CCQE selection at Super-K. Thus the result of including the Nieves 2p-2h model is to enhance the expected CCQE-like event rate at the far detector.

These events, which contribute to the CCQE-like event rate at Super-K, are particularly important as they follow a different kinematic distribution to CCQE events. As neutrino energy is reconstructed under the CCQE hypothesis, the neutrino energy of 2p-2h events is often mis-reconstructed, which is problematic for samples where the shape of the reconstructed neutrino energy spectrum is important. This is explored further in Chap. 11.

4.2.3 NC1γ

A study performed by Wang et. al [95] found that the Neutral Current one gamma (NC1γ) cross-section included in NEUT is roughly half that of the cross-section predicted from a model by Wang et. al calculated as a function of the neutrino and photon energies. The Wang et. al model has been included in this analysis by simply scaling the NEUT NC1γ cross-section by a factor of two and including an additional uncertainty described in Sec. 4.3.

4.2.4 Coherent Pion Production

An updated charged current coherent pion production (CCCoh) model to match the measured E_π distribution from neutrino interactions at MINERνA, detailed in [96], has also been made available. The updated model is produced by scaling the NEUT cross-section as a function of the outgoing π kinetic energy. The applied weights are detailed in Tab. 4.1.

E_π	Weight
0.00-0.25	0.135
0.25-0.50	0.4
0.50-0.75	0.294
0.75-1.00	1.206

Table 4.1: Scaling applied to the NEUT CCCoh interaction cross-section as a function of the outgoing π kinetic energy.

4.2.5 Resonant Pion Production

NEUT includes events considering 18 different resonances limited by an invariant hadronic mass of 2 GeV. The default included is a model driven by predictions made by Rein and Seghal [97].

An alternative resonant pion production model to that included in NEUT is used for this analysis. The resonant pion production events generated with NEUT were re-tuned to follow the predictions of the new model described in [98]. The tuning is a result of a re-analysis of the Argonne National Laboratory (ANL) and Brookhaven National Laboratory (BNL) bubble chamber data sets using form factors from Graczyk and Sobczyk [99].

In addition to pion production via a resonance, an additional channel of pion production without the need for a resonance is included. The model is included as proposed by Rein and Seghal in [97]. The non-resonant pion production background is assumed to be entirely $I = \frac{1}{2}$ which is chosen to match data.

4.2.6 Deep Inelastic Scattering

Deep inelastic scattering (DIS) interactions are included in NEUT for hadronic invariant masses greater than 1.3 GeV. To avoid a conflict between the resonant pion production and deep inelastic scattering, only interactions which produce multiple pions are included from the DIS calculation for hadronic invariant masses between 1.3 and 2 GeV. Beyond 2 GeV, both single pion and multiple pion events are included. The calculation is performed for charged-current interactions and the neutral-current interaction probabilities are inferred from measurements of the charged-current to neutral-current branching fraction [100].

4.3 Neutrino Interaction Uncertainties

The parameterisation of the neutrino interaction model uncertainties at T2K was developed by the NIWG group in parallel to the efforts described in Sec. 4.2. The uncertainties and scope of the prediction are included to cover both theoretical uncertainties and external data mostly taken from MINERνA, MiniBooNE, ANL and BNL [101].

Uncertainties in the neutrino interaction models are included in this analysis and each source of uncertainty is implemented in one of two ways.

- Normalisation Uncertainty An uncertainty on the total predicted cross-section for a process. Each normalisation uncertainty is modelled using a parameter which denotes the fraction of the event rate compared to the nominal (prior to the fit). To generate a prediction for any given parameter value, each event of the corresponding event class is weighted by the parameter value. The parameter is then constrained with either a Gaussian penalty or a flat prior, each bounded by a range defined for this analysis.

- Shape Uncertainty The term shape is used here to denote the fact that a "shape uncertainty" can affect the prediction for an event class in a non linear way and also affect areas of the differential cross-section phase space independently. The uncertainty is again modelled by a single parameter, constrained by either a Gaussian penalty or a flat prior over a defined range. The effect of each parameter on the prediction is defined by response functions, chosen because of the speed at which they can be used to generate MC predictions. The effect of the interaction parameters are stored in this way so they can be quickly applied to the MC in order to generate a prediction given a new set of parameters without the need for a new MC production.

  Each response function is valid over a defined range of neutrino flavour

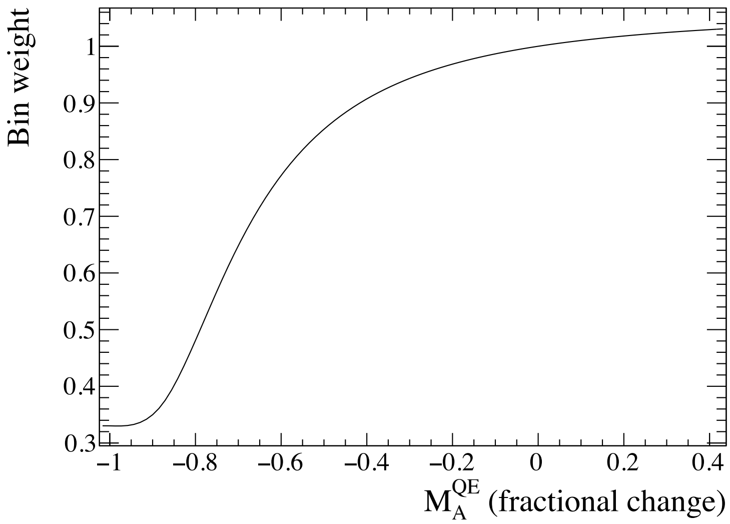

Figure 4.2: An example of a response function which determines the bin scaling factor for a given value of the interaction systematic parameter, M_A^{QE}, for a bin in the *CCQE e*-like ν-mode sample.

and interaction type (ν^i_{int}), true energy (E_{true}), reconstructed energy (E_{reco}), and reconstructed angle (E_θ) for a given interaction model parameter and Super-K sample.

The response functions are calculated by evaluating variations of the event rate in a given range of ν^i_{int}, E_{true}, E_{reco} and θ_{reco} for a range of values of each interaction model parameter. Neutrino event generators are used to determine the variation of the cross section of each event in the MC as interaction parameters are varied. The reweighted events are then binned to determine the variation in each bin with respect to each interaction parameter. A spline interpolation is employed to evaluate the prediction between each interaction parameter value queried in the reweighting. The effect of each interaction parameter is then applied multiplicatively to generate predictions as described in Eq. (5.4). An example of a response function is given in Fig. 4.2.

4.3.1 Shape Parameters

This section describes the origin and implementation of important interaction shape parameters used in the analysis presented in this thesis.

4.3.1.1 M_A^{QE}

As described in Sec. 4.2.1 the differential CCQE cross-section can be defined by six form factors F_1, F_2, F_A, F_P, F_{3V} and F_{3A}. F_1, F_2 are vector-like form factors and are well constrained from electron scattering data [102]. F_{3V} and F_{3A} have a negligible effect on the ν_μ interaction, on account of the lepton mass, and the resulting uncertainty in the ν_e cross-section is considered elsewhere. The remaining parameters F_A and F_P follow a linear relation for fixed Q^2 under the dipole approximation [87]. F_A is expected to follow a dipole like form as follows:

$$F_A(Q^2) = \frac{F_A(0)}{(1 + Q^2/(M_A^{QE})^2)^2} \tag{4.2}$$

The dipole form defines the Q^2 dependence of the form factor and is determined by a single free parameter, M_A^{QE}, as $F_A(0)$ is very well constrained by neutron beta decay measurements [103]. Given the constraint on the vector like form factors, the axial mass is assumed to be in the 1 GeV region. The uncertainty in the form of the CCQE cross-section included in this analysis is driven by the uncertainty on M_A^{QE}.

As axial couplings can only be measured in neutrino interaction experiments, precise measurement of it are problematic. In fact, an analysis of current data leads to conflicting measurements of M_A^{QE} [104]. Because of the apparent tension between measurements of M_A^{QE}, the recommendation from the NIWG was to use a flat prior for M_A^{QE} in the oscillation analysis to allow the T2K data to solely influence the parameter.

4.3.1.2 E_B

The binding energy is dependent on the nuclear target and included to take account of the fact that the neutrino interaction liberates a nucleon from the nucleus. The binding energy therefore has the effect to bias the reconstructed neutrino energy which can be seen in the energy reconstruction formula detailed in Sec. 5.3.4. The binding energy therefore pulls energy which would have gone into the outgoing lepton state into the nuclear state. Uncertainty in the binding energy therefore creates uncertainty in the outgoing lepton energy.

Although the binding energy of the oxygen and carbon nuclei is well constrained by nuclear data, an effective binding energy parameter E_B is used due to uncertainties in the contribution it makes in neutrino interactions. Effective parameters such as this are often used in neutrino physics as inclusion of such a degree of freedom in the calculation is easily justified from theory.

The T2K analysis employs effective E_B parameters for both carbon and oxygen which are uncorrelated prior to the near detector fit. The nominal values and uncertainties of both parameters are motivated by fits to external electron scattering data which found effective binding energies of 25 MeV for carbon with an uncertainty of around 3 MeV. Fits to MiniBooNE and MINERνA data sets resulted in similar constraints so an uncertainty of 9 MeV was chosen around a central value of 27.0 MeV for Oxygen.

4.3.1.3 Fermi Momentum (p_F)

The Fermi momentum defines the momentum of the initial state nucleon in an interaction. The Pauli blocking condition means that a final state nucleon must have a momentum greater than the Fermi momentum. As a result, increasing p_F has the effect to reduce the interaction cross-section. As with E_B, fits to external data sets showed broad agreement with measurements around 220 MeV/c for carbon and oxygen p_F parameters with uncertainties of around 30 MeV/c [89].

Uncorrelated flat priors were chosen for both carbon and oxygen p_F parameters in this analysis to allow for more freedom in the interaction model in the range 200 MeV/c - 275 MeV/c.

4.3.1.4 M_A^{RES}

As with CCQE, the resonant interaction can be approximated with a dipole like form and with a resonant axial mass as shown in Eq. (4.3). M_A^{RES} has the effect to change the shape and normalisation of the form factors in the resonant differential cross-section. The nominal value and prior for M_A^{RES}, 0.95 $GeV \pm$ 0.15 GeV, is motivated by fits to ANL and BNL single pion production data sets [105].

4.3.1.5 C_5^A

Also shown in Eq. (4.3) is a form factor normalisation parameter C_5^A. Unfortunately, C_5^A can not be constrained by beta decay measurements so it remains a free parameter to any measurement of resonant cross-sections. Prior information used for C_5^A in this analysis comes from fits to ANL and BNL single pion production data sets [105].

$$F_A^{RES}(Q^2) = \frac{C_5^A}{(1 + Q^2/(M_A^{RES})^2)^2} \tag{4.3}$$

4.3.1.6 Isospin $\frac{1}{2}$ Resonant Background (Bg^{RES})

As described in Sec. 4.2.5, an additional component to the pion production cross-section is required. An additional parameter, which defines the size of the contribution, is included to account for the uncertainty in the cross-section, further details can be found in [97]. Prior information for the parameter also comes from fits to the ANL and BNL data sets.

4.3.1.7 CC-Other Scale

A slightly ad-hoc uncertainty which is an energy dependant scale applying to all interactions defined as 'CC other' in this analysis. These include CC Multi-Pion interactions, CC DIS interactions and CC Resonant interactions where particles other than pions are produced. External data sets indicate that the uncertainty on the interaction type should be 10% at 4 GeV. This fractional uncertainty was extrapolated as shown in Eq. (4.4).

$$\delta_{\sigma_{CCother}}(E_\nu) = \frac{0.4}{E_\nu} \tag{4.4}$$

Although this uncertainty increases as E_ν approaches 0, there are very few events below $E_\nu \approx 0.8$ GeV and the threshold for these events in NEUT is $E_\nu = 0.6$ GeV.

4.3.2 Normalisation Parameters

This section describes the origin and implementation of important interaction normalisation parameters used in the analysis presented in this thesis.

4.3.2.1 2p-2h

2p-2h normalisation parameters are included to account for the uncertainty in the entire 2p-2h event rate. As the relation between the 2p-2h contribution in carbon and oxygen interactions is poorly understood, separate 2p-2h carbon and 2p-2h oxygen parameters are implemented. The parameters are also uncorrelated and given flat priors to allow the constraint to be driven solely by T2K data. These parameters apply to both neutrino and anti-neutrino interactions.

4.3.2.2 2p-2h ($\bar{\nu}$)

An additional 2p-2h normalisation parameter is included to scale only the anti-neutrino cross-section. The uncertainty is included to account for the differences between the Nieves model, implemented in NEUT, and an alternative model proposed by Martini et. al. [106]. A distinct difference in the model proposed by Martini and the Nieves model is the difference in the predicted neutrino and anti-neutrino cross-sections. A 2p-2h parameter which affects the absolute scale of the anti-neutrino cross-section on both carbon and oxygen is introduced to account for these differences.

The 2p-2h ($\bar{\nu}$) parameter is given a flat prior and no correlations with other parameters.

4.3.2.3 CC ($\frac{\sigma_{\nu_e}}{\sigma_{\nu_\mu}}$ and $\frac{\sigma_{\bar{\nu}_e}}{\sigma_{\bar{\nu}_\mu}}$)

The ν_e cross-section is an important input to determine the expected appearance signal at Super-K. As predominantly ν_μ are observed at the near detector, constraints on other cross-section parameters detailed in this section are driven by the effect they have on the ν_μ interactions. Therefore the CC $\frac{\sigma_{\nu_e}}{\sigma_{\nu_\mu}}$ and $\frac{\sigma_{\bar{\nu}_e}}{\sigma_{\bar{\nu}_\mu}}$ parameters are implemented to characterise any difference between the ν_μ and ν_e cross-sections from theoretical considerations. Two parameters are chosen to facilitate independent differences between the neutrino and anti-neutrino cross-sections.

The two largest contributions to the uncertainty are attributed to modifications to the ν_e cross-sections as a result of radiative corrections and second class currents (SCC). The uncertainty due to radiative corrections is accounted for by a 2% uncorrelated uncertainty on the $\frac{\sigma_{\nu_e}}{\sigma_{\nu_\mu}}$ and $\frac{\sigma_{\bar{\nu}_e}}{\sigma_{\bar{\nu}_\mu}}$ parameters and SCC by a 2%

anti-correlated uncertainty [107]. The total uncertainty is described by:

$$V_{err} = \underbrace{\begin{bmatrix} 0.02^2 & 0 \\ 0 & 0.02^2 \end{bmatrix}}_{\text{Radiative}} + \underbrace{\begin{bmatrix} 0.02^2 & -0.02^2 \\ -0.02^2 & 0.02^2 \end{bmatrix}}_{\text{SCC}} = \begin{bmatrix} 2\cdot 0.02^2 & -0.02^2 \\ -0.02^2 & 2\cdot 0.02^2 \end{bmatrix}$$

4.3.2.4 CC Coherent

Based on measurements made at MINERνA [96], a 30% uncertainty on the CC Coherent event rate is chosen for this analysis. Separate CC Coherent scaling parameters are included for carbon and oxygen, however they are given a correlation of 100% in the prior.

4.3.2.5 NC Coherent

NC Coherent interactions are interactions in which the neutrino scatters coherently off of a nucleus via a neutral current. As with CC Coherent, pions produced in the interaction can mimic signal at Super-K. A normalisation uncertainty, based on differences between the NEUT prediction and external data sets, of 30% is chosen for this analysis.

4.3.2.6 NC Gamma

Along with the tuning described in Sec. 4.2.3 a 100% normalisation uncertainty is included for the total NC Gamma cross-section. This choice was made as there is little external data to constrain the cross-section.

4.3.2.7 NC Other

The NC Other mode is a class of events made up of Multi-Pion, DIS, and Non-Pion resonant NC interactions. The event class is analogous to the CC Other class detailed above. A normalisation uncertainty of 30% on this event class is chosen for this analysis. As there is not much external data for NC other, a comparison of the model used in NEUT and a competing model is used to define the error. Separate NC Other parameters for events at ND280 and at Super-K are included in this analysis as the propagation of the constraint from the NC sample at ND280 to Super-K is deemed unreliable.

4.4 Final State and Secondary Interaction Uncertainties at Super-K

Another source of uncertainty related to those from interaction models are those that arise from final state and secondary interactions.

Final state interactions (FSI) are those which outgoing particles from an interaction can undergo as they escape the nuclear potential. Secondary interactions (SI) are those which outgoing particles have with a nucleus which did not participate in the initial interaction. In this analysis, only the uncertainty in pion FSI and SI are included as they are found to have the largest impact. FSI and SI are particularly important in Super-K as they can cause charged current pion interactions to mimic CCQE and therefore result in a reconstruction bias.

In NEUT the FSI are calculated with a semi-classical cascade model, where the outgoing particle is propagated through the nuclear potential in steps. At each step, the particle may undergo absorption, scattering or charge exchange. Secondary interactions are treated in a similar way in SKDETSIM, a custom GEANT3 simulation package [57], which propagates particles through the detector. The secondary interactions are driven by the same models as FSI.

The uncertainty due to FSI and SI are characterised by 44 normalisation parameters and a corresponding uncertainty matrix, with the same dimension as that which is used to model the Super-K detection uncertainty described in Sec. 5.3.6. The detector and FSI and SI matrices are then combined into one SKDet+FSI+SI uncertainty matrix. The parameters are each defined to act on specific interaction classes, listed in Sec. 5.4.1, and over specific reconstructed energy ranges on a single Super-K sample. As they have similar effects on observables at Super-K, the underlying FSI and SI parameters are varied simultaneously multiple times. The uncertainty due to FSI and SI on the event rate in each bin is then taken to be the covariance due to these variations. The variations of the FSI and SI parameters are chosen from fits to external data sets, which defined a set of 17 variations that fully explored the credible parameter space. Further details about the variation and the data driven constraints on the FSI and SI parameters can be found in [108].

Correlations between FSI and SI uncertainty between samples are only included for the ν-mode e-like and ν-mode CCπ^+ samples to account for the event migration caused by the FSI and SI uncertainties. All correlations between other samples are removed to allow the various samples to move independently due to FSI and SI variations.

This concludes the description of inputs to the oscillation analysis largely developed by collaborators and used for work presented in this thesis.

Chapter 5

The Oscillation Analysis

In the oscillation analysis presented here, an indirect MC extrapolation is employed, where the far detector expectation is tuned by constraints placed on the MC, taken from a fit to the near detector data. The ND280 data are first fit, independently, taking into account constraints from external data, and the results propagated toward a separate fit to the oscillation samples observed at Super-K. A flow diagram showing how the various components contribute into the final oscillation analysis is shown in Fig. 5.1. The main body of my work composing this thesis is highlighted at the end of the analysis chain, with important elements, such as the ND280 constraint, included in the form of a Gaussian penalty term; uncertainties associated with the Super-K samples due to the detector, FSI and SI; and the neutrino event generator feeding in as shown. This chapter includes a discussion of these three vital components and how they are incorporated in the oscillation analysis.

Constraints from the ND280 fit, on the flux and neutrino interactions, are propagated by a set of tuned systematic parameters and a covariance matrix detailing uncertainties and correlations to be used for the Super-K oscillation analysis. All parameters which do not explicitly affect the prediction at Super-K are marginalised in likelihood propagated from the ND280 fit. Finally the likelihood is modelled with a Gaussian covariance matrix to be used in the Super-K oscillation analysis in the form of a penalty term.

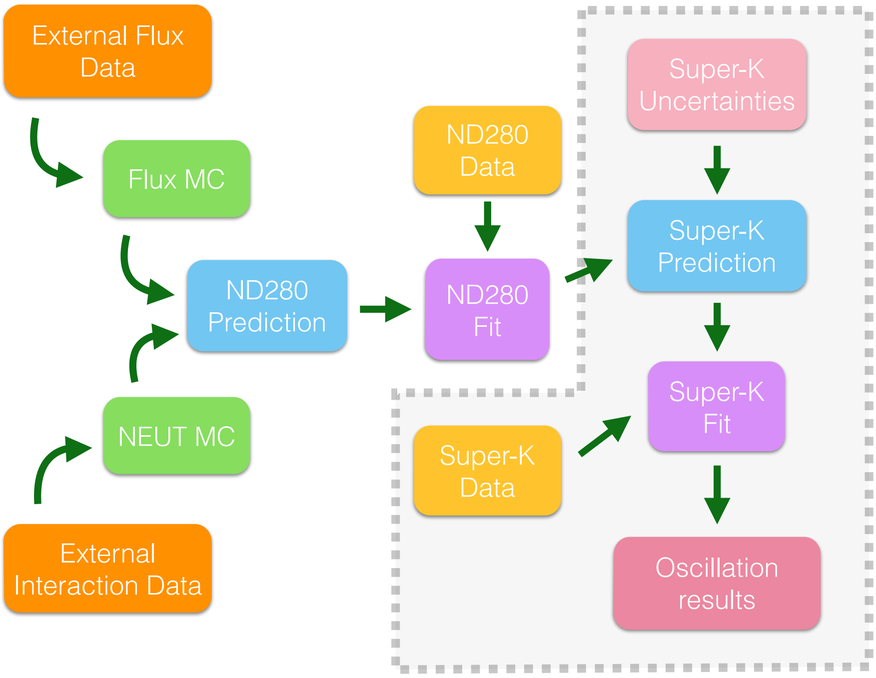

Figure 5.1: A brief schematic of the T2K oscillation analysis.

5.1 ND280 Samples

The ND280 analysis is a simultaneous fit to 14 samples, defined by the beam configuration, target sub-detector and event topology. All events are required to pass the following cuts:

- Data quality: All ND280 subsystems must be operational at the time of the event and the event must be associated with a proton bunch in a beam spill.

- Total multiplicity: At least one track in the event must be reconstructed in a TPC.

- Fiducial volume: The highest momentum charged track in the event must begin inside an FGD fiducial volume and be associated with a TPC object.

- PID: The highest momentum charged track must have a PID consistent with a muon or anti-muon.

- Upstream background veto: Events in which the muon or anti-muon could have originated in the PØD are vetoed. This is done by vetoing any event in which the second highest momentum track is starting 150 mm upstream of the muon or anti-muon track

Once an event has passed all of the cuts, further selections are applied before it enters one of the ND280 samples.

The samples for ν-mode are labelled CC0π, CC1π and CC other, defined by the number of reconstructed charged pions in the events that make up the sample. A further cut is applied to remove all events with a negatively charged muon in ν-mode. Pions are identified in ND280 by either pion like tracks in the TPCs or FGDs, a delayed Michel electron tag resulting from the decay chain of a pion at rest, or an electron and positron pair from a photon produced in the decay of a neutral pion. Positive tracks, in addition to the identified muon track, are tested against π^+, positron or proton hypotheses and negative tracks against π^- and electron hypotheses. A pull is constructed from the difference in expected and measured stopping power along the track (dE/dx) under each particle hypothesis.

Cuts are made in this space to determine if tracks are consistent with a π-like hypothesis. Events with 0 identified pion tracks pass into the CC0π sample, those with only one identified positive pion track and no electrons or positrons fall into the CC1π sample, and all other events make up the CC other sample. Events are further subdivided into FGD1 or FGD2 samples depending on which FGD the muon track originated. This makes a total of 6 ND280 samples for ν-mode data.

Shown in Tab. 5.1 is the fractional breakdown of each sample prior to the ND280 fit. The dominant contribution to the CC0π sample is from CCQE interactions with resonant the second largest. This allows the sample to lead the constraint on CCQE uncertainties. The resonant and other backgrounds are constrained by the other samples; the CC1π is composed of equal contributions of resonant and DIS events while the CC other sample provides a reasonably clean selection of DIS events.

When running in $\bar{\nu}$-mode, as described in Sec. 3.1.2, there is a non-negligible ν_μ contamination in the $\bar{\nu}_\mu$ beam. As the ν_μ and the $\bar{\nu}_\mu$ can not be distinguished at Super-K, a measurement of the ν_μ contamination at the near detector is vital to the oscillation analysis. $\bar{\nu}$-mode events are therefore separated into samples depending on the charge of the highest momentum track in the event, and also based on the total number of tracks in the event. These are the negatively charged highest momentum track (ν) or positively charged highest momentum track ($\bar{\nu}$), and CC1Track or CCnTrack selections. The percentage breakdown of the positively charged highest momentum track selections are listed in Tab. 5.2

and the negatively charged highest momentum track selections in Tab. 5.3. From Tab. 5.2, we see a that the CC1Track sample provides a relatively pure selection of CCQE $\bar{\nu}_\mu$ events. A simple CC1Track selection of this type is not possible in ν-mode as ν_μ interactions result in protons in the final state which produce tracks whereas $\bar{\nu}_\mu$ interactions make neutrons which are invisible in ND280.

The positive track CCnTrack sample provides a reasonable purity of DIS and resonance $\bar{\nu}_\mu$ events, however also includes a substantial amount of ν_μ events of the same type. This is due to the fact that protons and π^+ from DIS and resonance ν_μ events produce the highest momentum charged track a significant proportion of the time. As there is little freedom for DIS and resonance cross-sections to move independently in the interaction model used, the constraint from the CCnTrack sample is only limited by the $\frac{\nu_\mu}{\bar{\nu}_\mu}$ flux uncertainty.

It is clear from Tab. 5.3 that the negatively charged highest momentum track (ν) selection gives a very clean sample of ν_μ events which are used to constrain the contamination.

Production 6 of the ND280 software was used to process both MC and data used in the analysis presented in this thesis.

Sample		CCQE	2p-2h	Res	DIS	Coh	NC	$\bar{\nu}_\mu$	ν_e	Out of FV.
CC0π	FGD1	56.5	9.4	18.2	7.2	1.0	2.1	0.3	0.2	5.2
	FGD2	53.7	8.8	19.4	7.3	1.1	2.0	0.3	0.2	7.3
CC1π	FGD1	3.9	0.6	44.1	30.1	7.7	4.4	1.9	0.4	6.7
	FGD2	3.9	0.5	43.7	31.3	7.3	4.6	2.1	0.4	6.1
CCOther	FGD1	3.9	0.8	13.9	67.2	1.2	6.3	1.1	1.0	4.6
	FGD2	4.0	0.8	14.5	67.0	1.0	6.2	1.0	1.2	4.2

Table 5.1: Percentage breakdown of the ν-mode samples at ND280 by event type from MC.

Sample		CCQE	2p-2h	Res	DIS	Coh	NC	Bkg. ν_μ	ν_e	Out of FV.
CC1Track	FGD1	63.0	8.8	11.9	2.2	2.9	1.0	4.1	0.2	5.7
	FGD2	63.0	8.7	11.7	2.1	2.8	1.1	4.2	0.3	6.1
CCnTrack	FGD1	5.4	1.9	19.9	18.6	9.3	1.8	32.9	2.2	7.9
	FGD2	5.8	1.8	19.8	19.7	7.9	1.9	34.4	2.6	6.2

Table 5.2: Percentage breakdown of the positively charged highest momentum track (ν_μ) samples in $\bar{\nu}$-mode at ND280 by event type from MC.

Sample		ν_μ	$\bar{\nu}_\mu$	Other
CC1Track	FGD1	79.5	5.0	15.5
	FGD2	78.0	5.2	16.8
CCnTrack	FGD1	79.0	1.0	20
	FGD2	78.4	1.6	20

Table 5.3: Percentage of events in the negatively charged highest momentum track samples in $\bar{\nu}$-mode at ND280 as a result of ν_μ (wrong-sign) and $\bar{\nu}_\mu$ (right-sign) from MC. Relative fractions between ν_μ and $\bar{\nu}_\mu$ highlight the purity of the wrong-sign sample. The "Other" category is primarily made up of events in which charged pions produce the highest momentum track.

5.2 ND280 Fit Results

The ND280 fit was performed with the 14 samples and a total of 580 analysis bins, each defined by the momentum and angle of the highest momentum track. The post-fit distributions overlaid with data are shown in Figs. 5.3 and 5.4. There were a total of 656 free parameters in the ND280 fit: 50 attributed to the flux, 26 to interaction modelling and 580 to ND280 detection uncertainties. The 580 detection uncertainty parameters affected the normalisation of analysis bins and the detector uncertainty was modelled through an associated covariance matrix. The covariance matrix was calculated in a similar way to that of Super-K, described in Sec. 5.3.6, with 2000 throws which included both systematic and statistical fluctuations. Statistical fluctuations were included in this case to account for less populated areas of the MC production.

The ND280 fitting strategy was rigorously tested with alternative cross-section models and parameter pull studies described in [109] and Chap. 11. A small bias was found and the post-fit parameter values were shifted and their errors inflated accordingly.

The MIGRAD minimisation algorithm was used to determine the maximum likelihood found along with a p-value of 0.086. The best-fit values of the systematic parameters of interest are shown in App. A. Along with the corresponding 65 dimensional correlation matrix, shown in Fig. 5.2 after the application of the bias correction, these form the results of the ND280 fit which are propagated to the Super-K analysis. There is broad agreement between the post-fit MC and the data seen in Figs. 5.3 and 5.4, which is predominantly driven by an increase in the flux parameters, to roughly $+1\sigma$ of their prior values. This occurs to compensate for the under-prediction of the CC0π event rate. This is a feature of the ND280 data and was seen in previous analyses [110]. In fact, it is seen to a slightly larger extent in this analysis due to the updated priors on the interaction parameters. Although a slight discrepancy is seen between the data and MC prediction, this was found to have little impact on the constraints on Super-K flux and cross-section parameters from the fit as the post-fit data constraint was found to be consistent with that of sensitivity studies.

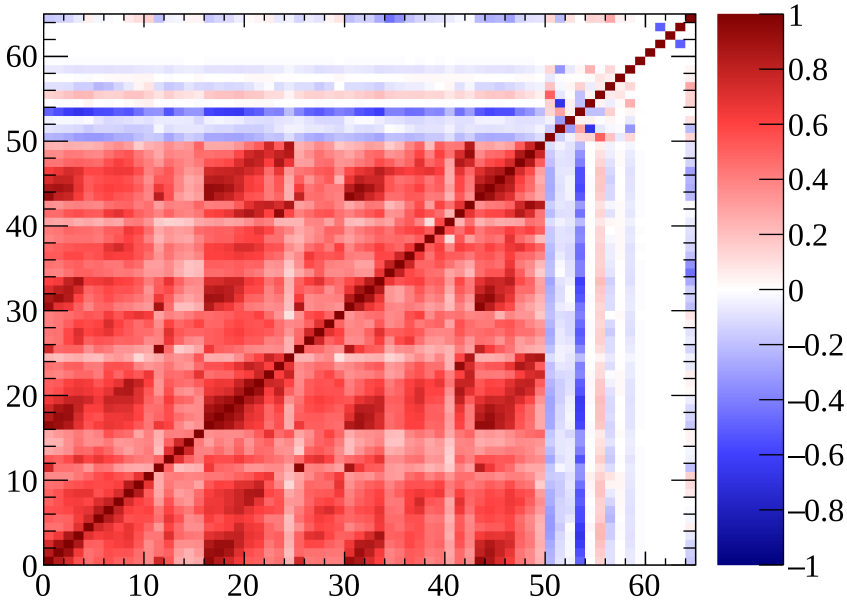

Figure 5.2: ND280 post-fit correlation matrix after the marginalisation of ND280 detector parameters. ν-mode flux (0-24), $\bar{\nu}$-mode flux (25-49) and interaction (50-64).

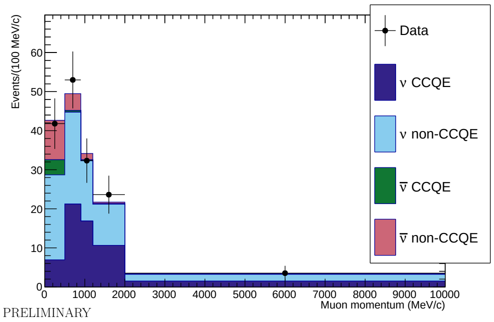

(a) $\bar{\nu}$ $-mode$ ν CC 1 Track

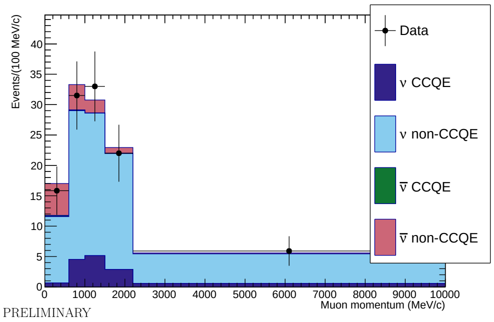

(b) $\bar{\nu}$ $-mode$ ν CC N Track

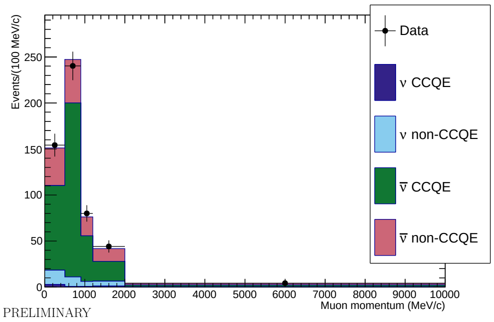

(c) $\bar{\nu}$ $-mode$ $\bar{\nu}$ CC 1 Track

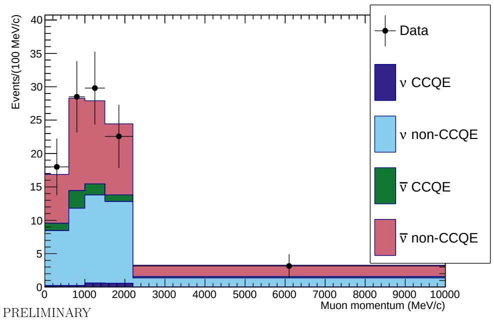

(d) $\bar{\nu}$ $-mode$ $\bar{\nu}$ CC N Track

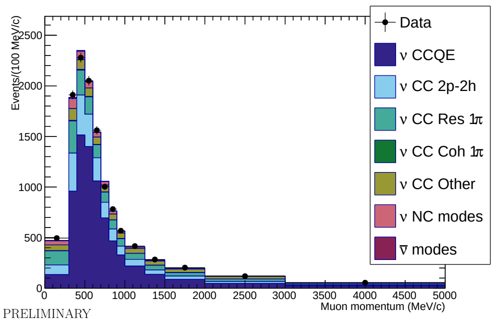

(e) ν $-$ $mode$ CC 0π

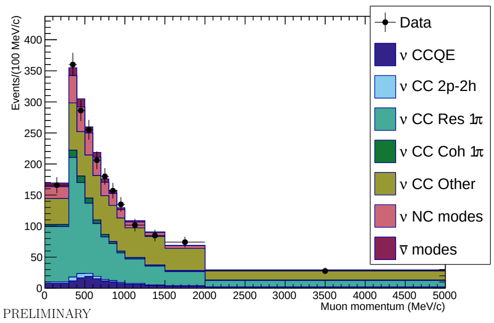

(f) ν $-$ $mode$ CC 1π

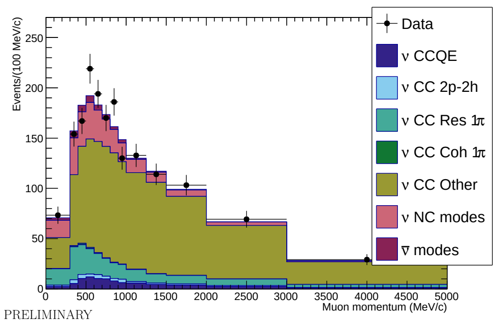

(g) ν $-$ $mode$ CC Other

Figure 5.3: Post-fit muon momentum spectra for the FGD1 samples with data overlaid.

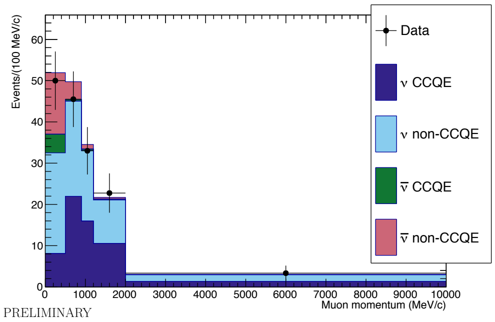

(a) $\bar{\nu}$ $-mode$ ν CC 1 Track

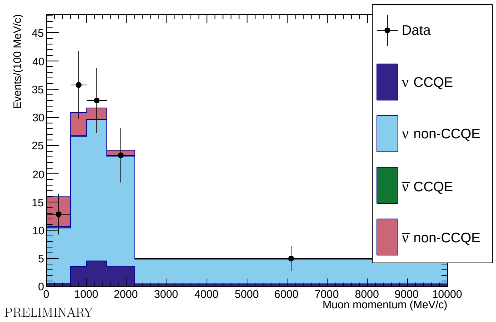

(b) $\bar{\nu}$ $-mode$ ν CC N Track

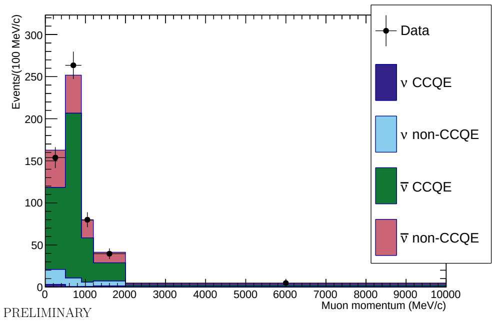

(c) $\bar{\nu}$ $-mode$ $\bar{\nu}$ CC 1 Track

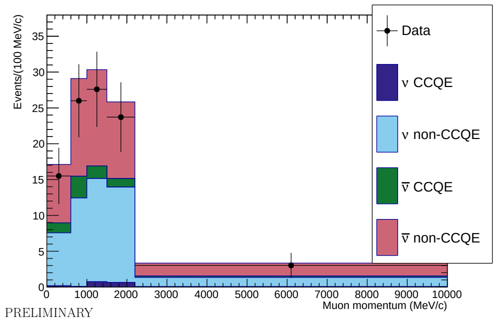

(d) $\bar{\nu}$ $-mode$ $\bar{\nu}$ CC N Track

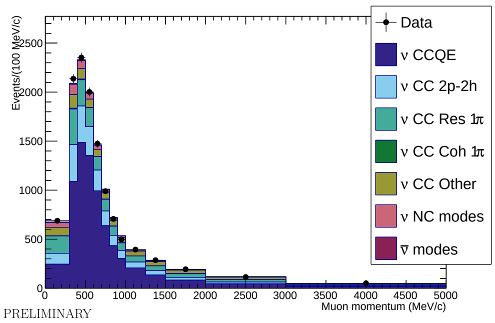

(e) ν $-$ $mode$ CC 0π

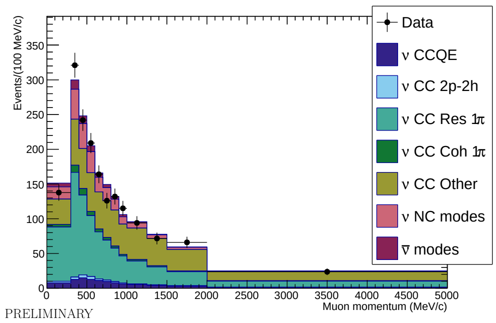

(f) ν $-$ $mode$ CC 1π

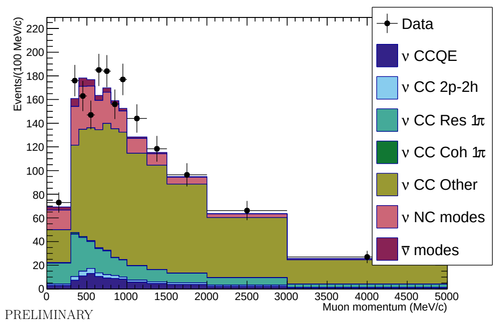

(g) ν $-$ $mode$ CC Other

Figure 5.4: Post-fit muon momentum spectra for the FGD2 samples with data overlaid.

5.3 Super-K Oscillation Samples

This section summarises the cuts and event selections of the five Super-K samples which go into the oscillation analysis presented in this thesis. All events must pass the following selection cuts that define the fully-contained fiducial volume (FCFV) one ring samples. The fiTQun reconstruction package was used for π^0 rejection in the appearance samples and APfit software package was used for all other cuts. Further details of data quality cuts and software versions used can be found in [111].

Selection cuts for the Super-K oscillation samples are as follows:

Data Quality: The Super-K DAQ must be operational and ready to accept a beam spill. The sub run must be deemed suitable, possibly not the case if there are issues with the DAQ or PMT flashers (caused by spontaneous discharge at the dynode). A pre-activity cut of 100 μs is applied to reduce the chance of a decay electron from a cosmic event contaminating the beam event.

Fiducial Volume: Each reconstructed event must be fully contained inside the Super-K fiducial volume.

One Ring: The ring counting algorithm at Super-K may only identify one ring.

Each one ring FCFV event can be defined to be either muon-like (μ-like) or electron-like (e-like). μ-like and e-like events pass through independent selection chains.

5.3.1 μ-like Selection Criteria

PID: The Super-K PID algorithm must define the Cherenkov ring as μ-like.

Reconstructed Momentum: The reconstructed muon momentum is larger than 200 $MeV/$c.

Decay Electron: The maximum number of reconstructed decay electrons in each event is one.

5.3.2 *e*-like Selection Criteria

PID: The Super-K PID algorithm must define the Cherenkov ring as *e*-like.

Reconstructed Momentum: The reconstructed ν_e energy may not be greater than 1250 MeV.

Visible energy: The total energy observed in the Cherenkov ring must be greater than that of a 100 MeV electromagnetic shower.

π^0: The observed *e*-like ring must pass a further π^0 rejection cut designed specifically to reduce NC π^0 backgrounds in the *e*-like samples detailed in Sec. 5.3.3.

Decay Electron: The electron-like samples are divided into two categories defined by the number of reconstructed decay electrons. Those with 0 decay electrons form the $CCQE$ FCFV *e*-like samples and those with 1 decay electron form the $CC\pi^+$ ν-mode sample.

The $CCQE$ *e*-like samples are optimised to select events with little energy in the hadronic final state. This enhances the CCQE purity, to reduce the bias when using the energy reconstruction formula. In ν_e events, decay electrons are usually a result of pions in the event. Therefore, a selection of *e*-like events with a single decay electrons is optimised for finding events with pions in the final state. Thus, it is denoted as the $CC\pi^+$ sample in this analysis and the others are denoted as the $CCQE$ samples. A full breakdown of the expected event rate each sample by interaction type is given in App. B.

5.3.3 π^0 Rejection

The aim of the π^0 rejection cut is to remove events from our e-like sample which are a result of background ν_μ interactions. In these background events a ν_μ can scatter off of a nucleus via the neutral current resulting in a π^0 in the final state. The issue arises as there is a non-negligible probability for the π^0 to be mis-reconstructed as an electron and therefore pass all selection criteria for the e-like samples. The rate of ν_μ induced neutral current events at Super-K can result in a substantial uncertainty in the search for ν_e appearance.

The issue with the π^0 is that it almost always decays into combinations of photons and electrons, and photons cause electromagnetic showers indistinguishable to those produced by electrons. As the pion is rarely at rest when it decays, the energy distribution between the two photons can be very asymmetric. If, in an event, the low energy photon is missed by the ring finding algorithm, the event would contain only one high energy electromagnetic shower which is the signature for charged current ν_e event. Another possibility is that the photons can be co-linear, leading to concentric Cherenkov rings which appear as one, also consistent with a ν_e event.

The procedure for removing the π^0 background events is as follows. Starting with a e-like event candidate, where one Cherenkov ring is found, a Super-K charge distribution is generated using the reconstructed lepton (*photon*) momentum and angle from the event. A second photon is simulated and its momentum varied until it best matches the observed event charge distribution. From the initial reconstruction there is the likelihood for the event to be lepton-like (L_e) and from the subsequent analysis π^0-like (L_{π^0}). Finally an invariant mass can be constructed from the two photons ($m_{\gamma\gamma}$). A cut is applied, in the two dimensional space of $\ln(L_{\pi^0}/L_e)$ vs $m_{\gamma\gamma}$, to reject π^0 events.

5.3.4 ν Energy Reconstruction

The incoming neutrino energy is calculated assuming the neutrino scattered quasi-elastically via a charged current with a nucleon at rest. This is done as it is expected that the majority of interactions at Super-K are CCQE and in fact, the beam profile is chosen as such to enhance the CCQE component and suppress other backgrounds. The reconstructed energy is given by:

$$E_\nu = \frac{2M'_i E_{lep} + M_f^2 - M_i'^2 - M_{lep}^2}{2 \cdot (M'_i - E_{lep} + p_{lep}\cos(\theta_{lep}))} \tag{5.1}$$

Where M'_i is the effective mass of the initial state nucleon, M_f is the mass of the outgoing nucleon, M_{lep} is the mass of the outgoing lepton, E_{lep} (p_{lep}) the reconstructed energy (momentum) of the outgoing lepton, and θ_{lep} the reconstructed angle of the outgoing lepton with respect to the beam direction. For the *CCQE* samples the initial and final nucleon masses are determined by the beam configuration, the neutron and proton mass respectively for ν-mode and proton and neutron mass respectively for $\bar{\nu}$-mode. In both cases the effective initial nucleon mass is related to the actual nucleon mass, as shown in Eq. (5.2) by the nuclear binding energy to account for the fact that the nucleon begins in a potential well.

$$M'_i = M_i - E_b \tag{5.2}$$

Where E_b is the effective nuclear binding energy per nucleon for Oxygen, 27 MeV, from electron scattering data [89].

For the $CC\pi^+$ sample, the energy is calculated in the absence of the nuclear potential. M_i is the proton mass and M_f the Δ^{++} mass which is shown in Eq. (5.3).

$$E_\nu = \frac{2M_p E_{lep} + M_{\Delta^{++}}^2 - M_p^2 - M_{lep}^2}{2 \cdot (M_p - E_{lep} + p_{lep}\cos(\theta_{lep}))} \tag{5.3}$$

5.3.5 Physics Data Set

The data analysed for this analysis was taken in T2K runs 1-7 (01/2010 - 06/2016). Over this time, Super-K was exposed to 7.482 $\times 10^{20}$ POT in ν-mode and 7.471 $\times 10^{20}$ POT in $\bar{\nu}$-mode. A summary of the data over the run period is given in Tab. 5.4. The selections used in this thesis include the $CC\pi^+$ e-like sample and the $CCQE$ samples; ν-mode μ-like, ν-mode e-like, $\bar{\nu}$-mode μ-like, and $\bar{\nu}$-mode e-like.

Beam mode	POT	Sample	Data
ν-mode	7.482 $\times 10^{20}$	$CCQE$ μ-like	135
		$CCQE$ e-like	32
		$CC\pi^+$ e-like	5
$\bar{\nu}$-mode	7.471 $\times 10^{20}$	$CCQE$ μ-like	66
		$CCQE$ e-like	4

Table 5.4: Summary of accumulated POT and observed events in the Super-K samples.

5.3.6 Detection Uncertainties

The Super-K detector uncertainties in the oscillation analysis are modelled by 44 normalisation parameters ($\mathbf{p_1}$), which scale the content of a total of 44 bins defined by true interaction type and reconstructed neutrino energy across the 5 samples. An error matrix defines the uncertainties and correlations between the parameters.

For the oscillation analysis, the 44 parameters are split into 12 for $CCQE$ μ-like samples, 24 for $CCQE$ e-like samples and 8 for the $CC\pi^+$ e-like sample. The interaction types and reconstructed energy ranges which they affect are given in

Tabs. 5.5 to 5.7. These are the same parameters used to model the FSI and SI uncertainties described in Sec. 4.4.

Fits are performed to the Super-K cosmic ray and atmospheric neutrino control samples to constrain the uncertainty on the fiducial volume selection, ring counting algorithm, outer detector activity veto, particle identification, momentum cuts and decay electron cuts. This is done with another set of parameters ($\mathbf{p_2}$), which are not necessarily normalisation parameters and not used explicitly in the oscillation analysis. The parameters $\mathbf{p_2}$ also have the ability to migrate events between selections. An MCMC is used to build a likelihood space with respect to the control sample data. Nuisance parameters such as those associated with the atmospheric neutrino flux uncertainty and interactions models are then marginalised.

What remains is a likelihood, in terms of a set of parameters ($\mathbf{p_2}$), which models the detection uncertainties. These constraints are then projected onto the $\mathbf{p_1}$ parameter space. This is done by taking 10^6 MC throws with the following method:

1. A set of parameter values $\mathbf{p_2^i}$ are randomly chosen based on the posterior of the fit to the control samples.
2. The bin content is calculated and stored for each bin defined by the set $\mathbf{p_1}$.
3. Steps 1 and 2 are repeated 10^6 times to build a distribution of the number of events in each $\mathbf{p_1}$ bin.
4. The distribution is used to determine the uncertainty and covariance between parameters $\mathbf{p_1}$ used in the oscillation analysis.

Interaction mode	NC	$\nu_e + \bar{\nu}_e$	$\nu_\mu + \bar{\nu}_\mu$ CCnonQE[1]	$\nu_\mu + \bar{\nu}_\mu$ CCQE + 2p-2h
Parameter range(s)	0 - 30	0 - 30	0 - 30	0.0 - 0.4
				0.4 - 1.1
				1.1 - 30

Table 5.5: Applicable energy range (in GeV) of Super-K detector and FSI systematic parameters for the μ-like samples.

Interaction mode	Oscillated $\nu_e + \bar{\nu}_e$	Beam $\nu_e + \bar{\nu}_e$	$\nu_\mu + \bar{\nu}_\mu$	NC
Parameter range(s)	0.0 - 0.35	0.0 - 0.35	0.0 - 0.35	0.0 - 0.35
	0.35 - 0.8	0.35 - 0.8	0.35 - 0.8	0.35 - 0.8
	0.8 - 1.25	0.8 - 1.25	0.8 - 1.25	0.8 - 1.25

Table 5.6: Applicable energy range (in GeV) of Super-K detector and FSI systematic parameters for the CCQE e-like samples.

5.3.6.1 Energy Scale Uncertainty

One final uncertainty which is unique in that it is not modelled by a normalisation parameter is the energy scale uncertainty. The energy scale at Super-K is characterised by a single parameter, with a 2.4% uncertainty, that can scale the reconstructed energy of predicted events at Super-K. It is also the only parameter in this analysis that can explicitly migrate events between bins. The parameter is applied on the reconstructed energy prediction, once all other tunings have been applied, assuming a uniform distribution of events across the width of each bin.

The energy scale uncertainty is estimated by taking the difference between

Interaction mode	Oscillated $\nu_e + \bar{\nu}_e$	Beam $\nu_e + \bar{\nu}_e$	$\nu_\mu + \bar{\nu}_\mu$	NC
Parameter range(s)	0.35 - 0.8	0.35 - 0.8	0.35 - 0.8	0.35 - 0.8
	0.8 - 1.25	0.8 - 1.25	0.8 - 1.25	0.8 - 1.25

Table 5.7: Applicable energy range (in GeV) of Super-K detector and FSI systematic parameters for the $CC\pi^+$ e-like sample.

Gaussian fits of the energy distributions in the MC and a control sample. The control sample used is one of cosmic ray muons with a momentum between 200 MeV and 440 MeV stopping within the detector. A maximum data-MC difference of 2.4% was found at 400 MeV. The size of the difference between the peak positions of the Gaussian fit, shown in Fig. 3.20, is used as the uncertainty in the analysis presented in this thesis.

5.4 MC Prediction

The observed energy (E_{reco}) and lepton angle (θ) spectra of each sample are compared with MC predictions to build a test statistic for this analysis. An accurate and reliable MC prediction is therefore vital to the oscillation analysis. This section describes the construction of the MC and how it is used in the analysis. The number of MC generated events which go into each sample are given in Tab. 5.8. The events for each neutrino flavour and sample are generated independently and scaled to the expected POT for predictions.

ν-mode			$\bar{\nu}$-mode	
μ CCQE	e CCQE	e CCπ	μ CCQE	e CCQE
540734	211059	28628	512615	200221

Table 5.8: Statistics for the Super-K MC samples.

5.4.1 Analysis Templates

For μ-like samples, the templates are built as a function of only the reconstructed neutrino energy, while the e-like sample templates are formed of a grid of uniformly spaced bins defined by reconstructed neutrino energy and reconstructed lepton angle. The analysis binning is optimised to give maximum sensitivity to oscillation physics whilst remaining computationally feasible. The binning is as follows:

μ-like Templates

E_{reco}:

- 60 bins from 0-3 *GeV* (50 *MeV*)
- 4 bins from 3-4 *GeV* (250 *MeV*)
- 4 bins from 4-6 *GeV* (500 *MeV*)

- 4 bins from 6-10 *GeV* (1 *GeV*)
- 1 bin from 10-30 *GeV* (20 *GeV*)

$\theta_{\mathbf{lep}}$:

- One bin from 0° to 180°

***e*-like Templates**

$\mathbf{E_{reco}}$:

- 25 bins from 0-1.25 *GeV* (50 *MeV*)

$\theta_{\mathbf{lep}}$:

- 14 bins from 0° to 140° (10°)
- 1 bin for $140° - 180°$ (40°)

The reconstructed variable information is not all that is required for an oscillation analysis. The ability to apply the effect of neutrino oscillation for any given hypotheses requires information about the true neutrino energy and neutrino flavour which make up each reconstructed bin. This analysis therefore utilises 6-dimensional MC templates, made up of bins defined by the Super-K sample, true neutrino flavour, neutrino interaction mode, true neutrino energy, reconstructed neutrino energy, and reconstructed lepton angle. The additional neutrino interaction mode information is necessary to evaluate the effects of interaction model parameters which are described in Sec. 4.3.

The 6-dimensional templates are then collapsed down to 3-dimensional analysis templates defined by only reconstructed variables to compare with observations at Super-K.

The binning for the 3 "hidden" dimensions, used for reweighting the MC prediction, is the same for all samples as follows.

$\mathbf{E_{true}}$:

- 6 bins from 0 to 0.3 GeV (50 MeV)
- 28 bins from 0.3 to 1 GeV (25 MeV)
- 40 bins from 1 GeV to 3 GeV (50 MeV).
- 5 bins from 3 GeV to 3.5 GeV (100 MeV)
- One bin from 3.5 to 4 GeV (0.5 GeV)
- One bin from 4 to 5 GeV (1 GeV)
- One bin from 5 to 7 GeV (2 GeV)
- One bin from 7 to 10 GeV (3 GeV)
- One bin for > 10 GeV

Interacting neutrino flavour:

- ν_μ
- $\bar{\nu}_\mu$
- ν_e
- $\bar{\nu}_e$
- Oscillated ν_e
- Oscillated $\bar{\nu}_e$

Interaction type:

- CCQE (Charged Current Quasi-Elastic)
- CC Coherent (Coherent Charged Current scatter off the nucleus)
- CC 2p-2h (Charged Current 2-particle–2-hole)
- CC 1π (Charged Current with a pion in the final state)

- CC Other (All other Charged Current interactions)
- NC $1\pi^0$ (Neutral Current with a π^0 in the final state)
- NC $1\pi^{\pm}$ (Neutral Current with a charged pion in the final state)
- NC Coherent (Coherent Neutral Current scatter off the nucleus)
- NC 1γ (Neutral Current with a photon in the final state)
- NC Other (All other Neutral Current interactions)

The oscillated ν_e and oscillated $\bar{\nu}_e$ MC templates are required for the prediction of events which are driven by the flux of ν_μ and $\bar{\nu}_\mu$ in the neutrino beam but interactions follow that of ν_e and $\bar{\nu}_e$ respectively.

The predicted number $N_{SK;E_{reco},\theta}$ of events in the E_{reco}-th and θ-th analysis bin is computed for each selected sample as follows:

$$N_{SK;E_{reco},\theta} = \sum_{m}\sum_{t}\sum_{E_{reco}\prime} P_{m;t} \cdot T_{E_{reco};E_{reco}\prime;f^{SK}_{E;E_{reco}}} \cdot S_{m;t;E_{reco}\prime,\theta;\vec{f}} \cdot N^{MC}_{SK;m;E_{reco}\prime,\theta;t} \tag{5.4}$$

Where $N^{MC}_{SK;m;E_{reco}\prime,\theta;t}$ is the input Super-K (MC) template containing the number of events in the MC sample with true reaction mode m in the true energy bin t, the reconstructed energy bin $E_{reco}\prime$, and reconstructed lepton angle bin θ.

$S_{m;t;r\prime,\theta;\vec{f}}$ is the overall, multiplicative, systematic error factor which is determined by a vector of systematic parameters $\vec{f}$. It is also a function of the reaction mode m, the true energy bin t, the reconstructed energy bin $E_{reco}\prime$, and the reconstructed lepton angle bin θ.

$T_{E_{reco};E_{reco}\prime;f^{SK}_{E;E_{reco}}}$ is a transfer function describing the migration of events between the reconstructed energy bins E_{reco} and $E_{reco}\prime$, due to the uncertainty in the Super-K reconstructed energy scale, expressed here in terms of the systematic parameter $f^{SK}_{E;E_{reco}}$.

Finally, $P_{m;t}$ is the 3-flavour neutrino oscillation probability applied to the true energy bin t of the Super-K MC template which corresponds to mode m.

5.4.2 Predicted Event Rate and Spectra

$\sin^2\theta_{23}$	$\sin^2\theta_{13}$	$\sin^2\theta_{12}$	δ_{CP}	Δm^2_{32}	Δm^2_{21}	Ordering
0.528	0.0217	0.304	-1.601	2.509×10^{-3}	7.53×10^{-5}	Normal

Table 5.9: Oscillation parameter set used for event rates prediction and validation.

The prediction of events at Super-K depends on systematic and oscillation parameters. The systematic parameters chosen for this section are the best-fit values from the ND280 fit and fits to Super-K control samples. The oscillation parameters are chosen from both previous T2K results and the 2015 PDG [39] to produce oscillation set A in Tab. 5.9.

The predicted event rates for the 5 samples broken down by interaction type and neutrino flavour are shown in Tab. 5.10, and a comparison of oscillated and un-oscillated event rates is shown in Tab. 5.11. A spectral comparison is also shown in Fig. 5.5 and the major event contributions to each sample are shown in Fig. 5.6. The ν contamination in $\bar{\nu}$-mode is apparent from Tab. 5.10 where the ν events make up a significant proportion of the total $\bar{\nu}$-mode μ-like and e-like events.

There is an interesting feature in the ν-mode CCπ sample where, although the sample is optimised to select appearance events, the expected event rate is greater for the hypothesis with no oscillation than for the oscillated. This can be understood by considering the breakdown of the sample by interaction type. The large event rate with the no oscillation hypothesis is due to the contamination in the sample coming from low energy ν_μ events. For the oscillated hypothesis the events make up 14% of the sample, however without oscillations the ν_μ flux increases significantly to make up 86% of the un-oscillated sample. The ν_μ contribution to the sample can be seen in Fig. 5.6.

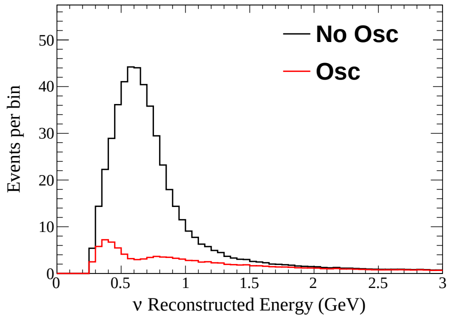

(a) CCQE μ-like (ν-mode)

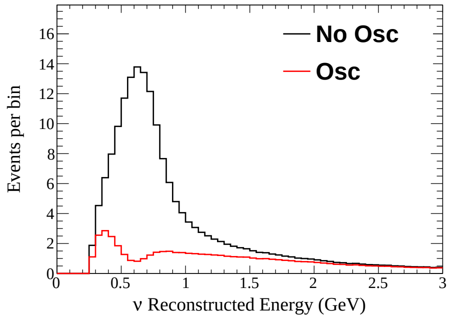

(b) CCQE μ-like ($\bar{\nu}$-mode)

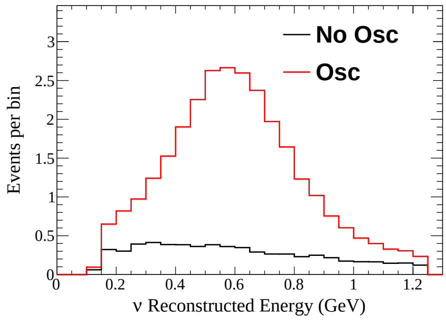

(c) CCQE e-like (ν-mode)

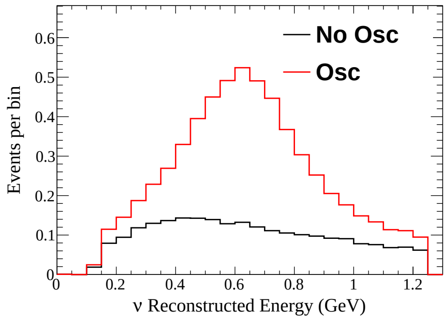

(d) *CCQE* e-like ($\bar{\nu}$-mode)

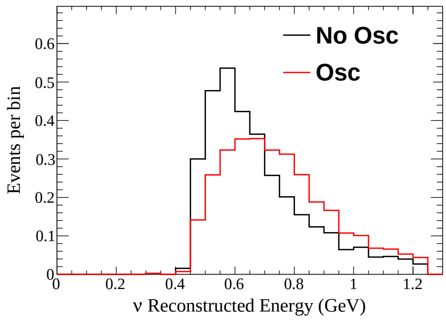

(e) $CC\pi^+$ e-like (ν-mode)

Figure 5.5: Comparison of predicted reconstructed neutrino energy spectra without oscillation and for the validation set given in Tab. 5.9.

5.4.3 θ_{lep} Information

An important component of this analysis is the ability to analyse the observation at Super-K in 2 dimensions, considering both reconstructed neutrino energy and lepton angle. The importance of the reconstructed neutrino energy is clear

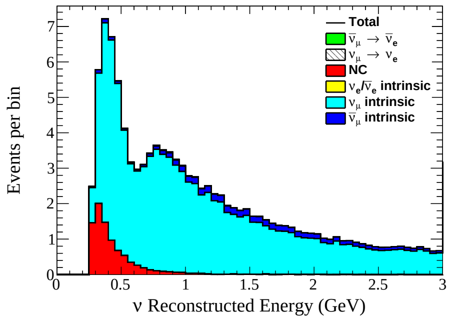

(a) CCQE μ-like (ν-mode)

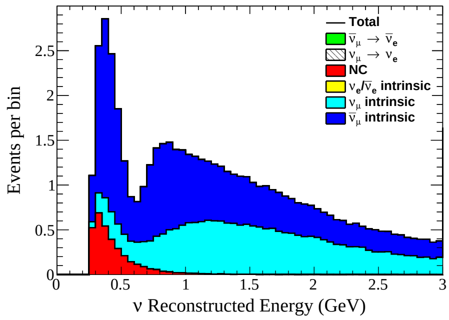

(b) CCQE μ-like ($\bar{\nu}$-mode)

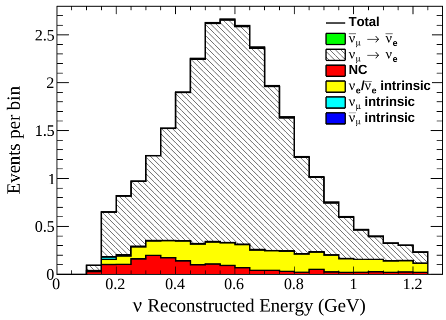

(c) CCQE e-like (ν-mode)

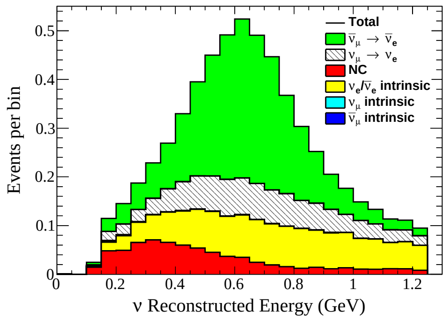

(d) $CCQE$ e-like ($\bar{\nu}$-mode)

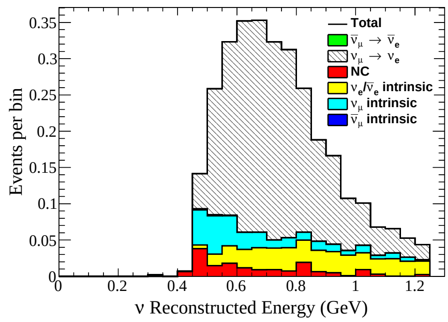

(e) $CC\pi^+$ e-like (ν-mode)

Figure 5.6: Predicted MC contribution to the spectra in each Super-K sample from dominant event classes. Event classes include interactions as a result of oscillated $\bar{\nu}_e$, oscillated $\bar{\nu}_e$, neutral current interactions, intrinsic (unoscillated) ν_e and $\bar{\nu}_e$, intrinsic (unoscillated) ν_μ and intrinsic (unoscillated) $\bar{\nu}_\mu$.

considering neutrino oscillations are a function of the true neutrino energy, but the additional information from the lepton angle is slightly more subtle. θ_{lep} is used as it has the power to discriminate between various interaction types. The reconstructed lepton angle from non quasi-elastic CC events and especially NC events is more isotropic than from CCQE and therefore θ_{lep}, in the electron like samples, has the power to differentiate between charged current signal events

Sample		ν_μ	$\bar{\nu}_\mu$	ν_e	$\bar{\nu}_e$	Osc-ν_e	Osc-$\bar{\nu}_e$	Total
ν-mode	μ CCQE	127	8.21	0.321	0.0271	0.372	0.00187	136
	e CCQE	1.58	0.0742	3.52	0.155	23.2	0.149	28.7
	e CCπ	0.429	0.0169	0.392	0.00254	2.29	0.00120	3.13
$\bar{\nu}$-mode	μ CCQE	27.3	36.6	0.0960	0.0594	0.0199	0.0352	64.2
	e CCQE	0.267	0.437	0.586	0.884	1.04	2.78	6.00

Table 5.10: A breakdown of the predicted event rate of Super-K samples by neutrino type.

	ν-mode			$\bar{\nu}$-mode	
	μ CCQE	e CCQE	e CCπ	μ CCQE	e CCQE
Oscillated	136	28.7	3.13	64.2	6
Un-oscillated	522	6.15	3.26	185	2.34
Data	135	32	5	66	4

Table 5.11: A comparison of predicted and observed event rates for the Super-K samples.

and neutral current backgrounds. An example of this is given in Fig. 5.7 which shows the distribution of signal and the major sources of background for the ν-mode *CCQE* e-like sample.

5.5 The Effect of Systematic Uncertainties

As mentioned previously, systematic uncertainties are important as they can mimic the effect of neutrino oscillation and thus weaken any measurement. This section details the impact of systematic uncertainty on the prediction at Super-K. Sources of systematic uncertainty are grouped into "ND280 constrained", which contain flux and cross-section uncertainties constrained in the ND280 fit, further cross-section uncertainties which ND280 has no power to constrain, Super-K de-

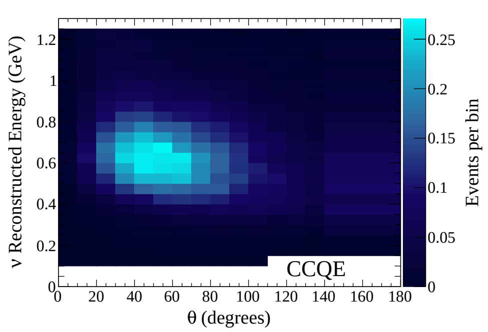

(a) CCQE

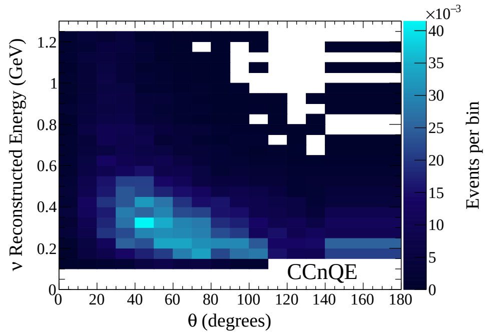

(b) CC not QE

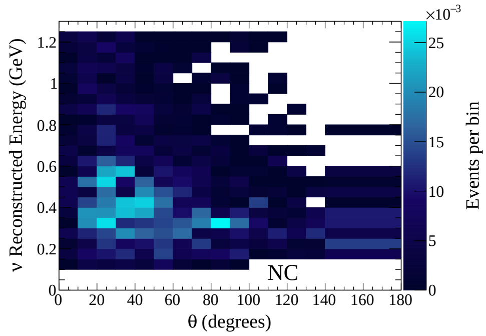

(c) NC

Figure 5.7: Predicted MC 2D-distribution of CCQE, CC not QE and NC events which make up the ν-mode *CCQE e*-like sample.

tection uncertainties, and FSI and SI uncertainties at Super-K. A comparison of the systematic uncertainty before and after the ND280 fit shows the power of the near detector to reduce the systematic error in the extrapolation. Shown in Tab. 5.12 is the fractional uncertainty on the total event rate in each sample as a result of various sources of uncertainty before and after the ND280 fit constraints. In Figs. 5.8 and 5.9 the variation is shown for each reconstructed neutrino energy bin in each sample comparing the effect of systematic uncertainty before and after the ND280 fit. In each case, the variation shown is the standard deviation of the event rate from 10,000 predictions, each defined by a set of systematic parameters randomly chosen in accordance with their uncertainty and correlations.

The impact that systematic uncertainty has on the extraction of oscillation parameters is of course a result of the way in which each systematic parameter can alter the predicted event rates and shapes of the Super-K spectra, and combine to mimic the effect of oscillation parameters. Nevertheless the information from Tab. 5.12 and Figs. 5.8 and 5.9 can be used to indicate the relative impact from various sources of systematic uncertainty. From these we can see that the flux and interaction uncertainties are dominant before they are constrained by the ND280 fit. The uncertainty on the absolute ν_e appearance rate, important for determining $\sin^2\theta_{23}$, $\sin^2\theta_{13}$ and δ_{CP}, is driven by the interaction uncertainties not constrained by ND280 in the $\bar{\nu}$-mode sample and detection uncertainties in the ν-mode CCπ sample. Fig. 5.8 also shows that the event rate in the region around the oscillation dip, used to determine $\sin^2\theta_{23}$ and Δm^2_{32}, is very well constrained by the ND280 fit.

The correlation between the flux and cross section uncertainties after the ND280 fit is immediately apparent from a comparison of Tab. 5.12 rows 2 and 7 for which only the flux and cross section uncertainties are varied and row 8 for which both were varied simultaneously. When both are varied simultaneously, the subsequent uncertainty on the event rate is smaller than the naive assumption if the individual uncertainties are added in quadrature.

The relative ν_e appearance rate in ν-mode and $\bar{\nu}$-mode is particularly important for any search of CP violation in neutrino oscillation. The uncertainty in the ratio of ν-mode events over $\bar{\nu}$-mode events is shown in Tab. 5.13. It is clear that the Super-K detection uncertainty is not an issue when measuring δ_{CP} but the FSI and SI uncertainty and the Interaction uncertainties not constrained by ND280 are very important.

Source of uncertainty	ν-mode			$\bar{\nu}$-mode	
	$CCQE$		$CC\pi^+$	$CCQE$	
	μ-like	e-like	e-like	μ-like	e-like
SKDet+FSI+SI	4.16%	3.52%	13.97%	3.91%	3.98%
Flux	3.56%	3.66%	3.58%	3.79%	3.80%
2p-2h (corr)	3.51%	3.90%	0.49%	2.96%	2.98%
2p-2h ($\bar{\nu}$) (corr)	0.21%	0.05%	0.01%	1.82%	2.32%
NC 1γ (uncorr)	0.00%	1.49%	0.43%	0.00%	2.97%
X-Sec ν_e/ν_μ	0.01%	2.62%	2.44%	0.00%	1.50%
X-Sec Tot	4.03%	5.12%	4.87%	4.16%	5.49%
Flux+X-Sec	2.93%	4.20%	5.02%	3.39%	4.67%
Oscillations	0.03%	0.49%	0.42%	0.03%	0.27%
All	5.11%	5.53%	14.84%	5.19%	6.31%
All Pre-ND280	12.02%	12.71%	21.88%	12.88%	14.06%

Table 5.12: The predicted uncertainty in the Super-K event rate defined as the RMS / Mean from 10k throws of the systematic parameters. The systematic parameters are thrown according to their post ND280 fit distributions unless otherwise stated. The prior uncertainties on $\sin^2\theta_{12}$ and Δm^2_{21} are also included. Other oscillation parameters were fixed to that of the oscillation set defined in Tab. 5.9.

Source of uncertainty	$\delta N_{SK}/N_{SK}$ e-like	$\delta N_{SK}/N_{SK}$ μ-like
SKDet+FSI+SI	3.86%	2.64%
Flux	1.72%	1.72%
2p-2h (corr)	0.90%	0.56%
2p-2h ($\bar{\nu}$) (corr)	2.31%	1.62%
NC 1γ (uncorr)	1.49%	0.00%
X-Sec ν_e/ν_μ	3.07%	0.01%
X-Sec Tot	4.26%	1.71%
Flux+X-Sec	4.13%	1.88%
Oscillations	0.00%	0.00%
All	5.83%	3.28%
All Pre-ND280	8.69%	6.76%

Table 5.13: The uncertainty in the $CCQE$ sample ν-mode to $\bar{\nu}$-mode ratio defined as the RMS / Mean from 10k throws of the systematic parameters. The prior uncertainties on $\sin^2\theta_{12}$ and Δm^2_{21} are also included. Other oscillation parameters were fixed to that of the oscillation set defined in Tab. 5.9.

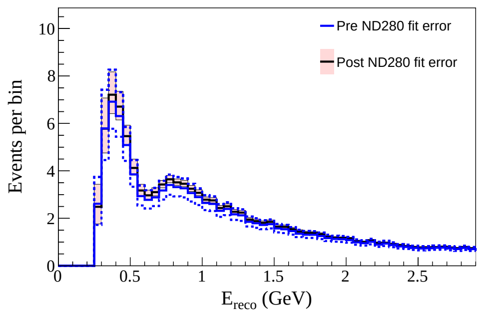

(a) CCQE μ-like (ν-mode)

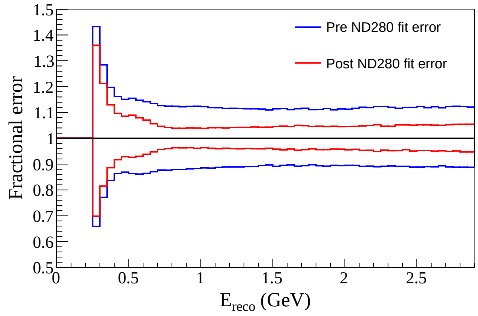

(b) CCQE μ-like (ν-mode) ratio

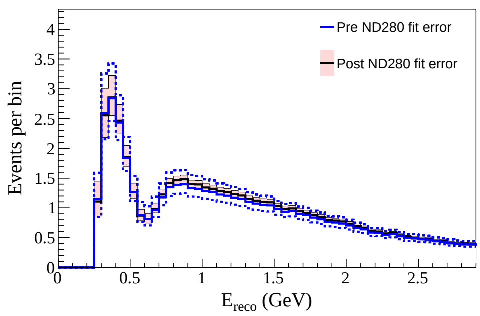

(c) CCQE μ-like ($\bar{\nu}$-mode)

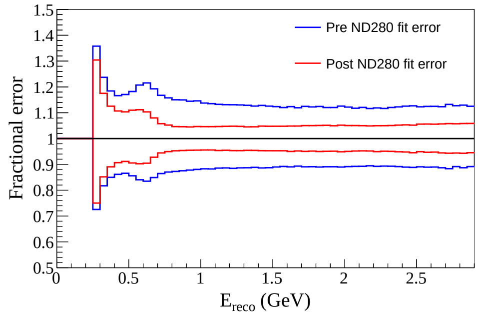

(d) CCQE μ-like ($\bar{\nu}$-mode) ratio

Figure 5.8: The prediction and the uncertainty on the μ-like Super-K spectra before and after the ND280 fit. The oscillation parameters of Tab. 5.9 and post ND280 fit systematic parameters are used for the nominal prediction.

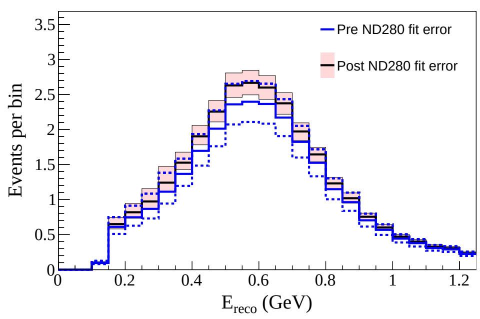

(a) CCQE e-like (ν-mode)

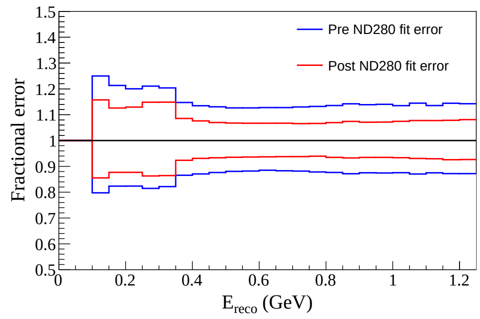

(b) CCQE e-like (ν-mode) ratio

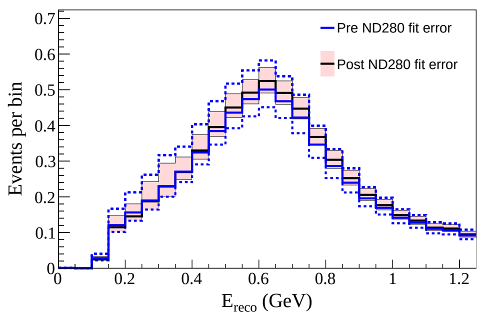

(c) CCQE e-like ($\bar{\nu}$-mode)

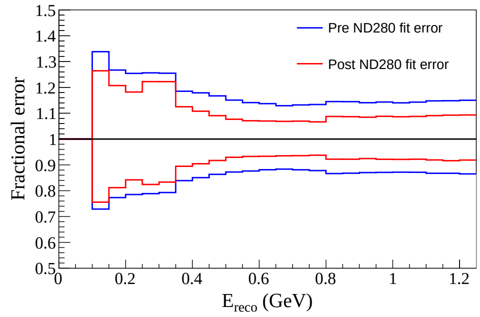

(d) CCQE e-like ($\bar{\nu}$-mode) ratio

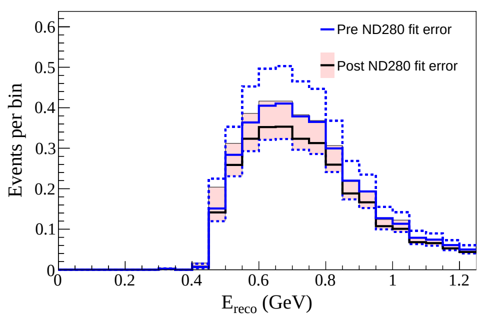

(e) CCπ^+ e-like (ν-mode)

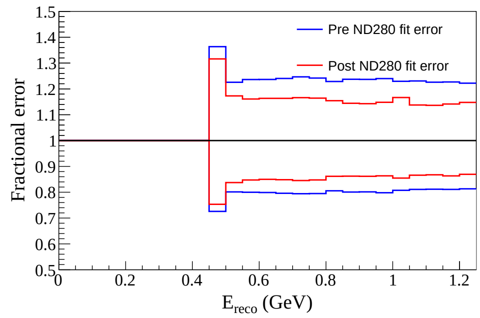

(f) CCπ^+ e-like (ν-mode) ratio

Figure 5.9: The prediction and the uncertainty on the e-like Super-K spectra before and after the ND280 fit. The oscillation parameters of Tab. 5.9 and post ND280 fit systematic parameters are used for the nominal prediction.

Chapter 6

Statistical Inference

The main objective of the analysis presented in this thesis is to provide point estimates, the best guess of a parameter of interest, and intervals of oscillation parameters with frequentist characteristics. These are defined by the Neyman construction where each interval has an associated confidence level (CL). The confidence level is defined to be the fraction of times a measurement of the parameter(s) of interest will fall within the confidence interval if the experiment were repeated many times under the same conditions. In order to construct these confidence intervals, one first requires a test statistic which facilitates the comparison of a data set with a prediction under a given hypothesis.

As the event rate in the detectors can be modelled by a Poisson distribution we begin with the Poisson likelihood. With a predicted rate μ and n events observed the Poisson likelihood is given by:

$$\lambda(n, \mu) = \frac{\lambda^n}{n!} e^{-\mu} \tag{6.1}$$

6.1 The Likelihood

The Poisson likelihood is a test statistic built from the predicted and observed event rates in Super-K analysis bins for a set of model parameters ($\vec{a}$). For N analysis bins and vectors of systematic model parameters $\vec{a}$ and oscillation model parameters $\vec{o}$ the natural logarithm of the likelihood is given by:

$$\begin{aligned} -2\ln\lambda(Data,\vec{o},\vec{a}) =& 2\cdot\sum_{i=0}^{N-1}\left(n_i^{obs}\cdot\ln(n_i^{obs}/n_i^{exp})+(n_i^{exp}-n_i^{obs})\right) \\ &+(\vec{a}-\vec{a}_0)^T\cdot\mathbf{C_a}^{-1}\cdot(\vec{a}-\vec{a}_0) \\ &+(\vec{o}-\vec{o}_0)^T\cdot\mathbf{C_o}^{-1}\cdot(\vec{o}-\vec{o}_0) \end{aligned} \tag{6.2}$$

Where n_i^{obs} is the observed number of events in the i^{th} bin and $n_i^{exp} = n_i^{exp}(\vec{o};\vec{a})$ is the prediction corresponding to $\vec{o}$ and $\vec{a}$.

The first term in Eq. (6.2) is from the classical Poisson likelihood, while the second and third are modifications to account for prior constraints on systematic parameters in $\vec{a}$ or oscillation parameters in $\vec{o}$. These are included to penalise the likelihood if the parameters stray too far away from the values which have been measured in the near detector or, for the case of the oscillation parameters, in external experiments.

One advantage of the binned likelihood method is that, in the large-sample limit, the quantity $-2\ln\lambda(\vec{o};\vec{a})$ follows a χ^2 distribution and it can therefore be used as a goodness-of-fit test [112]. The $\Delta\chi^2$ defined by the Baker-Cousins likelihood ratio, given in [112], follows a χ^2 distribution in the asymptotic limit. The Baker-Cousins likelihood ratio is the ratio of the best-fit likelihood in the model and the model independent maximum possible likelihood. For a bin with n events the maximum possible model independent likelihood is found when the predicted rate in each bin is given by the number of observed events. The

Baker-Cousins $\Delta\chi^2$ for a single bin is thus given by:

$$\begin{aligned}\Delta\chi^2 = -2\ln\frac{\lambda(N^{obs},N^{exp})}{\lambda_{Max}(N^{obs},N^{obs})} &= -\,n^{exp} + n^{obs}\cdot\ln(n^{exp}) - \ln(n^{obs}!) \\ &+ n^{obs} - n^{obs}\cdot\ln(n^{obs}) + \ln(n^{obs}!) \\ &= n^{obs} - n^{exp} + n^{obs}\cdot\ln(n^{exp}/n^{obs})\end{aligned} \tag{6.3}$$

Which has the form of the likelihood shown in Eq. (6.2).

6.1.1 The Marginal Likelihood

The likelihood, defined in Eq. (6.2), fully describes the data constraint but one drawback is that it is usually high dimensional. In order to ease the interpretation, it is usually necessary to project the likelihood onto a one or two dimensional space. There are many ways in which this can be done, the method chosen for this analysis is to integrate the likelihood with respect to all but the parameters of interest. Those parameters marginalised out of the likelihood, leaving it as a function of the parameters of interest, are labelled as nuisance parameters.

The marginal likelihood is derived using the following equation:

$$\lambda_{marg}(\vec{\theta}) = \int_B \lambda(\vec{\theta};\vec{b})\pi(\vec{b})db_0 db_1\ldots db_n \tag{6.4}$$

where $\vec{b}$ is a set of oscillation and systematic nuisance parameters and $\vec{\theta}$ the remaining parameters of interest. The prior on nuisance parameters appears as $\pi(\vec{b})$ and is included in the likelihood through terms including the matrices $\mathbf{C_a}$ and $\mathbf{C_{\tilde{o}}}$ as shown in Eq. (6.2).

This integration is performed numerically by randomly sampling the likelihood in the nuisance parameter space. The sampling is optimised as the priors on the nuisance parameters are included implicitly in the sampling, such that the integration is performed by averaging the likelihood from a large number of samples. This is shown in Eq. (6.5). 10,000 evaluations were deemed appropriate to approximate the marginal likelihood for this analysis. Studies performed are detailed in [113].

$$e^{-\chi^2_{marg}/2} = \lambda_{marg}(\vec{\theta}) = \int_B \lambda(\vec{\theta};\vec{b})\pi(\vec{b})db_0db_1\ldots db_n = \frac{1}{n}\sum_{i=1}^{n}\lambda(\vec{\theta};\vec{b}_i) \tag{6.5}$$

In some cases, the likelihood is converted to χ^2_{marg}, as defined in Eq. (6.5), as in the large-sample limit, when the likelihood can be approximated by a Gaussian, the χ^2_{marg} follows a χ^2 distribution.

Once there is a likelihood, which can be fully described by the parameters of interest, it is used for maximum likelihood parameter estimation. Sometimes it is not necessary to map out the full likelihood, when this is the case a steepest decent algorithm is used to evaluate the areas of the likelihood which are of interest.

The results of analyses, shown in this thesis, are often summarised by one or two dimensional likelihood surfaces and χ^2_{marg} differences from the point of maximum likelihood, $\Delta\chi^2_{marg}$ or $-2\Delta ln(\mathcal{L})$. One dimensional likelihoods are shown as a function of the parameter of interest and can be compared with critical likelihood values, from the Gaussian or other approximations, to determine exclusions of the parameters space. Two dimensional likelihood surfaces are more difficult to interpret on paper and are therefore often conveyed by contours of constant likelihood which mark exclusion regions in the Gaussian approximation. Finally the best fit point, defined as the position of maximum likelihood, is also marked. Examples are shown in Fig. 6.1.

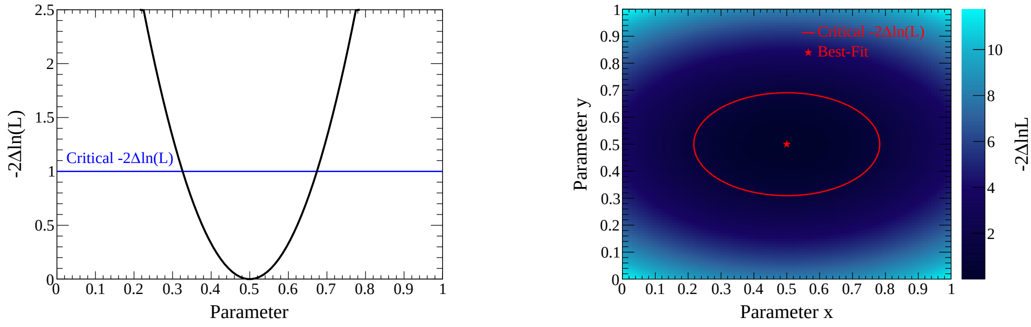

(a) 1D Fit

(b) 2D Fit

Figure 6.1: Example of results from a 1D and 2D fit.

6.2 Priors

The impact that priors can have on the likelihood is clear from Eq. (6.5). The priors on systematic parameters are detailed in Chap. 4 and Sec. 5.2. Priors used for the oscillation parameters are detailed in Tab. 6.1. Oscillation parameters $\sin^2\theta_{12}$ and Δm^2_{21} have very little impact on the likelihood, and are nonetheless well constrained by solar experiments as described in Sec. 2.6.1. $\sin^2\theta_{13}$ is a special parameter, in that it can have a large impact on the T2K prediction but is also well constrained by external experiments, described in Sec. 2.6.2. Fits are therefore performed both with and without the reactor constraint, with uniform and Gaussian priors respectively, to test the consistency of T2K data with that from previous experiments.

Without any previous measurement of δ_{CP} other than that using previous T2K data, a uniform prior over the full δ_{CP} phase space is used in all cases. For Δm^2_{32} and $\sin^2\theta_{23}$, uniform priors over suitable ranges are chosen to represent priors over the total physical range. The range of the priors are truncated to optimise the integration method responsible for producing the marginal likelihood. The mass ordering is never marginalised and fixed to either normal or inverted in each fit.

Parameter(s)	Prior	Range
$\sin^2\theta_{23}$	Uniform	$[0.3; 0.7]$
$\sin^2 2\theta_{13}$ (Reactors)	Gauss	0.085 ± 0.005
$\sin^2\theta_{13}$ T2K-Only	Uniform	$[0; 0.4]$
$\sin^2 2\theta_{12}$	Gauss	0.846 ± 0.021
$\lvert\Delta m^2_{32}\rvert$ (NO) ($\lvert\Delta m^2_{13}\rvert$ (IO))	Uniform	$[2; 3] \times 10^{-3}$ eV^{2}c^{-4}
Δm^2_{21}	Gauss	$(7.53 \pm 0.18) \times 10^{-5}$ eV^{2}c^{-4}
δ_{CP}	Uniform	$[-\pi; +\pi]$
Mass Ordering	Fixed	Normal or Inverted

Table 6.1: Oscillation parameter priors.

6.3 Features of Marginal Likelihoods

In the analysis presented here, marginal likelihoods are produced as a function of one or two parameters of interest. This is done so that correlations between parameters, detailed in Chap. 7, can be studied through outputs which can be visualised and interpreted intuitively. One slightly un-intuitive drawback of using marginal likelihoods is that a two dimensional likelihood $L(x, y)$ and a one dimensional $\int_y L(x, y)dy$ can appear inconsistent. The maximum likelihood point in a one dimensional space may not necessarily have the same x coordinate as the maximum likelihood point in a two dimensional space (x, y). This is usually caused by a correlation between the parameters x and y. In the two dimensional case, if the parameters are completely uncorrelated the likelihood can be written as:

$$L(x, y) = L^x(x) \cdot L^y(y) \tag{6.6}$$

Which allows the marginal 1D likelihood to be written as

$$L(x) = \int_y L(x, y)dy = L^x(x) \cdot \int_y L^y(y)dy = cL^x(x) \tag{6.7}$$

where c is a constant from the integral over y. When the parameters x and y are correlated, the likelihood can not be separated in this way and thus the integral over y depends on x. Consequently, the integral over y doesn't just introduce a constant normalisation factor, but changes the shape of the likelihood in x which can move the point of maximum likelihood and the χ^2 intervals.

6.4 Alternatives to the Gaussian Approximation

There are some cases where the Gaussian approximation falls short, and contours produced using the constant $\Delta\chi^2$ method fail to give the correct coverage. This is known to be the case when a parameter in an analysis is not continuous or close to a physical boundary. Parameters such as these appear in neutrino oscillations in the form of the mass ordering, which results in two discrete hypotheses, and physical boundaries in the parameter spaces of $\sin^2\theta_{23}$ and δ_{CP} as a result of maximum ν_μ disappearance and CP violation respectively. Great care must be taken in interpreting the results of any analysis which include these parameters.

6.4.1 Feldman-Cousins

The main objective of this analysis is the search for CP violation in neutrino oscillations, therefore the Feldman-Cousins method is used to construct confidence intervals for δ_{CP}. Feldman-Cousins is a method proposed to deal with the fact that classical, constant $\Delta\chi^2$, confidence regions can have under-coverage or over-coverage, where the intervals are deemed to be too narrow or too wide respectively, under the correct frequentist interpretation [114]. The approach is to use the MC to construct fully frequentist confidence regions which have the correct coverage under the Neyman construction [115]. Corrected confidence intervals are obtained though an adjustment to the critical $\Delta\chi^2$ values, at each point in the parameter space, based on an ensemble of toy MC experiments.

The new critical values for a specific mass ordering and value of δ_{CP} are calculated for this analysis in the following way:

1. Many MC toy data sets (e.g. 10k) are produced assuming the oscillation hypothesis of δ_{CP}^{True}, mass ordering MO_{true} and nuisance systematic and oscillation parameters $\vec{\theta}_{nuis}$ which take into account fluctuations in statistics and nuisance parameters.

2. Two 1D fits for δ_{CP} are performed, for each toy MC data set, to find the best-fit δ_{CP}^{BF} and χ^2_{min} from both normal and inverted ordering hypotheses. All other nuisance parameters are marginalised in this fit.

3. The marginal χ^2 is calculated for the true value of δ_{CP} and mass ordering; $\chi^2(\delta_{CP}^{True}, \text{MO}^{True})$

4. The test statistic, $\Delta\chi^2_{FC}$, is defined as

$$\Delta\chi^2_{FC}(\delta_{CP}, \text{MO}) = \chi^2(\delta_{CP}^{True}, \text{MO}^{True}) - \chi^2(\delta_{CP}^{BF}, \text{MO}^{BF}) \tag{6.8}$$

5. The steps 2 and 3 are repeated for each toy MC to build a distribution of $\Delta\chi^2_{FC}$; $f(\Delta\chi^2_{FC})$

6. The distribution is used to find several critical $\Delta\chi^2$ values for X% CL (e.g. 68%, 90%...), by solving for $\Delta\chi^2_{crit}$ as follows:

$$\Delta\chi^2_{Crit} : \int_{-\infty}^{\Delta\chi^2_{FC}} f(\Delta\chi^2_{FC}) d(\Delta\chi^2_{FC}) = X\% \tag{6.9}$$

7. This procedure is repeated for all points δ_{CP}^{True} of interest

For this calculation, the mass ordering is treated as a free parameter meaning the $\chi^2(bf)$ is chosen to be the minimum χ^2 out of both ordering hypotheses.

This is done so that both normal and inverted ordering contours, for δ_{CP}, could be considered on the same $\Delta\chi^2$ axis and interpreted as an exclusion for either ordering.

Due to computational limitations, the procedure is performed for 9 values of δ_{CP} in both the normal and inverted ordering hypotheses. The results of the Feldman-Cousins critical value study can be found in Sec. 8.2.

6.4.2 Oscillation Parameter Uncertainty

A truly frequentist critical value only exists for a specific model, which is defined by a single set of both nuisance parameters and those of interest. As this analysis contains 125 parameters, to produce and interpret critical values in this large dimensional phase space is inconvenient. To account for their effect, systematic uncertainties on the nuisance parameters are taken into account when generating toy data sets by allowing the parameter values to fluctuate for each toy.

Systematic parameters and some oscillation, such as $\sin^2\theta_{12}$, $\sin^2\theta_{13}$ and Δm^2_{21}, are well constrained by control samples and external experiments before the oscillation data analysis. These constraints provide reliable distributions from which to draw random parameter values used to construct the ensemble of toy MC experiments. This is however not the case for $\sin^2\theta_{23}$ and Δm^2_{32}, therefore, in order to account for variations in $\sin^2\theta_{23}$ and Δm^2_{32}, their values are drawn from the marginal likelihood obtained from the data fit of $\sin^2\theta_{23}$ and Δm^2_{32} under the mass ordering hypothesis corresponding to the critical values considered.

Chapter 7

Sensitivity to Oscillation Parameters

The ability to measure an oscillation parameter is predominantly determined by the effect the parameter has on the predicted observables in an experiment. If small changes in a parameter result in significant changes in the prediction, a comparison of prediction to data can yield a narrow constraint for that parameter. This chapter describes the expected sensitivity of T2K to the oscillation parameters and the origin of that sensitivity.

7.1 The Effect Of Oscillation Parameters

This section details the effect that each of the oscillation parameters of interest; $\sin^2\theta_{23}$, $\sin^2\theta_{13}$, δ_{CP}, Δm^2_{32} and mass ordering, can have on the predicted reconstructed neutrino energy spectra, all other oscillation parameters are set to that of Tab. 5.9 and thus how well they can be constrained at T2K. If not stated otherwise, oscillation and systematic parameters used here are those used for the Super-K predictions shown in Sec. 5.4.2.

In the analysis presented in this thesis, the observables are the reconstructed neutrino energy and the outgoing lepton momentum. However, as described in Sec. 5.4, the neutrino oscillation parameters primarily affect the prediction in reconstructed neutrino energy. Only the effects on the reconstructed neutrino energy predictions are shown in this section for clarity.

7.1.1 $\sin^2\theta_{13}$

A comparison of the predicted spectra for two reasonable values of $\sin^2\theta_{13}$ from external experiments is shown in Fig. 7.1. As described in Sec. 2.5, the leading term in the ν_e appearance probability is proportional to the double angle $\sin^2 2\theta_{13}$, while it only appears in sub-leading terms of the muon neutrino disappearance probability. For this reason, the appearance spectra have an almost linear dependence on the value of $\sin^2\theta_{13}$ whereas the disappearance spectra are mostly independent of it.

7.1.2 $\sin^2\theta_{23}$

$\sin^2\theta_{23}$ is present in the leading terms for both appearance and disappearance probabilities and therefore affects all observed spectra at T2K. The effect of $\sin^2\theta_{23}$ is shown in Fig. 7.2. For the μ-like spectra, the effect of $\sin^2\theta_{23}$ is strongest at the oscillation dip. To first order, maximising $\sin^2 2\theta_{23}$ results in the deepest oscillation dip and moving away in either direction increases the event rate. Considering higher order terms in the oscillation formula, the point of maximum disappearance is more accurately given by $\sin^2\theta_{23}= \frac{1}{2(1-\sin^2\theta_{13})}$. For the value of $\sin^2\theta_{13}$ measured from the reactor experiments, maximal disappearance occurs when $\sin^2\theta_{23}= 0.511$. For the appearance measurement the leading term in the appearance probability is proportional to $\sin^2\theta_{23}$, this creates the opportunity to measure the octant of the angle θ_{23}. It is clear from a comparison of Figs. 7.1 and 7.2 that $\sin^2\theta_{23}$ and $\sin^2\theta_{13}$ can have similar effects on the appearance samples. This is why the inclusion of disappearance samples in

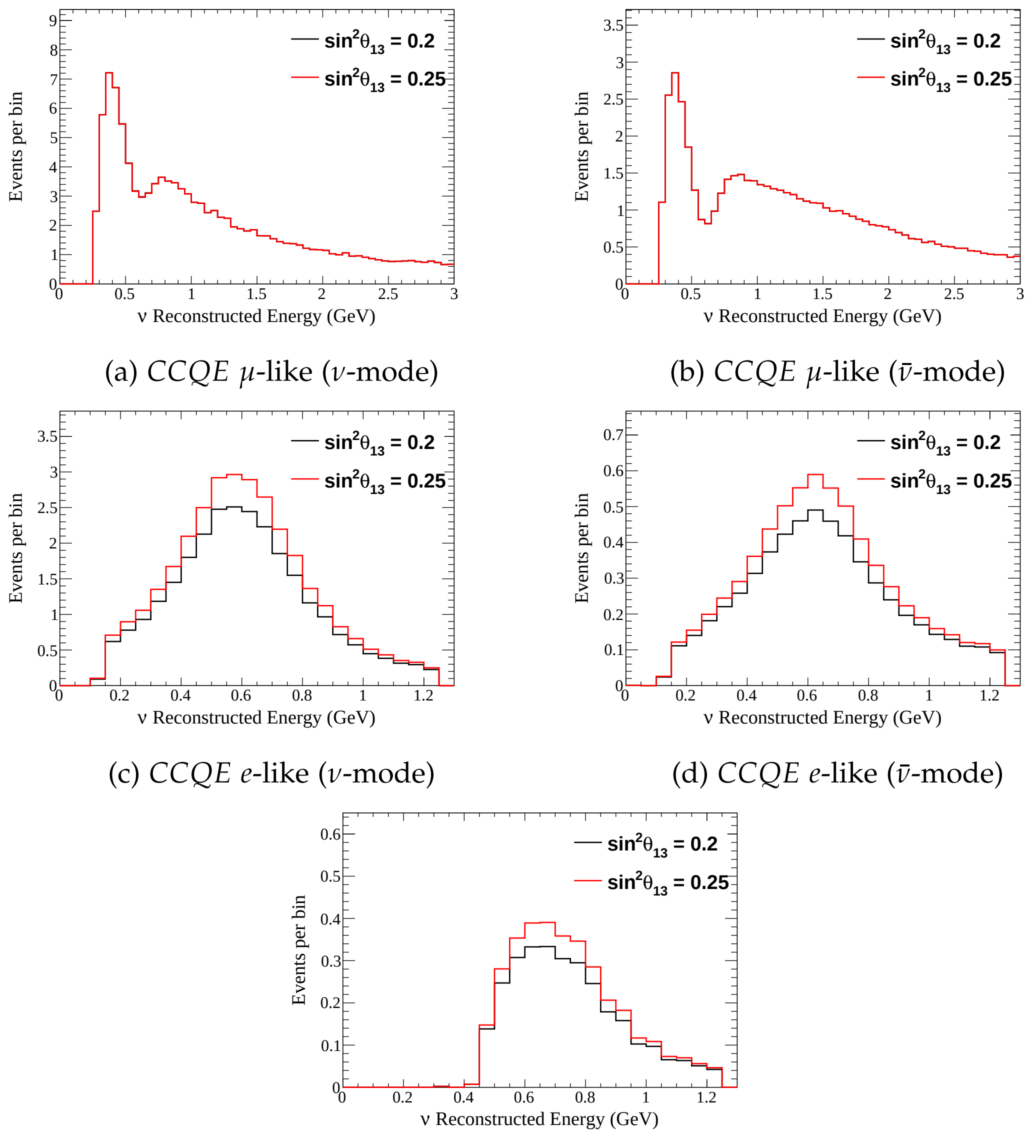

(a) *CCQE* μ-like (ν-mode)

(b) *CCQE* μ-like ($\bar{\nu}$-mode)

(c) *CCQE* e-like (ν-mode)

(d) *CCQE* e-like ($\bar{\nu}$-mode)

(e) $CC\pi^+$ e-like (ν-mode)

Figure 7.1: The effect of $\sin^2\theta_{13}$ on the predicted Super-K reconstructed neutrino energy spectra, all other oscillation parameters are set to that of Tab. 5.9.

a joint oscillation analysis is essential to break the degeneracy between the two parameters.

7.1.3 δ_{CP}

The parameter δ_{CP}, responsible for CP violation in neutrino oscillations, appears in the oscillation probabilities as the argument of a sine or a cosine. Under a CP transformation $\cos\delta_{CP}$ remains unchanged whereas $\sin\delta_{CP}$ changes sign. Thus,

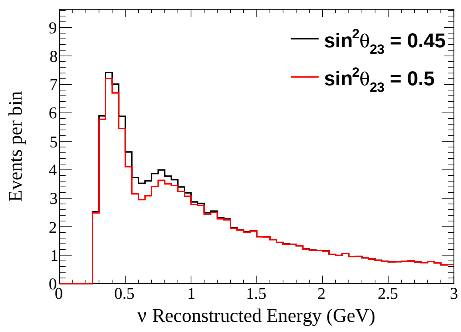

(a) *CCQE* μ-like (ν-mode)

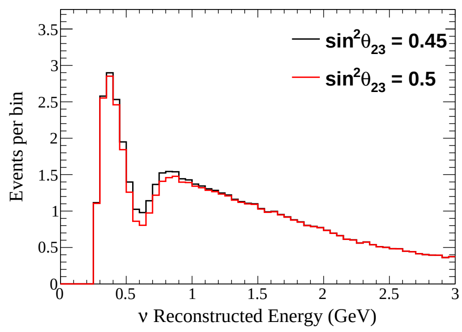

(b) *CCQE* μ-like ($\bar{\nu}$-mode)

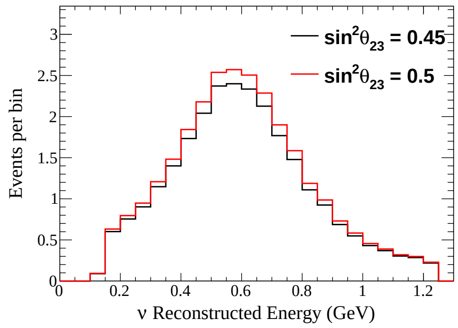

(c) *CCQE* e-like (ν-mode)

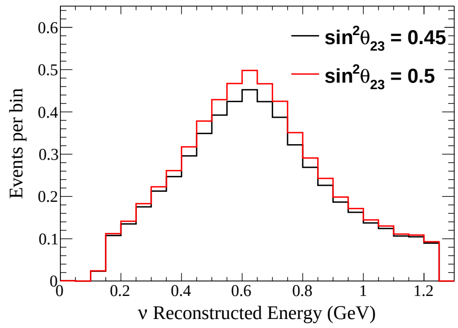

(d) *CCQE* e-like ($\bar{\nu}$-mode)

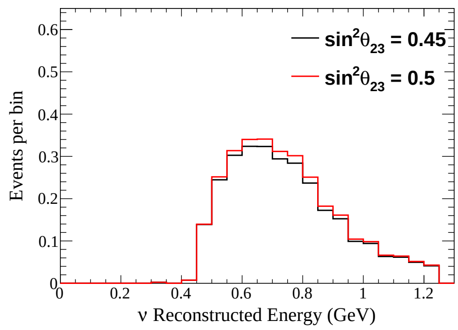

(e) $CC\pi^+$ e-like (ν-mode)

Figure 7.2: The effect of $\sin^2\theta_{23}$ on the predicted Super-K reconstructed neutrino energy spectra, all other oscillation parameters are set to that of Tab. 5.9.

only $\sin\delta_{CP}$ terms are CP violating. Both $\cos\delta_{CP}$ and $\sin\delta_{CP}$ appear in the the appearance probability, however the effects due to each are very different.

$\sin\delta_{CP}$ appears as a normalisation on the sub-leading term in the appearance probability and its effect is clearly visible from the spectral comparisons of predictions with $\delta_{CP} = +\pi/2$ and $\delta_{CP} = -\pi/2$ shown in Fig. 7.3. This maximum variation in $\sin\delta_{CP}$ results in a $\sim$38% spread in the event rate with respect to $\delta_{CP} = 0$ at T2K. The effect of δ_{CP} on the T2K spectra is very similar to that of

$\sin^2\theta_{13}$, the degeneracy is only broken by the anti-symmetric effect δ_{CP} has on the ν-mode and $\bar{\nu}$-mode spectra. The same is also true but to a lesser extent for $\sin^2\theta_{23}$ due to the effect it has on the disappearance spectra.

A comparison of the predicted spectra when $\delta_{CP} = \pi$ and $\delta_{CP} = 0$ shows how $\cos\delta_{CP}$ acts to effect the energy dependence of the oscillation predicted at T2K. The significant overlap of the two predictions also highlights how little sensitivity there is in T2K to distinguish between the two hypotheses and confirms the insensitivity to terms in the oscillation formula which include $\cos\delta_{CP}$.

This outcome can be understood by considering the CP conserving terms which include δ_{CP} in the appearance formula, shown in Eqs. (7.1) and (7.2) and taken from [116]. The term shown in Eq. (7.1) is highly suppressed at T2K due to the dependence on the square of the mass splitting, Δm^2_{21}, and can therefore be neglected.

$$-8\cos^2\theta_{13}\sin^3\theta_{12}\sin\theta_{13}\sin\theta_{23}\cos\theta_{12}cos\theta_{23}\cos(\delta_{CP})\sin^2\frac{\Delta m^2_{21}L}{4E} \qquad (7.1)$$

$$2\cos^2\theta_{13}\sin 2\theta_{12}\sin\theta_{13}\sin 2\theta_{23}\cos(\delta_{CP})\cos\frac{\Delta m^2_{23}L}{4E}\sin\frac{\Delta m^2_{31}L}{4E}\sin\frac{\Delta m^2_{21}L}{4E} \qquad (7.2)$$

The effect on the shape of the appearance spectra originates from the term shown in Eq. (7.2). The T2K beam energy and baseline were chosen to maximise $\sin(\Delta m^2_{32}L/4E)$ and, as a result, the $\cos(\Delta m^2_{32}L/4E)$ term is suppressed. Consequently the $\sin\delta_{CP}$ term, shown in Eq. (2.33), has a much more significant impact on the appearance spectra than any including $\cos\delta_{CP}$. The gradient of $\cos(\Delta m^2_{32}L/4E)$, is however much steeper than $\sin(\Delta m^2_{32}L/4E)$ at T2K, which is the origin of the energy dependence. When $\cos\delta_{CP}$ is positive, $\cos(\Delta m^2_{32}L/4E)$ enhances the oscillation probability when $\Delta m^2_{32}L/4E < \pi/2$ and decreases that when $\Delta m^2_{32} L/4E > \pi/2$. The opposite effect occurs for negative $\cos\delta_{CP}$.

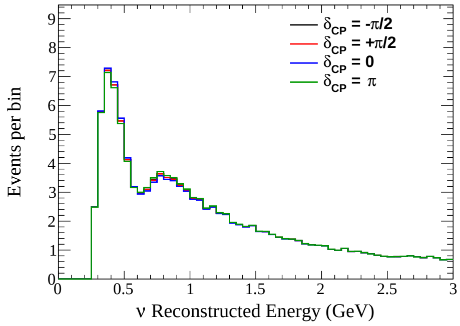

(a) *CCQE* μ-like (ν-mode)

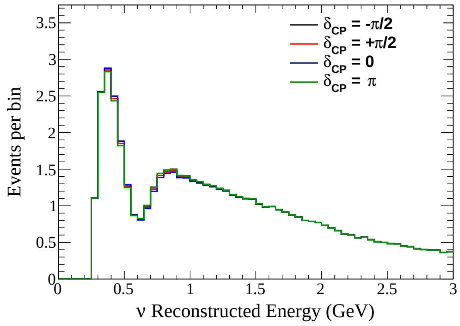

(b) *CCQE* μ-like ($\bar{\nu}$-mode)

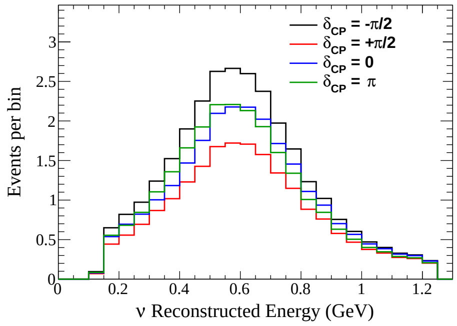

(c) *CCQE* e-like (ν-mode)

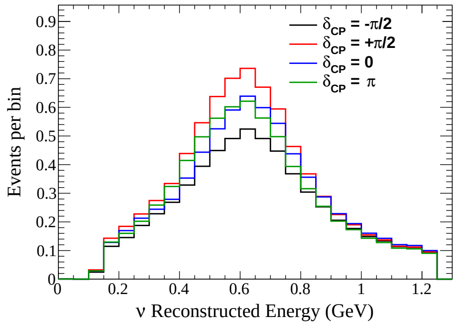

(d) *CCQE* e-like ($\bar{\nu}$-mode)

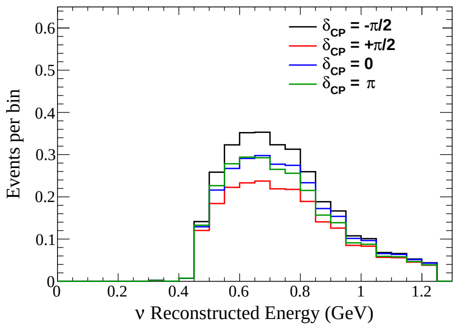

(e) $CC\pi^+$ e-like (ν-mode)

Figure 7.3: The effect of δ_{CP} on the predicted Super-K reconstructed neutrino energy spectra, all other oscillation parameters are set to that of Tab. 5.9.

7.1.4 Δm^2_{32}

The effect of the mass splitting is shown in Fig. 7.4. It is clear from the oscillation formula that the effect of the mass splitting is to stretch the oscillation probability along the energy axis. This can be observed in all of the Super-K spectra, though it is most apparent in the disappearance spectra due to the amount of large 2-3 mixing. The primary result of increasing Δm^2_{32} is the change in the position in energy of the ν_μ disappearance maximum or oscillation dip. Because of this, the measurement of Δm^2_{32} is particularly sensitive to the energy reconstruction and any systematic uncertainty or bias associated with it at Super-K.

The effect on the spectra also suggests a slight correlation with the $\cos\delta_{CP}$ oscillation terms at T2K discussed in Sec. 7.1.3. However, as the same is not true for the disappearance spectra, the degeneracy is easily broken.

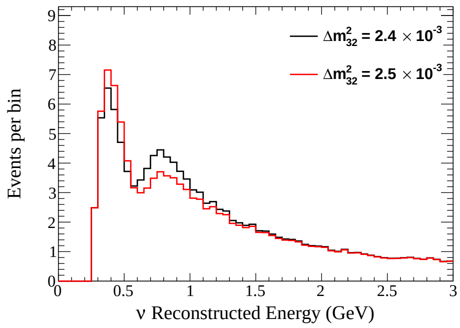

(a) *CCQE* μ-like (ν-mode)

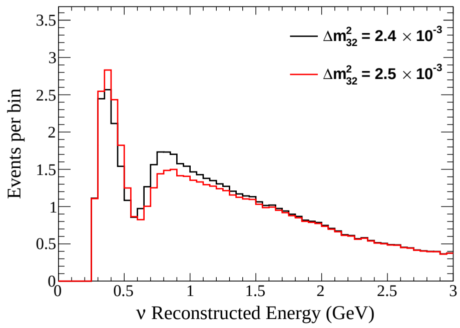

(b) *CCQE* μ-like ($\bar{\nu}$-mode)

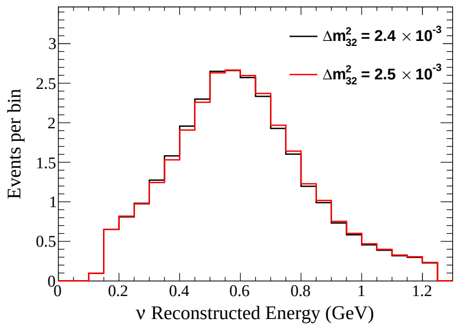

(c) *CCQE* e-like (ν-mode)

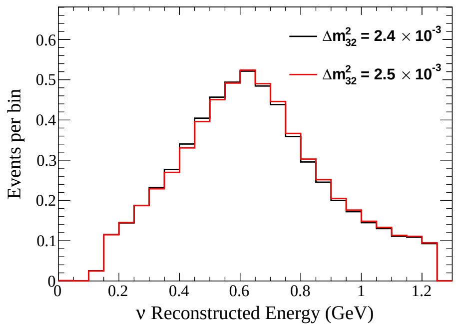

(d) *CCQE* e-like ($\bar{\nu}$-mode)

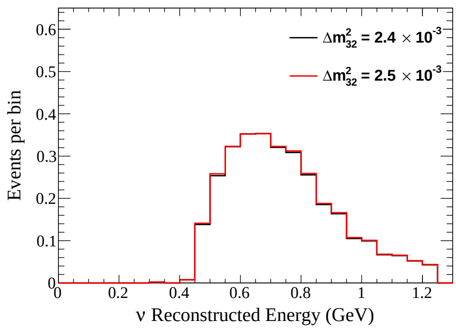

(e) $CC\pi^+$ e-like (ν-mode)

Figure 7.4: The effect of Δm^2_{32} on the predicted Super-K reconstructed neutrino energy spectra, all other oscillation parameters are set to that of Tab. 5.9.

7.1.5 Mass Ordering

The effect of swapping the mass ordering from normal to inverted is shown in Fig. 7.5. It has a similar effect to Δm^2_{32} in the disappearance spectra, which is what causes a slight correlation between the two parameters, however the size of the effect is approximately equal to a 5×10^{-5} shift in Δm^2_{32}. T2K is more sensitive to the effect on the appearance spectra which appears as more of a normalisation on the event rate. A comparison of Figs. 7.5c and 7.5d shows an asymmetry between the effect on the ν-mode and $\bar{\nu}$-mode spectra. This asymmetry is almost indistinguishable to that resulting from δ_{CP}, and consequently the two parameters are correlated.

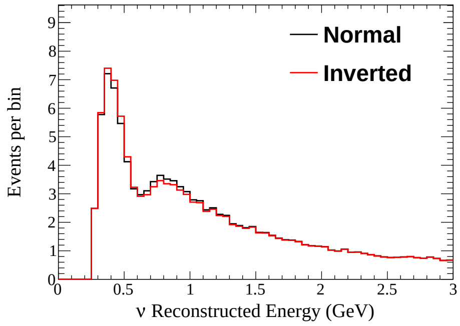

(a) *CCQE* μ-like (ν-mode)

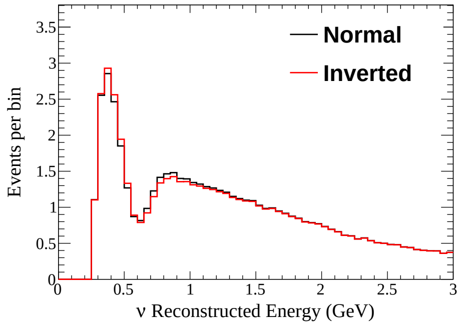

(b) *CCQE* μ-like ($\bar{\nu}$-mode)

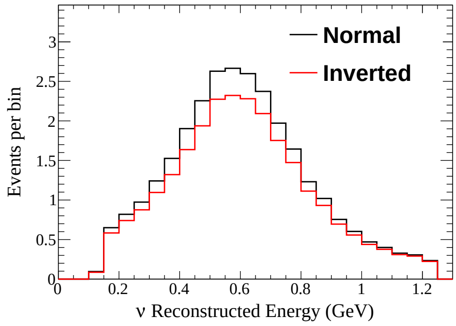

(c) *CCQE* e-like (ν-mode)

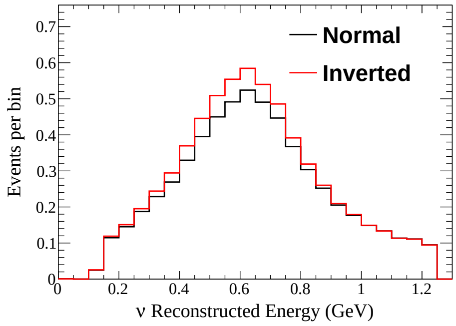

(d) *CCQE* e-like ($\bar{\nu}$-mode)

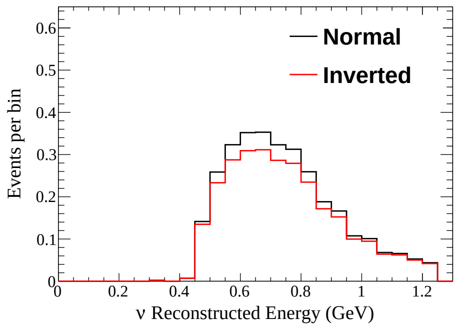

(e) $CC\pi^+$ e-like (ν-mode)

Figure 7.5: The effect of the mass ordering on the predicted Super-K reconstructed neutrino energy spectra, all other oscillation parameters are set to that of Tab. 5.9.

7.2 Sensitivity and Fitter Validations

An Asimov test is a useful tool to determine the expected sensitivity of an analysis [117]. The test is performed by first generating an Asimov data set, which is the nominal prediction under a given oscillation hypothesis. The Asimov data set is unique in that it often contains non-integer numbers of events in bins. Nonetheless, they are used as their results, free from statistical fluctuations, are easy to interpret and they also predict the median constraint from an ensemble of statistical fluctuations. The oscillation hypotheses chosen for the studies presented in this thesis are described in Tab. 7.1.

The Asimov fits are also used to validate the fitting mechanism through comparisons of results produced by other analysis groups in T2K. Several different groups perform independent oscillation analysis at T2K, each employing slightly different fitting and statistical techniques. Three groups performed the oscillation analysis presented in this thesis, VALOR (described in this thesis), $p-\theta$ which employs the same marginalisation technique as VALOR but fits using reconstructed outgoing lepton momentum and angle information, and MaCh3 which uses an MCMC[1] to sample the likelihood.

As there are different analysis binnings used between the analysis groups, the Asimov studies are very useful as they do not contain fluctuations which can affect binning schemes differently. The analysis groups are independent and therefore have slight differences in their implementations. However, validations using the event rates and effects of oscillation and systematic parameters are performed to ensure they do not result in any discrepancies. An example of the comparison is shown in Fig. 7.6 and more can be found in [80].

Likelihood scans are used to validate the application of the oscillation probability and likelihood calculations between the different analysis groups. A like-

[1]Markov chain Monte-Carlo

Parameter(s)	Asimov				
	A	B	C	D	E
$\sin^2\theta_{23}$	0.528	0.45	0.528	0.528	0.528
$\sin^2 2\theta_{13}$ ($\sin^2\theta_{13}$)	0.085 (0.0217)				
$\sin^2 2\theta_{12}$	0.846				
$\lvert\Delta m^2_{32}\rvert$ (NO) / $\lvert\Delta m^2_{31}\rvert$ (IO)	$2.509\ 10^{-3}\ \mathrm{eV^2c^{-4}}$				
Δm^2_{21}	$7.53\ 10^{-5}\ \mathrm{eV^2c^{-4}}$				
δ_{CP}	-1.601	0	0	π	$\pi/2$
Mass Ordering	Normal				

Table 7.1: Values of oscillation parameters used to compute the event rates, systematic effects and sensitivity studies. Nominal values of $\sin^2 2\theta_{13}$, $\sin^2 2\theta_{12}$ and Δm^2_{21} are taken from [39], A selection of reasonable and interesting values are chosen for $\sin^2\theta_{23}$, δ_{CP} and Δm^2_{32}.

lihood scan is produced from the likelihood calculation over a fixed set of model parameters. In the example given in Fig. 7.7, the likelihood is calculated for values of δ_{CP} and $\sin^2\theta_{13}$ to form the graph shown, while all other parameters are fixed to that of Asimov set A. As Asimov data set A is also chosen to be used as the mock data for the likelihood scan, the maximum likelihood was found to be in perfect agreement with expectation. As likelihood scans have no dependence on marginalisation, which is where differences are expected, they provide a method for validating the three analyses against each other to the extent that we expect them to agree.

The results of studies considering Asimov data sets A and B are included here as they are representative of data near the T2K best-fit point and away from physical boundaries respectively. Data sets C, D and E are considered to study the impact of the true value of δ_{CP} and are detailed in App. C. As with real data,

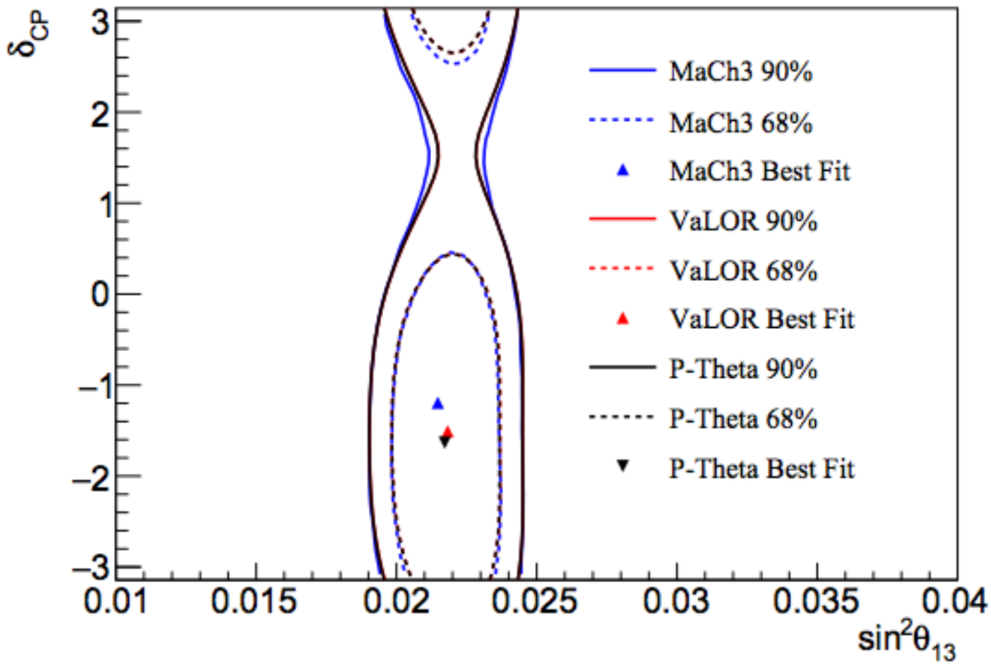

Figure 7.6: Comparison of the Asimov fit A results from the three T2K oscillation analysis groups.

fits are performed with both a flat prior and a Gaussian prior on $\sin^2 2\theta_{13}$ taken from the reactor experiments [39].

7.2.1 Results Without the Reactor Constraint

The results of interest from fits to Asimov data sets A and B are shown in Fig. 7.8. Figs. 7.8a and 7.8b show the likelihood surfaces projected down onto δ_{CP} in the normal and inverted ordering hypotheses. As described in Sec. 6.1, the normal and inverted ordering surfaces are drawn on the same axis only to give an indication of how well the analysis can distinguish between the two hypothesis and not a statement about the statistical separation. Figs. 7.8c and 7.8d show the results of a 2-dimensional fit, δ_{CP} vs $\sin^2\theta_{13}$ under the normal and inverted ordering hypotheses, contours in each case are produced independently.

The shape of the δ_{CP} likelihoods, shown in Figs. 7.8a and 7.8b, is unique due to the cyclical nature of δ_{CP}. As detailed in Sec. 7.1.3, the T2K spectra are

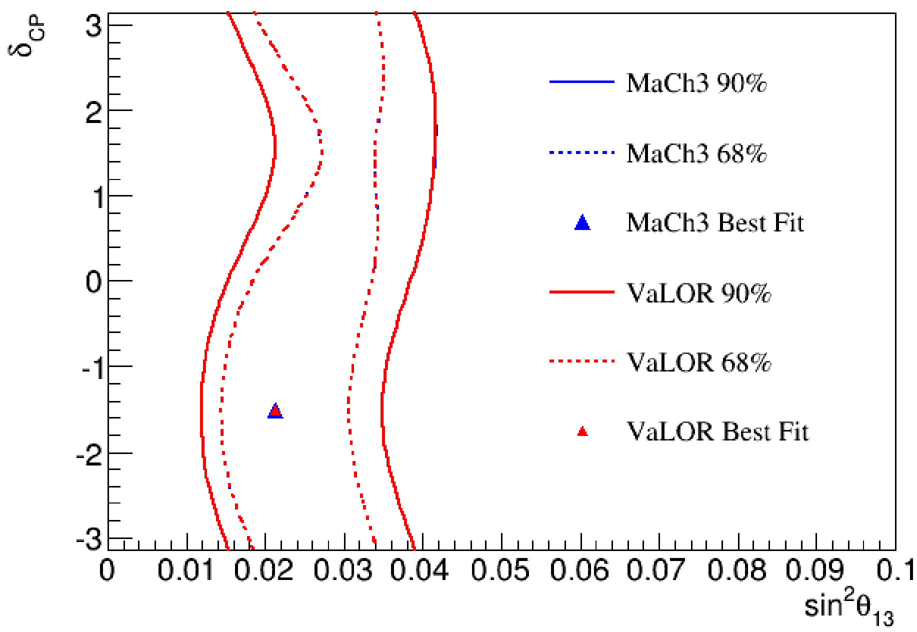

Figure 7.7: Comparison of likelihood scans from the VALOR and MaCh3 T2K oscillation analysis groups.

sensitive to the value of $\sin\delta_{CP}$, which is degenerate in the phase space of δ_{CP}. This can often result in multiple minima when considering the likelihood as a function of δ_{CP}, an example of which can be seen in Fig. 7.8b. Fig. 7.8a is an example of a fit in which this does not occur, however there is instead a relatively flat minimum at $\delta_{CP} = -\pi/2$ which is due to the fact that the sine function has an extremum at $-\pi/2$. Another feature resulting from the cyclical nature of δ_{CP} are the peaks in the likelihood surfaces at values of δ_{CP} which are least preferred by the data.

The correlation between δ_{CP} and $\sin^2\theta_{13}$ is highlighted in the 2-dimensional fits by the curved shape of the contours and the stronger constraint on $\sin^2\theta_{13}$ near δ_{CP} =$+\pi/2$. A clear correlation is also visible between the mass ordering and $\sin^2\theta_{13}$, particularly in Fig. 7.8c where a larger value of $\sin^2\theta_{13}$ is preferred in the inverted ordering hypothesis. This is due to the fact Asimov data set A was generated with normal ordering and δ_{CP} close to δ_{CP} =$-\pi/2$. These are values which result in the maximum amount of ν_e appearance at T2K. As the constraint on $\sin^2\theta_{13}$ is driven by the ν_e appearance sample, moving to inverted ordering reduces the amount of predicted ν_e appearance and $\sin^2\theta_{13}$ is forced up to compensate. This is also visible, although to a lesser extent, in Fig. 7.8d as the data set has less ν_e appearance.

The relation between the mass ordering and δ_{CP} is most visible in Figs. 7.8a and 7.8b where for Asimov data set A, fitting under the inverted ordering hypothesis produces a stronger constraint on δ_{CP}. This is because moving from the normal to inverted ordering hypothesis causes the data set to move beyond the boundary of maximal CP violation at $\delta_{CP} = -\pi/2$. This is more clearly visible in Asimov B where when moving from the normal to inverted ordering hypothesis, fitting with the "wrong" ordering introduces a small amount of CP violation. This is apparent from the δ_{CP} constraint. This feature can be seen in both Figs. 7.8b and 7.8d where the exclusion of δ_{CP} =$+\pi/2$ is much greater for the inverted than for the normal ordering case.

Fitting to Asimov set B also shows a weak symmetry around δ_{CP} =0 as expected. Under normal ordering, the symmetry is broken because moving away from δ_{CP} =$-\pi/2$ reduces the prediction of ν_e appearance faster than the prediction of $\bar{\nu}_e$ appearance increases. The lower event rate in the $\bar{\nu}_e$ sample results in a weaker exclusion of δ_{CP} =$+\pi/2$ than δ_{CP} =$-\pi/2$.

Regarding the sensitivity, from Asimov data set A it is expected that δ_{CP} =$+\pi/2$ will be excluded at 68% CL confidence from in the 1-dimensional fit to δ_{CP} and an ordering separation of $\Delta\chi^2 = 0.5$ will be found at the best fit value. There are also no values of δ_{CP} close to 90% exclusion, which is reflected in Fig. 7.8c, where the fit under normal ordering shows how the size of the uncertainty on $\sin^2\theta_{13}$ at the 90% CL is largely independent of the value of δ_{CP}. This is not the case for the fit under inverted ordering where the stronger constraint on δ_{CP} results in a closed 68% contour and narrowing of the 90% contour near δ_{CP} =$+\pi/2$. In both cases the best-fit point is a good prediction of the true values of δ_{CP} and $\sin^2\theta_{13}$ with slight deviations resulting from correlations and the marginalisation over $\sin^2\theta_{23}$.

For Asimov data set B the expectation is consistent with that of Asimov A. Although, as the data set lies away from maximal CP violation at $\delta_{CP} = -\pi/2$, there is a weaker exclusion of some values of δ_{CP}. The fit to $\sin^2\theta_{13}$ is pulled slightly below the true value and slightly above for δ_{CP}, again due to the correlation with $\sin^2\theta_{23}$. However, the significance between the true and best-fit values in both cases is negligible.

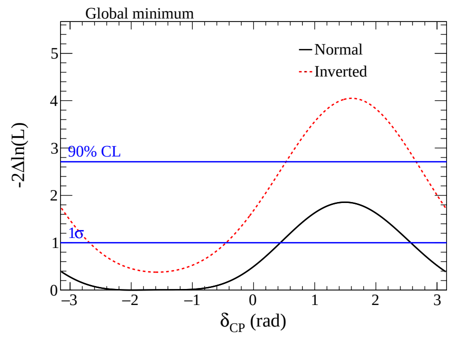

(a) Asimov A: δ_{CP}

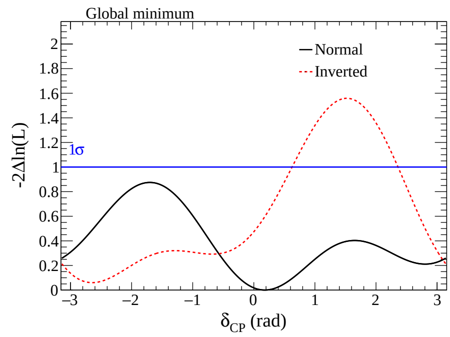

(b) Asimov B: δ_{CP}

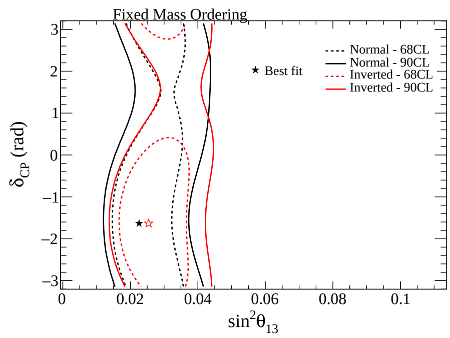

(c) Asimov A: $\sin^2\theta_{13}$ Vs δ_{CP}

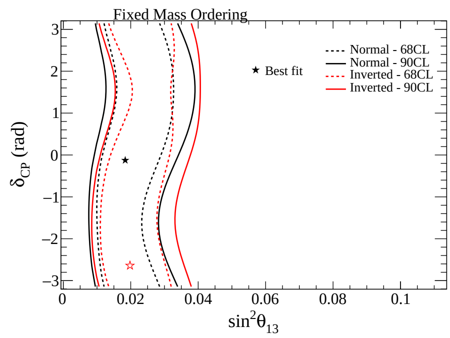

(d) Asimov B: $\sin^2\theta_{13}$ Vs δ_{CP}

Figure 7.8: Asimov fits without the reactor constraint.

7.2.2 Results with the Reactor Constraint

The following are results of fits to Asimov data sets A and B when the reactor constraint on $\sin^2 2\theta_{13}$ is applied. In addition to the fits shown in Sec. 7.2.1, a 2-dimensional fit to $\sin^2\theta_{23}$ and Δm^2_{32} is included. All are shown in Fig. 7.9. The most apparent difference between the fits with and without the reactor constraint is the uncertainty on $\sin^2\theta_{13}$, clear from the change in scale of the x-axis Figs. 7.9c and 7.9d. The fact that the reactor experiments have much better sensitivity to $\sin^2\theta_{13}$ means that the reactor constraint is the dominant contribution to the $\sin^2\theta_{13}$ contour. For the purposes of T2K, the value of $\sin^2\theta_{13}$ can be assumed to be fixed to the reactor best-fit value. This is also reflected in the shape of the contours in Figs. 7.9c and 7.9d, where the effect of the reactor constraint is to break the degeneracy between δ_{CP} and $\sin^2\theta_{13}$ as δ_{CP} has much more freedom to affect the rate of predicted ν_e appearance. Figs. 7.9a and 7.9b show how the correlation between the ordering and δ_{CP} are largely unaffected by the reactor constraint.

The greatest impact of the reactor constraint is the additional sensitivity to δ_{CP} which is clear from comparisons of Figs. 7.9a and 7.9b with Figs. 7.8a and 7.8b respectively. With the reactor constraint applied, there is a significant region of δ_{CP} excluded at 90% for Asimov data set A and at 68% CL for Asimov data set B. There is also a slightly greater ordering separation for Asimov data set A, though it still remains below 68% CL near $\delta_{CP} = -\pi/2$. The 2-dimensional fits to Asimov A have closed 68% contours under both orderings and a closed 90% contour under the inverted ordering. The 68% CL exclusion of CP conservation under the inverted ordering hypothesis is a positive for searches of CP violation.

Fits to the 2-3 sector parameters are shown in Figs. 7.9e and 7.9f. The different values of $\sin^2\theta_{23}$ used for data sets A and B have a clear impact on the size of the contours. Asimov set A, generated near the physical boundary of maximal disappearance, has a smaller uncertainty on $\sin^2\theta_{23}$ than Asimov set B. In both cases the likelihood surface is very flat in the region of the best-fit but decreases rapidly moving away from the physical boundary.

The strong correlation between the mass ordering and mass splitting is clear from fits to both Asimov set A and B in Figs. 7.9e and 7.9f, however the effect is approximately $0.04 \times 10^{-3} eV^2 c^{-4}$ and irrespective of $\sin^2\theta_{23}$. Thus, constraints under both the normal and inverted ordering are very consistent with each other. Under both ordering hypotheses, there is a 68% CL constraint of order $0.2 \times 10^{-3} eV^2 c^{-4}$ for the mass splitting and 0.16 (0.2) for Asimov set A (B) for $\sin^2\theta_{23}$.

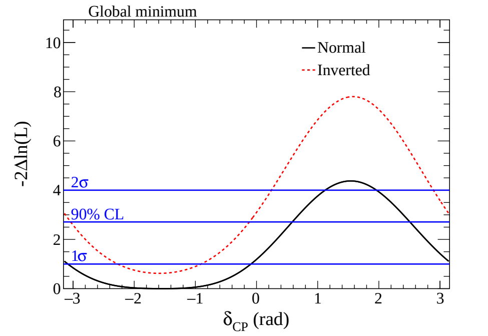

(a) Asimov A: δ_{CP} w/ reactor

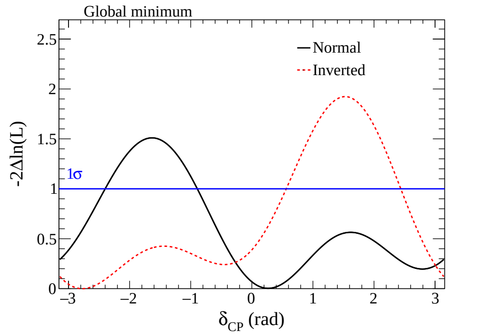

(b) Asimov B: δ_{CP} w/ reactor

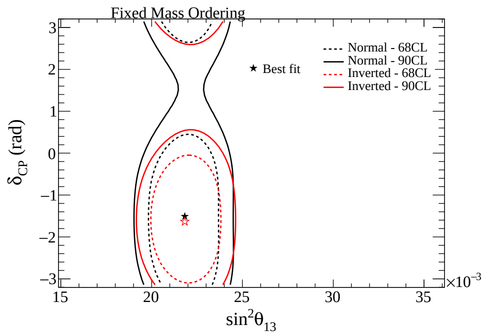

(c) Asimov A: $\sin^2\theta_{13}$ Vs δ_{CP} w/ reactor

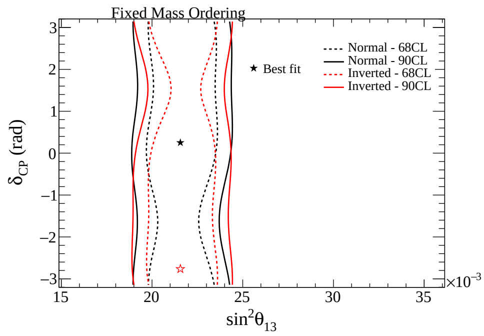

(d) Asimov B: $\sin^2\theta_{13}$ Vs δ_{CP} w/ reactor

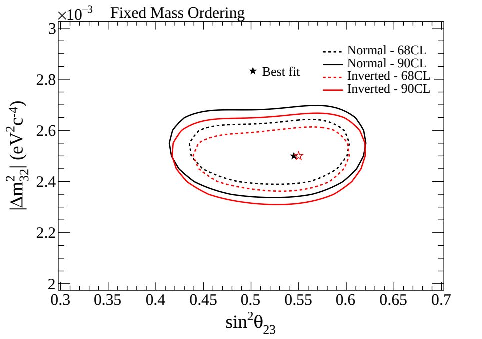

(e) Asimov A: $\sin^2\theta_{23}$ Vs Δm^2_{32} (m^2_{13}) w/ reactor

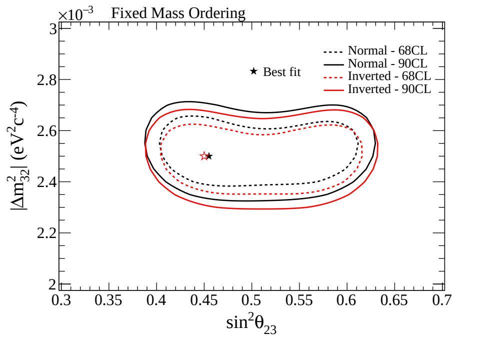

(f) Asimov B: $\sin^2\theta_{23}$ Vs Δm^2_{32} (m^2_{13}) w/ reactor

Figure 7.9: Asimov fits with the reactor constraint.

Chapter 8

Results

The results of the fit to the T2K Run 1-7 data set are detailed in this chapter. As was done for the sensitivity studies, fits are performed both with and without the reactor constraint. Fits with the reactor constraint are denoted as "T2K + Reactor" and those without as "T2K-only". A comparison of the observed number of events in each sample, with the expectation from various hypotheses and the best-fit, is shown in Tab. 8.1. Comparisons of the reconstructed neutrino energy spectra are also shown in Fig. 8.1.

The observed number of events in the μ-like samples appear to be in agreement with prediction. However, a feature of the data set which is immediately apparent is the slight excess of observed events in the ν-mode appearance spectra and fewer expected appearance events in $\bar{\nu}$-mode. Although consistent when considering the statistical uncertainty, this feature has implications for the exclusion of values of δ_{CP} which predict event rates less consistent with the data. This asymmetry between the ν-mode and $\bar{\nu}$-mode data sets is discussed further in Sec. 8.5 and Chap. 9. In all other aspects, the results are consistent with that from the sensitivity studies presented in Sec. 7.2.

Beam	Sample	Asimov A	Asimov B	Asimov C	No Osc	Obs.	Best-Fit
ν	μ-like	135.8	140.7	135.5	521.8	135	135.4
ν	e-like	28.7	21.5	24.2	6.15	32	29.7
ν	$CC\pi^+$-like	3.13	2.51	2.74	3.26	5	3.40
$\bar{\nu}$	μ-like	64.2	65.6	64.1	184.8	66	63.9
$\bar{\nu}$	e-like	6.00	6.25	6.90	2.34	4	6.31

Table 8.1: Comparison of the number of events in each sample expected from Asimov data sets, the best-fit spectra and data.

8.1 Results Under the Constant $\Delta\chi^2$ Approximation

1-dimensional marginal $\Delta\chi^2$ distributions are shown in Fig. 8.2 for the oscillation parameters of interest and the results summarised in Tab. 8.2. Listed are the 68% confidence regions produced under the constant $\Delta\chi^2$ approximation. 2-dimensional marginal $\Delta\chi^2$ distributions are shown in Fig. 8.3.

8.1.1 T2K-Only

Fits to δ_{CP} with and without the reactor constraint are shown in Figs. 8.2a and 8.2c respectively. For the T2K-only data fit, best-fits around maximal CP violation are found for both the normal and inverted ordering hypotheses with a preference, of approximately 2 units of $\Delta\chi^2$, for normal ordering. Also found is a 68% exclusion of $\sin\delta_{CP} = 0$ in both normal and inverted ordering hypotheses. A fit to $\sin^2\theta_{13}$ is shown in Fig. 8.2b, with the yellow band representing the reactor constraint. A slightly higher value of $\sin^2\theta_{13}$ is preferred to that from the reactor measurements, however both are in agreement at the 1σ level. Both 1-dimensional fits are consistent with what is seen in the 2-dimensional spectra shown in Fig. 8.3a. There is significant overlap between the contours and the reactor measurement of $\sin^2\theta_{13}$ and, for both normal and inverted orderings, there

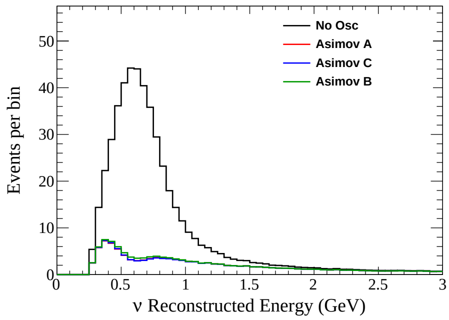

(a) μ-like ν-mode

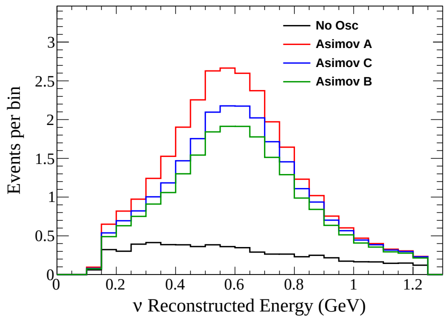

(b) e-like ν-mode

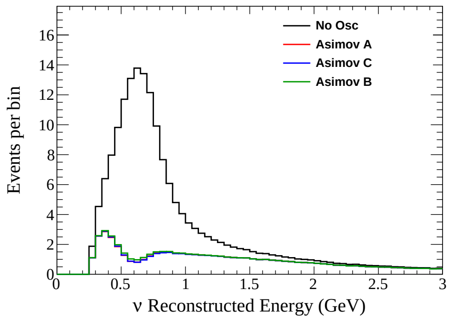

(c) μ-like $\bar{\nu}$-mode

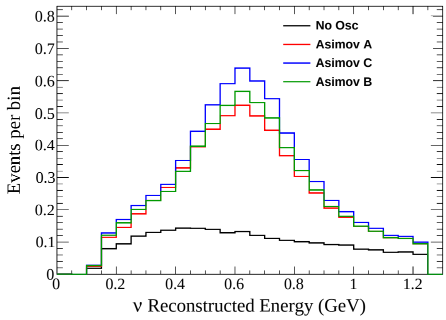

(d) e-like $\bar{\nu}$-mode

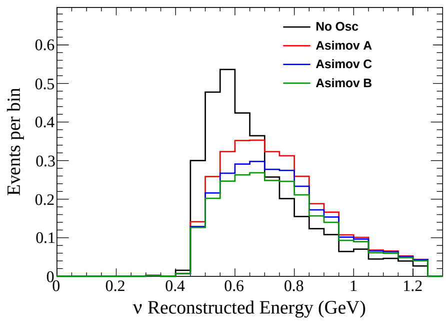

(e) $CC\pi^+$-like, ν-mode

Figure 8.1: A comparison of the expected Super-K spectra for various oscillation hypotheses with data.

are closed 90% confidence contours constraining δ_{CP}. $\sin\delta_{CP} = 0$ is excluded for all $\sin^2\theta_{13}$ under inverted ordering, while the normal ordering fit shows a slight preference for $\delta_{CP} = \pi$ over $\delta_{CP} = 0$.

8.1.2 T2K+Reactor

When the reactor constraint is included in the fit, the data constraint on δ_{CP} increases while the best-fit values remain relatively unchanged. $\sin\delta_{CP} = 0$ is excluded at the 90% CL and $\delta_{CP} = \pi/2$ excluded at the 3σ CL under the constant $\Delta\chi^2$ approximation. The exclusion of inverted ordering also moves close to 90% in all fits. The δ_{CP} vs $\sin^2\theta_{13}$ fit, shown in Fig. 8.3b, shows consistent results with a close to 90% exclusion of $\delta_{CP} = 0$ for all $\sin^2\theta_{13}$ and mass orderings. As is the case with the Asimov fits in Sec. 7.2, the constraint on $\sin^2\theta_{13}$ is almost completely driven by the reactor constraint when it is included.

Fits to δ_{CP} vs Δm^2_{32} and δ_{CP} vs $\sin^2\theta_{23}$ are shown in Figs. 8.3c and 8.3d respectively. Both are consistent with the results of the 1-dimensional fits, however Fig. 8.3d also shows clear correlation between δ_{CP} and $\sin^2\theta_{23}$ not visible in the Asimov fits presented in Sec. 7.2. This correlation is due to the fact that smaller values of $\sin^2\theta_{23}$ lead to a stronger constraints on δ_{CP}. This is also apparent from the comparison of the 1-dimensional fits of δ_{CP} and $\sin^2\theta_{23}$ with the 2-dimensional δ_{CP} vs $\sin^2\theta_{23}$ fit. The correlation causes the best-fit values for δ_{CP} and $\sin^2\theta_{23}$ to move as nuisance parameters are marginalised. Lastly, the fits also show a clear preference for the upper octant, which is another result of the large appearance rate observed.

The fits to $\sin^2\theta_{23}$ and Δm^2_{32}, shown in Fig. 8.3e, have a clear preference for maximal disappearance.

Parameter	Reactors	Normal ordering		Inverted ordering	
		Best-fit	$\pm 1\sigma$	Best-fit	$\pm 1\sigma$
δ_{CP}	Yes	-1.728	[-2.538; -0.877]	-1.445	[-2.170; -0.768]
δ_{CP}	No	-1.791	[-2.789; -0.764]	-1.382	[-2.296;-0.524]
$\sin^2\theta_{13}$	No	0.0271	[0.0209; 0.0342]	0.0299	[0.0232; 0.0380]
$\sin^2\theta_{23}$	Yes	0.550	[0.465; 0.601]	0.5525	[0.470; 0.601]
Δm^2_{32} / Δm^2_{13} (10^{-3} eV$^2/c^4$)	Yes	2.54	[2.460; 2.621]	2.51	[2.429; 2.588]

Table 8.2: Results of the 1-dimensional fits under the Gaussian approximation.

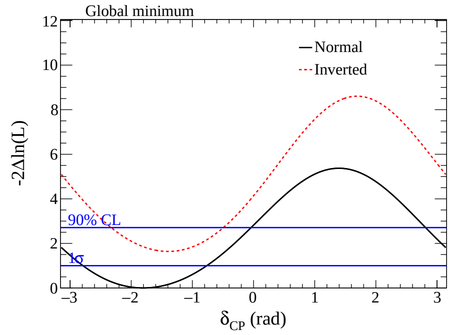

(a) δ_{CP} w/o reactor

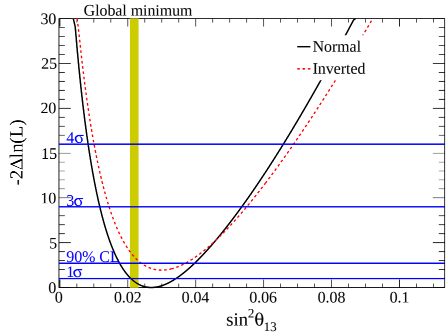

(b) $\sin^2\theta_{13}$ w/o reactor

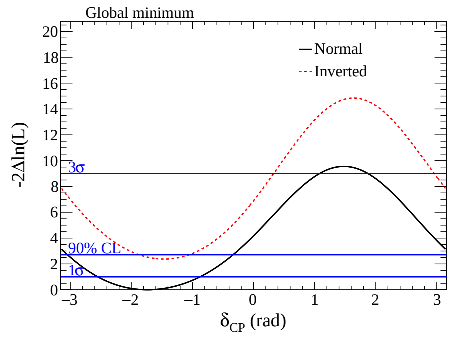

(c) δ_{CP} w/ reactor

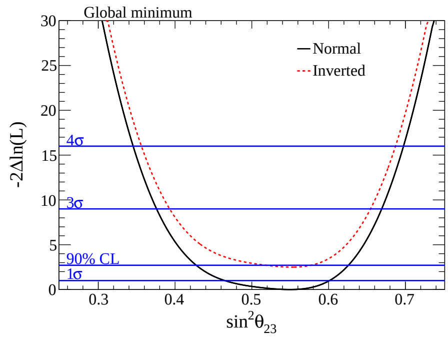

(d) $\sin^2\theta_{23}$ w/ reactor

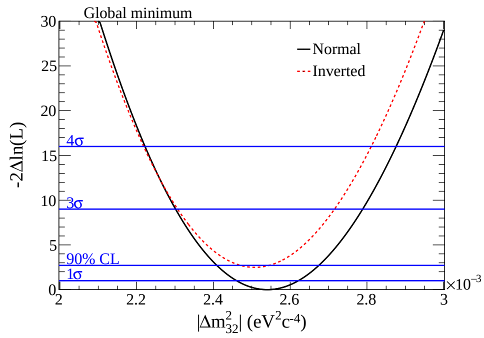

(e) Δm^2_{32} (Δm^2_{13}) w/ reactor

Figure 8.2: Measured 1-dimensional confidence intervals produced under the Gaussian approximation from the data fit.

8.2 Feldman-Cousins δ_{CP}

The exclusion regions, found from the Feldman-Cousins method described in Sec. 6.4.1, are shown in Fig. 8.4 and results summarised in Tab. 8.3. The critical values, at both the 90% and 2σ CL, are computed, for both normal and inverted mass ordering, for the following true values of δ_{CP}: -2.356, $-\pi/2$, -0.785, 0,

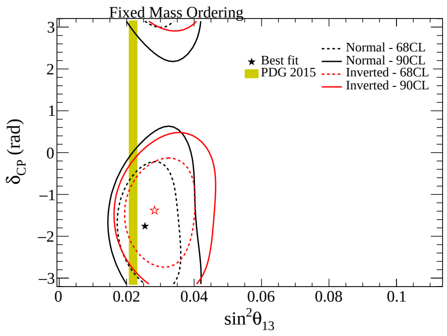

(a) $\sin^2\theta_{13}$ vs δ_{CP} w/o reactor

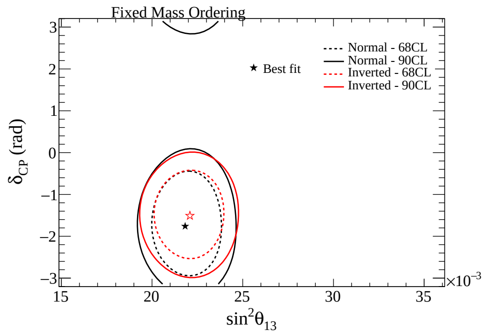

(b) $\sin^2\theta_{13}$ vs δ_{CP} w/ reactor

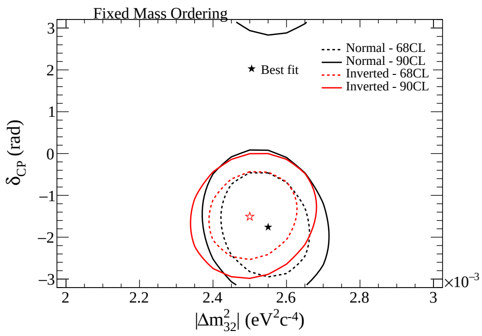

(c) Δm^2_{32} (Δm^2_{13}) vs δ_{CP} w/ reactor

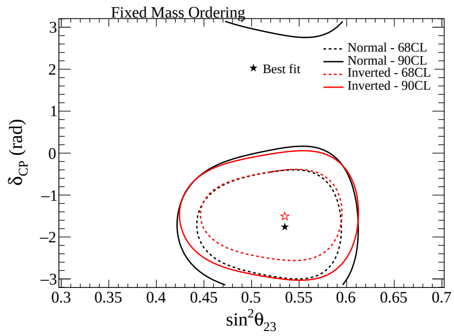

(d) $\sin^2\theta_{23}$ vs δ_{CP} w/ reactor

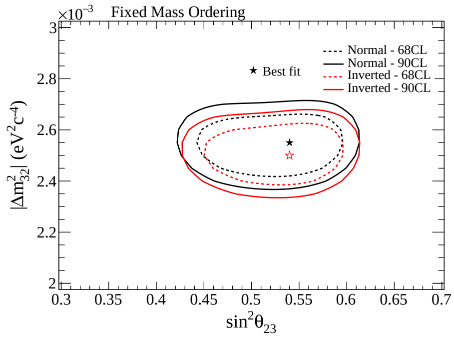

(e) $\sin^2\theta_{23}$ vs Δm^2_{32} (Δm^2_{13}) w/ reactor

Figure 8.3: Measured 2-dimensional confidence intervals produced under the Gaussian approximation from the data fit.

+0.785, $+\pi/2$, -2.356, $+\pi$. A linear interpolation is used to determine the critical χ^2 values between these points. More than 10k pseudo-experiments are used for each point to minimise the statistical uncertainty on the critical values. The need for such a computationally intensive procedure is highlighted in Fig. 8.5, which clearly shows how the coverage deviates from that expected assuming Wilks theorem.

Under normal ordering, the data excludes both $\delta_{CP} = 0$ and $\delta_{CP} = \pi$ at the

90% CL and $\delta_{CP} = 0$ at the 2σ level. There is also a strong exclusion of the inverted ordering hypothesis, almost excluded for all values of δ_{CP} at a 90% CL. Only a small region near $\delta_{CP} = -\pi/2$ remains. The effect of the statistical uncertainty in the critical $\Delta\chi^2$ values is shown in Fig. 8.4b and is clearly negligible for the level of significance which is presented.

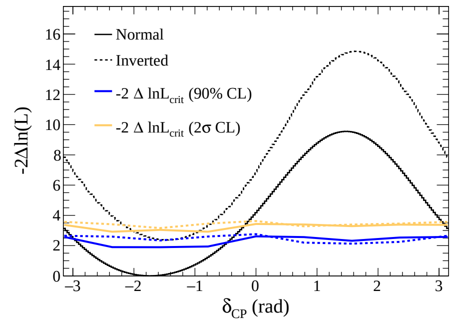

(a) 90% and 2σ CL

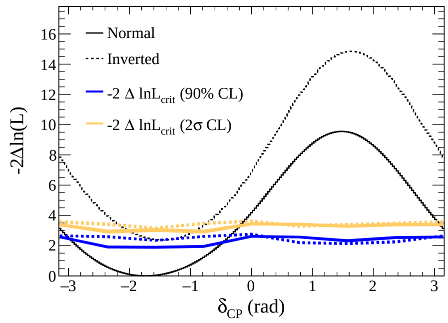

(b) 90% and 2σ CL with uncertainty

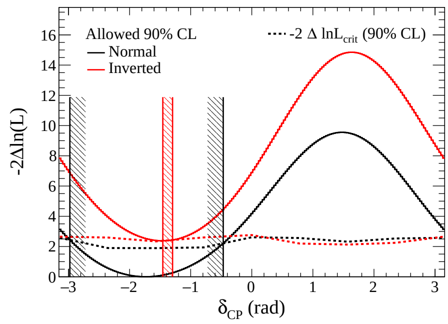

(c) 90% CL with exclusion region

Figure 8.4: Measured $\Delta\chi^2$ distributions from the data fit and critical values obtained from the Feldman-Cousins method. In Fig. 8.4b, the thickness of the line represent the uncertainty in the critical values.

Parameter	Normal ordering	Inverted ordering
δ_{CP}	[-2.98; -0.47]	[-1.47; -1.27]

Table 8.3: The confidence intervals at 90% CL obtained with the Feldman-Cousins method from the data fit.

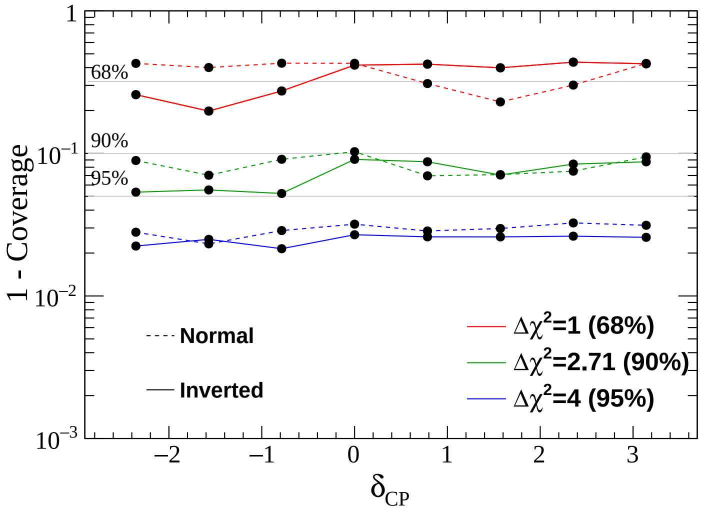

Figure 8.5: Comparison of the expected coverage, under the Gaussian approximation, with that obtained when considering an ensemble of MC experiments.

8.3 Marginal Best-Fit Spectra

Best-fit spectra provide an easy way to observe the consistency of T2K data with the prediction by eye. As only marginal likelihood surfaces for a maximum of two parameters at a time are computed for this analysis, there doesn't exist a single set of preferred oscillation and systematic parameters. Therefore a traditional best-fit spectrum, defined as the MC prediction for a single set of model parameters, which best matches the observed data, is impossible to produce. Instead a set of marginal best-fit spectra are used.

To produce a marginal spectrum, some oscillation parameters are fixed to their best fit values based on the maximum marginal likelihood in a given fit and others are averaged based on the observed data. The oscillation parameters chosen to be fixed are those which have the largest impact on each spectrum. For the μ-like spectra, $\sin^2\theta_{23}$ and Δm^2_{32} are chosen as the fixed parameters, and $\sin^2\theta_{23}$ and δ_{CP} are chosen for the e-like. These are the marginal likelihoods shown in Figs. 8.3d and 8.3e respectively.

A marginal spectrum for each sample is then produced by taking the likelihood weighted average of the prediction, independently for each analysis bin. The likelihood defined in Eq. (6.2) based on the observed data and nuisance parameter penalties is calculated and used to weight each MC prediction which goes into the marginal spectrum. This weighted average therefore includes the constraint on systematic and oscillation parameters from both data and priors. As 10k MC expected spectra with these exact properties are already used in the procedure to produce the marginal likelihoods during the fit, they are used again in the construction of the marginal best-fit spectra.

It is important to note that the marginal best-fit spectra shown here may not necessarily exist as a MC prediction for a given set of 'best-fit' parameters, but instead they represent the model predictions preferred by the data. The best-fit spectra are shown under the normal ordering in Fig. 8.6 and are compared to the un-oscillated nominal spectra. The best-fit spectra are produced in the binning used for the analysis, however they have been shown here projected onto only reconstructed neutrino energy to provide an easier comparison with the data and un-oscillated prediction.

Both μ-like best-fit spectra feature an "oscillation dip" which is a clear indication of near maximal ν_μ disappearance. The data and the best-fit spectra also show clear deviation from the un-oscillated hypothesis which is consistent with the conclusions drawn from fits to $\sin^2\theta_{23}$ and Δm^2_{32} in Sec. 8.1. In all appearance spectra the best-fit shows clear deviation from the un-oscillated, background only, prediction. However, it is important to note that the best-fit in all cases is determined by a fit to all samples. As the problem is over constrained, with 5 samples and effectively 3 oscillation parameters, the best-fit spectra are dominated by the high statistics samples. This affects the best-fit shown in Fig. 8.6d where, although the data seem slightly more consistent with the background hypothesis, the best-fit prefers oscillation. This is explored further in Sec. 10.1.

The ν-mode e-like best-fit spectrum, shown in Fig. 8.6b, which is the only appearance spectrum with a population large enough to make meaningful interpretations about the fit by eye, shows a significant excess from the background prediction. The fact that the data points are also more often above rather than below the best-fit spectrum also demonstrates how the event rate is slightly underpredicted by the model.

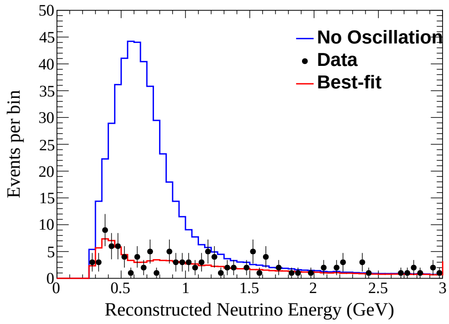

(a) μ-like ν-mode

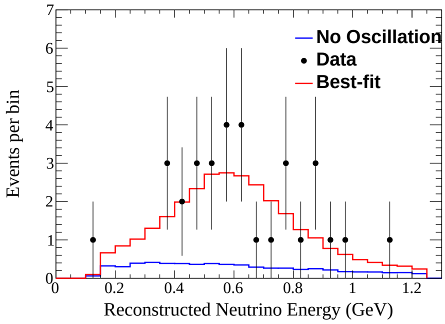

(b) e-like ν-mode

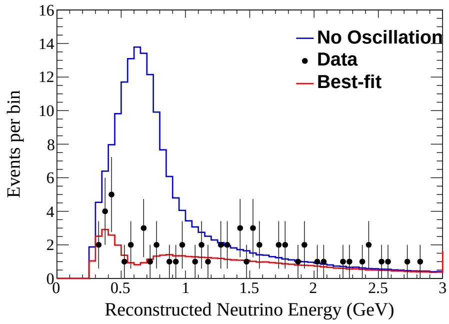

(c) μ-like $\bar{\nu}$-mode

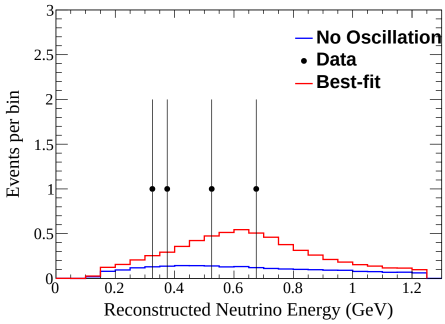

(d) e-like $\bar{\nu}$-mode

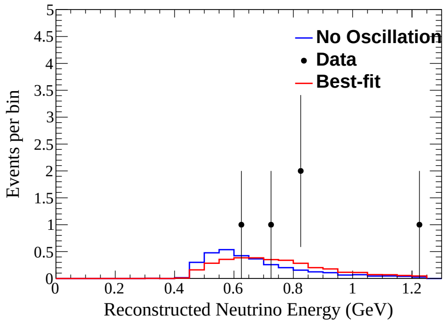

(e) $CC\pi^+$-like, ν-mode

Figure 8.6: The marginal best-fit spectra as a function of the neutrino reconstructed energy are shown for each Super-K sample. Also shown for reference are the nominal spectra under the no oscillation hypothesis and the observed data.

8.4 Goodness-of-fit

Best-fit spectra can be used to construct statistical tests to provide more rigorous means of testing the compatibility of data with the experimental model used in the analysis. A goodness-of-fit is an example of this kind of test.

The method chosen is similar to that used in this analysis to infer oscillation parameters within a frequentist framework. The goodness-of-fit test is performed by calculating a test statistic, from the data, and comparing it to the expected distribution of the statistic given statistical fluctuations. For this test, the statistic is chosen to be the Poisson likelihood defined by the best-fit spectra and the observed data. The statistic is defined as such because, in the large sample limit of over 5 events per bin, $\chi^2 = -2ln(\mathcal{L})$ follows a χ^2 distribution. In this case, the expected distribution is theoretically defined and does not require computation [112].

In order to fulfil the condition of the large sample limit, a binning different to that used in the oscillation analysis is used for the goodness-of-fit. 5 reconstructed neutrino energy bins (0-0.4, 0.4-0.7, 0.7-1.0, 1.0-2.0 and 2.0-30.0 GeV) are used for ν-mode and $\bar{\nu}$-mode μ-like samples and a single bin for all e-like samples.

The χ^2 and resulting p-value for each spectrum is shown in Tab. 8.4. The theoretical χ^2 distribution, and therefore the p-value, depends on the number of degrees of freedom in the analysis. Therefore the goodness-of-fit test can be performed with and without considering the mass ordering as a free parameter. The number of degrees of freedom, defined as the number of bins in the test less the number of free parameters not marginalised in the fit, can be 12 or 11 depending on whether or not the mass ordering is considered as a fixed or free parameter. As the mass ordering is a discrete choice, it doesn't behave as a typical free parameter in a statistical sense in the same way as say $\sin^2\theta_{13}$. Therefore for this test we can consider both extremes.

In both cases, the data seem to be very consistent with the best-fit spectra. The p-value, which is the probability of producing a data set less consistent than the observed data, is 97% and 95% for the fixed and free mass ordering respectively.

Mass ordering d.o.f.	χ^2 / ndf	p-value
fixed	4.55575 / 12	0.97
free	4.55575 / 11	0.95

Table 8.4: goodness-of-fit for the best-fit spectra.

8.5 Comparison With Sensitivity

Once the data fit is performed, it is natural to wonder if the results are consistent with those expected from sensitivity studies. A comparison of the predicted and observed event rates, shown in Tab. 8.1, show a small deviation for the appearance samples however it is unclear how much of an impact this has on the extraction of oscillation parameters. A comparison of the results from the data fit and fits to Asimov data set A are shown with T2K data only in Fig. 8.7 and with the reactor constraint in Fig. 8.8. Asimov A is chosen as the data set for comparison as the true oscillation parameters values for the data set most closely resemble the values measured in the data fit. The standout difference between the data and Asimov fits in both Figs. 8.7 and 8.8 is in the constraint of δ_{CP}. In Fig. 8.7, where the reactor constraint is not applied, there is much larger exclusion of $\delta_{CP} = \pi/2$ in the data fit than in the Asimov, even though the best-fit values are consistent. Although the disparity seems greater for the normal ordering hypothesis, the maximum difference, near $+\pi/2$, is approximately 3.5 units of $\Delta\chi^2$ under both orderings. This indicates that the data includes an additional amount of CP violation which is irrespective of the mass ordering.

These observations are consistent with the 2-dimensional fits, shown in Figs. 8.7c and 8.7d, which show closed contours from the data fit when those from the Asimov are open. For both the normal and inverted ordering, although the data prefers a slightly larger value of $\sin^2\theta_{13}$ than the value used in Asimov A, the measured constraint on $\sin^2\theta_{13}$ is consistent between the Asimov and data fits in the region around $\delta_{CP} = -\pi/2$.

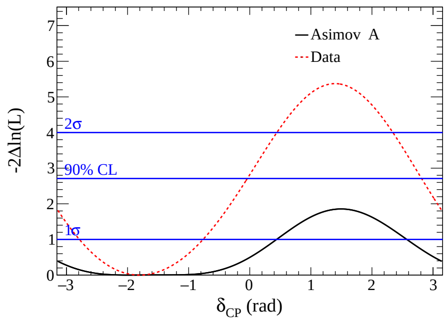

(a) δ_{CP}; Normal

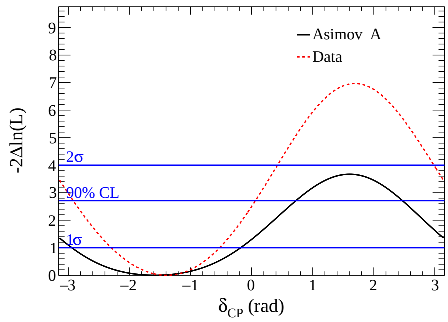

(b) δ_{CP}; Inverted

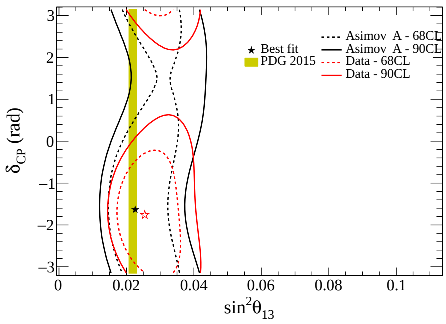

(c) $\sin^2\theta_{13}$ vs δ_{CP}; Normal

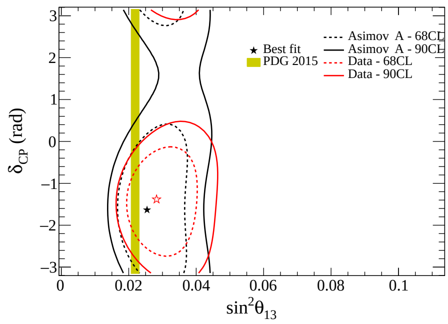

(d) $\sin^2\theta_{13}$ vs δ_{CP}; Inverted

Figure 8.7: Comparison of sensitivity, from Asimov data set A, with the data constraint found without using the reactor constraint.

In the T2K+Reactor fits, shown in Figs. 8.8c and 8.8d, the value of $\sin^2\theta_{13}$ is constrained and therefore unable to move toward a larger value preferred by the ν-mode e-like sample. In fact, the $\sin^2\theta_{13}$ measurement is almost entirely dominated by the reactor constraint. This is apparent from the fact the contour from the data fit overlaps considerably with the that from the Asimov and the reactor band when the reactor constraint is applied. Whereas in the T2K-only case, the size of the separation of the Asimov and the data fit contours is comparable to the uncertainty on $\sin^2\theta_{13}$ from the reactor experiments.

This preference for a larger $\sin^2\theta_{13}$ is not apparent in the Asimov fit, and therefore leads to an additional constraint on δ_{CP} as it is the only parameter available to increase the ν-mode e-like and ν-mode $CC\pi^+$ sample event rates in order to resemble the data. The difference between the Asimov and data δ_{CP} constraint, seen in the T2K+Reactor fits, is therefore a combination of this and the additional CP asymmetry observed in the T2K-only fits.

This additional CP violation is clearly apparent when comparing the best-fit event rates, which represent the model configuration which most closely resembles the data, with the observed data as there exists more CP asymmetry in data than there is available in the model. Thus, the data prefers a value of $\sin\delta_{CP}$ which is in the un-physical region beyond $-\pi/2$ that naturally leads to a stronger exclusion of δ_{CP} as it moves away from $-\pi/2$.

As expected from observations of the T2K-only fits, the mass ordering has little effect on the difference seen between the Asimov data set and the data which, for the case of the T2K+Reactor fits, is found to be approximately 5 units of $\Delta\chi^2$ near $+\pi/2$.

Comparisons of the fits to $\sin^2\theta_{23}$ vs Δm^2_{32} can be found in Figs. 8.8e and 8.8f. Other than a slightly larger preferred value in the data fit, the size of the Asimov and data fit contours are very consistent with regards to Δm^2_{32}. The opposite is true for $\sin^2\theta_{23}$ where both Asimov and data fits prefer close to maximal disappearance however the Asimov contour is wider than that of the data fit. This implies that the data prefers a hypothesis with fewer muon neutrinos than the Asimov data set and therefore excludes values of $\sin^2\theta_{23}$ which are away from maximal disappearance to a greater significance.

Evidence for an effect such as this can be found in the marginal best-fit spectra for the disappearance samples shown in Figs. 8.6a and 8.6c. As the ν-mode sample has much greater statistical power than the $\bar{\nu}$-mode, it dominates the constraint on $\sin^2\theta_{23}$ and it is clear from the data shown in Fig. 8.6a that the observed event rate in the 0.55 − 0.60 GeV and 0.65 − 0.70 GeV energy bins disfavours values of $\sin^2\theta_{23}$ away from maximal mixing. The data are nonetheless consistent with the model, found from the goodness-of-fit test in Sec. 8.4, which indicates that the narrow contour may be a result of a statistical fluctuation in favour of slightly more muon neutrino disappearance than there is available in the model.

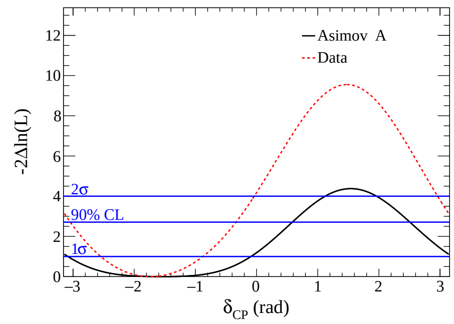

(a) δ_{CP}; Normal

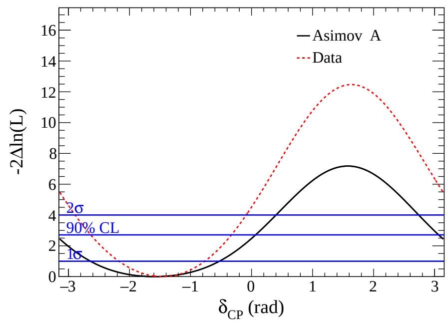

(b) δ_{CP}; Inverted

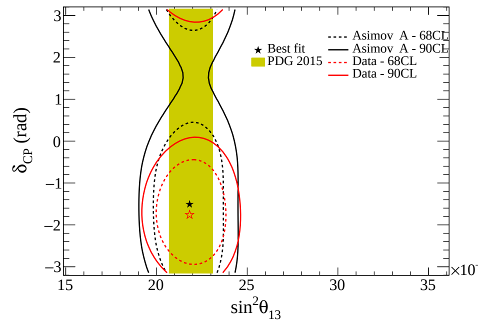

(c) $\sin^2\theta_{13}$ vs δ_{CP}; Normal

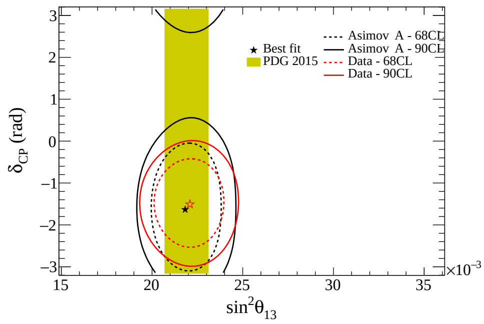

(d) $\sin^2\theta_{13}$ vs δ_{CP}; Inverted

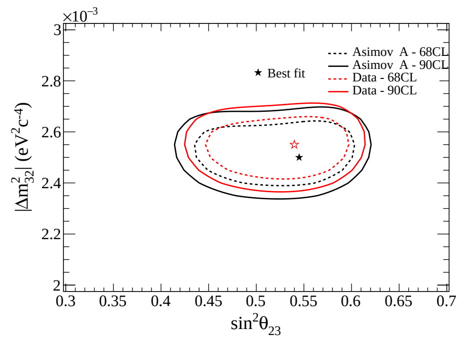

(e) $\sin^2\theta_{23}$ vs Δm^2_{32}; Normal

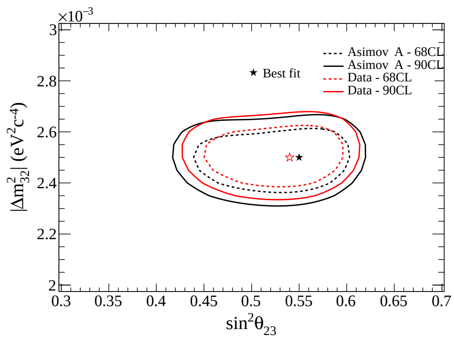

(f) $\sin^2\theta_{23}$ vs Δm^2_{13}; Inverted

Figure 8.8: Comparison of sensitivity, from Asimov data set A, with the data constraint found when including the reactor constraint.

8.6 Consistency with Other Results

Whenever an experiment releases a new analysis it is important to question whether the new results are consistent with those previously produced by the experiment, and also those of experiments conducting similar measurements. The following are a series of comparisons which determine the level of compatibility of the results presented here with those in the field.

8.6.1 5 Sample vs 4 Sample Analysis Comparison

The major difference between the analysis presented here and that of previous T2K results is the inclusion of the $CC\pi^+$ sample at Super-K. This sample amounts to an additional 14% of appearance events when compared to the previous data set. For this reason, large changes in the data fits and the conclusions about oscillation parameters drawn from them are not expected. A comparison with the previous result is therefore an ideal way to firstly validate the results obtained from this analysis, and study the impact of the new $CC\pi^+$ sample.

Asimov

Before considering the data constraint, the effect of the additional sample can be studied with Asimov data set A as described in Sec. 7.2. Comparisons of note under normal mass ordering are shown in Fig. 8.9. The impact of the additional sample is clearly visible in fits to all parameters which are influenced by the appearance data sets. These are shown in Figs. 8.9a and 8.9c, where the impact can be mostly seen in the stronger exclusion of $\delta_{CP} = \pi/2$. Fig. 8.9b shows how the additional sample improves the constraint on $\sin^2\theta_{13}$ rather than δ_{CP}. This is expected given the fact that additional data in ν-mode can only help to constrain the absolute appearance rate, which is sensitive to $\sin^2\theta_{13}$, rather than any ν-mode vs $\bar{\nu}$-mode asymmetry which constrains δ_{CP}. This result is reconciled with the observations in Figs. 8.9a, 8.9c and 8.9d when considering that any improvement in the $\sin^2\theta_{13}$ constraint is projected onto δ_{CP}, due to their correlation, when it is marginalised or constrained by the reactor measurement.

The effect of the new sample on the $\sin^2\theta_{23}$ vs Δm^2_{32} fit is shown in Fig. 8.9e and is clearly negligible as those parameters are mostly constrained by the disappearance samples which remain unchanged from the previous analysis.

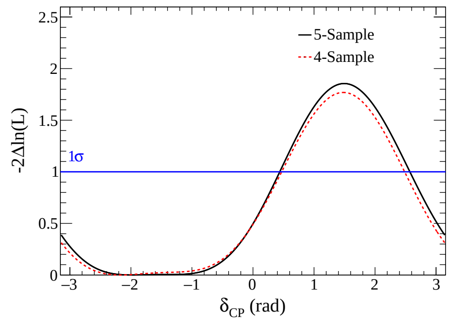

(a) δ_{CP} w/o reactor

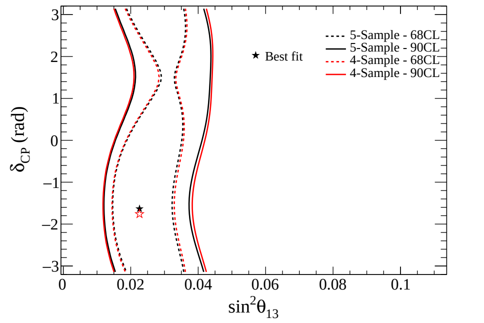

(b) $\sin^2\theta_{13}$ vs δ_{CP} w/o reactor

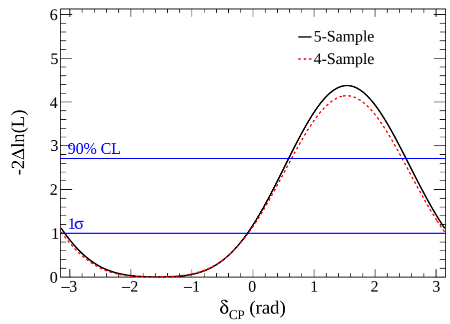

(c) δ_{CP} w/ reactor

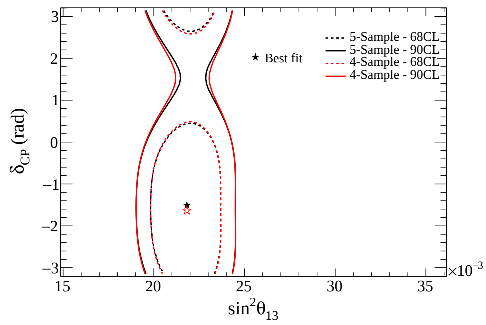

(d) $\sin^2\theta_{13}$ vs δ_{CP} w/ reactor

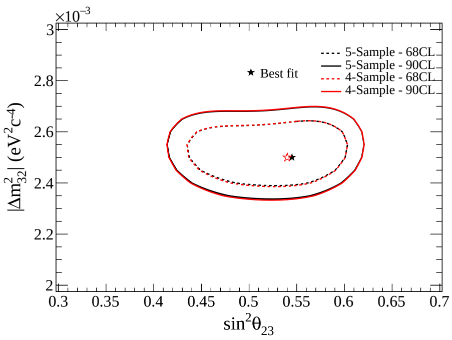

(e) $\sin^2\theta_{23}$ vs Δm^2_{32} w/ reactor

Figure 8.9: The comparison of sensitivities, from Asimov data set A, from the *CCQE* sample analysis (4-Sample) and the *CCQE* + $CC\pi^+$ sample analysis (5-Sample).

Data

The improvement in the oscillation parameters constraints are comparable to what is found in the Asimov studies. In both cases, the data constraints on δ_{CP} are slightly stronger than what is expected from the respective Asimov data sets. This is mainly a consequence of the observed appearance rate in ν-mode compared to the prediction from the reactor measurement. The improvement in the $\sin^2\theta_{13}$ constraint, seen in Fig. 8.10a is consistent with that in Fig. 8.9b however the preferred value of $\sin^2\theta_{13}$ is slightly larger when the $CC\pi^+$-like sample is included. This is consistent with the $CC\pi^+$-like observation which is over 50% larger than the predicted rate, whereas the $CCQE$ is only 10%. The fact that $\sin^2\theta_{13}$ is slightly less compatible with the reactor constraint when the $CC\pi^+$-like sample is included is also the primary cause of the stronger δ_{CP} constraint observed when the reactor constraint is applied.

There is also a difference in the $\sin^2\theta_{23}$ vs Δm^2_{32} fit unseen in the Asimov studies. The stronger preference for the upper θ_{23} octant when the $CC\pi^+$-like sample is included can also be attributed to the high observed appearance rate.

8.6.2 Comparison With Other T2K Analysis Groups

The agreement between the three oscillation analysis groups at T2K described in Sec. 7.2 is best summarised with the comparison shown in Fig. 8.11. As the MaCh3 fit shown in Fig. 8.11 is performed without the information of the outgoing lepton angle, it is best compared to the VALOR analysis of the same form, denoted as "E_{Rec} only". Near perfect agreement is found between the analysis groups with small deviations expected given the contrasting methods used in each.

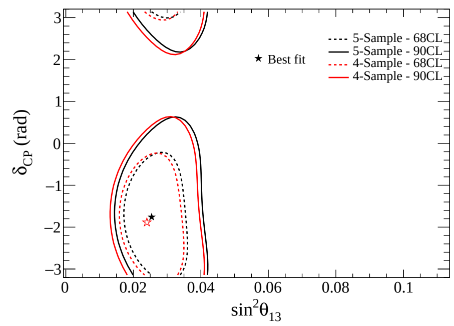

(a) $\sin^2\theta_{13}$ vs δ_{CP} w/o reactor

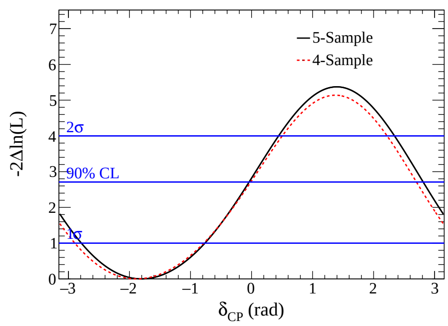

(b) δ_{CP} w/o reactor

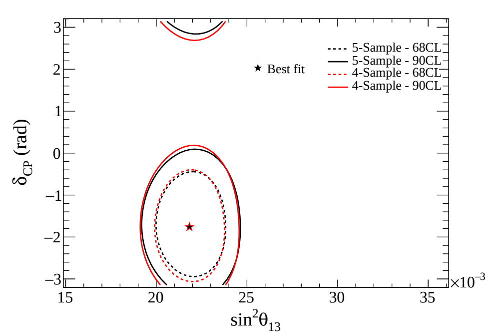

(c) $\sin^2\theta_{13}$ vs δ_{CP} w/ reactor

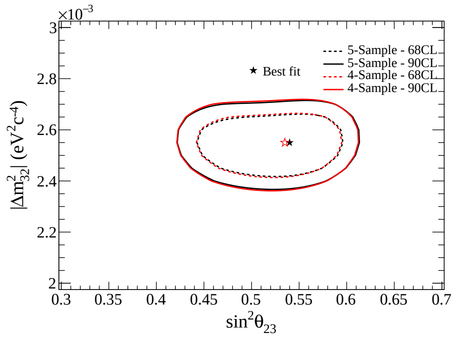

(d) $\sin^2\theta_{23}$ vs Δm^2_{32} w/ reactor

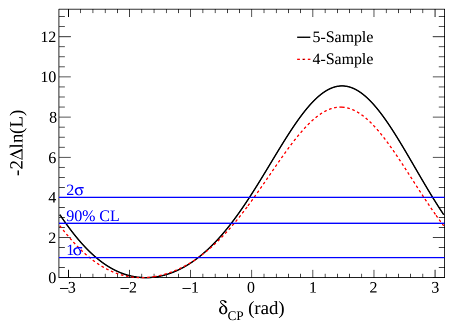

(e) δ_{CP} w/ reactor

Figure 8.10: The comparison of the results of data fits under normal ordering from the *CCQE* sample analysis (4-Sample), and the *CCQE* and $CC\pi^+$ sample analysis (5-Sample).

8.6.3 Comparison With Other Experiments

A comparison of the results obtained in this analysis with those of other leading experiments in the field is shown in Fig. 8.12. They are shown independently under the normal and inverted ordering hypotheses. Independent inverted ordering contours for $NO\nu A$ and Ice Cube are unavailable and are therefore not included. It is important to note that the size of the contours do not solely determ-

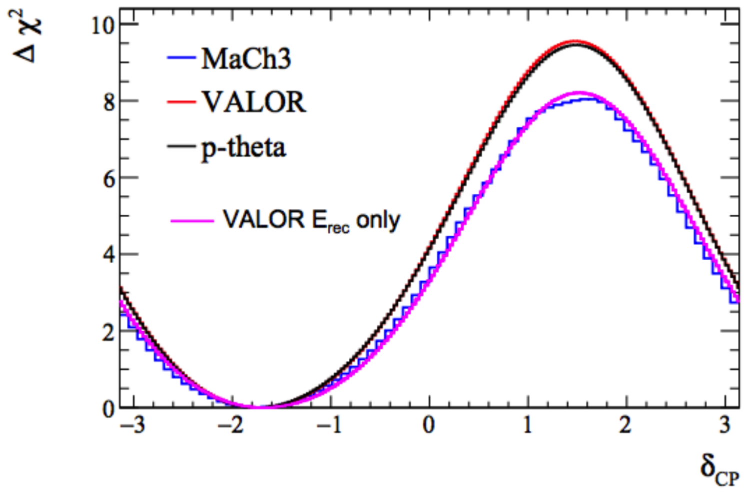

Figure 8.11: Comparison of the 1-dimensional δ_{CP} likelihood with the reactor constraint between the three oscillation analysis groups at T2K. The normal ordering is assumed for all fits. Figure taken from [80].

ine the ability of an experiment to measure a parameter. The shape and gradient of the likelihood surface is highly dependent on the values of $\sin^2\theta_{23}$ and Δm^2_{32}, especially in regions near the $\sin^2 2\theta_{23}= 1$ physical boundary as shown here.

Nonetheless, the T2K constraint on both $\sin^2\theta_{23}$ and Δm^2_{32} is both competitive and consistent with all other experiments given the significant overlap in the 90% confidence regions. It is clear that, neglecting T2K, the strongest constraint on the disappearance oscillation parameters which comes from $NO\nu A$ has a preference for non-maximal over maximal disappearance. This is not however not a great cause for concern as there is still a small region at the 68% CL which overlaps from both experiments even though the T2K contour is narrower in $\sin^2\theta_{23}$ than expected from sensitivity studies.

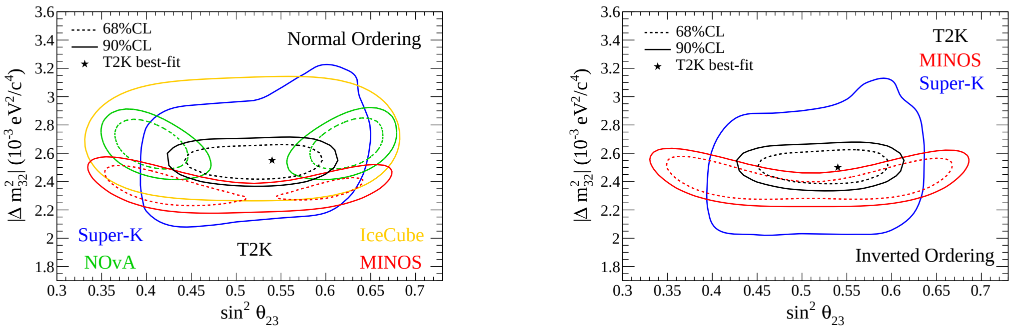

(a) Normal Ordering

(b) Inverted Ordering

Figure 8.12: The measured T2K confidence intervals for $\sin^2\theta_{23}$ vs Δm^2_{32} (Δm^2_{13}) from this analysis under the Gaussian approximation. For the normal ordering the other experiment results are: Super-K (PoS ICRC2015 (2015) 1062), Minos+ (Neutrino 2014 conference), NOνA (Neutrino 2016 conference) and IceCube DeepCore (Phys.Rev. D91 (2015) 072004, arXiv 1410.7227). For the inverted ordering the other experiment results are: Super-K (PoS ICRC2015 (2015) 1062) and Minos+ (Neutrino 2014 conference).

Chapter 9

Further Discussion

The studies presented in the following section are performed to provide further insight into the results obtained in this analysis. These tests focus primarily on the measurement of δ_{CP} and the significance of the exclusion of $\sin\delta_{CP} = 0$ and $\delta_{CP} = \pi/2$ obtained when considering the reactor measurement of $\sin^2 2\theta_{13}$. The first study aims to shed light on the driving factors behind the δ_{CP} constraint by considering the dominant constraints independently while the second is a study of the statistical significance of the exclusion obtained under frequentist principles.

A simple comparison of the observed event rate with that predicted by various model configurations is shown in Fig. 9.1. It is clear from this that the data live in a region which is inaccessible by the model, even when considering the statistical uncertainty. The fact that the data lives beyond the maximal CP violating prediction is also the origin of the stronger than expected exclusion of CP conservation and $\delta_{CP} = \pi/2$. Although there is some freedom in the model from systematic parameters to modify the event rates so as to match the observation, the conclusions remain valid as the effect of the systematic parameters is only on the order of 6% on the total event rate as shown in Tab. 5.12.

Further studies are therefore useful to understand the level of tension which is observed.

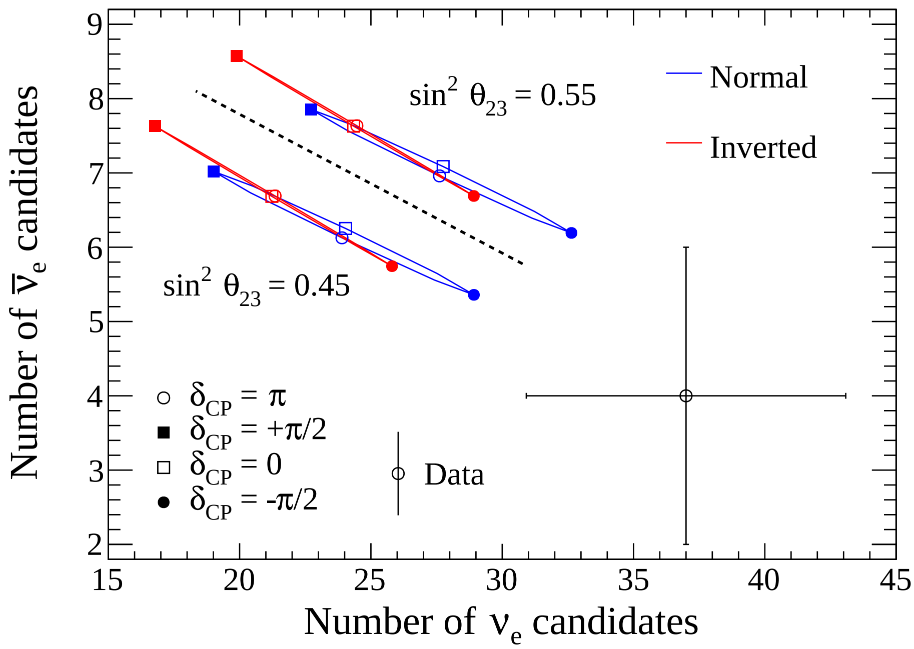

Figure 9.1: The ellipses show the total predicted event rates in the e-like ν-mode and $\bar{\nu}$-mode samples for various values of δ_{CP}, $\sin^2\theta_{23}$ and mass ordering hypotheses. The statistical uncertainty is shown for the T2K event rate. All other oscillation parameters are set to that of Asimov data set A and systematic parameters set to the ND280 post-fit values.

9.1 Comparison of ν and $\bar{\nu}$ Appearance

As discussed previously, the measured constraint on δ_{CP} is driven primarily by a comparison of the predicted ν-mode e-like sample with that observed. The same is true, to a lesser extent, for the $\bar{\nu}$-mode e-like sample, however it is important to note the asymmetry where the data are slightly over predicted for the $\bar{\nu}$-mode e-like and under predicted for the ν-mode e-like and ν-mode $CC\pi^+$.

The reactor experiments and the disappearance samples provide strong constraints on $\sin^2 2\theta_{13}$ and $\sin^2\theta_{23}$ respectively, which leaves δ_{CP} as the only free oscillation parameter available to adjust the predicted event rates. It is therefore important to consider whether or not consistent results are produced, when the fits are given the appropriate freedom, and the ν-mode and $\bar{\nu}$-mode appearance samples are considered independently.

To test this, two fits using only T2K data are performed. One in which the ν-mode appearance samples in addition to both ν-mode and $\bar{\nu}$-mode disappearance samples are used, and another in which the $\bar{\nu}$-mode appearance sample in addition to both ν-mode and $\bar{\nu}$-mode disappearance samples are used. Both are fits to δ_{CP} and $\sin^2\theta_{13}$, for the normal and inverted ordering hypotheses, and are shown in Fig. 9.2.

Unsurprisingly, when considering the samples independently, there is little sensitivity to δ_{CP} due to the degeneracy with $\sin^2\theta_{13}$. A comparison of the ν-mode and $\bar{\nu}$-mode fits shows a clear preference for differing values of $\sin^2\theta_{13}$ driven by the respective rate of appearance. Although the $\bar{\nu}$-mode constraint on $\sin^2\theta_{13}$ appears slightly more compatible with the reactor measurement, it is mainly due to the large uncertainty, given the weak statistical power of the sample, and neither the ν-mode or $\bar{\nu}$-mode measurements can be considered incompatible with the reactor measurement.

The results however give clear insight into the measurement of δ_{CP} when considering all samples and the reactor constraint. For both mass orderings, the region with the largest 90% CL overlap between the fits and the reactor measurement is near the preferred value of $-\pi/2$. Whereas $+\pi/2$, which is excluded to more than 2σ in Fig. 8.4, contains no overlapping regions. In fact, there is a slightly smaller overlapping region under inverted ordering, which is a strong indication that the model is less preferred than normal ordering. This is complementary to what is observed in the joint fit.

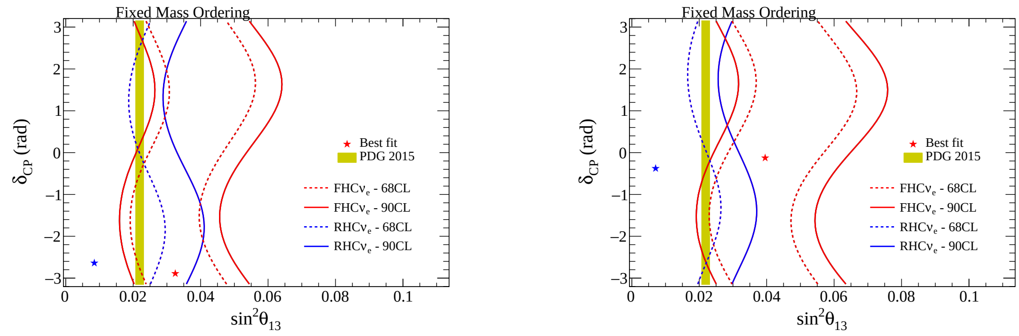

(a) Normal Ordering (b) Inverted Ordering

Figure 9.2: The contours of $\sin^2\theta_{13}$ Vs δ_{CP} without the reactor constraint using either the ν or the $\bar{\nu}$ appearance data sets and all available disappearance samples are used in both fits.

9.2 Comparisons of the 1D δ_{CP} Exclusion with MC Predictions

To further understand the statistical significance of the exclusion of the CP conserving values of δ_{CP}, the result of the data fit can be compared with an ensemble of pseudo-experiments. Over 10,000 pseudo-experiments are generated for various true values of δ_{CP} and the mass ordering. Nuisance parameters in the pseudo-experiments are randomised in accordance with the procedure used in Sec. 6.4.1. The procedure to form a distribution of the measured exclusion from the pseudo-experiments for δ_{CP} =-$\pi/2$ is as follows:

- Generate ∼10k pseudo data sets with oscillation hypothesis $\delta_{CP} = -\pi/2$ and the normal ordering while randomising other oscillation and nuisance parameters.
- Compute the δ_{CP} $\Delta\chi^2$ surface, in accordance with the procedure for the real data, under both the normal and inverted ordering hypotheses, with respect to the global minimum χ^2 found in either hypothesis.
- Discretise the δ_{CP} range into 201 bins

- For each δ_{CP} bin, order the $\Delta\chi^2$ found in each pseudo-experiment from smallest to largest.

This creates a distribution of $\Delta\chi^2$ for each combination of δ_{CP} and the mass ordering, which can be compared to the $\Delta\chi^2$ of the data fit. The distribution produced here is similar to that used for the Feldman-Cousins procedure, but not the same. In this procedure, the test statistic at each point in the δ_{CP} mass ordering surface is

$$\Delta\chi^2(\delta_{CP}, \mathrm{MO}, i) = \chi^2(\delta^i_{CP}, \mathrm{MO}^i) - \chi^2(\delta^{bf}_{CP}, \mathrm{MO}^{bf}) \tag{9.1}$$

where the best-fit is from the minimum χ^2 point in each pseudo-experiment. Only for the special case where the value of δ_{CP} and the mass ordering matches that used to generate the pseudo data sets does the statistic coincide with that used in the Feldman-Cousins procedure.

The resulting $\Delta\chi^2$ distributions are presented as shown in Fig. 9.3. The dark and light grey regions indicate the $\Delta\chi^2$ values which contain 68% and 95% of the pseudo-experiments. The information from the pseudo-experiments can also be presented in a slightly different way, shown in Fig. 9.4, where the distribution of $\Delta\chi^2$ can be instead used to calculate the probability to exclude each value of δ_{CP} at the 90% and 2σ CL, found using the Feldman-Cousins procedure.

The distribution of the $\Delta\chi^2$, for each combination of the mass ordering and δ_{CP}, can then be compared with the measured $\Delta\chi^2$ from the data to determine the statistical significance of such a result. The test is performed by generating ensembles of pseudo-experiments at a number of points in the δ_{CP} and mass ordering phase space. The results of a few of these points follow.

9.2.1 $\delta_{CP} = -\pi/2$ - Normal Ordering

The oscillation hypothesis of $\delta_{CP} = -\pi/2$ and the normal ordering is chosen as it creates maximum CP violation of the kind observed in the data. A compar-

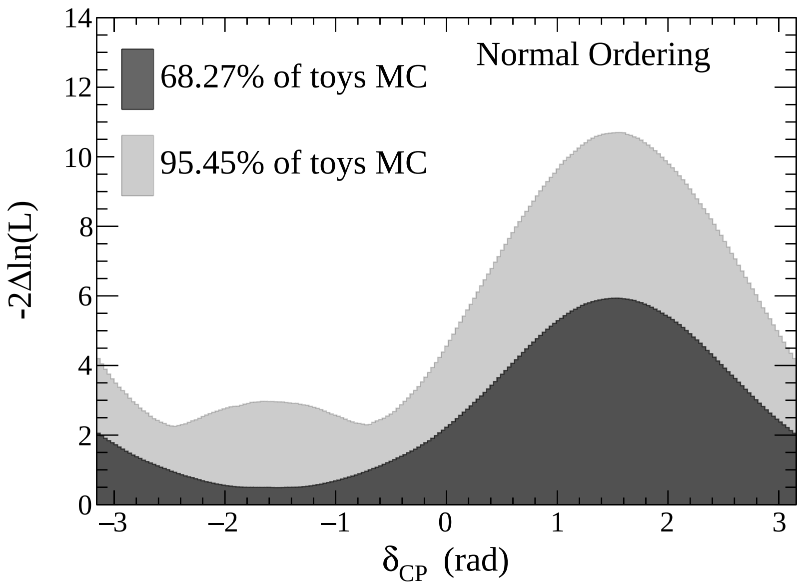

Figure 9.3: Example of the distribution of exclusion for an ensemble of pseudo-experiments.

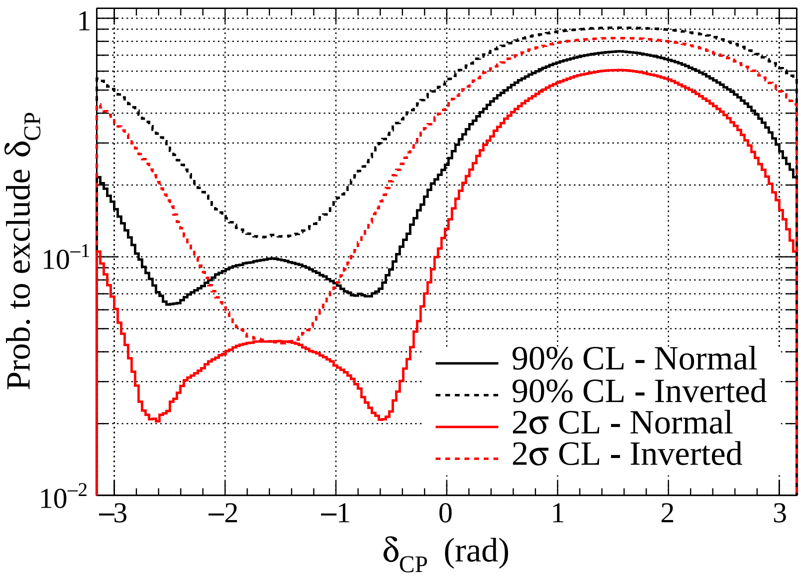

Figure 9.4: Example showing the fraction of pseudo-experiments which exclude δ_{CP} to 90% and 2σ.

ison of the $\Delta\chi^2$ distribution with the ensemble of pseudo-experiments is shown in Fig. 9.5, along with the 90% exclusion surface from the Feldman-Cousins procedure.

It is clear that the data contours, for both the normal and inverted ordering, are within the 95% band of exclusion from pseudo-experiments. This suggests that the data constraint is consistent with a fluctuation of true $\delta_{CP} = -\pi/2$ and normal ordering below the 2σ level.

There is also an interesting feature near $\delta_{CP} = -\pi/2$ in Fig. 9.5a, where there is a slight bump in the 95% band. It also appears in Fig. 9.5c where values of δ_{CP} near -$\pi/2$ are more likely to be excluded than those near -$\pi/4$. At first glance, this appears counter-intuitive given that the pseudo data sets are generated for the normal ordering at $\delta_{CP} = -\pi/2$. Naively, one would expect that $\delta_{CP} = -\pi/2$ should be the least likely out of all values of δ_{CP} to be excluded at any significance given it matches the true value.

This feature is due to the boundary of maximal CP violation at $\delta_{CP} = -\pi/2$. The fact that it does not appear in the 68% $\Delta\chi^2$ contour shown in Fig. 9.5a indicates that the effect is in the tail of the $\Delta\chi^2$ distribution. The effect of the boundary is to reduce the $\Delta\chi^2$ in pseudo-experiments where the fit is pushed beyond the maximum available CP violation in the model. When this occurs, the best-fit χ^2 is larger than expected given that the model is pushed up against the boundary at $\delta_{CP} = -\pi/2$, resulting in a smaller $\Delta\chi^2$. For δ_{CP} near -$\pi/2$, the pseudo-experiments where this effect occurs tend to be the ones which populate the 90% and 2σ tails of the distributions, which leads to a reduction in the probability to exclude precisely those values. Whereas, for the case of true $\delta_{CP} = -\pi/2$, these pseudo-experiments appear near $\Delta\chi^2 \approx 0$.

Lastly, from Fig. 9.5c, we see that $\delta_{CP} = 0$ is excluded at 90% CL in about 22% of the pseudo-experiments and the 2σ CL between 1% and 2% of the pseudo-experiments. $\delta_{CP} = \pi$ is excluded in slightly fewer pseudo-experiments than $\delta_{CP} = 0$ in each case, which matches what is seen in the data fit results.

9.2.2 $\delta_{CP} = -1.728$ - Normal Ordering

$\delta_{CP} = -1.728$ in the normal ordering hypothesis is chosen for study as it is the preferred value from the data fit. The results of the study are shown in

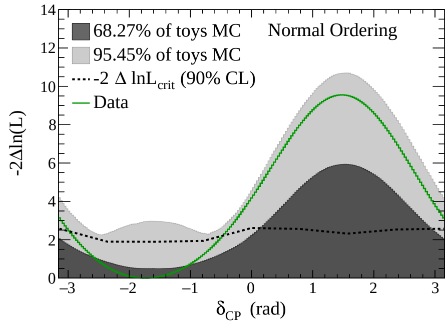

(a) Normal Ordering

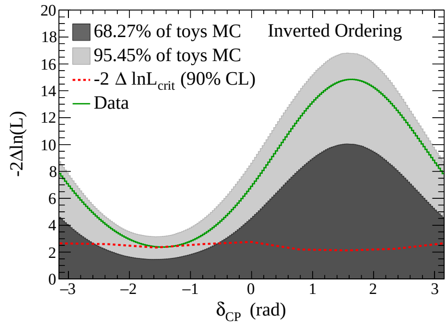

(b) Inverted Ordering

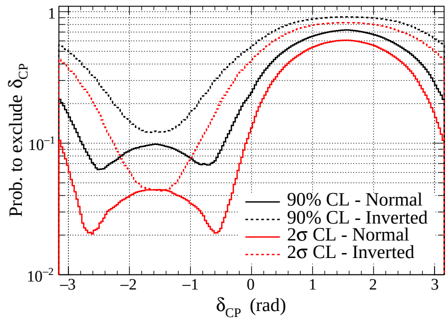

(c) Exclusion probability

Figure 9.5: The distribution of exclusion for an ensemble of pseudo-experiments generated with $\delta_{CP} = -\pi/2$ and normal ordering.

Fig. 9.6. As expected, the overall conclusions match those from the study of the maximal CP violating hypothesis in Sec. 9.2.1. The data exclusion is however slightly more consistent with the ensemble of pseudo-experiments generated with $\delta_{CP} = -\pi/2$ than in this case.

9.2.3 $\delta_{CP} = -\pi/2$ - Inverted Ordering

Considering the clear preference for normal ordering over the inverted ordering, it is important to consider the maximally CP violating model within the inverted ordering hypothesis. A comparison of the data constraint and the statistical ensemble is shown in Fig. 9.7.

The data exclusion of the CP conserving $\delta_{CP} = \pi$ is consistent within a 2σ fluctuation which can be seen in Fig. 9.7a, though the exclusions of $\delta_{CP} = 0$ and $\delta_{CP} = \pi/2$ are beyond the 2σ band. Interestingly, Fig. 9.7b shows that the

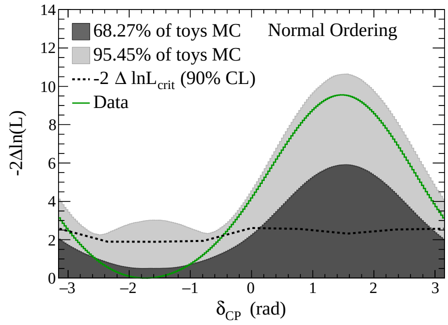

(a) Normal Ordering

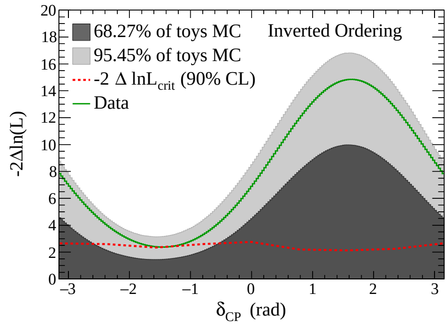

(b) Inverted Ordering

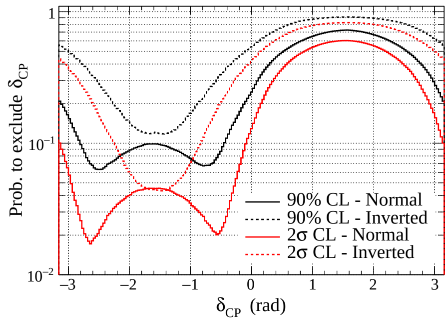

(c) Data χ^2 probability

Figure 9.6: The distribution of exclusion for an ensemble of pseudo-experiments generated with the T2K best-fit point $\delta_{CP} = -1.728$ and normal ordering.

data exclusion of inverted ordering, near $\delta_{CP} = -\pi/2$, is also consistent with the ensemble of pseudo-experiments at the 2σ level. This result is partially aided by the feature, described in Sec. 9.2.1, which causes a small peak in the exclusion probability near $\delta_{CP} = -\pi/2$ when inverted ordering is assumed.

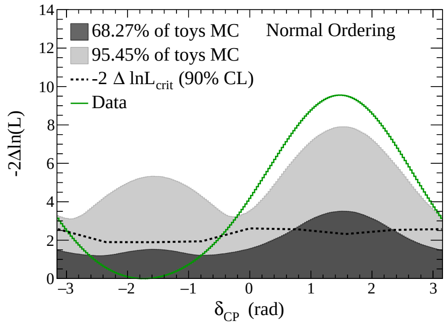

(a) Normal Ordering

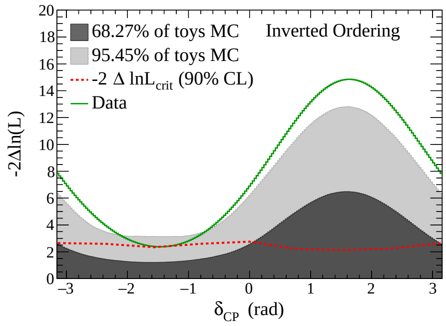

(b) Inverted Ordering

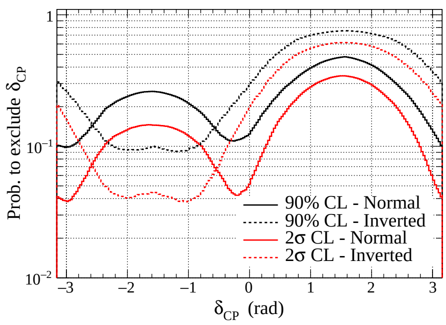

(c) Data χ^2 probability

Figure 9.7: The distribution of exclusion for an ensemble of pseudo-experiments generated with $\delta_{CP} = -\pi/2$ and inverted ordering.

Chapter 10

Supplementary Analyses

This chapter details two studies, which were aimed toward testing the compatibility of PMNS neutrino oscillations and the T2K data set. Although independent from the 5 sample joint analysis presented in this thesis, the results from these studies are complimentary as they provide useful insight into the factors which drive the oscillation constraints in the full analysis. In both studies the analysis technique centred around extending the PMNS formalism and measuring how far the T2K measurements moved into the new non-PMNS region. The first, the search for $\bar{\nu}_e$ appearance, considers the $\bar{\nu}$-mode e-like sample alone to determine if it is consistent with the oscillation model predicted by other T2K samples. The second, the ν_μ and $\bar{\nu}_\mu$ disappearance analysis, is a compatibility test of the ν-mode μ-like and $\bar{\nu}$-mode μ-like samples. An overview of both analyses are given here as a detailed review would be impractical however, more information can be found in [116] and [118].

Both studies do however make use of the same framework used for the joint oscillation analysis and described in Chap. 4. Any modifications which impact the results have been clearly outlined.

10.1 $\bar{\nu}_e$ Appearance

This section describes the search for the first ever measurement of significant $\bar{\nu}_e$ appearance from a $\bar{\nu}_\mu$ beam at T2K. Unlike the search for ν_e appearance, described in [65], the $\bar{\nu}_e$ appearance search suffers from a significant background of appearance events coming from the ν_e contamination. The measurement relies on an accurate prediction of the ν_e component such that any excess can be interpreted as $\bar{\nu}_e$ appearance. The ν-mode e-like, ν-mode μ-like and $\bar{\nu}$-mode μ-like Super-K samples were used, along with the ND280 measurement, to constrain the ν_e component and all other systematic uncertainties throughout the analysis.

The analysis is based around a new parameter, β, which can scale the $\bar{\nu}_e$ appearance probability as such:

$$P(\bar{\nu}_\mu \to \bar{\nu}_e) = \beta \cdot P_{PMNS}(\bar{\nu}_\mu \to \bar{\nu}_e) \tag{10.1}$$

β is introduced as a discreet parameter which can take the values of either 0, which corresponds to no $\bar{\nu}_e$ appearance, or 1, which corresponds to PMNS $\bar{\nu}_e$ appearance. For the analysis β provides cases for two null hypotheses which can be used in p-value tests to determine the consistency of the $\bar{\nu}_e$ data set with no $\bar{\nu}_e$ appearance or the PMNS prediction.

A p-value test requires a test statistic and this analysis makes use of two. The first is simply the number of events observed in the $\bar{\nu}$-mode e-like sample, whereas the second is defined from the marginal likelihood ratio of two alternate hypotheses. The likelihood ratio considers the full 2-dimensional distribution of expected and observed events as used in the joint oscillation analysis. These are labelled as the "Rate-Only" and "Rate+Shape" statistics respectively.

The advantage of using both statistics is that they are at opposite ends of the spectrum of discriminating power available in the T2K analysis. The Rate-Only statistic relies only on an accurate prediction of the total $\bar{\nu}_e$ appearance rate, whereas the Rate+Shape depends upon the event distribution in the reconstructed neutrino energy and outgoing lepton angle. Consequently, the latter is expected to provide stronger statements about $\bar{\nu}_e$ appearance, while the former is less dependent on the shape of the MC expectation.

The Rate+Shape statistic is derived from the marginal likelihood like so:

$$\chi^2_{marg}(\beta) = -2\ln\lambda_{marg}(\beta) = -2\ln\left(\int_A \lambda(\beta;\mathbf{a})\pi(\mathbf{a})d\mathbf{a}\right) \tag{10.2}$$

where the likelihood is converted to $\chi^2_{marg}(\beta)$ for convenience. The difference between this and the marginal likelihood described in Chap. 6 is that all oscillation and systematic parameters other than β are marginalised in Eq. (10.2).

The Rate+Shape statistic is defined to be the marginal χ^2 difference between the two hypotheses as shown in Eq. (10.3).

$$\Delta\chi^2 = \chi^2_{marg}(\beta = 0) - \chi^2_{marg}(\beta = 1) \tag{10.3}$$

Constructed in this way, the statistic has the the power to directly discriminate between the PMNS oscillation ($\beta = 1$) and the no appearance ($\beta = 0$) hypothesis. Another advantage of a statistic of this form is that it is only affected by regions of the samples where $\bar{\nu}_e$ appearance is expected. Although the $\bar{\nu}$-mode e-like, ν-mode e-like, ν-mode μ-like and the $\bar{\nu}$-mode μ-like Super-K samples are used in the construction of the Rate+Shape statistic, there is little discriminating power from the latter three samples due to a negligible contamination of $\bar{\nu}_e$ appearance events either. The predicted breakdown of each sample is given for the joint oscillation analysis in Tab. 5.10. The fractional composition remains applicable for this analysis as the prediction only differs by a POT scale factor for the ν-mode samples. The latter samples do however remain important as they constrain nuisance parameters, which can affect the expected $\bar{\nu}_e$ signal due to correlations during marginalisation.

The marginalisation is performed numerically as described in Chap. 6, however 100,000 throws are used to sample the $\bar{\nu}_e$ appearance likelihood due to the increase in size of the nuisance parameter phase space to 117, including all oscillation parameters and the mass ordering.

10.1.1 MC Ensemble

For both the Rate-Only and Rate+Shape analyses, an MC is used to generate an ensemble of toy experiments, and statistics, for comparison with data. As for the Feldman-Cousins procedure described in Sec. 6.4.1 it is necessary to take the uncertainty on oscillation and systematic parameters into account when constructing an ensemble of MC experiments. A slightly different method is used to incorporate these uncertainties in the $\bar{\nu}_e$ appearance analysis.

The key difference in the $\bar{\nu}_e$ appearance analysis is that three Super-K samples exist which are unaffected by β[1]. They therefore can be employed as control samples to select appropriate MC expectations. A simple accept-reject algorithm is used to select MC toys in the following way:

1. β is fixed to either 0 or 1
2. The maximum likelihood considering the control samples, λ_{max}, is found using MINUIT, a software package which uses the MIGRAD steepest decent algorithm [119]
3. Oscillation and systematic parameters are drawn randomly from the prior distributions listed in Tab. 6.1
4. An MC expectation, MC_{exp} for all four data samples is generated from drawn oscillation and systematic parameters
5. The likelihood is calculated with the control samples $\lambda_{exp}(MC_{exp}|Data)$
6. A random number, R, is drawn between 0 and 1

[1] The $CC\pi^+$ sample was unavailable at the time of this analysis.

7. The MC_{exp} is accepted if $\frac{\lambda_{exp}}{\lambda_{max}} \geq R$, rejected otherwise

8. If accepted, statistical fluctuations are applied on MC_{exp} to generate MC toy data sets

9. The statistic is calculated for each MC toy data set and enters the MC ensemble

With this method, the MC ensemble is filled with MC toy experiments which most closely resemble the observed data in the control samples.

10.1.2 Data Analysed

The data set for the $\bar{\nu}_e$ appearance analysis is a subset of that used for the joint oscillation analysis. This is 7.002×10^{20} POT and 7.471×10^{20} POT in ν-mode and $\bar{\nu}$-mode respectively. This amounts to the total available $\bar{\nu}$-mode data set and greater than 90% of the ν-mode. The near detector data set is the same as that described in Sec. 3.6.

A total of 4 events are observed in the $\bar{\nu}$-mode e-like sample which is slightly greater than the background ($\beta = 0$) MC prediction of 3.219 but less than the PMNS ($\beta = 1$) MC prediction of 6.00. The MC predictions are calculated with the same model parameters as Asimov data set A. The uncertainty on the event rate due to various sources of uncertainty considered in the oscillation analysis can be found in Tab. 5.12.

10.1.3 Rate-Only

As with the oscillation analysis, an Asimov data set is used to assess the sensitivity of the data set of interest. A comparison of the number of events in Asimov data set A with the expected distribution considering the $\beta = 0$ and $\beta = 1$ hypotheses are shown in Fig. 10.1. When comparing the MC ensemble generated under the no oscillation ($\beta = 0$) hypothesis, a right tailed p-value is

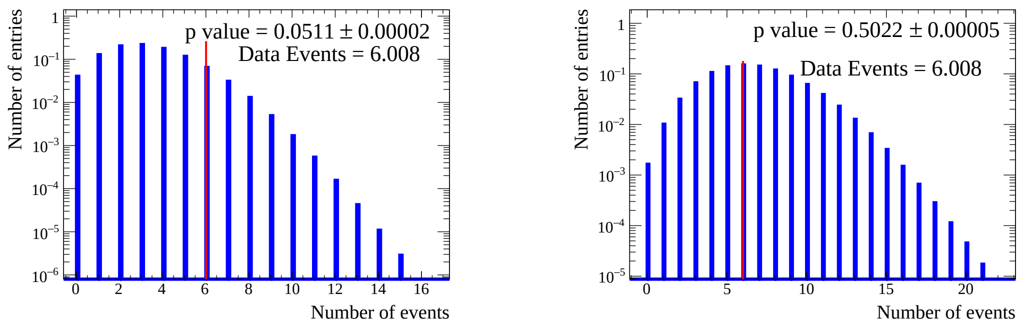

(a) $\beta = 0$ (b) $\beta = 1$

Figure 10.1: The distribution of the number of events in the $\bar{\nu}$-mode e-like sample from the MC ensemble for the no $\bar{\nu}_e$ appearance ($\beta = 0$) and PMNS oscillation ($\beta = 1$) hypotheses. Also shown is the number of events in Asimov data set A and the corresponding p-value with statistical uncertainty from the MC ensemble.

calculated to determine the probability of a fluctuation resulting in a more significant observation than the data. However, a left tailed p-value is calculated when considering the PMNS oscillation ($\beta = 1$) to determine if the observed rate is more background-like than expected.

As expected the Asimov data set is found to be consistent with the PMNS oscillation ($\beta = 1$) hypothesis with a p-value of close to 50%. In the search for $\bar{\nu}_e$ appearance the Asimov data set results in a p-value of roughly 5%, meaning reasonable evidence against the no oscillation ($\beta = 0$) hypothesis is expected from the analysis.

The data comparison, shown in Fig. 10.2, results in a $\bar{\nu}_e$ appearance p-value of 41%. Subsequently, the analysis finds no substantial evidence to reject the hypothesis that there is no $\bar{\nu}_e$ appearance in T2K. As a consequence of the lower than expected event rate in the $\bar{\nu}$-mode e-like sample, a slightly smaller p-value of 22% is found for the PMNS oscillation hypothesis. The result is also not significant enough to provide meaningful evidence.

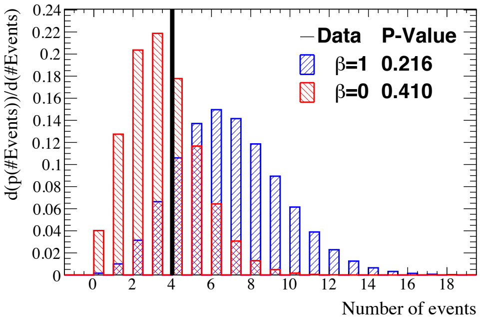

Figure 10.2: The distribution of the number of events in the $\bar{\nu}$-mode e-like sample from the MC ensemble for the no $\bar{\nu}_e$ appearance ($\beta = 0$) and PMNS oscillation ($\beta = 1$) hypotheses. Also shown is the number of events observed in data and the corresponding p-value. The absolute statistical uncertainty on either p-value is less that 0.01%.

10.1.4 Rate+Shape

The Rate+Shape analysis is structured in a similar way to the Rate-Only. Comparisons of the Asimov data set statistic with MC ensembles, from the two oscillation hypotheses, are shown in Fig. 10.3. The Asimov statistic ($\Delta\chi^2 = 2.61$) is found to be consistent with the PMNS oscillation hypothesis, with a p-value of 44%, and provide evidence against the no $\bar{\nu}_e$ appearance hypothesis with a p-value of 4%. As expected, the Rate+Shape analysis is found to be slightly more sensitive than the Rate-Only due to the additional shape information available to discriminate between $\beta = 0$ and $\beta = 1$ models.

The data statistic of -1.93 is compared to the MC ensembles in Fig. 10.4. A p-value of 37% is found for no $\bar{\nu}_e$ appearance ($\beta = 0$) meaning that the data provides no evidence against the hypothesis. When considering the PMNS oscillation ($\beta = 1$) hypothesis, a p-value of 9.9% is found. The conclusion is that the extent to which the no oscillation ($\beta = 0$) hypothesis is preferred over the PMNS oscillation ($\beta = 1$) hypothesis by data is only seen in a fraction of the pseudo

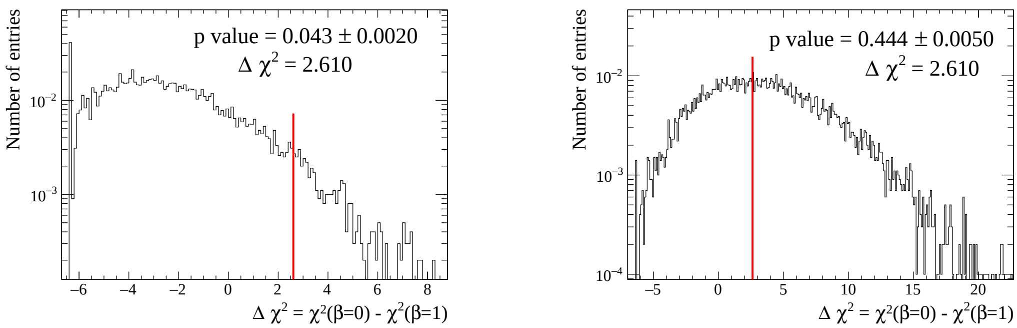

(a) $\beta = 0$ (b) $\beta = 1$

Figure 10.3: The distribution of the Rate+Shape statistic from the MC ensemble for the no $\bar{\nu}_e$ appearance ($\beta = 0$) and PMNS oscillation ($\beta = 1$) hypotheses shown with the statistic from the Asimov data set and the corresponding p-value with statistical uncertainty from the MC ensemble.

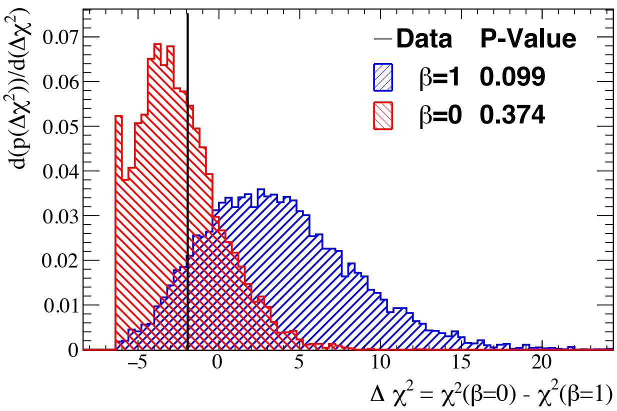

Figure 10.4: The distribution of the Rate+Shape statistic from the MC ensemble for the no $\bar{\nu}_e$ appearance ($\beta = 0$) and PMNS oscillation ($\beta = 1$) hypotheses with the observed statistic from data and the corresponding p-values.

experiments assuming PMNS oscillation. The absolute statistical uncertainty in the no $\bar{\nu}_e$ appearance ($\beta = 0$) and PMNS oscillation ($\beta = 1$) p-values from the MC ensemble is 0.5% and 0.3% respectively.

10.1.5 Bayes Factor

As the $\Delta\chi^2$ statistic considered in this analysis is marginalised over all nuisance parameters the statistic can be interpreted in a Bayesian framework as a Bayes factor. The Bayes factor is a quantity (fully defined by the $\Delta\chi^2$ statistic of the Rate+Shape analysis) that indicates how much the data prefers one hypothesis over another, and can therefore be used as a Bayesian test of alternate hypotheses. It is defined as the marginal likelihood ratio of the two hypotheses in question and is related to the Rate+Shape statistic as shown in Eq. (10.4).

$$\mathbf{B_{01}} = \frac{e^{-\chi^2_{\beta=0}/2}}{e^{-\chi^2_{\beta=1}/2}} = e^{\frac{-\Delta\chi^2}{2}} \tag{10.4}$$

It it important to distinguish between the Bayes factor and the posterior probability here as the Bayes factor contains no information of the prior odds of each $\bar{\nu}_e$ appearance hypothesis. The posterior odds for each hypothesis and the Bayes factor are related by the prior probability ratio as shown in Eq. (10.5).

$$\frac{P_{post}(\beta = 0|Data)}{P_{post}(\beta = 1|Data)} = \mathbf{B_{01}} \cdot \frac{P_{prior}(\beta = 0)}{P_{prior}(\beta = 1)} \tag{10.5}$$

Only for the unique case where the prior probabilities of each hypothesis are equivalent does the Bayes factor equal the posterior probability ratio.

The Bayes factor can be interpreted using the Jeffreys scale [120] to determine how much one hypothesis is preferred over the other. The Asimov data set results in a Bayes factor of 3.69 in favour of the PMNS oscillation hypothesis, which implies weak preference using the Jeffreys scale. The data statistic of -1.930 leads to a Bayes factor of 2.62 which indicates weak preference for the no $\bar{\nu}_e$ appearance ($\beta = 0$) hypothesis over the PMNS oscillation ($\beta = 1$).

Although the Bayes factor signifies a weak preference for the no $\bar{\nu}_e$ appearance ($\beta = 0$) hypothesis it is important to consider the effect of priors. As the $\beta = 0$ hypothesis explicitly breaks PMNS oscillation, and confirmation of such a hypothesis would lead to a re-evaluation of neutrino theory, it is natural to require strong evidence before rejecting the $\beta = 1$ alternative. Assuming an a priori probability that PMNS oscillation is 50 times more likely than the alternate hypothesis yields posterior odds of $\frac{2.62}{50}$ meaning that the PMNS appearance ($\beta = 1$) hypothesis is 20 times more likely than the alternative.

10.1.6 Summary

A summary of the results from the $\bar{\nu}_e$ appearance analysis can be found in Tab. 10.1. The analysis finds no substantial evidence for $\bar{\nu}_e$ appearance from a $\bar{\nu}_\mu$ beam and is unable to reject either the no appearance ($\beta = 0$) or PMNS appearance ($\beta = 1$) hypothesis. A slight preference is found for the no appearance ($\beta = 0$) hypothesis, however both frequentist and Bayesian results indicate that it is not significant. The results are driven by the contrast between the expected number of events in the $\bar{\nu}$-mode e-like sample in the Asimov data set and that observed.

This effect is stronger in the Rate+Shape analysis as the distribution of data events in the sample cause them to appear less signal-like. Comparisons of the data with the prediction from the Asimov data set are shown in Fig. 10.5. Also highlighted in Fig. 10.5 is the separation power between signal and background from the 2-dimensional templates used in the construction of the statistic. This leads to a stronger than expected exclusion of the PMNS appearance ($\beta = 1$) hypothesis in the Rate+Shape analysis due to the fact that two of the four events in the $\bar{\nu}$-mode e-like sample do not fall into the $\bar{\nu}_e$ appearance signal region.

	# Obs	Rate-Only		$\Delta\chi^2$	Rate+Shape		**B_{01}**
		$\beta = 0$	$\beta = 1$		$\beta = 0$	$\beta = 1$	
Asimov A	6	0.0511	0.5022	2.610	0.043	0.444	0.27 (1/3.69)
Data	4	0.410	0.2155	-1.930	0.3742	0.099	2.62

Table 10.1: A summary of observed number of events, the $\Delta\chi^2$, Rate+Shape Bayes factor, and Rate-Only and Rate+Shape p-values for both the Asimov and observed data sets.

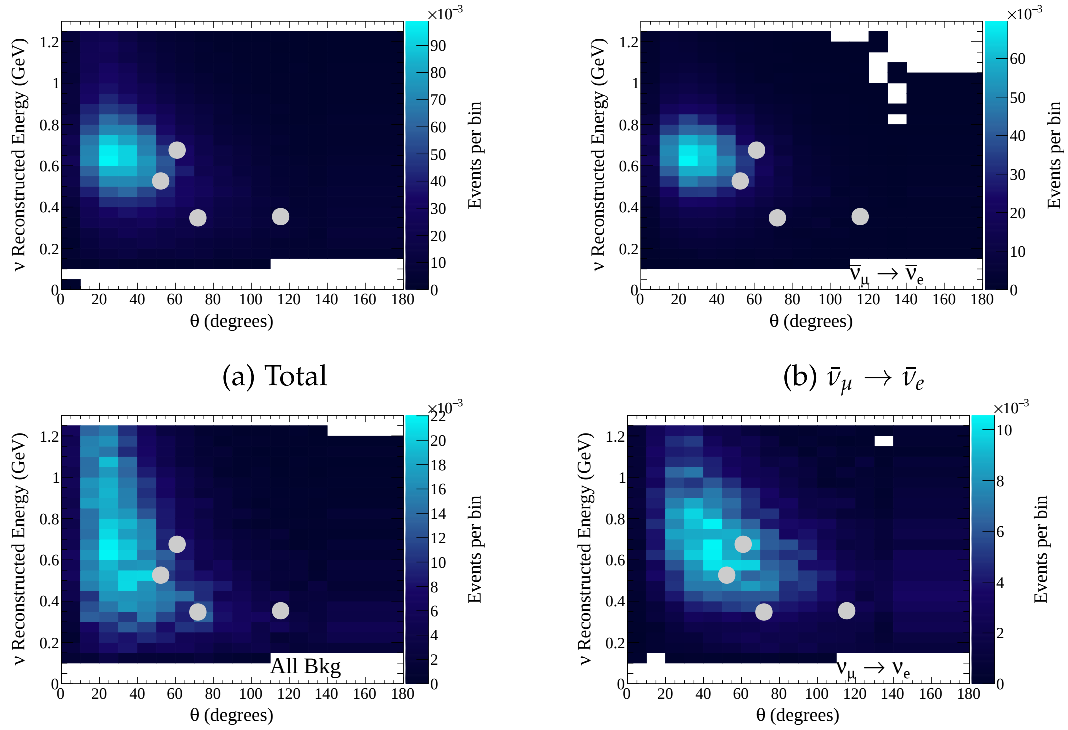

(a) Total

(b) $\bar{\nu}_\mu \rightarrow \bar{\nu}_e$

(c) Neutral current & Beam ν_e

(d) $\nu_\mu \rightarrow \nu_e$

Figure 10.5: A comparison of the expected MC distribution of Asimov data set A and the observed data. The MC is also broken down in terms of true event type for comparison.

10.2 $\bar{\nu}_\mu$-Disappearance

The analysis presented in this section is a simultaneous measurement of ν_μ and $\bar{\nu}_\mu$ disappearance using only the ν-mode μ-like and $\bar{\nu}$-mode μ-like samples. The analysis follows the same procedure as the joint 5 sample oscillation analysis and only key differences are outlined here in the interest of brevity.

Within the standard PMNS oscillation framework, CPT invariance results in identical ν_μ and $\bar{\nu}_\mu$ disappearance probabilities. The aim of this analysis is to determine if the disappearance observed in the ν-mode μ-like and $\bar{\nu}$-mode μ-like samples could be explained by the same oscillation probabilities, and therefore is a test for CPT violation or other beyond standard model effects apparent in the T2K data. Additional degrees of freedom are included in the analysis which allow for differing disappearance probabilities for ν_μ and $\bar{\nu}_\mu$ and conclusions drawn on how much the T2K data explore the extended region.

To achieve this effect the oscillation framework in the analysis is extended from the standard PMNS oscillation in such a way to allow for distinct ν_μ and $\bar{\nu}_\mu$ disappearance oscillation parameters. As the dominant parameters that determine the ν_μ disappearance probability at T2K are $\sin^2\theta_{23}$ and Δm^2_{32}, new parameters $\sin^2\bar{\theta}_{23}$ and $\Delta\bar{m}^2_{32}$ are introduced so that the former only affect the ν_μ probability and the latter the $\bar{\nu}_\mu$ probability. Therefore, any discrepancy between $\sin^2\theta_{23}$ and $\sin^2\bar{\theta}_{23}$ or Δm^2_{32} and $\Delta\bar{m}^2_{32}$ can be interpreted as new physics.

The appearance samples were intentionally left out of the analysis in order to eliminate any effects of the CP violation, from the ν_e and $\bar{\nu}_e$ appearance probabilities allowed in the PMNS framework, from the search for physics beyond the PMNS, such as CPT violation.

The motivation of a simultaneous fit of both ν-mode μ-like and $\bar{\nu}$-mode μ-like data sets is a consequence of the non-negligible neutrino background in the $\bar{\nu}$-mode μ-like sample, detailed in Tab. 5.10. The contamination means that the

Parameter(s)	Prior	Range
$\sin^2\theta_{23}$	Uniform	$[0.3; 0.7]$
$\sin^2\bar{\theta}_{23}$	Uniform	$[0.3; 0.7]$
$\sin^2 2\theta_{13}$ ($\sin^2\theta_{13}$)	Gauss	0.085 ± 0.005
$\sin^2 2\theta_{12}$	Gauss	0.846 ± 0.021
$\lvert\Delta m^2_{32}\rvert$ (NO) / $\lvert\Delta m^2_{13}\rvert$ (IO)	Uniform	$[2; 3] \times 10^{-3}$ eV^{2}c^{-4}
$\lvert\Delta \bar{m}^2_{32}\rvert$ (NO) / $\lvert\Delta \bar{m}^2_{13}\rvert$ (IO)	Uniform	$[2; 3] \times 10^{-3}$ eV^{2}c^{-4}
Δm^2_{21}	Gauss	$(7.53 \pm 0.18) \times 10^{-5}$ eV^{2}c^{-4}
δ_{CP}	Fixed	0
Mass Ordering	Fixed	Normal or Inverted

Table 10.2: Oscillation parameter priors.

neutrino oscillation parameters $\sin^2\theta_{23}$ and Δm^2_{32} can have a noticeable effect on the $\bar{\nu}$-mode μ-like sample expectation, and therefore there exists a need to constrain them when they are considered to be nuisance parameters. Following the priors used in the joint 5 sample analysis, those used in this analysis are listed in Tab. 10.2. Uniform priors are chosen for the additional anti-neutrino oscillation parameters in accordance with the neutrino parameters. Consequently, when fitting the anti-neutrino parameters $\sin^2\bar{\theta}_{23}$ and $\Delta\bar{m}^2_{32}$, the ν-mode μ-like sample is used as a control sample to constrain the background. The same is not required when fitting the neutrino parameters as the ν-mode μ-like sample has a negligible contamination of anti-neutrino events. Additionally, δ_{CP} is fixed in the analysis as it has very little effect on the μ-like samples at Super-K as shown in Fig. 7.3.

This analysis makes use of the total available T2K data set as described in Sec. 3.6.

Parameter(s)	Asimov F
$\sin^2\theta_{23}$	0.528
$\sin^2\bar{\theta}_{23}$	0.45
$\sin^2 2\theta_{13}$ ($\sin^2\theta_{13}$)	0.085 (0.0217)
$\sin^2 2\theta_{12}$	0.846
$\lvert\Delta m^2_{32}\rvert$ (NO) / $\lvert\Delta m^2_{31}\rvert$ (IO)	2.509×10^{-3} eV^{2}c^{-4}
$\lvert\Delta\bar{m}^2_{32}\rvert$ (NO) / $\lvert\Delta\bar{m}^2_{31}\rvert$ (IO)	2.509×10^{-3} eV^{2}c^{-4}
Δm^2_{21}	7.53×10^{-5} eV^{2}c^{-4}
δ_{CP}	0
Mass Ordering	Normal

Table 10.3: Oscillation parameter values for $\bar{\nu}_\mu$-disappearance sensitivity studies.

10.2.1 Sensitivity

The expected sensitivity is assessed through a fit to an Asimov data set F, generated within the extended PMNS space as shown in Tab. 10.3. The parameters for the data set are chosen based on the results of previous analyses which found that the ν-mode data preferred maximal mixing in the 2-3 sector whereas the $\bar{\nu}$-mode preferred non-maximal [121]. The analysis contains four parameters of interest, and as a result there are multiple 2-D projections of the marginal χ^2 which can be used to infer physics results.

A comparison of the conventional $\sin^2\theta_{23}$ vs Δm^2_{32} CL contours and $\sin^2\bar{\theta}_{23}$ vs $\Delta\bar{m}^2_{32}$ CL contours is shown for Asimov data set F in Fig. 10.6. The choice of parameter values for $\sin^2\theta_{23}$ and $\sin^2\bar{\theta}_{23}$ is apparent from the result as the anti-neutrino data set prefers a value of $\sin^2\bar{\theta}_{23}$ away from maximal mixing. Although the best-fit point found for $\sin^2\bar{\theta}_{23}$ is in the upper octant, this analysis has little sensitivity to the octant and the corresponding point in the lower octant has a $\Delta\chi^2$ value of below 10^{-2}. Another feature, apparent from Fig. 10.6, is the large uncertainty on the $\bar{\nu}$ parameters. This is primarily due to the low statistics of the $\bar{\nu}$-mode μ-like sample and the fact that data falls further away from the physical boundary of maximal disappearance, but also partly caused by slightly larger systematic uncertainties shown in Fig. 5.8. Comparison of the ν and $\bar{\nu}$ parameter CL contours shows that the $\bar{\nu}$ data set prefers an off maximal value of $\sin^2\theta_{23}$, however the size of the $\bar{\nu}$ CL contour makes it difficult to draw any strong conclusions from the result.

The preference of the data to explore the extended oscillation parameter region is better displayed in Fig. 10.7, where the likelihood is projection onto the surface of $\sin^2\theta_{23}$ vs $\sin^2\bar{\theta}_{23}$ and Δm^2_{32} vs $\Delta\bar{m}^2_{32}$. Each figure contains a guide line $x = y$ along which the oscillation behaves as PMNS. Any deviation from the line, and in particular significant exclusion of it, would be a strong indication of new physics in the T2K data set. The results from the Asimov fit do not indicate new physics in the way expected. The mass splitting measurement shows perfect agreement with the PMNS model hypothesis as expected, however the θ_{23} mixing measurement, although finding a best-fit point away from PMNS oscillation, is consistent with it at the 68% CL.

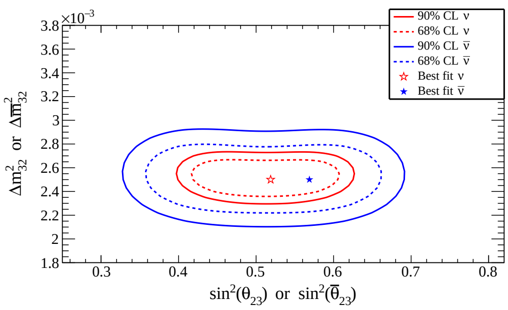

(a) Normal ordering

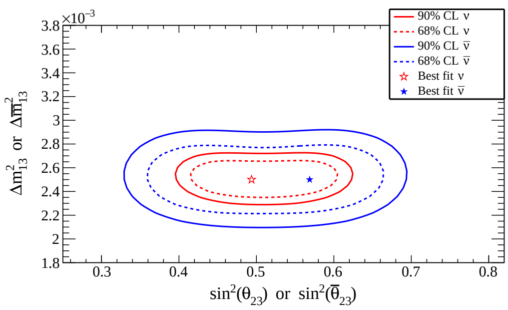

(b) Inverted ordering

Figure 10.6: A comparison of the $\sin^2\theta_{23}$ vs Δm^2_{32} and $\sin^2\bar{\theta}_{23}$ vs $\Delta\bar{m}^2_{32}$ measurements from a fit to Asimov data set F.

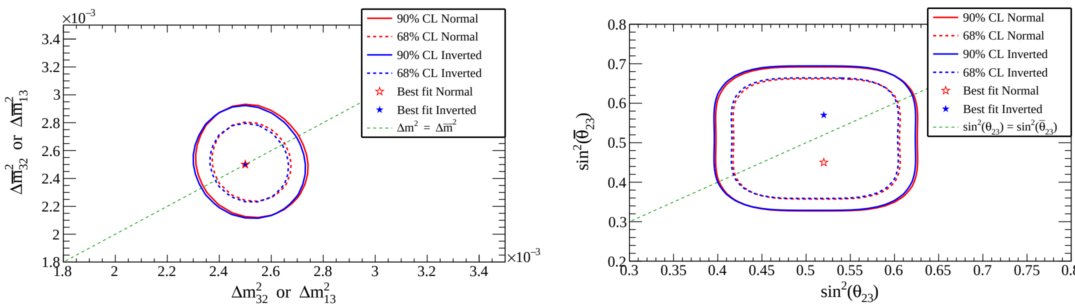

(a) $\Delta\bar{m}^2_{32}$ vs Δm^2_{32} (b) $\sin^2\bar{\theta}_{23}$ vs $\sin^2\theta_{23}$

Figure 10.7: 2D measurements of the parameters Δm^2_{32} vs $\Delta\bar{m}^2_{32}$ and $\sin^2\theta_{23}$ vs $\sin^2\bar{\theta}_{23}$ from a fit to Asimov data set F.

10.2.2 Data Fit

The marginal best-fit spectra, made with the procedure described in Sec. 8.3, are shown in Fig. 10.8. The parameters $\sin^2\theta_{23}$ and Δm^2_{32} ($\sin^2\bar{\theta}_{23}$ and $\Delta\bar{m}^2_{32}$) were fixed and all others marginalised in the construction of the ν-mode μ-like ($\bar{\nu}$-mode μ-like) best-fit spectrum. It is clear how the data points around the oscillation dip drive the measurement of $\sin^2\theta_{23}$ in both ν-mode and $\bar{\nu}$-mode. The ν-mode μ-like sample contains at least two data points which are below the best-fit prediction whereas the opposite is true for the $\bar{\nu}$-mode μ-like.

The results of the data fit are shown in Figs. 10.9 and 10.10. The features follow from those observed in the fit to the Asimov data set. The ν parameters have a noticeably smaller 90% CL contour due to fewer than expected events near the oscillation dip which leads to a preference for beyond maximal disappearance in the ν-mode μ-like data set. The $\bar{\nu}$ parameter contours appear to be beginning to exclude regions with maximal mixing, however remain completely compatible with the ν parameters over a large area of the phase space. The CL contours of Δm^2_{32} vs $\Delta\bar{m}^2_{32}$, shown in Fig. 10.10a, are very consistent with those from the Asimov fits and do not indicate any preference for physics beyond PMNS oscillation.

The fit of $\sin^2\theta_{23}$ vs $\sin^2\bar{\theta}_{23}$, shown in Fig. 10.10b, is also consistent with that from the Asimov data set however contains an interesting feature near $\sin^2\bar{\theta}_{23}$= 0.5. Both 90% and 68% CL contours are pulled inwards as the $\bar{\nu}$-mode μ-like data set begins to disfavour some regions of maximal disappearance. Although not significant at this time, if the trend were to continue, a large area of the space which is consistent with the PMNS hypothesis could be excluded at 68% CL.

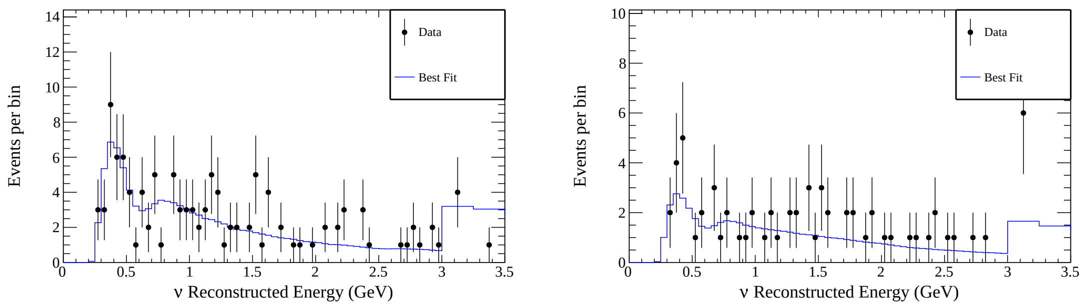

(a) ν-mode (b) $\bar{\nu}$-mode

Figure 10.8: Shown are the best-fit ν-mode and $\bar{\nu}$-mode spectra overlaid with the observed data.

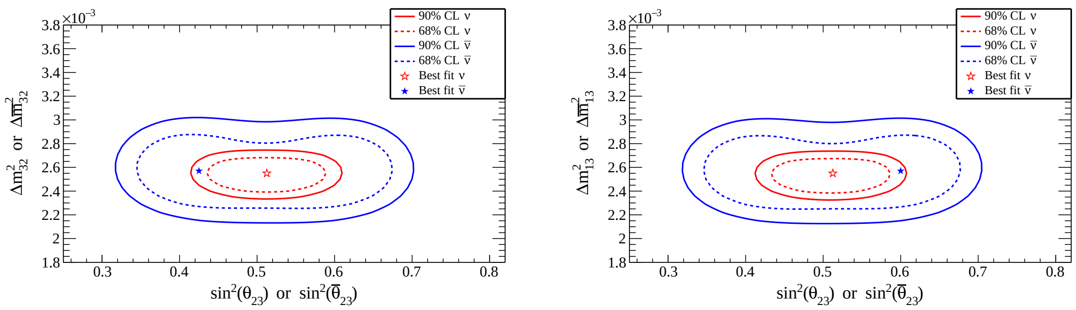

(a) Normal (b) Inverted

Figure 10.9: A comparison of the $\sin^2\theta_{23}$ vs Δm^2_{32} and $\sin^2\bar{\theta}_{23}$ vs $\Delta\bar{m}^2_{32}$ measurements from a the data fit.

10.2.3 Summary

No evidence of physics beyond standard PMNS oscillation is found in the analysis. A slight tension is observed between the ν-mode μ-like and $\bar{\nu}$-mode μ-like data sets where a non-maximal value of $\sin^2 2\theta_{23}$ is preferred by the $\bar{\nu}$-mode sample, but maximal is preferred by the ν-mode sample. However, the tension is

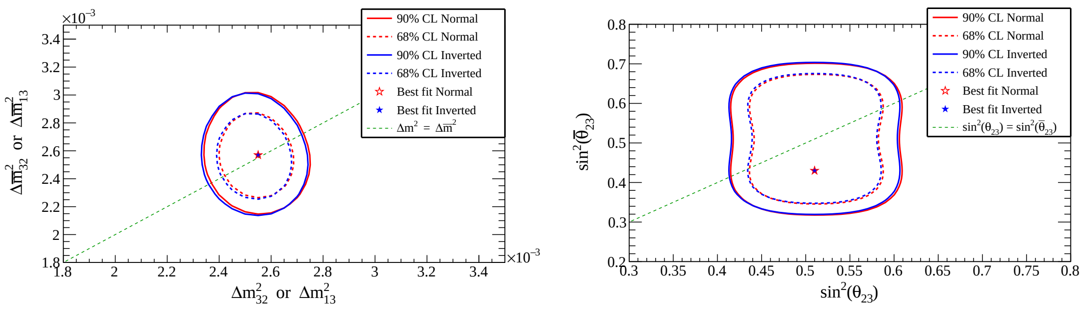

(a) $\Delta\bar{m}^2_{32}$ vs Δm^2_{32}

(b) $\sin^2\bar{\theta}_{23}$ vs $\sin^2\theta_{23}$

Figure 10.10: 2D measurements of the parameters Δm^2_{32} vs $\Delta\bar{m}^2_{32}$ and $\sin^2\theta_{23}$ vs $\sin^2\bar{\theta}_{23}$ from the data fit.

not significant as the 68% CL contours for the ν and $\bar{\nu}$ parameters in this analysis were very consistent with one another.

As the fit to the $\bar{\nu}$-mode μ-like data set is dominated by the oscillation parameters $\sin^2\bar{\theta}_{23}$ and $\Delta\bar{m}^2_{32}$, the measurement can be used in a direct comparison with other experiments observing $\bar{\nu}_\mu$ disappearance. A comparison with the Super-K atmospheric and MINOS measurements are shown in Fig. 10.11. Although the Super-K data set prefers maximal disappearance at $\sin^2\theta_{23}= 0.5$, and T2K and MINOS prefer non-maximal, a large overlap between all the $\bar{\nu}_\mu$ confidence contours from all three experiments highlights the compatibility of the measurements.

10.3 Conclusions

In summary neither analysis presented in this chapter found substantial evidence for physics beyond PMNS oscillations in the T2K data. As both analyses are reliant on statistically limited $\bar{\nu}$-mode data sets, stronger statements could however be made given more data in the future. Even though the results found were not significant in either case, the willingness of the data fits to explore the regions beyond PMNS oscillation is interesting in the context of the 5 sample joint oscillation analysis. When restricted to the PMNS oscillation region any

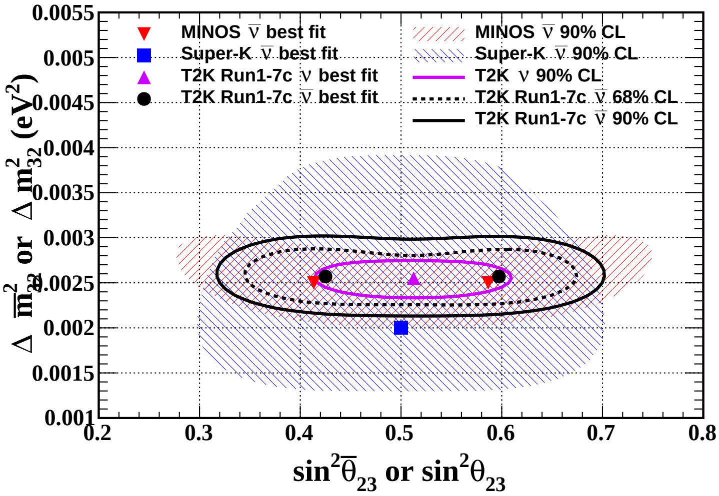

Figure 10.11: A comparison of $\sin^2\theta_{23}$ vs Δm^2_{32} $\bar{\nu}_\mu$ data set confidence regions from T2K, Super-K [122] and MINOS [123]. The T2K ν_μ data set measurement is shown for comparison and Normal ordering is assumed for all measurements.

physics beyond the PMNS can cause unexpected results on parameters in the analysis. This is the case for any additional ν vs $\bar{\nu}$ asymmetry as δ_{CP} remains the only parameter able to facilitate this in the PMNS model. Fortunately there does not appear to be any significant additional ν vs $\bar{\nu}$ asymmetry in either analysis presented here.

Chapter 11

Model Bias Studies

This chapter describes a set of studies which were performed to validate the oscillation analysis against potential bias as a result of model dependant assumptions for neutrino interactions. A full review of the work can be found in [124] and a summary is also available in [116].

At its core, the T2K oscillation analysis requires a neutrino interaction model to make predictions for the observables at Super-K, this is denoted as the analysis model. Although much work has been done to include systematic uncertainties which cover a variety of predictions, as described in Sec. 4.3, there are some limitations which require further study. The aim of these studies was to determine the extent to which incorrect modelling of neutrino interactions at T2K can affect the oscillation analysis results.

Alternative models were chosen based on their availability and the degree to which they affect the prediction at Super-K. Those which were found to have the largest impact on the oscillation analysis are described here.

To perform the studies, alternative T2K MC data sets were generated for all ND280 and Super-K samples under a given oscillation hypothesis. Each alternative data set was then passed through the full T2K analysis chain as was done with the Asimov data sets. The resulting constraints on oscillation parameters were studied to determine if the T2K analysis was robust enough to accept the alternative data set.

The results from the alternative data fits were compared to the result when the analysis model was identical to the MC data set, labelled as the nominal fit. All studies shown here were performed under the T2K best fit oscillation hypothesis shown in Tab. 11.1.

$\sin^2\theta_{23}$	$\sin^2\theta_{13}$	$\sin^2\theta_{12}$	δ_{CP}	Δm^2_{32}	Δm^2_{21}	Ordering
0.532	0.02198	0.304	-1.767	2.537×10^{-3}	7.53×10^{-5}	Normal

Table 11.1: Oscillation parameter set used for the alternative model studies.

11.1 Martini 2p-2h

The T2K 2p-2h analysis model, described in Sec. 4.2.2, comes from a calculation made by Nieves et. al.. Martini et. al. make an alternative prediction for the multi-nucleon contribution to the cross-section described in [106]. A comparison of the predicted 2p-2h cross-section on Carbon is shown in Fig. 11.1. The cross-section, predicted by Martini et. al., is much larger over the T2K energy range for both ν and $\bar{\nu}$. The contrast between the ν and $\bar{\nu}$ predictions is however potentially problematic for a δ_{CP} measurement as it introduces an additional ν_e vs $\bar{\nu}_e$ appearance imbalance.

A comparison of the ND280 fit prediction including systematic uncertainty fro them the ND280 constraint, from a fit to the alternative model, and the alternative model expectation for the Super-K appearance samples is shown in Fig. 11.2. The ND280 fit prediction is represented by a band which shows the standard deviation of the event rate in each bin due to systematic uncertainties. Although the alternative 2p-2h model is well predicted by the ND280 fit in $\bar{\nu}$-mode, the ν-mode prediction is slightly low, especially at the low energy end

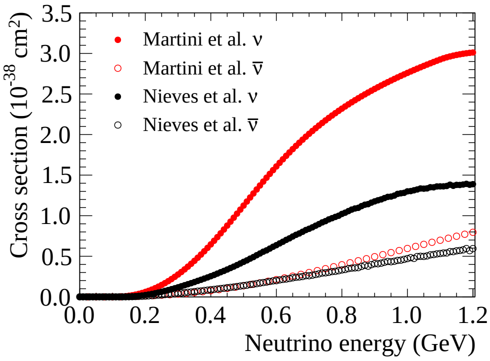

Figure 11.1: Predictions of the 2p-2h interaction cross-section from Martini et. al. and Nieves et. al. Figure taken from [116].

of the spectra. This under-prediction is what is subsequently covered by the oscillation parameters.

Results of fits to the alternative Martini et. al 2p-2h data set are shown in Fig. 11.3. The result of incorrect model assumptions in the fit is most apparent in Fig. 11.3a where the exclusion of $\delta_{CP} = \pi/2$ is larger by approximately one unit of $\Delta\chi^2$ when compared to the nominal fit. The effect is also visible in the 2-dimensional contours, shown in Figs. 11.3c and 11.3d, where the alternative data contour is much tighter than the nominal. The fit results appear consistent with the comparison of predictions seen in Fig. 11.2. The under-prediction in the appearance sample event rate results in a stronger exclusion of low values of $\sin^2\theta_{13}$ which is seen in Fig. 11.3c. This observed model bias is not restricted to δ_{CP} and $\sin^2\theta_{13}$ but appears to a limited extent when considering other parameters as shown in Fig. 11.3b.

11.2 Nieves 1p-1h

Nieves et. al. propose an alternative 1p-1h interaction model to the analysis model implemented in NEUT. The alternative 1p-1h data set was generated, based on a comparison of the NEUT and Nieves et. al. predictions, as a function of the true neutrino energy and outgoing lepton angle. The prediction of the mo-

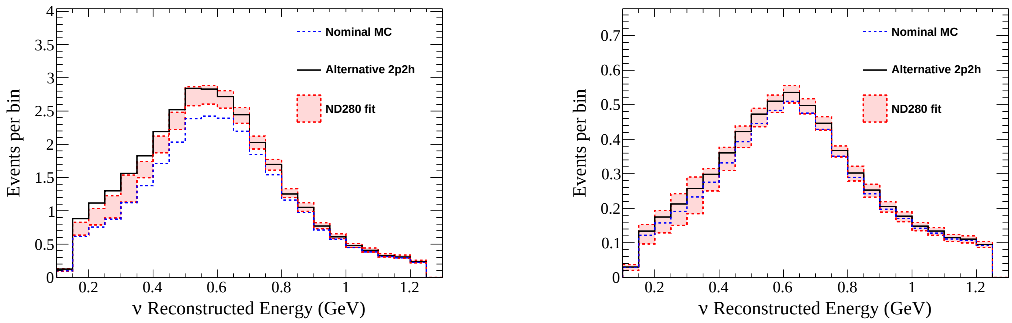

(a) CCQE ν-mode (b) CCQE $\bar{\nu}$-mode

Figure 11.2: Comparison of the ND280 fit prediction including systematic uncertainty and the expectation at Super-K for the Martini et. al. 2p-2h model. The nominal MC is also shown for reference.

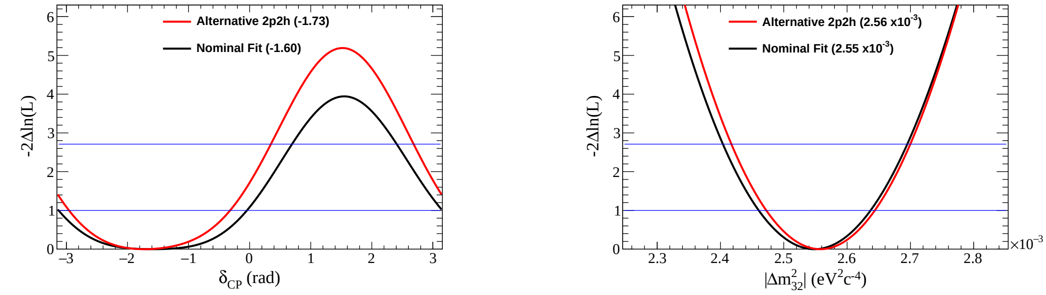

(a) δ_{CP} w/ Reactors (b) Δm^2_{32} w/ Reactors

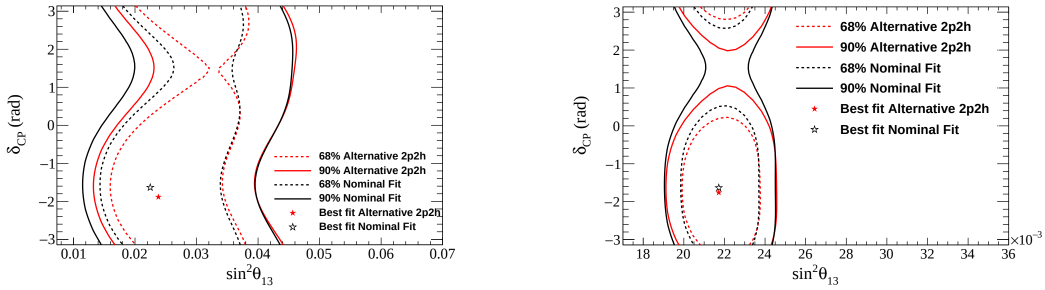

(c) δ_{CP} vs $\sin^2\theta_{13}$ w/o Reactors (d) δ_{CP} vs $\sin^2\theta_{13}$ w/ Reactors

Figure 11.3: Results of fits to the alternative Martini et. al. model.

mentum of the outgoing lepton was found to be the primary difference between the two models. The alternative data set was therefore created by providing additional momentum "kick" to the reconstructed lepton momentum of each NEUT generated event.

A comparison of the ND280 fit prediction including systematic uncertainty and the expected data at Super-K are shown in Fig. 11.4. The difference between the Nieves et. al. and the analysis model is apparent in all spectra. There is an over-prediction at lower reconstructed neutrino energy and over-prediction at higher energies from the ND280 fit in the e-like samples, effectively appearing as the entire spectrum shifted to higher neutrino energy when compared with the prediction. The conclusion is the same in the μ-like samples however the effect on the prediction is slightly different. As the predicted spectra appear shifted to lower reconstructed neutrino energy there is an under-prediction at the low energy end of the oscillation dip and an over-prediction at the higher.

The effects of these incorrect predictions is most apparent in the measurement of Δm^2_{32}, shown in Figs. 11.5a and 11.5b. Although the constraint on Δm^2_{32} is consistent with the nominal fit, there appears to be a bias of $0.018 \times 10^{-3} eV^2 c^{-4}$, approximately 10% of the 68% confidence interval. Fig. 11.5b also highlights how $\sin^2\theta_{23}$ is unaffected and the bias is localised to Δm^2_{32}.

Results of the fits to the alternative data set are shown in Fig. 11.5. The effect on δ_{CP} is shown in Figs. 11.5c and 11.5d, the alternative 1p-1h data fit results in a weaker constraint on δ_{CP}. This is mainly due to the fact that the fit to the alternative data set finds a best-fit further away from maximum CP violation when compared to the nominal fit. This effect is expected given the slight correlation between δ_{CP} and Δm^2_{32}, particularly due to the $\cos\delta_{CP}$ terms in the oscillation formula, which are not CP violating, but can move the appearance peak as shown in Fig. 7.3. Although the δ_{CP} minima found in the two fits are 0.6 rad apart, the likelihood is very flat around $\delta_{CP} = -\pi/2$ and therefore the results are consistent.

11.3 2p-2h Shape

Incorrect modelling of the 2p-2h contribution has been known to bias the neutrino energy reconstruction, especially when Cherenkov light is used in the detection method [125]. The Nieves et. al. 2p-2h analysis model implemented in

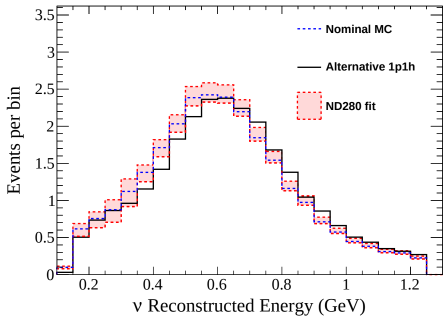

(a) CCQE ν-mode

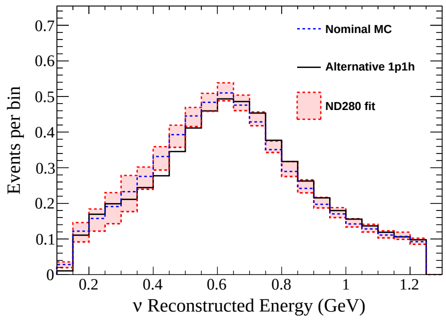

(b) CCQE $\bar{\nu}$-mode

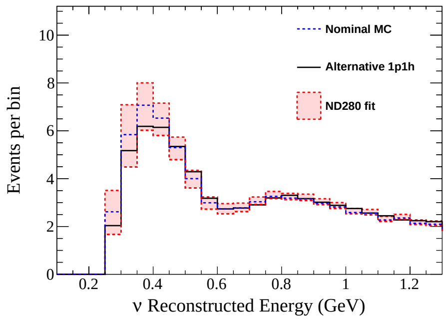

(c) CCQE ν-mode

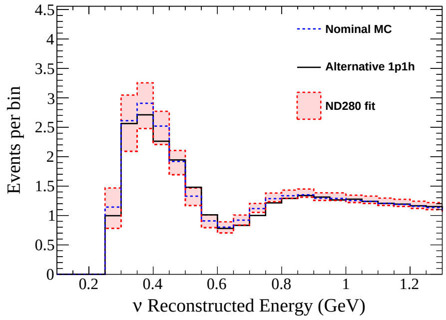

(d) CCQE $\bar{\nu}$-mode

Figure 11.4: Comparison of the ND280 fit prediction including systematic uncertainty and the expectation at Super-K for the Nieves et. al. 1p-1h model. The nominal MC is also shown for reference.

NEUT is made from two key components. These are enhancements in the neutrino interaction cross-section attributed to meson exchange currents and that attributed to nucleon-nucleon correlations. As the two components cause different biases on the CCQE energy reconstruction used on T2K, an incorrect prediction of the relative proportion of each can lead to an overall bias in the prediction.

Two alternative data sets, from each extreme case, were considered to estimate the level of bias from this effect. The "Δ-enhanced 2p-2h", which is made purely from meson exchange current events; and the "not-Δ 2p-2h", from nucleon-nucleon correlation events. A comparison of the reconstruction bias from the two alternative data sets is shown in Fig. 11.6. In both cases the alternative data set was produced by reweighting the Nieves et. al. model, which contains both types of interactions, as a function of the true neutrino energy, the outgoing lepton angle and outgoing lepton momentum.

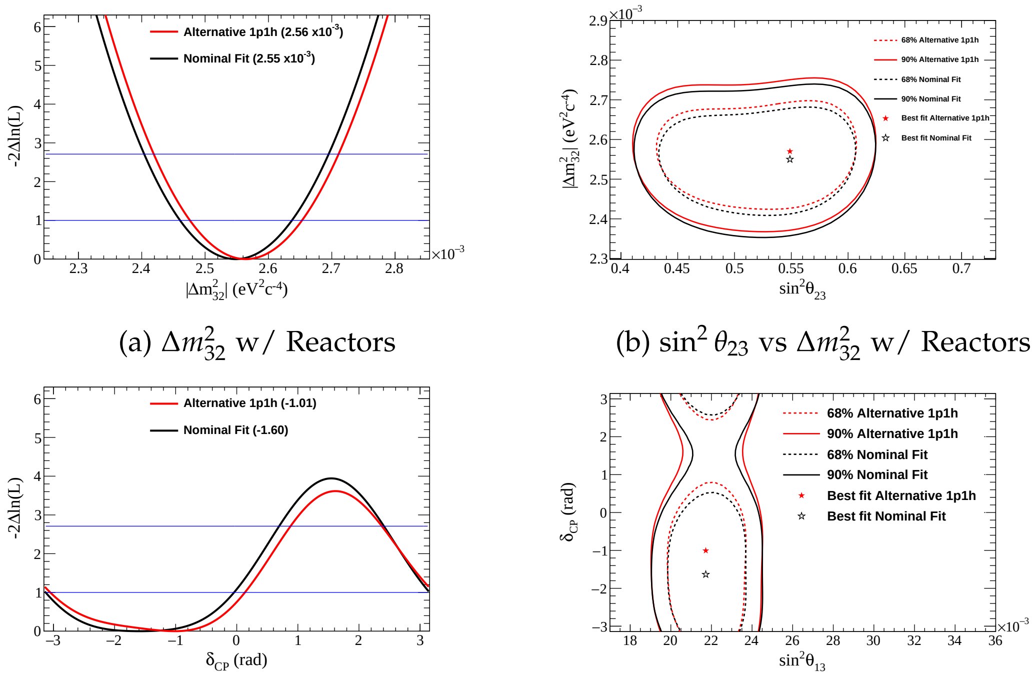

(a) Δm^2_{32} w/ Reactors

(b) $\sin^2\theta_{23}$ vs Δm^2_{32} w/ Reactors

(c) δ_{CP} w/ Reactors

(d) δ_{CP} vs $\sin^2\theta_{13}$ w/ Reactors

Figure 11.5: Results of fits to the alternative Nieves et. al 1p-1h model.

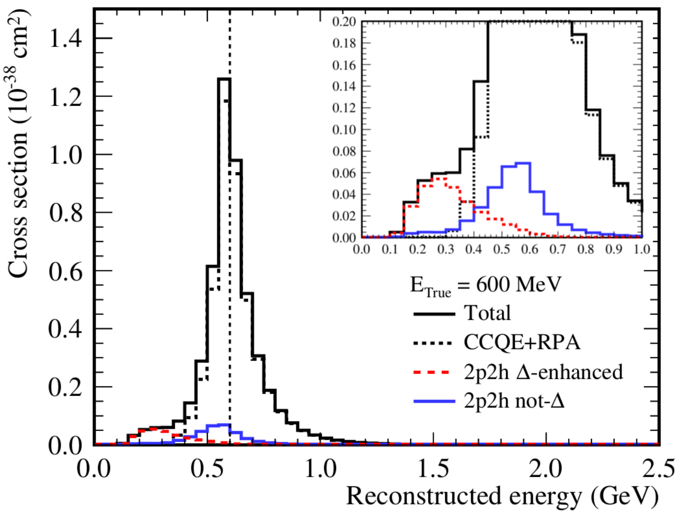

Figure 11.6: Reconstructed neutrino energy, using the CCQE formula, for 600 MeV CCQE and 2p-2h interactions on ^{12}C. The 2p-2h events are taken from the Δ-enhanced and not-Δ alternative models. Figure taken from [116].

11.3.1 Δ-Enhanced 2p-2h

Comparisons of the ND280 predictions and alternative data expectations for the μ-like data sets are shown in Fig. 11.7. In all cases the expected alternative data is within the errors of the ND280 prediction. Only around the high energy region of the ν-mode μ-like sample does the expectation approach the upper edge of the prediction.

The resulting fits which show the largest deviation from the nominal are shown in Fig. 11.8. The largest effect is on the disappearance parameters $\sin^2\theta_{23}$ and Δm^2_{32}. The Δ-enhanced 2p-2h fit results in a weaker constraint on Δm^2_{32}, and a preference for slightly more non-maximal mixing. The effect on the δ_{CP} fit, shown in Fig. 11.8d, is insignificant.

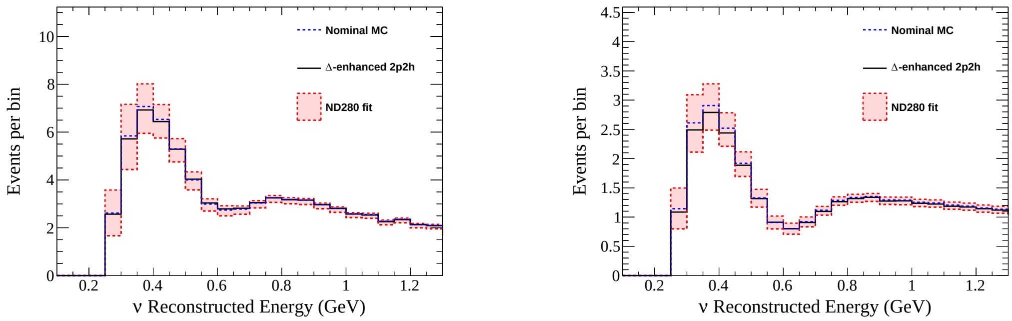

(a) CCQE ν-mode

(b) CCQE $\bar{\nu}$-mode

Figure 11.7: Comparison of the ND280 fit prediction including systematic uncertainty and the expectation at Super-K for the Δ-enhanced 2p-2h model. The nominal MC is also shown for reference.

11.3.2 Not-Δ 2p-2h

Comparisons of the ND280 predictions and alternative data expectations for the μ-like data sets are shown in Fig. 11.9. As is the case for the Δ-enhanced 2p-2h data fits, disagreement is only observed in the ν-mode μ-like sample. In this case however, the alternative data expectation is at the lower end of the prediction. As expected, this causes the opposite effect in the oscillation results, shown in Fig. 11.10. The not-Δ 2p-2h alternative data set fit prefers more maximal mixing than what is found in the nominal fit. The Δm^2_{32} constraint is also narrower than in the nominal fit, as expected from the correlation between Δm^2_{32} and $\sin^2\theta_{23}$. The appearance results remain unaffected by the alternative data fit.

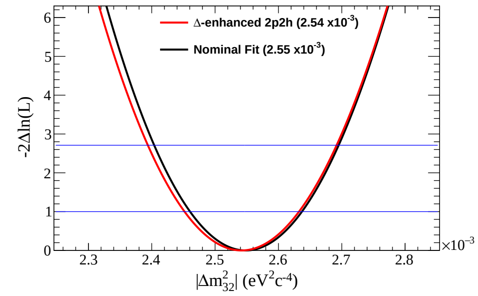

(a) Δm^2_{32} w/ Reactors

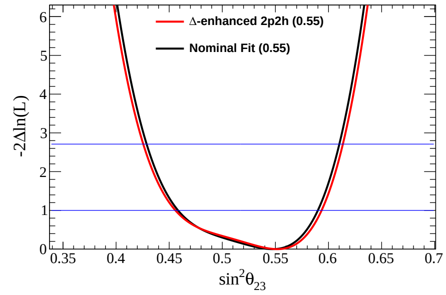

(b) $\sin^2\theta_{23}$ w/ Reactors

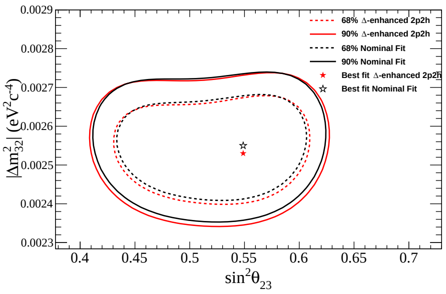

(c) $\sin^2\theta_{23}$ vs Δm^2_{32} w/ Reactors

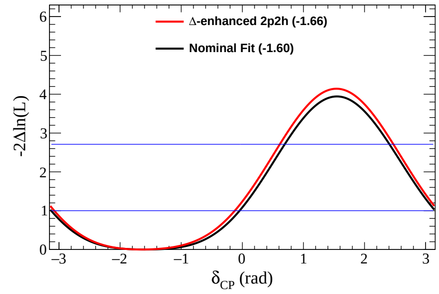

(d) δ_{CP} w/ Reactors

Figure 11.8: Results of fits to the alternative Δ-enhanced 2p-2h model.

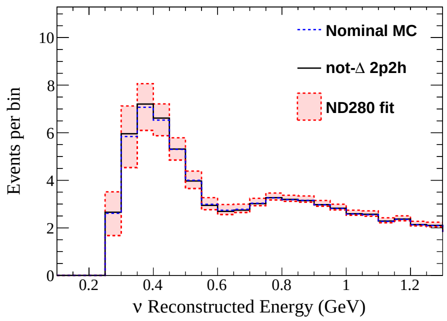

(a) CCQE ν-mode

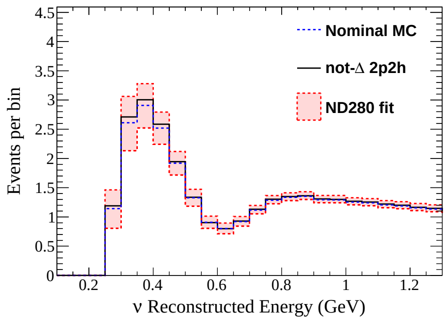

(b) CCQE $\bar{\nu}$-mode

Figure 11.9: Comparison of the ND280 fit prediction including systematic uncertainty and the expectation at Super-K for the not-Δ 2p-2h model. The nominal MC is also shown for reference.

11.4 Conclusions

Extensive studies were performed on many alternative data sets and no significant biases, with respect to the nominal fit, were observed in almost all cases. The largest effect on oscillation parameter extraction was found to come when considering the Nieves et. al. 1p-1h and Martini et. al. 2p-2h data sets. For

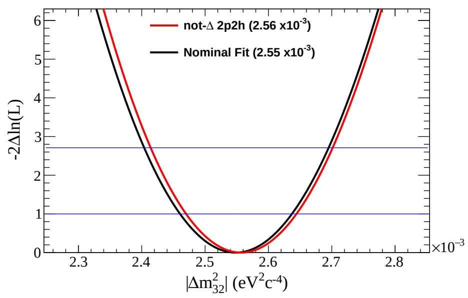

(a) Δm^2_{32} w/ Reactors

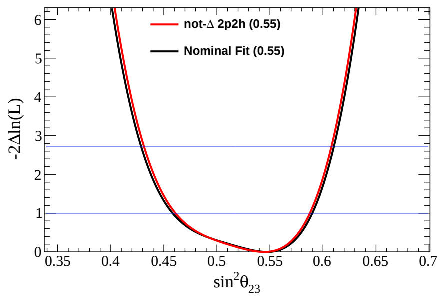

(b) $\sin^2\theta_{23}$ w/ Reactors

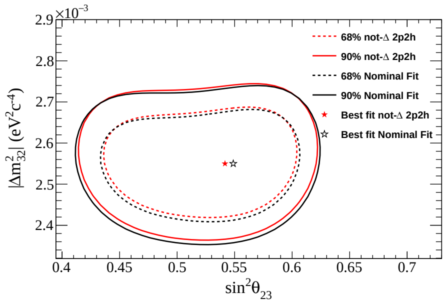

(c) $\sin^2\theta_{23}$ vs Δm^2_{32} w/ Reactors

Figure 11.10: Results of fits to the alternative not-Δ 2p-2h model.

the alternative 2p-2h model, the largest effect, found to be on the measurement of δ_{CP}, was deemed acceptable given the current sensitivity. The results of the Nieves et. al. 1p-1h model study were slightly more troubling. In fact, modifications were made to the ND280 analysis in order to mitigate the bias observed in the oscillation parameters. The pre-fit uncertainty in the ND280 fit was inflated to cover the difference between the NEUT and Nieves et. al. 1p-1h data sets as the extrapolation of the alternative data constraint was found to create a larger bias without.

Although the effect of incorrect model assumptions was deemed manageable for the analysis presented here, studies which were performed with larger statistics are available in [124]. These found that the biases increase with larger data sets as statistical uncertainty is reduced, expected at T2K in the coming years. Therefore extensive studies of this kind will become important in future oscillation analyses.

Chapter 12

The Future of Long Baseline Neutrino Physics

Although the experiments leading the search for CP violation in neutrino oscillations, T2K and NOVA [126], have recently provided strong statements about δ_{CP}, sensitivity studies show that towards the end of their lifespan even a combined analysis of both data sets is unlikely to say something definitive about CP violation [127]. For confirmation the physics community will look to the next generation of experiments currently in their research and development stages. There are currently two proposals leading the pack, DUNE, the Deep Underground Neutrino Experiment and Hyper-K, Hyper-Kamiokande.

12.1 DUNE

DUNE, shown in Fig. 12.1, relies on the construction of the LBNF (Long Baseline Neutrino Facility) designed at Fermilab in Batavia, IL. which plans to deliver the worlds highest intensity neutrino beam to the DUNE far detector. The DUNE far detector, making use of the knowledge from the vast LAr neutrino program at Fermilab, will be a large liquid Argon TPC (LArTPC) 1,300 km downstream of a wide-band on-axis beam. The primary goal of DUNE is to study neutrino oscillation and thus measure δ_{CP}, $\sin^2\theta_{23}$, $\sin^2\theta_{13}$, Δm^2_{32} and the mass ordering. The long baseline and subsequent matter effects put DUNE in a unique position to provide a measurement of the neutrino mass ordering under almost all oscillation scenarios [128]. Along with the long baseline neutrino aspect, DUNE has a rich program of physics including searches for nucleon decay, WIMP dark matter, and measurements of supernova and atmospheric neutrinos. Details of the final far and near detector designs are still currently under review.

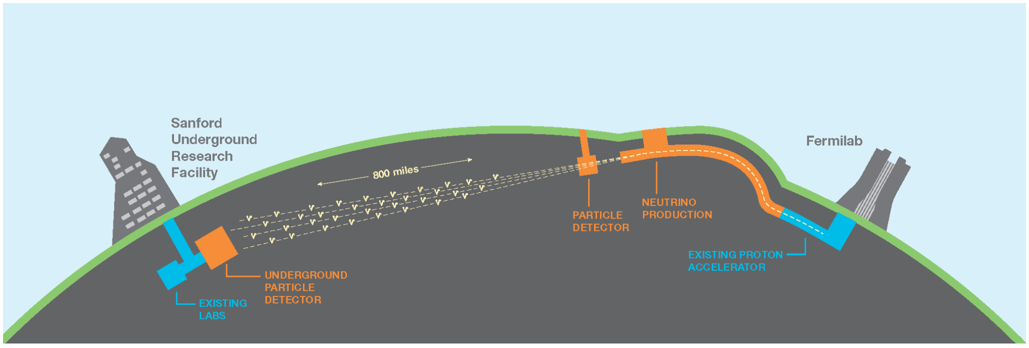

Figure 12.1: The DUNE experiment. Figure taken from [129].

12.2 Hyper-K

Hyper-K is an experiment consisting of a large megaton scale water Cherenkov detector and the successor of the Super-K and T2K experiments. The Hyper-K experiment has potential to study the oscillation of accelerator neutrinos, atmospheric neutrinos, neutrinos of astrophysical origin, WIMP dark matter, nucleon decay and more [130]. Hyper-K aims to improve on the T2K experiment in its statistical power and with reduced susceptibility to systematic uncertainties. The baseline and neutrino energy spectrum of Hyper-K are expected to be consistent with that of T2K, however there are plans to upgrade the J-PARC accelerator facility to beyond 1 MW for the Hyper-K era. The sensitivity of Hyper-K to CP violation under the normal ordering hypothesis is shown in Fig. 12.2, assuming Hyper-K era systematic uncertainties. The figure is produced by plotting the exclusion of $\sin \delta_{CP} = 0$ found from fits to Asimov data sets generated across the δ_{CP} phase space.

It is expected that Hyper-K will be able to measure CP violation to 5σ (3σ) for 58% (76%) of the δ_{CP} phase space. This fraction of δ_{CP} space for which a measurement of CP violation is expected with Hyper-K is used through this section as a measure of sensitivity to CP violation and denoted as the "CPV fraction".

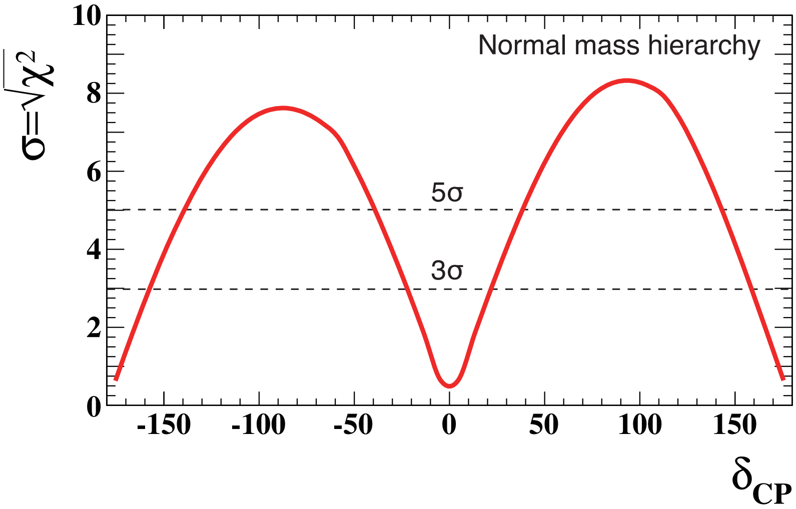

Figure 12.2: The sensitivity of Hyper-K to measure CP violation. Figure taken form [130].

Improvements such as stronger focusing horns for the secondary beam line, Gadolinium doping and water based near detectors are proposed, and expected to reduce systematic uncertainties in oscillation analyses. Improvements to the focusing horns aid by limiting the amount of wrong-sign background contamination, a problem especially during $\bar{\nu}$ running. Gadolinium doping can be used for a rough statistical separation of ν from $\bar{\nu}$ and CCQE from CCnQE[1] events, by tagging events with delayed light. The delayed photon cascade is produced when neutrons from the neutrino interaction are captured by Gadolinium nuclei [131]. CCnQE and $\bar{\nu}$ interactions are more likely to result in neutron ejection from the interacting nucleus than CCQE and ν interactions respectively. Finally,

[1] Charged current not-quasi-elastic

water target near detectors can help reduce model dependencies in the extrapolation of near detector data to the far detector prediction. Although the T2K near detector, ND280, contains water, the target mass it provides is minimal and therefore constraints are statistically limited.

This chapter is a review of studies I performed to determine the dominant systematic uncertainties associated with measurements of δ_{CP} and $\sin^2\theta_{23}$ with the aim of providing requirements for the near detector design. The only improvements from the T2K setup included in the studies are the reduction in flux uncertainty from a replica target data constraint and stronger focusing horns (250 kA to 320 kA) expected during the Hyper-K era. All other inputs are as described in Chap. 4. A more thorough description of the studies carried out can be found in [132] and were expanded further in [133]. Results were also presented at numerous Hyper-K open meetings [134].

The upgraded beam power, coupled with the increase in fiducial volume from Super-K($\sim$25x), result in a significant improvement in the statistics available for a search for CP violation at Hyper-K. Fig. 12.3 shows the predicted Hyper-K reconstructed neutrino energy distributions of μ-like and e-like candidate events assuming a 1 Mt detector in operation for 10 years with a 0.75 MW beam and a ratio of 1:3 between ν-mode and $\bar{\nu}$-mode respectively, taken from the design proposal presented in [130]. Upwards of 3000 neutrino events are predicted in each sample with dominant backgrounds of beam ν_e events for both ν (14%) and $\bar{\nu}$ (18%) modes and oscillated ν_e events (12%) in $\bar{\nu}$-mode.

12.2.1 CPV Sensitivity

Neutrino oscillation experiments such as T2K and Hyper-K have systematic uncertainties which roughly fall into four categories which are flux model uncertainties, interaction model uncertainties, far detector detection uncertainties and near detector detection uncertainties. As these studies were motivated by near

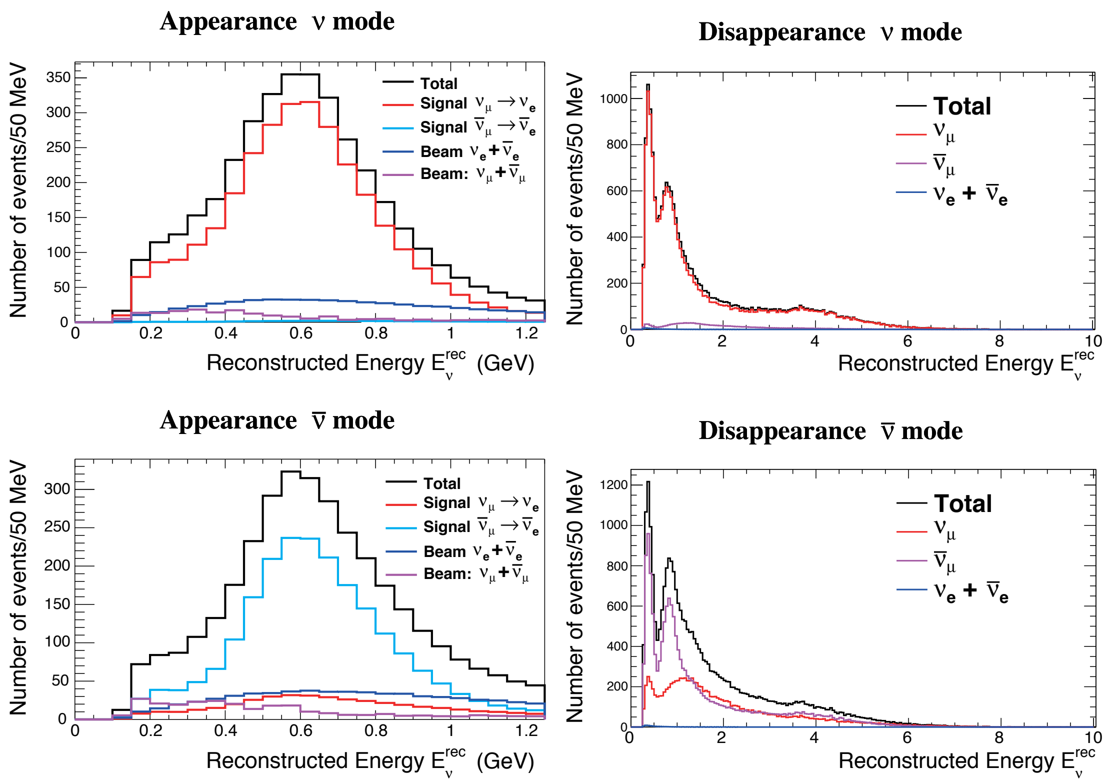

Figure 12.3: Hyper-K expected spectra, figure taken from [130]

detector requirements they were performed without a near detector constraint to determine the level of one which is necessary.

All studies presented here were performed for true normal mass ordering, $\sin^2\theta_{23} = 0.5$, $\sin^2(2\theta_{13}) = 0.1$, $\Delta m^2_{32} = 2.5 \times 10^{-3} eV^2$, $\sin^2(2\theta_{12}) = 0.857$, $\Delta m^2_{21} = 7.5 \times 10^{-5} eV^2$ and assuming the mass ordering is known.

Fig. 12.4 shows the sensitivity to CP violation when specific groups of systematics are considered independently. The inclusion of the Hyper-K detector uncertainties has little effect on the sensitivity to determine CP violation whereas the effect of flux and interaction model uncertainties is significant. The interaction model uncertainties alone bring the CPV fraction at 5σ down from 74% to 61% and flux uncertainties to 68%.

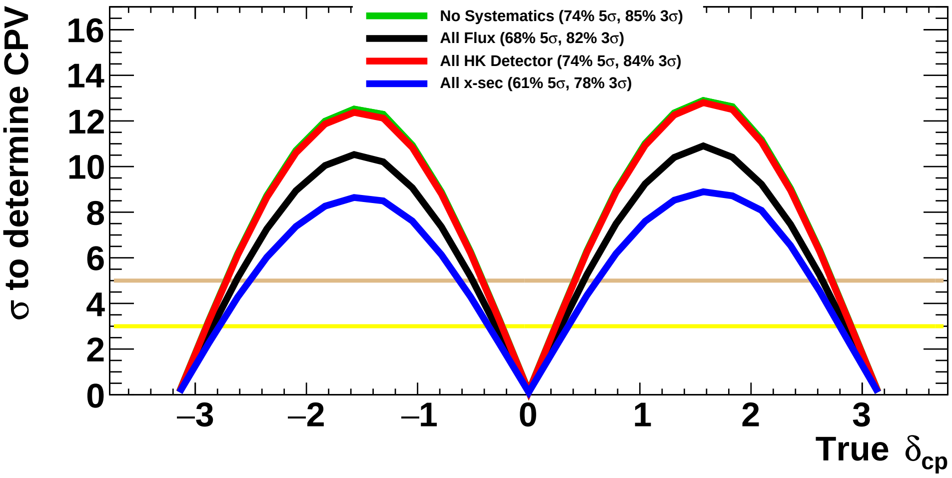

Figure 12.4: Hyper-K CPV sensitivity when considering groups of systematic uncertainty individually.

12.2.1.1 Interaction Uncertainties

When considered independently, the dominant sources of systematic uncertainty from the neutrino interaction models are those that affect the normalisation of the 2p-2h interaction component and the ν_e and $\bar{\nu}_e$ cross-section ratios. Fig. 12.5 shows the sensitivity when only including the systematic uncertainty which were found to be dominant. Including the 2p-2h uncertainties alone decreases the CPV fraction at 5σ to 70% while the effect of CC ν_e uncertainties is almost twice as large decreasing the fraction to 67%.

This result also highlights the importance of the μ-like samples, which limit the effect of the 2p-2h uncertainty. The 2p-2h event contribution to the total appearance event rate is ∼3%, while the total CC ν_e event contribution is ∼96%. Therefore the 100% uncertainty on the 2p-2h event rate results in a ∼3% uncertainty on the total appearance event rate, while the 2% uncertainty on the ν_e and $\bar{\nu}_e$ cross-section is a ∼2% effect on the total appearance event rate. Although the sources of error have similar effects on the ν_e appearance event rate, the CC ν_e normalisation has a ∼0% effect on the μ-like event rate whereas the 2p-2h uncertainty has a ∼3% effect. It is this ∼3% effect which allows the μ-like sample to constrain the 2p-2h uncertainty and limit its effect in the search for CP violation.

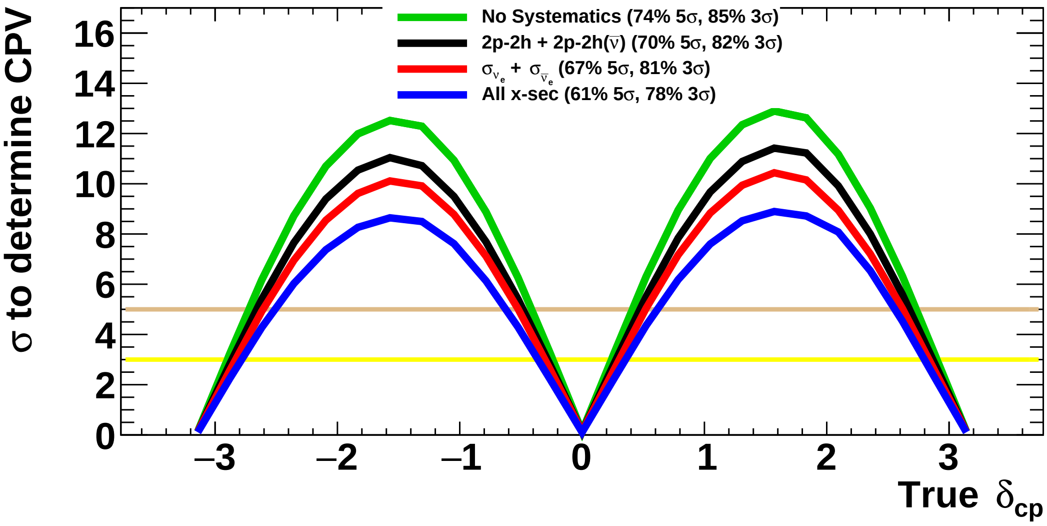

(a) Dominant interaction systematics

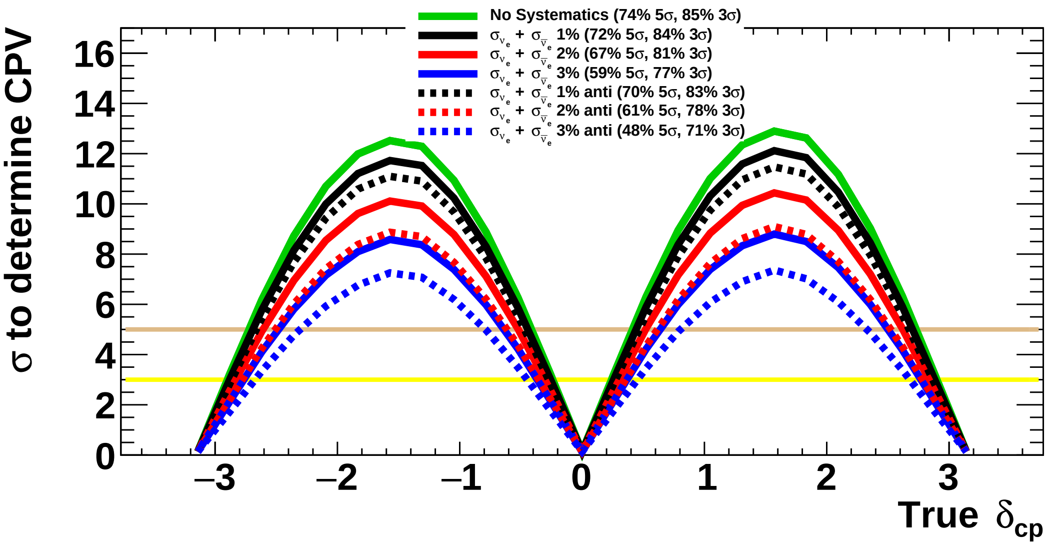

(b) σ_{ν_e} and $\sigma_{\bar{\nu}_e}$

Figure 12.5: Dominant neutrino interaction model systematic uncertainties for the CPV measurement with Hyper-K. Solid curves were produced with uncorrelated ν_e and $\bar{\nu}$ uncertainties and broken curves with anti-correlated. 1% (black), 2% (red) and 3% (blue) uncertainties were considered. The fraction of CP space for which a measurement of CP violation is expected from the curve is shown for 5σ and 3σ significance in the legend.

A detailed description of the theoretical uncertainties in the $\frac{\nu_e}{\nu_\mu}$ and $\frac{\bar{\nu}_e}{\bar{\nu}_\mu}$ cross-section ratios can be found in [107]. The paper suggests that there could be effects not currently accounted for in neutrino interaction generators which change the neutrino cross-section by up to 10%. Therefore a range of uncertainties on the $\frac{\nu_e}{\nu_\mu}$ and $\frac{\bar{\nu}_e}{\bar{\nu}_\mu}$ cross-sections are shown in Fig. 12.5b. The legend captions indicate the size of the uncertainty on each cross-section ratio and the correlation between the systematic parameters which affect the $\frac{\nu_e}{\nu_\mu}$ and $\frac{\bar{\nu}_e}{\bar{\nu}_\mu}$ cross-section ratios. The curves with the label "anti" are produced with 100% anti-correlation between the two parameters and those without with 0% correlation.

Ideally a $\sim$1% constraint is required to maximise the discovery potential of Hyper-K so that both correlated and anti-correlated uncertainties have a limited effect on the sensitivity. There is however a significant decline in the 5σ discovery potential as the uncertainty is increased further with a 3% uncorrelated uncertainty reducing the amount of CP space to 59%. The importance of a constraint on any anti-correlation is also clear here as a 2% anti-correlated uncertainty reduces the 5σ CPV fraction to 61%, comparable to the effect of a 3% uncorrelated uncertainty.

12.2.1.2 Flux Uncertainties

In the context of studies for near detector design, a constraint on the ν_e cross-section is coupled to the uncertainty on the ν_e flux, which is also found to impact the sensitivity to CP violation. The two significant systematic errors regarding the flux model are those that affect the intrinsic ν_e flux and the wrong-sign background in $\bar{\nu}$-mode. The uncertainties were studied independently and results are shown in Fig. 12.6.

With a 100% uncertainty on the wrong sign background component the 5σ CPV fraction is reduced by 8%. A constraint at the 5% level appears to be ideal as it has little impact on the CPV measurement. The intrinsic ν_e flux uncertainty is found to have a larger impact on the sensitivity, with a 20% uncertainty reducing the 5σ CPV fraction by 11%. The dependence on the uncertainty is relatively strong, especially between 5% and 20%, meaning a constraint below 5% is required to maximise the CPV discovery potential of Hyper-K.

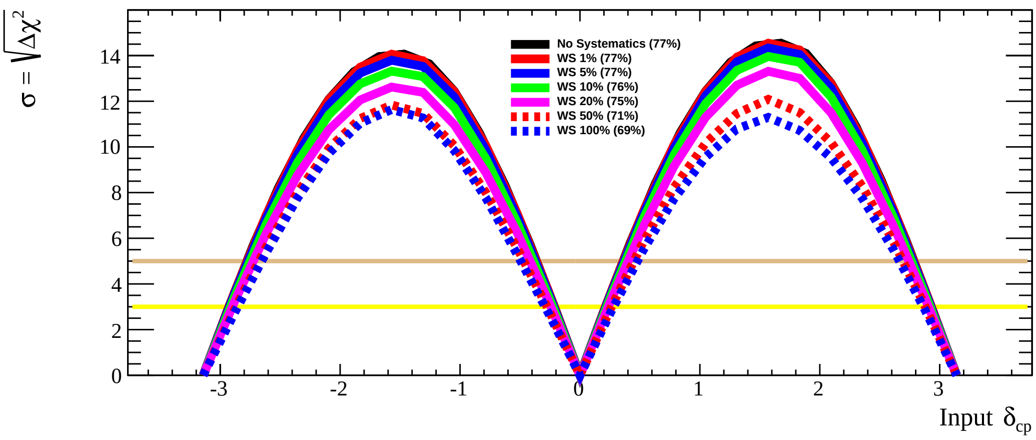

(a) Wrong-sign (ν_μ) background

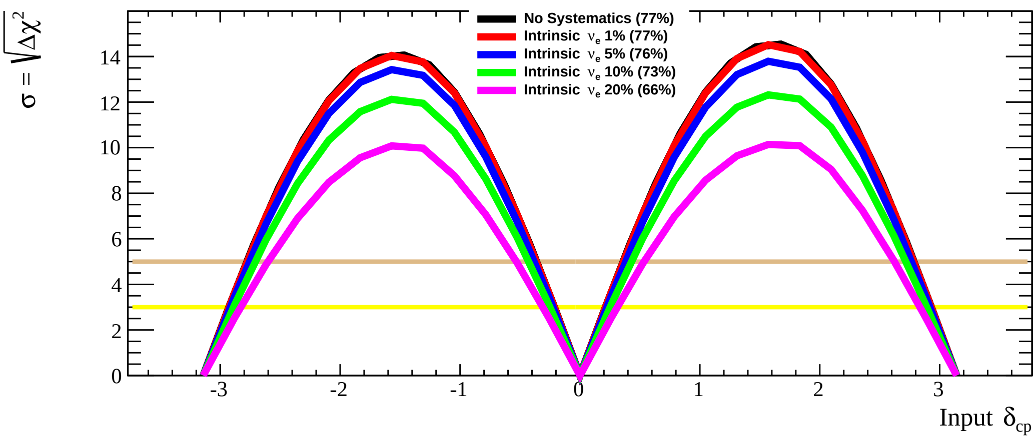

(b) Intrinsic ν_e

Figure 12.6: Dominant neutrino flux model systematic uncertainties for the CPV measurement with Hyper-K. Uncertainties of 1% (solid red), 5% (solid blue), 10% (solid green), 20% (solid pink), 50% (broken red), and 100% (broken blue) were considered. The fraction of CP space for which a 5σ measurement is expected is shown in the brackets.

Sensitivity studies have shown that in the current near detector analysis the ν_μ flux in $\bar{\nu}$-mode is constrained to between 13% and 5% and the intrinsic ν_e component to between 7% and 5% across the whole T2K energy range [109]. It is important to note however, when considering near detector designs, that the wrong-sign component constraint at T2K relies on the magnetisation of the ND280 detector. Furthermore, stronger focusing horns are expected to reduce the ν_μ contamination of the $\bar{\nu}_\mu$ beam.

The constraint on the ν_e flux component is however not only important for its direct effect on the CPV sensitivity, but also for a measurement of the ν_e cross-section at any near detector. The intrinsic ν_e component of the T2K beam is constrained by making use of the ν_μ - ν_e correlations predicted from MC simulation. The uncertainties of which are expected to decrease with the inclusion of hadron production data from a full replica T2K target taken at NA61/SHINE [130].

12.2.2 Exclusion of Maximal Mixing in the 2-3 Sector

One of the many secondary goals of Hyper-K is a constraint on θ_{23} strong enough to distinguish between maximal and non-maximal mixing in the 2-3 sector. Measurements of this kind can help to determine whether or not the neutrino mixing pattern is related to a fundamental flavour symmetry [135]. The significance of non-maximal mixing is defined as $\sqrt{\Delta\chi^2}$ with $\Delta\chi^2 = \chi^2_{\sin^2\theta_{23}=0.5} - \chi^2_{BestFit}$. Studies were performed for true δ_{CP}=0 with all other oscillation parameters identical to those used in the CPV studies in this chapter.

A comparison of the sensitivity when considering specific groups of systematic uncertainty is shown in Fig. 12.7a. When no systematic error is assumed, Hyper-K is expected to exclude maximal mixing for 91.6% of $\sin^2\theta_{23}$ space at 5σ. This is then reduced to 90.7%, 90% and 89.7% when detector, flux and interaction errors are considered respectively. The combination of all sources of systematic uncertainty results in a 5σ coverage of 88%. It is clear that there is no source of error which dominates the $\sin^2\theta_{23}$ sensitivity, the flux and interaction uncertainties have a similar effect on the sensitivity, while the effect of detector errors is smaller but not negligible.

12.2.2.1 Interaction Uncertainties

The effects of individual interaction model uncertainties were studied independently and the results shown in Fig. 12.7b. The uncertainties which are found to have the largest effect on the sensitivity are the 2p-2h interaction normalisation uncertainty and those associated with events in which pions are produced. The uncertainties included in the latter group are specifically those which affect the shape of cross-sections rather than just normalisations.

An interesting conclusion from this study was that the CCQE uncertainties have a negligible effect on the $\sin^2\theta_{23}$ sensitivity. Uncertainties in the CCQE interaction model result in by far the largest uncertainty in the total predicted event rate at Hyper-K as the selections are made up mostly of CCQE events. An explanation for this effect can be found considering Fig. 12.8, which shows that a significant contribution to the event rate around the oscillation dip is from CCnQE and NC events. As fractional uncertainties for the CCnQE and NC event rates are much larger than the CCQE, they become the most significant sources of error near the oscillation dip, which is used to constrain $\sin^2\theta_{23}$ and Δm^2_{32}.

12.2.3 Summary

The effect of many sources of error for a measurement of CPV and $\sin^2\theta_{23}$ without a near detector constraint were studied, and the most influential identified. For the case of CPV, the most significant are found to be cross-section normalisation errors on CC ν_e, CC $\bar{\nu}_e$, 2p-2h(ν) and 2p-2h($\bar{\nu}$). Anti-correlations in the CC ν_e and CC $\bar{\nu}_e$ prior uncertainty are also found to have a considerable impact on the sensitivity. The $\sin^2\theta_{23} \neq 0.5$ sensitivity is found not to be driven by any single source of uncertainty. From the interaction model uncertainties, the 2p-2h and interaction shape uncertainties which affect events with pions in the final state are found to have largest impact however the flux and Hyper-K detector uncertainties need to be studied in more detail.

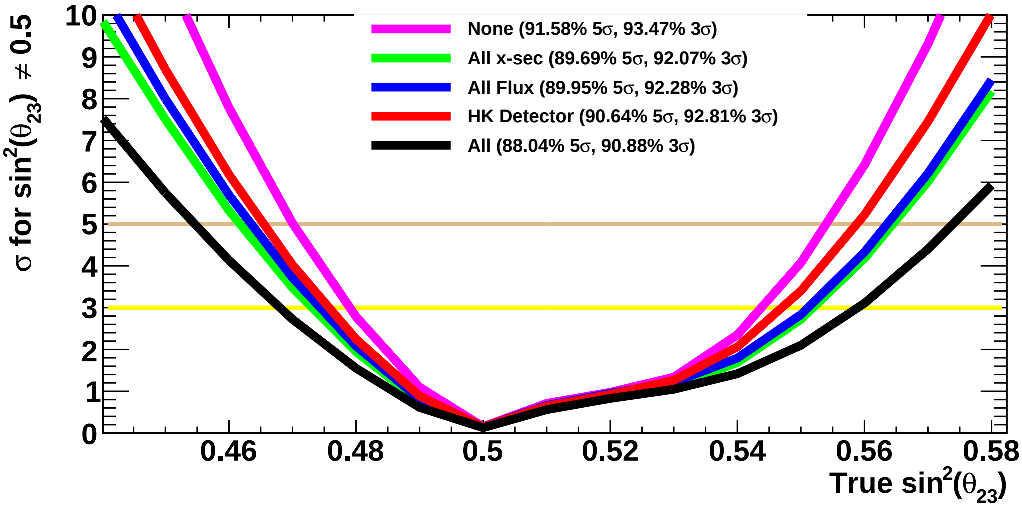

(a) Independent uncertainties

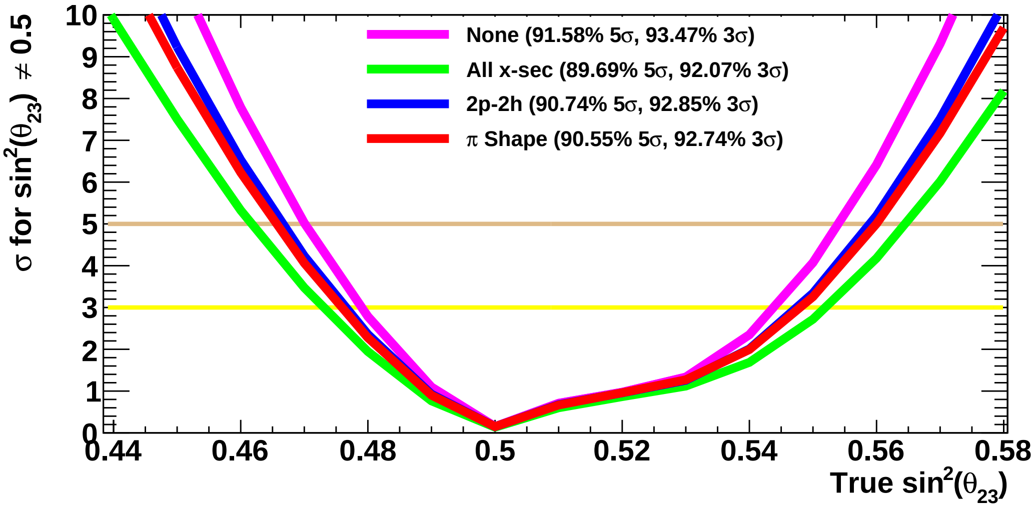

(b) Dominant interaction uncertainties

Figure 12.7: Dominant systematic uncertainties for the measurement of non-maximal mixing with Hyper-K.

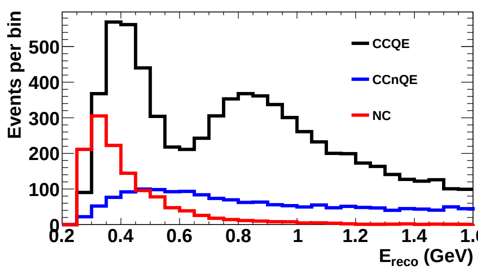

(a) ν-mode

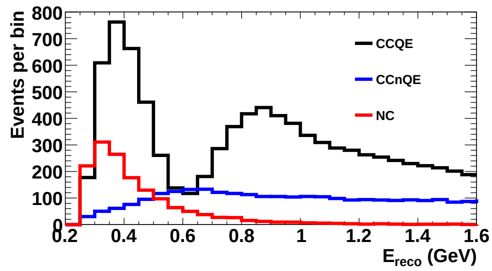

(b) $\bar{\nu}$-mode

Figure 12.8: Predicted contribution of μ-like spectra broken down by interaction type.

Chapter 13

Conclusions

A detailed review of the search for CP violation in neutrino oscillations at T2K has been presented in this thesis. The primary oscillation analysis presented was the first to include the $CC\pi^+$ appearance sample at Super-K, and make use of the full T2K data set available of 7.482 $\times 10^{20}$ POT in ν-mode and 7.471 $\times 10^{20}$ POT in $\bar{\nu}$-mode. The data were found to prefer maximal CP violation and the normal ordering, mostly driven by the large appearance rate observed in the ν-mode appearance samples at Super-K. Fits to the data also lead to a constraint of $-2.978 < \delta_{CP} < -0.467$ at 90% confidence and an exclusion of $\delta_{CP} = 0$ at the 2σ level under the normal mass ordering, and almost complete exclusion of the inverted ordering hypothesis at the 90% confidence level.

Secondary analyses on the T2K data set presented in this thesis found no substantial evidence for $\bar{\nu}_e$ appearance in a $\bar{\nu}$-mode beam or asymmetry between ν_μ and $\bar{\nu}_\mu$ disappearance. The limitations of the oscillation analysis, due to possible flaws in the modelling of neutrino interactions, were also explored and found to have minimal impact on the physics results at the current time. Studies of this kind lead to interesting conclusions which aid the interpretation of the results from the primary oscillation analysis and are therefore recommended for future analyses.

Finally, studies with an outlook to the next generation of long-baseline neutrino physics experiments were presented. These found that, although there are limitations resulting from uncertainties in the modelling of both flux and interaction uncertainties, there is great potential for the discovery of CP violation in the near future.

Appendix A

ND280 Fit Results

Parameter	Prefit	Postfit
Norm; MEC	1.0 ± -	1.55 ± 0.343
C_A^5 RES	1.01 ± 0.12	0.797 ± 0.0623
BgRES Isospin 1/2	1.3 ± 0.2	1.36 ± 0.174
Ma^{QE}	1.2 ± -	1.12 ± 0.0339
Ma^{RES}	0.95 ± 0.15	0.844 ± 0.0388
Fermi Momentum	225.0 ± -	234.0 ± 23.7
Shape; CC Oth	0.0 ± 0.4	-0.0 ± 0.208
E_b	27.0 ± 9	23.8 ± 7.61
Norm; CC Coh	1.0 ± 0.3	0.858 ± 0.228
Norm; NC Coh	1.0 ± 0.3	0.931 ± 0.298
Norm; NC Oth	1.0 ± 0.3	1.0 ± 0.3
Norm; ν_e To ν_μ	1.0 ± 0.0283	1.0 ± 0.0283
Norm; NC 1 Gamma	1.0 ± 1.0	1.0 ± 1.0
Norm; $\bar{\nu}_e$ To $\bar{\nu}_\mu$	1.0 ± 0.0283	1.0 ± 0.0283
Norm; MEC $\bar{\nu}$	1.0 ± -	0.578 ± 0.177

Table A.1: Variations of cross-section parameters in the ND280 fit.

Parameter	Prefit	Postfit
Super-K ν_μ flux; 0.0 - 0.4 GeV (ν-mode)	1.0 ± 0.0987	1.13 ± 0.0638
Super-K ν_μ flux; 0.4 - 0.5 GeV (ν-mode)	1.0 ± 0.103	1.16 ± 0.0613
Super-K ν_μ flux; 0.5 - 0.6 GeV (ν-mode)	1.0 ± 0.0964	1.15 ± 0.0514
Super-K ν_μ flux; 0.6 - 0.7 GeV (ν-mode)	1.0 ± 0.0867	1.13 ± 0.0426
Super-K ν_μ flux; 0.7 - 1.0 GeV (ν-mode)	1.0 ± 0.113	1.1 ± 0.0467
Super-K ν_μ flux; 1.0 - 1.5 GeV (ν-mode)	1.0 ± 0.0917	1.1 ± 0.045
Super-K ν_μ flux; 1.5 - 2.5 GeV (ν-mode)	1.0 ± 0.0702	1.13 ± 0.0439
Super-K ν_μ flux; 2.5 - 3.5 GeV (ν-mode)	1.0 ± 0.0737	1.12 ± 0.0478
Super-K ν_μ flux; 3.5 - 5.0 GeV (ν-mode)	1.0 ± 0.0874	1.12 ± 0.0494
Super-K ν_μ flux; 5.0 - 7.0 GeV (ν-mode)	1.0 ± 0.0979	1.08 ± 0.0532
Super-K ν_μ flux; 7.0 - 30.0 GeV (ν-mode)	1.0 ± 0.114	1.06 ± 0.0649
Super-K $\bar{\nu}_\mu$ flux; 0.0 - 0.7 GeV (ν-mode)	1.0 ± 0.103	1.1 ± 0.0811
Super-K $\bar{\nu}_\mu$ flux; 0.7 - 1.0 GeV (ν-mode)	1.0 ± 0.0785	1.11 ± 0.0484
Super-K $\bar{\nu}_\mu$ flux; 1.0 - 1.5 GeV (ν-mode)	1.0 ± 0.0845	1.11 ± 0.06
Super-K $\bar{\nu}_\mu$ flux; 1.5 - 2.5 GeV (ν-mode)	1.0 ± 0.0856	1.12 ± 0.0702
Super-K $\bar{\nu}_\mu$ flux; 2.5 - 30.0 GeV (ν-mode)	1.0 ± 0.0864	1.16 ± 0.0692
Super-K ν_e flux; 0.0 - 0.5 GeV (ν-mode)	1.0 ± 0.0897	1.13 ± 0.0519
Super-K ν_e flux; 0.5 - 0.7 GeV (ν-mode)	1.0 ± 0.09	1.13 ± 0.0491
Super-K ν_e flux; 0.7 - 0.8 GeV (ν-mode)	1.0 ± 0.086	1.13 ± 0.0472
Super-K ν_e flux; 0.8 - 1.5 GeV (ν-mode)	1.0 ± 0.0809	1.12 ± 0.0428
Super-K ν_e flux; 1.5 - 2.5 GeV (ν-mode)	1.0 ± 0.079	1.11 ± 0.0464
Super-K ν_e flux; 2.5 - 4.0 GeV (ν-mode)	1.0 ± 0.0838	1.11 ± 0.0497
Super-K ν_e flux; 4.0 - 30.0 GeV (ν-mode)	1.0 ± 0.0939	1.12 ± 0.067
Super-K $\bar{\nu}_e$ flux; 0.0 - 2.5 GeV (ν-mode)	1.0 ± 0.074	1.12 ± 0.0568
Super-K $\bar{\nu}_e$ flux; 2.5 - 30.0 GeV (ν-mode)	1.0 ± 0.128	1.15 ± 0.117

Table A.2: Variations of ν-mode flux parameters in the ND280 fit.

Parameter	Prefit	Postfit
Super-K ν_μ flux; 0.0 - 0.7 GeV; ($\bar{\nu}$-mode)	1.0 ± 0.0937	1.1 ± 0.0721
Super-K ν_μ flux; 0.7 - 1.0 GeV; ($\bar{\nu}$-mode)	1.0 ± 0.0793	1.12 ± 0.0538
Super-K ν_μ flux; 1.0 - 1.5 GeV; ($\bar{\nu}$-mode)	1.0 ± 0.0767	1.13 ± 0.0487
Super-K ν_μ flux; 1.5 - 2.5 GeV; ($\bar{\nu}$-mode)	1.0 ± 0.0806	1.15 ± 0.0549
Super-K ν_μ flux; 2.5 - 30.0 GeV; ($\bar{\nu}$-mode)	1.0 ± 0.0803	1.11 ± 0.0563
Super-K $\bar{\nu}_\mu$ flux; 0.0 - 0.4 GeV; ($\bar{\nu}$-mode)	1.0 ± 0.104	1.12 ± 0.0711
Super-K $\bar{\nu}_\mu$ flux; 0.4 - 0.5 GeV; ($\bar{\nu}$-mode)	1.0 ± 0.102	1.13 ± 0.0603
Super-K $\bar{\nu}_\mu$ flux; 0.5 - 0.6 GeV; ($\bar{\nu}$-mode)	1.0 ± 0.0962	1.12 ± 0.0532
Super-K $\bar{\nu}_\mu$ flux; 0.6 - 0.7 GeV; ($\bar{\nu}$-mode)	1.0 ± 0.0846	1.12 ± 0.0441
Super-K $\bar{\nu}_\mu$ flux; 0.7 - 1.0 GeV; ($\bar{\nu}$-mode)	1.0 ± 0.125	1.16 ± 0.0701
Super-K $\bar{\nu}_\mu$ flux; 1.0 - 1.5 GeV; ($\bar{\nu}$-mode)	1.0 ± 0.105	1.13 ± 0.0612
Super-K $\bar{\nu}_\mu$ flux; 1.5 - 2.5 GeV; ($\bar{\nu}$-mode)	1.0 ± 0.08	1.14 ± 0.0539
Super-K $\bar{\nu}_\mu$ flux; 2.5 - 3.5 GeV; ($\bar{\nu}$-mode)	1.0 ± 0.0739	1.14 ± 0.0548
Super-K $\bar{\nu}_\mu$ flux; 3.5 - 5.0 GeV; ($\bar{\nu}$-mode)	1.0 ± 0.094	1.15 ± 0.0713
Super-K $\bar{\nu}_\mu$ flux; 5.0 - 7.0 GeV; ($\bar{\nu}$-mode)	1.0 ± 0.0925	1.13 ± 0.0705
Super-K $\bar{\nu}_\mu$ flux; 7.0 - 30.0 GeV; ($\bar{\nu}$-mode)	1.0 ± 0.13	1.08 ± 0.112
Super-K ν_e flux; 0.0 - 2.5 GeV; ($\bar{\nu}$-mode)	1.0 ± 0.0689	1.12 ± 0.0514
Super-K ν_e flux; 2.5 - 30.0 GeV; ($\bar{\nu}$-mode)	1.0 ± 0.0849	1.11 ± 0.0714
Super-K $\bar{\nu}_e$ flux; 0.0 - 0.5 GeV; ($\bar{\nu}$-mode)	1.0 ± 0.0947	1.13 ± 0.058
Super-K $\bar{\nu}_e$ flux; 0.5 - 0.7 GeV; ($\bar{\nu}$-mode)	1.0 ± 0.091	1.13 ± 0.0514
Super-K $\bar{\nu}_e$ flux; 0.7 - 0.8 GeV; ($\bar{\nu}$-mode)	1.0 ± 0.091	1.13 ± 0.0523
Super-K $\bar{\nu}_e$ flux; 0.8 - 1.5 GeV; ($\bar{\nu}$-mode)	1.0 ± 0.0839	1.13 ± 0.047
Super-K $\bar{\nu}_e$ flux; 1.5 - 2.5 GeV; ($\bar{\nu}$-mode)	1.0 ± 0.0796	1.13 ± 0.0569
Super-K $\bar{\nu}_e$ flux; 2.5 - 4.0 GeV; ($\bar{\nu}$-mode)	1.0 ± 0.089	1.12 ± 0.0707
Super-K $\bar{\nu}_e$ flux; 4.0 - 30.0 GeV; ($\bar{\nu}$-mode)	1.0 ± 0.156	1.17 ± 0.142

Table A.3: Variations of $\bar{\nu}$-mode flux parameters in the ND280 fit.

Appendix B

Super-K Oscillation Sample Event Rates

A full breakdown by interaction type of the expected event rate for the Super-K samples given for the data POT and the validation set given in Tab. 5.9..

	ν_μ	ν_e	$\bar{\nu}_\mu$	$\bar{\nu}_e$	Osc. ν_e	Osc. $\bar{\nu}_e$	Total
CCQE	71.26079	0.03725	4.63401	0.00187	0.24312	0.00114	76.17818
CC1π	18.30962	0.01864	1.69079	0.00103	0.07190	0.00042	20.09241
CCcoherent	0.35206	0.00027	0.08627	0.00003	0.00119	0.00003	0.43985
2p-2h	20.53202	0.01096	0.91267	0.00032	0.05392	0.00024	21.51012
CCother	8.34849	0.00913	0.53311	0.00057	0.00195	0.00005	8.89329
NC1π^0	0.57972	0.01777	0.01866	0.00125	N/A	N/A	0.61740
NC1$\pi^\pm$	4.25309	0.09626	0.15291	0.00889	N/A	N/A	4.51115
NCcoherent	0.01705	0.00019	0.00155	0.00010	N/A	N/A	0.01889
NCother	3.22888	0.13029	0.17780	0.01319	N/A	N/A	3.55017
NC1gamma	0.00390	0.00000	0.00012	0.00000	N/A	N/A	0.00402
Total	126.88563	0.32075	8.20790	0.02725	0.37208	0.00187	135.81549

Table B.1: Predicted number of events in the ν-mode *CCQE* μ-like sample for the data POT and the validation set given in Tab. 5.9.

	ν_μ	ν_e	$\bar{\nu}_\mu$	$\bar{\nu}_e$	Osc. ν_e	Osc. $\bar{\nu}_e$	Total
CCQE	13.19436	0.00664	23.83240	0.00856	0.01155	0.02589	37.07941
CC1π	5.10184	0.00490	5.65512	0.00367	0.00470	0.00485	10.77509
CCcoherent	0.10170	0.00006	0.31428	0.00020	0.00001	0.00060	0.41685
2p-2h	4.71879	0.00225	3.83018	0.00155	0.00321	0.00366	8.55964
CCother	2.41002	0.00254	1.64472	0.00088	0.00038	0.00015	4.05870
NC1π^0	0.11340	0.00467	0.09275	0.00249	N/A	N/A	0.21331
NC1$\pi^\pm$	0.71338	0.02835	0.70828	0.01935	N/A	N/A	1.46937
NCcoherent	0.00251	0.00012	0.01193	0.00012	N/A	N/A	0.01468
NCother	0.99673	0.04648	0.55030	0.02256	N/A	N/A	1.61607
NC1gamma	0.00064	0.00000	0.00000	0.00000	N/A	N/A	0.00064
Total	27.35338	0.09601	36.63997	0.05937	0.01986	0.03516	64.20374

Table B.2: Predicted number of events in the $\bar{\nu}$-mode *CCQE* μ-like sample for the data POT and the validation set given in Tab. 5.9.

	ν_μ	ν_e	$\bar{\nu}_\mu$	$\bar{\nu}_e$	Osc. ν_e	Osc. $\bar{\nu}_e$	Total
CCQE	0.06080	2.29713	0.00085	0.09533	17.12951	0.10726	19.69088
CC1π	0.01720	0.37587	0.00027	0.02697	1.82143	0.01847	2.26021
CCcoherent	0.00012	0.00263	0.00000	0.00193	0.01628	0.00182	0.02278
2p-2h	0.00860	0.76550	0.00008	0.02370	4.20736	0.02055	5.02579
CCother	0.00142	0.04860	0.00005	0.00351	0.03130	0.00123	0.08611
NC1π^0	0.56512	0.01248	0.01835	0.00096	N/A	N/A	0.59691
NC1$\pi^\pm$	0.10698	0.00251	0.00352	0.00023	N/A	N/A	0.11323
NCcoherent	0.18816	0.00386	0.01990	0.00096	N/A	N/A	0.21288
NCother	0.13569	0.00547	0.00832	0.00061	N/A	N/A	0.15009
NC1gamma	0.50065	0.00800	0.02283	0.00108	N/A	N/A	0.53256
Total	1.58473	3.52204	0.07418	0.15529	23.20588	0.14933	28.69144

Table B.3: Predicted number of events in the ν-mode *CCQE e*-like sample for the data POT and the validation set given in Tab. 5.9.

	ν_μ	ν_e	$\bar{\nu}_\mu$	$\bar{\nu}_e$	Osc. ν_e	Osc. $\bar{\nu}_e$	Total
CCQE	0.00392	0.35323	0.00567	0.62877	0.71080	2.14728	3.84968
CC1π	0.00310	0.07557	0.00191	0.10984	0.10810	0.24865	0.54716
CCcoherent	0.00005	0.00057	0.00004	0.01123	0.00091	0.03515	0.04795
2p-2h	0.00146	0.12956	0.00062	0.11748	0.21603	0.34387	0.80902
CCother	0.00205	0.01557	0.00004	0.00786	0.00674	0.00426	0.03651
NC1π^0	0.08545	0.00364	0.09084	0.00237	N/A	N/A	0.18230
NC1$\pi^\pm$	0.02157	0.00080	0.01494	0.00037	N/A	N/A	0.03770
NCcoherent	0.03855	0.00136	0.15037	0.00234	N/A	N/A	0.19262
NCother	0.04144	0.00168	0.02214	0.00069	N/A	N/A	0.06595
NC1gamma	0.06918	0.00360	0.15039	0.00316	N/A	N/A	0.22633
Total	0.26678	0.58559	0.43695	0.88411	1.04258	2.77920	5.99522

Table B.4: Predicted number of events in the $\bar{\nu}$-mode *CCQE* e-like sample for the data POT and the validation set given in Tab. 5.9.

	ν_μ	ν_e	$\bar{\nu}_\mu$	$\bar{\nu}_e$	Osc. ν_e	Osc. $\bar{\nu}_e$	Total
CCQE	0.15777	0.00192	0.00412	0.00002	0.01434	0.00002	0.17819
CC1π	0.05822	0.30131	0.00263	0.00096	1.92990	0.00054	2.29356
CCcoherent	0.00041	0.04269	0.00039	0.00003	0.29643	0.00007	0.34002
2p-2h	0.05610	0.00225	0.00047	0.00005	0.00963	0.00002	0.06852
CCother	0.01207	0.03733	0.00080	0.00094	0.03633	0.00054	0.08800
NC1π^0	0.00610	0.00012	0.00019	0.00000	N/A	N/A	0.00641
NC1$\pi^\pm$	0.03533	0.00134	0.00222	0.00021	N/A	N/A	0.03910
NCother	0.08631	0.00471	0.00588	0.00034	N/A	N/A	0.09725
NC1gamma	0.01690	0.00000	0.00023	0.00000	N/A	N/A	0.01713
Total	0.42923	0.39166	0.01693	0.00254	2.28662	0.00120	3.12818

Table B.5: Predicted number of events in the ν-mode $CC\pi^+$ e-like sample for the data POT and the validation set given in Tab. 5.9.

Appendix C

Supplementary Asimov Studies

C.1 Asimov Data Set C, D & E

Sensitivity studies for various values of true δ_{CP} were performed to give some context to the data constraint on δ_{CP}. Asimov data sets C, D and E are defined in Tab. 7.1 . The effect of the true value of δ_{CP} was studied in the $\sin^2\theta_{13}$ vs δ_{CP}, with and without the reactor constraint, and 1D δ_{CP} parameter spaces. The results are shown in Figs. C.1 and C.2. Fits to Asimov data set C and D have similar results to Asimov data set B but provide slightly stronger constraints due to the additional events in the appearance samples as a result of more maximal disappearance. The fit to Asimov data set E is similar to that to Asimov data set A, both provide similar constraints on δ_{CP} however the more CP violating data set (E) naturally provides a stronger constraint.

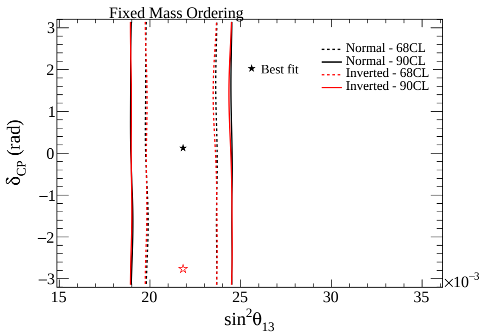

(a) C: $\sin^2\theta_{13}$ vs δ_{CP} w/ reactor

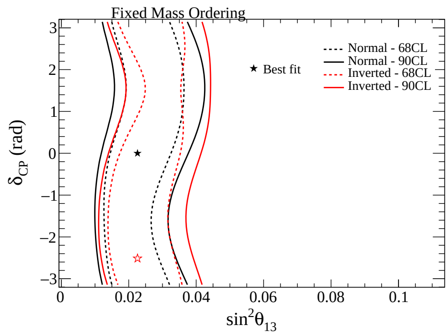

(b) C: $\sin^2\theta_{13}$ vs δ_{CP}

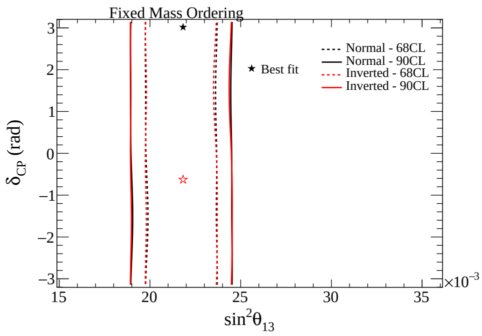

(c) D: $\sin^2\theta_{13}$ vs δ_{CP} w/ reactor

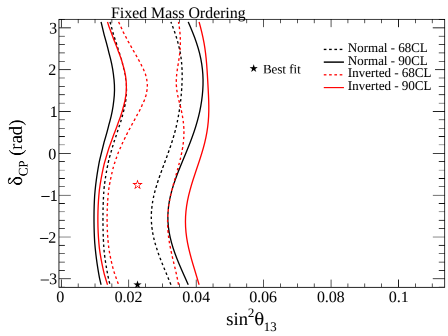

(d) D: $\sin^2\theta_{13}$ vs δ_{CP}

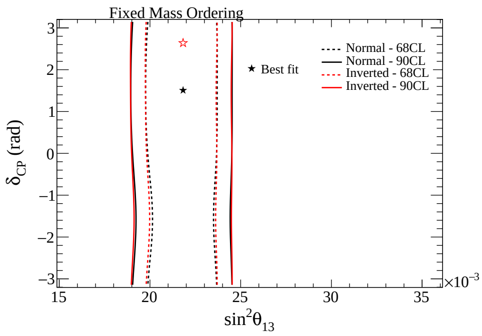

(e) E: $\sin^2\theta_{13}$ vs δ_{CP} w/ reactor

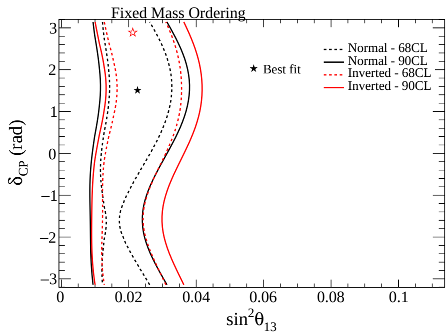

(f) E: $\sin^2\theta_{13}$ vs δ_{CP}

Figure C.1: The contours at 68% and 90% CL with reactor constraint for the Asimov data sets C, D and E of Tab. 7.1.

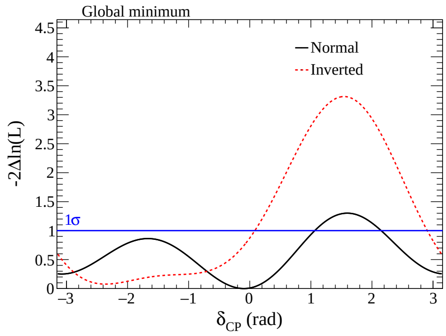

(a) Asimov C

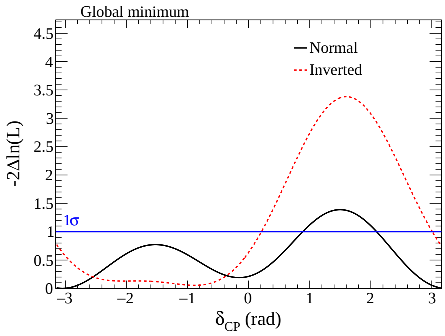

(b) Asimov D

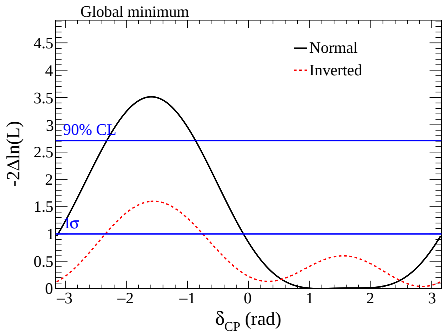

(c) Asimov E

Figure C.2: The contours 1D δ_{CP} contours for the Asimov data sets C, D and E of Tab. 7.1 with the reactor constraint.

Appendix D

Glossary

2p-2h 2 Particle 2 Hole, an interaction model to account for the probability of scattering off of multi-nucleon bound states.

ν-mode Neutrino mode, running mode of T2K in which the beam is composed primarily of ν.

$\bar{\nu}$-mode Anti-neutrino mode, running mode of T2K in which the beam is composed primarily of $\bar{\nu}$.

μ-like Events identified as muon-like by the Super-K reconstruction.

Asimov data A mock data set produced from the MC expectation for a specific set of model parameters without any statistical fluctuations applied. Often used in sensitivity studies.

CC Charged Current scattering.

CCQE Charged Current Quasi-Elastic, an interaction in which the neutrino scatters off of a single nucleon transferring little energy to the nucleon.

CL Confidence Level, percentage confidence defined by a contour or area. The confidence level indicates the probability a measurement will fall in the region under repeat experiments.

CPV Fraction Fraction of δ_{CP} space for which the exclusion of $\sin\delta_{CP} = 0$ is expected at a given significance level.

DAQ Data Acquisition.

DIS Deep Inelastic Scattering, a neutrino interaction in which the incoming neutrino scatters off of an individual quark.

e**-like** Events identified as electron-like by the Super-K reconstruction.

ECAL Electromagnetic Calorimeter, an ND280 subdetector.

EReco Reconstructed neutrino energy.

FGD Fine-Grained Detector, an ND280 subdetector which provides the target material used for the oscillation analysis. ND280 contains two FGDs, FGD1 made of only scintillator, and FGD2 made of both scintillator and water.

FSI Final State Interaction, interactions which outgoing particles may undergo as they exit the nucleus.

LFG Local Fermi Gas, a theory used to model the effect of a nuclear potential on nucleons which participate in neutrino interactions. The calculation of the Fermi sea is localised to a smaller region of the nucleus.

Marginalisation The removal of nuisance parameters from a multidimensional distribution via integration of the dimensions which are superfluous.

Marginal Likelihood A likelihood constructed as a function of only the parameters of interest. Nuisance parameters are marginalised in the construction.

MC Monte-Carlo simulation.

MCMC Markov Chain Monte Carlo, an algorithm used for sampling from a probability distribution.

MIGRAD A minimisation algorithm employed by the MINUIT software package.

NA61/SHINE A hadron production experiment based in CERN which makes measurements of particles produced as 30 *GeV* protons interact with a replica T2K graphite target. Measurements from NA61/SHINE are used for the prediction of the T2K beam neutrino flux.

NEUT A neutrino interaction generator used to simulate neutrino interactions for the Super-K MC.

NC Neutral Current scattering.

NIWG Neutrino Interaction Working Group, an analysis group in T2K studying neutrino interaction models which enter the oscillation analysis.

Nuisance parameter A model parameter which is not of concern in the analysis. Nuisance parameters are often marginalised in the construction of the marginal likelihood used to determine the oscillation parameters of interest.

PØD π^0 Detector, an ND280 subdetector.

POT Protons On Target, a measure of the neutrino flux collected by Super-K during the T2K runs.

Prior The prior probability distribution of a model parameter before T2K data are analysed.

p-value The probability of finding the observed or more extreme results given the null hypothesis is true.

Reactor Constraint A combination of the measurements made from reactor neutrino experiments constraining $\sin^2\theta_{13}$.

RFG Relativistic Fermi Gas, a theory used to model the effect of a nuclear potential on nucleons which participate in neutrino interactions.

RPA Random Phase Approximation, a theory to model the nuclear screening effect and nucleon correlations inside the nucleus.

SF Spectral function, a theory used to model the effect of a nuclear potential on nucleons which participate in neutrino interactions. An extenuation to a simple RFG model which includes short range correlations between nucleons.

SI Secondary Interaction, interactions which outgoing particles may undergo as they pass through the detector.

SKDet Uncertainties associated with particle measurements at Super-K.

SMRD Side Muon Range Detector, an ND280 subdetector.

Super-K Super-Kamiokande, a 50 kt water Cherenkov detector used as the far detector for the T2K oscillation analysis.

TPC Time Projection Chamber, and ND280 subdetector used mainly for particle identification and tracking. ND280 contains three identical TPCs.

X-Sec Cross section.

References

[1] James Chadwick and Charles D Ellis, “A Preliminary Investigation of the Intensity Distribution in the β-Ray Spectra of Radium B and C”, in “Proceedings of the Cambridge Philosophical Society”, vol. 21, pp. 274–280 (1922)

[2] J. Chadwick, “Possible Existence of a Neutron”, Nature Physics vol. 129 p. 312 (1932), doi:10.1038/129312a0

[3] Fred L. Wilson, “Fermi's Theory of Beta Decay”, American Journal of Physics vol. 36 (12) pp. 1150–1160 (1968), doi:10.1119/1.1974382, `http://dx.doi.org/10.1119/1.1974382`, URL `http://dx.doi.org/10.1119/1.1974382`

[4] C. L. Cowan et al., “Detection of the Free Neutrino: a Confirmation”, Science vol. 124 (3212) pp. 103–104 (1956), doi:10.1126/science.124.3212.103, `http://science.sciencemag.org/content/124/3212/103.full.pdf`, URL `http://science.sciencemag.org/content/124/3212/103`

[5] G. Danby et al., “Observation of High-Energy Neutrino Reactions and the Existence of Two Kinds of Neutrinos”, Phys. Rev. Lett. vol. 9 pp. 36–44 (1962), doi:10.1103/PhysRevLett.9.36, URL `https://link.aps.org/doi/10.1103/PhysRevLett.9.36`

[6] C. Franzinetti, “Neutrino interactions in the CERN heavy liquid bubble chamber”, (1966)

[7] J. K. Bienlein et al., "Spark chamber study of high-energy neutrino interactions", Phys. Lett. vol. 13 pp. 80–86 (1964), doi:10.1016/0031-9163(64)90316-6

[8] K. Kodama et al. (DONUT), "Observation of tau neutrino interactions", Phys. Lett. vol. B504 pp. 218–224 (2001), doi:10.1016/S0370-2693(01)00307-0, hep-ex/0012035

[9] The ALEPH Collaboration et al., "Precision electroweak measurements on the Z resonance", Physics Reports vol. 427 (5–6) pp. 257 – 454 (2006), doi:http://dx.doi.org/10.1016/j.physrep.2005.12.006, http://www.sciencedirect.com/science/article/pii/S0370157305005119

[10] M. Goldhaber, L. Grodzins, and A. W. Sunyar, "Helicity of Neutrinos", Phys. Rev. vol. 109 pp. 1015–1017 (1958), doi:10.1103/PhysRev.109.1015, URL https://link.aps.org/doi/10.1103/PhysRev.109.1015

[11] GUIDO BARBIELLINI and GIUSEPPE COCCONI, "Electric charge of the neutrinos from SN1987A", Nature vol. 329 (6134) pp. 21–22 (1987), URL http://dx.doi.org/10.1038/329021b0

[12] A. G. Beda et al., "Gemma experiment: The results of neutrino magnetic moment search", Phys. Part. Nucl. Lett. vol. 10 pp. 139–143 (2013), doi:10.1134/S1547477113020027

[13] V. N. Aseev et al. (Troitsk), "An upper limit on electron antineutrino mass from Troitsk experiment", Phys. Rev. vol. D84 p. 112003 (2011), doi:10.1103/PhysRevD.84.112003, 1108.5034

[14] Ch. Kraus et al., "Final results from phase II of the Mainz neutrino mass search in tritium beta decay", Eur. Phys. J. vol. C40 pp. 447–468 (2005), doi:10.1140/epjc/s2005-02139-7, hep-ex/0412056

[15] Nathalie Palanque-Delabrouille et al., "Neutrino masses and cosmology with Lyman-alpha forest power spectrum", Journal of Cosmology and Astroparticle Physics vol. 2015 (11) p. 011 (2015), URL http://stacks.iop.org/1475-7516/2015/i=11/a=011

[16] D. A. Krakauer et al., "Direct experimental lower bound on the radiative lifetime of the muon neutrino", Phys. Rev. D vol. 44 pp. R6–R9 (1991), doi:10.1103/PhysRevD.44.R6, URL https://link.aps.org/doi/10.1103/PhysRevD.44.R6

[17] Erasmo Recami, "Ettore Majorana: his work and his life", Int. J. Mod. Phys. vol. D23 p. 1444009 (2014), doi:10.1142/S0218271811400094, 1412.7485

[18] J. Schechter and J. W. F. Valle, "Neutrinoless double-β decay in SU(2) x U(1) theories", Phys. Rev. D vol. 25 pp. 2951–2954 (1982), doi:10.1103/PhysRevD.25.2951, URL https://link.aps.org/doi/10.1103/PhysRevD.25.2951

[19] Alex Wright, "Future Neutrinoless Double Beta Decay Search Experiments and Related R and D", Journal of Physics: Conference Series vol. 888 (1) p. 012036 (2017), URL http://stacks.iop.org/1742-6596/888/i=1/a=012036

[20] Raymond Davis, Don S. Harmer, and Kenneth C. Hoffman, "Search for Neutrinos from the Sun", Phys. Rev. Lett. vol. 20 pp. 1205–1209 (1968), doi:10.1103/PhysRevLett.20.1205, http://link.aps.org/doi/10.1103/PhysRevLett.20.1205

[21] Bruce T. Cleveland et al., "Measurement of the Solar Electron Neutrino Flux with the Homestake Chlorine Detector", The Astrophysical Journal vol. 496 (1) p. 505 (1998), URL http://stacks.iop.org/0004-637X/496/i=1/a=505

[22] J.N. Abdurashitov et al., “Solar neutrino flux measurements by the Soviet-American gallium experiment (SAGE) for half the 22-year solar cycle”, Journal of Experimental and Theoretical Physics vol. 95 (2) pp. 181–193 (2002), doi:10.1134/1.1506424, http://dx.doi.org/10.1134/1.1506424

[23] M. Cribier et al., “Results of the whole {GALLEX} experiment”, Nuclear Physics B - Proceedings Supplements vol. 70 (1–3) pp. 284 – 291 (1999), doi:http://dx.doi.org/10.1016/S0920-5632(98)00438-1, proceedings of the Fifth International Workshop on topics in Astroparticle and Underground Physics, http://www.sciencedirect.com/science/article/pii/S0920563298004381

[24] K. S. Hirata et al., “Observation of ^{8}B solar neutrinos in the Kamiokande-II detector”, Phys. Rev. Lett. vol. 63 pp. 16–19 (1989), doi:10.1103/PhysRevLett.63.16, http://link.aps.org/doi/10.1103/PhysRevLett.63.16

[25] Q. R. Ahmad et al. (SNO Collaboration), “Direct Evidence for Neutrino Flavor Transformation from Neutral-Current Interactions in the Sudbury Neutrino Observatory”, Phys. Rev. Lett. vol. 89 p. 011301 (2002), doi:10.1103/PhysRevLett.89.011301, http://link.aps.org/doi/10.1103/PhysRevLett.89.011301

[26] M. R. Krishnaswamy et al., “The Kolar Gold Fields Neutrino Experimen. I. The Interactions of Cosmic Ray Neutrinos”, Proceedings of the Royal Society of London. Series A, Mathematical and Physical Sciences vol. 323 (1555) pp. 489–509 (1971), URL http://www.jstor.org/stable/78070

[27] W. W. M. Allison et al. (Soudan-2), “The Atmospheric neutrino flavor ratio from a 3.9 fiducial kiloton year exposure of Soudan-2”, Phys. Lett. vol. B449 pp. 137–144 (1999), doi:10.1016/S0370-2693(99)00056-8, hep-ex/9901024

[28] R. Becker-Szendy et al. (IMB), "A Search for muon-neutrino oscillations with the IMB detector", Phys. Rev. Lett. vol. 69 pp. 1010–1013 (1992)

[29] Y. Fukuda et al. (Super-Kamiokande Collaboration), "Evidence for Oscillation of Atmospheric Neutrinos", Phys. Rev. Lett. vol. 81 pp. 1562–1567 (1998), doi:10.1103/PhysRevLett.81.1562, http://link.aps.org/doi/10.1103/PhysRevLett.81.1562

[30] K. Eguchi et al. (KamLAND Collaboration), "First Results from KamLAND: Evidence for Reactor Antineutrino Disappearance", Phys. Rev. Lett. vol. 90 p. 021802 (2003), doi:10.1103/PhysRevLett.90.021802, http://link.aps.org/doi/10.1103/PhysRevLett.90.021802

[31] Z. Maki, M. Nakagawa, and S. Sakata, "Remarks on the Unified Model of Elementary Particles", Progress of Theoretical Physics vol. 28 pp. 870–880 (1962), doi:10.1143/PTP.28.870

[32] B. Pontecorvo, "Neutrino Experiments and the Problem of Conservation of Leptonic Charge", Journal of Experimental and Theoretical Physics vol. 26 pp. 984–988 (1968), http://jetp.ac.ru/cgi-bin/e/index/e/26/5/p984?a=list

[33] Teppei Katori and Marco Martini, "Neutrino-Nucleus Cross Sections for Oscillation Experiments", (2016), 1611.07770

[34] K. Abe et al. (Super-Kamiokande), "Solar Neutrino Measurements in Super-Kamiokande-IV", Phys. Rev. vol. D94 (5) p. 052010 (2016), doi:10.1103/PhysRevD.94.052010, 1606.07538

[35] F. P. An et al., "Observation of Electron-Antineutrino Disappearance at Daya Bay", Phys. Rev. Lett. vol. 108 p. 171803 (2012), doi:10.1103/PhysRevLett.108.171803, http://link.aps.org/doi/10.1103/PhysRevLett.108.171803

[36] Jun Cao and Kam-Biu Luk, "An overview of the Daya Bay Reactor Neutrino Experiment", Nucl. Phys. vol. B908 pp. 62–73 (2016), doi:10.1016/j.nuclphysb.2016.04.034, 1605.01502

[37] Y. Abe et al., "First measurement of from delayed neutron capture on hydrogen in the Double Chooz experiment", Physics Letters B vol. 723 (1–3) pp. 66 – 70 (2013), doi:http://dx.doi.org/10.1016/j.physletb.2013.04.050, http://www.sciencedirect.com/science/article/pii/S0370269313003390

[38] J. K. Ahn et al. (RENO Collaboration), "Observation of Reactor Electron Antineutrinos Disappearance in the RENO Experiment", Phys. Rev. Lett. vol. 108 p. 191802 (2012), doi:10.1103/PhysRevLett.108.191802, http://link.aps.org/doi/10.1103/PhysRevLett.108.191802

[39] K. A. Olive et al. (Particle Data Group), "Review of Particle Physics", Chin. Phys. vol. C38 p. 090001 ((2014) and 2015 update), doi:10.1088/1674-1137/38/9/090001

[40] P. Adamson et al., "Combined Analysis of ν_μ Disappearance and $\nu_\mu \rightarrow \nu_e$ Appearance in MINOS Using Accelerator and Atmospheric Neutrinos", Phys. Rev. Lett. vol. 112 p. 191801 (2014), doi:10.1103/PhysRevLett.112.191801, http://link.aps.org/doi/10.1103/PhysRevLett.112.191801

[41] K. Abe et al. ((T2K Collaboration)), "Precise Measurement of the Neutrino Mixing Parameter θ_{23} from Muon Neutrino Disappearance in an Off-Axis Beam", Phys. Rev. Lett. vol. 112 p. 181801 (2014), doi:10.1103/PhysRevLett.112.181801, http://link.aps.org/doi/10.1103/PhysRevLett.112.181801

[42] K. Abe et al. (T2K Collaboration), "Measurements of neutrino oscillation in appearance and disappearance channels by the T2K experiment with 6.6×10^{20} protons on target", Phys. Rev. D vol. 91 p. 072010 (2015), doi:10.1103/PhysRevD.91.072010, http://link.aps.org/doi/10.1103/PhysRevD.91.072010

[43] K. Abe et al., "The {T2K} experiment", Nuclear Instruments and Methods in Physics Research Section A: Accelerators, Spectrometers, Detectors and Associated Equipment vol. 659 (1) pp. 106 – 135 (2011), doi:http://dx.doi.org/10.1016/j.nima.2011.06.067, http://www.sciencedirect.com/science/article/pii/S0168900211011910

[44] K. Abe et al., "Measurements of the {T2K} neutrino beam properties using the {INGRID} on-axis near detector", Nuclear Instruments and Methods in Physics Research Section A: Accelerators, Spectrometers, Detectors and Associated Equipment vol. 694 pp. 211 – 223 (2012), doi:http://dx.doi.org/10.1016/j.nima.2012.03.023, http://www.sciencedirect.com/science/article/pii/S0168900212002987

[45] "Figure taken from https://j-parc.jp/public/Acc/en/index.html",

[46] Shoji Nagamiya, "J-PARC Program Overview", Nuclear Physics A vol. 827 (1) pp. 179c – 186c (2009), doi:http://dx.doi.org/10.1016/j.nuclphysa.2009.05.033, pANIC08, URL http://www.sciencedirect.com/science/article/pii/S0375947409002954

[47] S. Bhadra et al., "Optical Transition Radiation Monitor for the T2K Experiment", Nucl. Instrum. Meth. vol. A703 pp. 45–58 (2013), doi:10.1016/j.nima.2012.11.044, 1201.1922

[48] T. Sekiguchi et al., "Development and operational experience of magnetic horn system for T2K experiment", Nuclear Instruments and Methods in Physics Research, Section A: Accelerators, Spectrometers, Detectors and Associated Equipment vol. 789 pp. 57–80 (2015), doi:10.1016/j.nima.2015.04.008

[49] K. Abe et al. (T2K Collaboration), "T2K neutrino flux prediction", Phys. Rev. D vol. 87 p. 012001 (2013), doi:10.1103/PhysRevD.87.012001, http://link.aps.org/doi/10.1103/PhysRevD.87.012001

[50] The T2K beam group, "Flux releases summary", Tech. Rep. TN-264, T2K (2015), www.t2k.org/docs/technotes/264

[51] Y. Figure by Uchida

[52] P.-A. Amaudruz et al., "The {T2K} fine-grained detectors", Nuclear Instruments and Methods in Physics Research Section A: Accelerators, Spectrometers, Detectors and Associated Equipment vol. 696 pp. 1 – 31 (2012), doi:http://dx.doi.org/10.1016/j.nima.2012.08.020, http://www.sciencedirect.com/science/article/pii/S0168900212008789

[53] Georges Charpak, J. Derre, Y. Giomataris, and P. Rebourgeard, "MICROMEGAS, a multipurpose gaseous detector", Nucl. Instrum. Meth. vol. A478 pp. 26–36 (2002), doi:10.1016/S0168-9002(01)01713-2

[54] N. Abgrall et al., "Time projection chambers for the {T2K} near detectors", Nuclear Instruments and Methods in Physics Research Section A: Accelerators, Spectrometers, Detectors and Associated Equipment vol. 637 (1) pp. 25 – 46 (2011), doi:http://dx.doi.org/10.1016/j.nima.2011.02.036, http://www.sciencedirect.com/science/article/pii/S0168900211003421

[55] S. Aoki et al., "The T2K Side Muon Range Detector (SMRD)", Nucl. Instrum. Meth. vol. A698 pp. 135–146 (2013), doi:10.1016/j.nima.2012.10.001, 1206.3553

[56] K. Abe et al. (T2K), "Measurement of the muon neutrino inclusive charged-current cross section in the energy range of 1–3 GeV with the T2K INGRID detector", Phys. Rev. vol. D93 (7) p. 072002 (2016), doi:10.1103/PhysRevD.93.072002, 1509.06940

[57] S. Fukuda et al., "The Super-Kamiokande detector", Nuclear Instruments and Methods in Physics Research Section A: Accelerators, Spectrometers, Detectors and Associated Equipment vol. 501 (2–3) pp. 418 – 462 (2003), doi:http://dx.doi.org/10.1016/S0168-9002(03)00425-X, http://www.sciencedirect.com/science/article/pii/S016890020300425X

[58] Shirley Weishi Li and John F. Beacom, "First calculation of cosmic-ray muon spallation backgrounds for MeV astrophysical neutrino signals in Super-Kamiokande", Phys. Rev. vol. C89 p. 045801 (2014), doi:10.1103/PhysRevC.89.045801, 1402.4687

[59] I. M. Frank and I. Tamm, "Coherent visible radiation of fast electrons passing through matter", Compt. Rend. Acad. Sci. URSS vol. 14 pp. 109–114 (1937)

[60] Y. Ashie et al. (Super-Kamiokande), "A Measurement of atmospheric neutrino oscillation parameters by SUPER-KAMIOKANDE I", Phys. Rev. vol. D71 p. 112005 (2005), doi:10.1103/PhysRevD.71.112005, hep-ex/0501064

[61] M. Shiozawa, "Reconstruction algorithms in the Super-Kamiokande large water Cherenkov detector", Nuclear Instruments and Methods in Physics Research Section A: Accelerators, Spectrometers, Detectors and Associated Equipment vol. 433 (1) pp. 240 – 246 (1999),

doi:http://dx.doi.org/10.1016/S0168-9002(99)00359-9, URL http://www.sciencedirect.com/science/article/pii/S0168900299003599

[62] K. Abe et al. (Super-Kamiokande Collaboration), "Search for proton decay via $p \to \nu K^+$ using 260 kiloton · year data of Super-Kamiokande", Phys. Rev. D vol. 90 p. 072005 (2014), doi:10.1103/PhysRevD.90.072005, URL https://link.aps.org/doi/10.1103/PhysRevD.90.072005

[63] K. Abe et al., "Calibration of the Super-Kamiokande Detector", Nucl. Instrum. Meth. vol. A737 pp. 253–272 (2014), doi:10.1016/j.nima.2013.11.081, 1307.0162

[64] J. Highnight et al., "Super-Kamiokande events and data quality studies for T2K Run 4", Tech. Rep. TN-148, T2K (2015), www.t2k.org/docs/technotes/148

[65] K. Abe et al. ((T2K Collaboration)), "Observation of Electron Neutrino Appearance in a Muon Neutrino Beam", Phys. Rev. Lett. vol. 112 p. 061802 (2014), doi:10.1103/PhysRevLett.112.061802, http://link.aps.org/doi/10.1103/PhysRevLett.112.061802

[66] K. Abe et al. (T2K), "Search for short baseline ν_e disappearance with the T2K near detector", Phys. Rev. vol. D91 p. 051102 (2015), doi:10.1103/PhysRevD.91.051102, 1410.8811

[67] K Abe et al., "Search for Lorentz and C P T violation using sidereal time dependence of neutrino flavor transitions over a short baseline", Physical Review D vol. 95 (11) p. 111101 (2017)

[68] K. Abe et al. (The T2K Collaboration), "Measurement of Coherent π^+ Production in Low Energy Neutrino-Carbon Scattering", Phys. Rev. Lett. vol. 117 p. 192501 (2016), doi:10.1103/PhysRevLett.117.192501, URL https://link.aps.org/doi/10.1103/PhysRevLett.117.192501

[69] K. Abe et al. (T2K), "First measurement of the muon neutrino charged current single pion production cross section on water with the T2K near detector", Phys. Rev. vol. D95 (1) p. 012010 (2017), doi:10.1103/PhysRevD.95.012010, 1605.07964

[70] Ko Abe et al. (T2K), "Measurement of double-differential muon neutrino charged-current interactions on C_8H_8 without pions in the final state using the T2K off-axis beam", Phys. Rev. vol. D93 (11) p. 112012 (2016), doi:10.1103/PhysRevD.93.112012, 1602.03652

[71] K. Abe et al. (T2K Collaboration), "Measurement of the Inclusive Electron Neutrino Charged Current Cross Section on Carbon with the T2K Near Detector", Phys. Rev. Lett. vol. 113 p. 241803 (2014), doi:10.1103/PhysRevLett.113.241803, URL https://link.aps.org/doi/10.1103/PhysRevLett.113.241803

[72] K. Abe et al. (T2K Collaboration), "Measurement of the inclusive ν_μ charged current cross section on iron and hydrocarbon in the T2K on-axis neutrino beam", Phys. Rev. D vol. 90 p. 052010 (2014), doi:10.1103/PhysRevD.90.052010, URL https://link.aps.org/doi/10.1103/PhysRevD.90.052010

[73] K. Abe et al. (The T2K Collaboration), "Measurement of the ν_μ charged current quasielastic cross section on carbon with the T2K on-axis neutrino beam", Phys. Rev. D vol. 91 p. 112002 (2015), doi:10.1103/PhysRevD.91.112002, URL https://link.aps.org/doi/10.1103/PhysRevD.91.112002

[74] K. Abe et al. (T2K Collaboration), "Measurement of the neutrino-oxygen neutral-current interaction cross section by observing nuclear deexcitation γ rays", Phys. Rev. D vol. 90 p. 072012 (2014),

doi:10.1103/PhysRevD.90.072012, URL https://link.aps.org/doi/10.1103/PhysRevD.90.072012

[75] K. Abe et al. (Super-Kamiokande), "Search for proton decay via $p \to e^+\pi^0$ and $p \to \mu^+\pi^0$ in 0.31 ??megaton years exposure of the Super-Kamiokande water Cherenkov detector", Phys. Rev. vol. D95 (1) p. 012004 (2017), doi:10.1103/PhysRevD.95.012004, 1610.03597

[76] "Figure taken from http://t2k.org",

[77] G. Battistoni et al., "The FLUKA code: description and benchmarking", AIP Conference Proceedings vol. 896 (1) pp. 31–49 (2007), doi:http://dx.doi.org/10.1063/1.2720455, http://scitation.aip.org/content/aip/proceeding/aipcp/10.1063/1.2720455

[78] R. Brun, F. Carminati, and S. Giani, "GEANT: Detector Description and Simulation Tool", Technical Report No. CERN-W5013 (1994)

[79] "http://www.phy.duke.edu/ raw22/public/Prob3++/",

[80] Leila Haegel for the MaCh3 group, "MaCh3 run 1-7 joint fit with SK ν_e CC-1π^+ sample", Tech. Rep. TN-300, T2K (2017), www.t2k.org/docs/technotes/300

[81] K. Iwamoto for the P-theta group, "P-theta nue CC1pi+ Appearance Analysis Run1-6, Run1-7b, Run1-7c", Tech. Rep. TN-293, T2K (2017), www.t2k.org/docs/technotes/293

[82] Y. Hayato, "A Neutrino Interaction Simulation Program Library NEUT", Acta Physica Polonica B vol. 40 pp. 2477–2489 (2009), http://www.actaphys.uj.edu.pl/fulltext?series=Reg&vol=40&page=2477

[83] "http://jnusrv01.kek.jp/ ichikawa/tmp/jnubeam/jnubeam.htm",

[84] A. Fasso, A. Ferrari, J. Ranft, and P.R. Sala, Proceedings of the International Conference on Calorimetry in High Energy Physics (1994)

[85] N. Abgrall et al. (The NA61/SHINE Collaboration), "Measurements of cross sections and charged pion spectra in proton-carbon interactions at 31 GeV/c", Phys. Rev. C vol. 84 p. 034604 (2011), doi:10.1103/PhysRevC.84.034604, http://link.aps.org/doi/10.1103/PhysRevC.84.034604

[86] A. Bercellie et al., "Implementation of additional NIWG cross section parameterizations for 2014 analyses", Tech. Rep. TN-193, T2K (2015), www.t2k.org/docs/technotes/193

[87] C. H. Llewellyn Smith, "Neutrino Reactions at Accelerator Energies", Phys. Rept. vol. 3 pp. 261–379 (1972), doi:10.1016/0370-1573(72)90010-5

[88] R.A. Smith and E.J. Moniz, "Neutrino reactions on nuclear targets", Nuclear Physics B vol. 43 pp. 605 – 622 (1972), doi:http://dx.doi.org/10.1016/0550-3213(72)90040-5, URL http://www.sciencedirect.com/science/article/pii/0550321372900405

[89] E. J. Moniz et al., "Nuclear Fermi Momenta from Quasielastic Electron Scattering", Phys. Rev. Lett. vol. 26 pp. 445–448 (1971), doi:10.1103/PhysRevLett.26.445, URL https://link.aps.org/doi/10.1103/PhysRevLett.26.445

[90] Omar Benhar and Adelchi Fabrocini, "Two-nucleon spectral function in infinite nuclear matter", Phys. Rev. C vol. 62 p. 034304 (2000), doi:10.1103/PhysRevC.62.034304, http://link.aps.org/doi/10.1103/PhysRevC.62.034304

[91] A. Furmanski, “Implementing the spectral function nuclear model in NEUT, and parametrizing systematic uncertainties”, Tech. Rep. TN-184, T2K (2013), www.t2k.org/docs/technotes/184

[92] J. Nieves, I. Ruiz Simo, and M. J. Vicente Vacas, “Inclusive charged-current neutrino-nucleus reactions”, Phys. Rev. C vol. 83 p. 045501 (2011), doi:10.1103/PhysRevC.83.045501, URL https://link.aps.org/doi/10.1103/PhysRevC.83.045501

[93] R. Gran, J. Nieves, F. Sanchez, and M. J. Vicente Vacas, “Neutrino-nucleus quasi-elastic and 2p2h interactions up to 10 GeV”, Phys. Rev. vol. D88 (11) p. 113007 (2013), doi:10.1103/PhysRevD.88.113007, 1307.8105

[94] C. Wilkinson et al., “Testing charged current quasi-elastic and multinucleon interaction models in the NEUT neutrino interaction generator with published datasets from the MiniBooNE and MINERνA experiments”, Phys. Rev. D vol. 93 p. 072010 (2016), doi:10.1103/PhysRevD.93.072010, http://link.aps.org/doi/10.1103/PhysRevD.93.072010

[95] E. Wang et al., “Photon emission in neutral current interactions at the T2K experiment”, Phys. Rev. D vol. 92 p. 053005 (2015), doi:10.1103/PhysRevD.92.053005, http://link.aps.org/doi/10.1103/PhysRevD.92.053005

[96] A. Higuera et al. (MINERvA Collaboration), “Measurement of Coherent Production of $\pi^{\pm}$ in Neutrino and Antineutrino Beams on Carbon from E_{ν} of 1.5 to 20 GeV”, Phys. Rev. Lett. vol. 113 p. 261802 (2014), doi:10.1103/PhysRevLett.113.261802, URL https://link.aps.org/doi/10.1103/PhysRevLett.113.261802

[97] Dieter Rein and Lalit M Sehgal, “Neutrino-excitation of baryon resonances and single pion production”, Annals of Physics vol. 133 (1) pp. 79 – 153

(1981), doi:http://dx.doi.org/10.1016/0003-4916(81)90242-6, http://www.sciencedirect.com/science/article/pii/0003491681902426

[98] P. Rodrigues et al., "Tuning the NEUT resonance model", Tech. Rep. TN-197, T2K (2014), www.t2k.org/docs/technotes/197

[99] Krzysztof M. Graczyk and Jan T. Sobczyk, "Form factors in the quark resonance model", Phys. Rev. D vol. 77 p. 053001 (2008), doi:10.1103/PhysRevD.77.053001, URL https://link.aps.org/doi/10.1103/PhysRevD.77.053001

[100] Jihn E. Kim, Paul Langacker, M. Levine, and H. H. Williams, "A theoretical and experimental review of the weak neutral current: a determination of its structure and limits on deviations from the minimal $SU(2)_L \times U(1)$ electroweak theory", Rev. Mod. Phys. vol. 53 pp. 211–252 (1981), doi:10.1103/RevModPhys.53.211, URL https://link.aps.org/doi/10.1103/RevModPhys.53.211

[101] M. Dunkman et al., "Updated Recommendation of the 2014-5 Oscillation Parameters", Tech. Rep. TN-265, T2K (2015), www.t2k.org/docs/technotes/265

[102] Konstantin S. Kuzmin, Vladimir V. Lyubushkin, and Vadim A. Naumov, "Quasielastic axial-vector mass from experiments on neutrino-nucleus scattering", Eur. Phys. J. vol. C54 pp. 517–538 (2008), doi:10.1140/epjc/s10052-008-0582-x, 0712.4384

[103] Hartmut Abele, "The Standard Model and the neutron β-decay", Nuclear Instruments and Methods in Physics Research Section A: Accelerators, Spectrometers, Detectors and Associated Equipment vol. 440 (3) pp. 499 – 510 (2000), doi:https://doi.org/10.1016/S0168-

9002(99)01027-X, URL http://www.sciencedirect.com/science/article/pii/S016890029901027X

[104] A. Bercellie et al., "Cross section parameters for 2014 oscillation analysis", Tech. Rep. TN-192, T2K (2015), www.t2k.org/docs/technotes/192

[105] K. M. Graczyk, D. Kiełczewska, P. Przewłocki, and J. T. Sobczyk, "C_5^A axial form factor from bubble chamber experiments", Phys. Rev. D vol. 80 p. 093001 (2009), doi:10.1103/PhysRevD.80.093001, URL https://link.aps.org/doi/10.1103/PhysRevD.80.093001

[106] M. Martini, M. Ericson, G. Chanfray, and J. Marteau, "Unified approach for nucleon knock-out and coherent and incoherent pion production in neutrino interactions with nuclei", Phys. Rev. C vol. 80 p. 065501 (2009), doi:10.1103/PhysRevC.80.065501, http://link.aps.org/doi/10.1103/PhysRevC.80.065501

[107] Melanie Day and Kevin S. McFarland, "Differences in Quasi-Elastic Cross-Sections of Muon and Electron Neutrinos", Phys. Rev. vol. D86 p. 053003 (2012), doi:10.1103/PhysRevD.86.053003, 1206.6745

[108] Patrick de Perio, "NEUT Systematic Studies for 2010a Analysis", Tech. Rep. TN-032, T2K (2010), www.t2k.org/docs/technotes/032

[109] M. Hartz et al., "ND280 Flux and Cross Section Constraint (BANFF) for 2015/16", Tech. Rep. TN-230, T2K (2014), www.t2k.org/docs/technotes/230

[110] Asher Kaboth Jordan Myslik, Mark Hartz and Mark Scott, "ND280 Flux and Cross Section Constraint for 2014", Tech. Rep. TN-220, T2K (2014), www.t2k.org/docs/technotes/220

[111] J. Imber et al., "Super-Kamiokande events and data quality studies for T2K Run 7", Tech. Rep. TN-284, T2K (2016), www.t2k.org/docs/technotes/284

[112] S. Baker and R. D. Cousins, "Clarification of the use of CHI-square and likelihood functions in fits to histograms", Nuclear Instruments and Methods in Physics Research vol. 221 pp. 437–442 (1984), doi:10.1016/0167-5087(84)90016-4

[113] C. Andreopoulos et al., "T2K 6.914×10^{20}-POT Neutrino 4.011×10^{20}-POT Anti-Neutrino 3-Flavour Joint Analysis", Tech. Rep. TN-266, T2K (2016), www.t2k.org/docs/technotes/266

[114] Gary J. Feldman and Robert D. Cousins, "A Unified approach to the classical statistical analysis of small signals", Phys. Rev. vol. D57 pp. 3873–3889 (1998), doi:10.1103/PhysRevD.57.3873, physics/9711021

[115] J. Neyman, "Outline of a Theory of Statistical Estimation Based on the Classical Theory of Probability", Phil. Trans. Roy. Soc. Lond. vol. A236 (767) pp. 333–380 (1937), doi:10.1098/rsta.1937.0005

[116] K. Abe et al. (T2K), "Measurement of neutrino and antineutrino oscillations by the T2K experiment including a new additional sample of ν_e interactions at the far detector", (2017), 1707.01048

[117] Glen Cowan, Kyle Cranmer, Eilam Gross, and Ofer Vitells, "Asymptotic formulae for likelihood-based tests of new physics", Eur. Phys. J. vol. C71 p. 1554 (2011), doi:10.1140/epjc/s10052-011-1554-0, 10.1140/epjc/s10052-013-2501-z, [Erratum: Eur. Phys. J.C73,2501(2013)], 1007.1727

[118] K. Abe et al. (T2K), "Updated T2K measurements of muon neutrino and antineutrino disappearance using 1.5×10^{21} protons on target", Phys. Rev. vol. D96 (1) p. 011102 (2017), doi:10.1103/PhysRevD.96.011102, 1704.06409

[119] F. James, "MINUIT Function Minimization and Error Analysis – Reference Manual, Version 94.1", CERN Program Library Long Writeup D506, https://root.cern.ch/sites/d35c7d8c.web.cern.ch/files/minuit.pdf

[120] H. Jeffreys, The Theory of Probability, OUP Oxford (1998), https://books.google.ca/books?id=vh9Act9rtzQC

[121] K. Abe et al. (T2K Collaboration), "Measurement of Muon Antineutrino Oscillations with an Accelerator-Produced Off-Axis Beam", Phys. Rev. Lett. vol. 116 p. 181801 (2016), doi:10.1103/PhysRevLett.116.181801, URL https://link.aps.org/doi/10.1103/PhysRevLett.116.181801

[122] K. Abe et al. (Super-Kamiokande Collaboration), "Search for Differences in Oscillation Parameters for Atmospheric Neutrinos and Antineutrinos at Super-Kamiokande", Phys. Rev. Lett. vol. 107 p. 241801 (2011), doi:10.1103/PhysRevLett.107.241801, http://link.aps.org/doi/10.1103/PhysRevLett.107.241801

[123] P. Adamson et al. (The MINOS Collaboration), "Improved Measurement of Muon Antineutrino Disappearance in MINOS", Phys. Rev. Lett. vol. 108 p. 191801 (2012), doi:10.1103/PhysRevLett.108.191801, URL https://link.aps.org/doi/10.1103/PhysRevLett.108.191801

[124] S. Bolognesi et al., "Assessing the effect of cross-section model uncertainties on the T2K oscillation analyses with fake data studies using the BANFF, MaCh3 and VALOR frameworks", Tech. Rep. TN-285, T2K (2016), www.t2k.org/docs/technotes/285

[125] J. Nieves, I. Ruiz Simo, F. Sánchez, and M. J. Vicente Vacas, "CCQE, 2p2h excitations and ν-energy reconstruction", AIP Conf. Proc. vol. 1663 p. 080005 (2015), doi:10.1063/1.4919493, 1304.1032

[126] R. B. Patterson (NOvA), "First Oscillation Results from NOvA", Fermilab JETP Seminar (2015), http://nova-docdb.fnal.gov/cgi-bin/ShowDocument?docid=13883

[127] Ko Abe et al., “Proposal for an Extended Run of T2K to 20×10^{21} POT”, (2016), 1609.04111

[128] C. Adams et al. (LBNE), “The Long-Baseline Neutrino Experiment: Exploring Fundamental Symmetries of the Universe”, (2013), 1307.7335

[129] “http://www.dunescience.org/”,

[130] K. Abe et al. (Hyper-Kamiokande Working Group), “A Long Baseline Neutrino Oscillation Experiment Using J-PARC Neutrino Beam and Hyper-Kamiokande”, (2014), 1412.4673, URL https://inspirehep.net/record/1334360/files/arXiv:1412.4673.pdf

[131] Andrew Renshaw (Super-Kamiokande), “Research and Development for a Gadolinium Doped Water Cherenkov Detector”, Phys. Procedia vol. 37 pp. 1249–1256 (2012), doi:10.1016/j.phpro.2012.02.467, 1201.1017

[132] Proceedings, 10th International Workshop on Neutrino-Nucleus Interactions in the Few GeV Region (NuInt15), vol. 12 (2016)

[133] C. Andreopoulos et al., “TITUS: the Tokai Intermediate Tank for the Unoscillated Spectrum”, (2016), 1606.08114

[134] “http://indico.ipmu.jp/indico/event/52/”,

[135] Florian Plentinger and Werner Rodejohann, “Deviations from tribimaximal neutrino mixing”, Phys. Lett. vol. B625 pp. 264–276 (2005), doi:10.1016/j.physletb.2005.08.092, hep-ph/0507143